

8-2009

# DEVELOPMENT OF A RIGID RING TIRE MODEL AND COMPARISON AMONG VARIOUS TIRE MODELS FOR RIDE COMFORT SIMULATIONS

Norm Frey

Clemson University, norman.frey@us.michelin.com

Follow this and additional works at: [https://tigerprints.clemson.edu/all\\_theses](https://tigerprints.clemson.edu/all_theses)



Part of the [Engineering Mechanics Commons](#)

---

## Recommended Citation

Frey, Norm, "DEVELOPMENT OF A RIGID RING TIRE MODEL AND COMPARISON AMONG VARIOUS TIRE MODELS FOR RIDE COMFORT SIMULATIONS" (2009). *All Theses*. 615.

[https://tigerprints.clemson.edu/all\\_theses/615](https://tigerprints.clemson.edu/all_theses/615)

This Thesis is brought to you for free and open access by the Theses at TigerPrints. It has been accepted for inclusion in All Theses by an authorized administrator of TigerPrints. For more information, please contact [kokeefe@clemson.edu](mailto:kokeefe@clemson.edu).

DEVELOPMENT OF A RIGID RING TIRE MODEL AND COMPARISON AMONG  
VARIOUS TIRE MODELS FOR RIDE COMFORT SIMULATIONS

---

A Thesis

Presented to

the Graduate School of

Clemson University

---

In Partial Fulfillment

of the Requirements for the Degree

Master of Science

Mechanical Engineering

---

by

Norman W. Frey

August 2009

Advisor: Dr. E. Harry Law

## ABSTRACT

One vehicle subassembly that is of great importance to automobile manufacturers for tuning final vehicle performance is the pneumatic tire. Pneumatic tires present themselves as unique tuning tools as they 1) are the sole link between the roadway surface and the integrated vehicle suspension, chassis and steering systems, and 2) provide a wide range of tunability over many vehicle performances, including handling (steering feel as well as chassis dynamics), traction (braking, driving, and cornering), and ride comfort (roadway isolation). Therefore the vehicle manufacturing industry continues to research and refine various aspects of tire modeling to improve up-front integrated tire/vehicle CAE/CAD model fidelity over a wide range of operating conditions.

Because tires are highly complex, nonlinear, viscous-elastic composite structures they prove to be difficult to accurately model over their entire operating range. As a result, vehicle and tire manufacturers continue to work with relatively simple models that adequately represent the tire for the integrated vehicle performance over an operating regime of interest. This paper evaluates several simple tire models in order to compare their relative advantages and applicability. One of the tire models being compared is a new embodiment in MatLab Simulink of a rigid ring tire model designed for ride comfort modeling of low-frequency and moderate amplitude roadway inputs, and whose data file is capable of being populated quickly using inexpensive standardized laboratory test methods. In addition to the aforementioned tire models, several iterations of an F-Tire tire model are interfaced with Intec's SIMPACK multi-body simulation software as an industry reference.

## DEDICATION

I would like to dedicate this thesis to my parents and my loving wife and family, who have been so supportive of my endeavors. Without them, completion of this thesis would have never been possible.

## ACKNOWLEDGMENTS

I would like to express my deepest gratitude to my advisor, Dr. E. Harry Law, for the guidance and encouragement he provided throughout this research. Without his support, I could have never completed this thesis. I would also like to sincerely thank Michelin Americas Research Company for their invaluable support, Mr. Robert Solomon of Intec Incorporated for giving me the opportunity to conduct portions of this research using their SIMPACK multi-body simulation software, and Dr. Michael Gipser of Cosin Inc. for the use of his FTire tire model. I am also extremely grateful to Dr. Imtiaz-Ul Haque and Dr. Tim Rhyne for not only serving as my committee members and for the insights they provided, but also their patience and understanding. Finally, I would like to acknowledge my colleague and fellow Clemson Graduate, Robert Lawson, who helped me stay true to my course.

## TABLE OF CONTENTS

	Page
TITLE PAGE .....	i
ABSTRACT .....	ii
DEDICATION .....	iii
ACKNOWLEDGMENTS .....	iv
LIST OF TABLES .....	viii
LIST OF FIGURES .....	ix
EXPLANATION OF SYMBOLS .....	xiv
1. INTRODUCTION .....	1
Research Motivation and Problem Statement .....	1
Background and Literature Review .....	9
Outline of Thesis .....	12
2. RIDE COMFORT TIRE MODELS .....	14
Introduction .....	14
Considerations for Selecting a Ride Comfort Tire Model .....	16
Ride Comfort Tire Model Functional Requirements .....	16
Ride Comfort Tire Model Implementation Considerations .....	18
Investigated Tire Models .....	20
Overview of Tire Models .....	20
Spring-Type Ride Comfort Tire Models .....	23
Adaptation of Spring Tire Models for Fixed Spindle Testing .....	26
Two Point Contact, Rigid Ring, Ride Comfort Tire Model .....	29
Five Point Contact Follower Rigid Ring Ride Comfort Tire Model ....	31
Cosin FTire and Intec SIMPACK MBS Automotive Plus .....	31
3. DERIVATION OF THE RIGID RING TIRE MODELS .....	33
Introduction .....	33
Equations of Motion for the Two Point Follower Rigid Ring Tire Model .....	38
Extending from a Two Point to a Five Point Follower for the Rigid Ring .....	53
4. CONDUCTING THE INVESTIGATION OF THE TIRE MODEL .....	60
Introduction .....	60

Cleat Phase – Laboratory Measurement to Validate Tire Models .....	63
Simulation Software.....	63
Laboratory Tests .....	63
Testing for Tire Model Parameters .....	66
Development of Tire Models in Simulink .....	68
Implementation Strategy.....	68
Obstacle “Conditioning” .....	70
Implementation of the Tire Models in Simulink.....	73
Development of the FTire and Simulink Combined Model .....	77
Implementation of the Tire Models in SIMPACK Vehicle Plus .....	80
Ride Phase – Ride Comfort Predictions of Quarter Vehicle Models.....	87
Tire Selection and Tire Modeling Considerations .....	89
5. RESULTS OF FIXED SPINDLE, CLEAT PHASE .....	95
Introduction.....	95
Cleat Phase Results – Fixed Spindle Road Wheel Investigation .....	97
Fixed Spindle Road Wheel Cleat Testing.....	102
Load and Speed Effects on Laboratory Road Wheel Cleat Tests.....	104
Fixed Spindle Results – Point Contact Follower .....	107
Fixed Spindle Results – Ring Contact Follower.....	114
Fixed Spindle Results – Constant Footprint Model.....	119
Fixed Spindle Results – Adaptive Footprint Model .....	124
Fixed Spindle Results – Two Point Follower Rigid Ring Model .....	128
Fixed Spindle Results – Five Point Follower Rigid Ring Model .....	132
Fixed Spindle Results – Cosin FTire and SIMPACK MBS .....	135
FTire Simulation Considerations .....	137
Cleat Phase Results – Analysis.....	139
Cleat Phase Peak Spindle Force Objective Metrics.....	139
Cleat Phase Objective Metric Analysis.....	142
6..RESULTS OF QUARTER VEHICLE, RIDE PHASE .....	147
Ride Phase Simulation Overview .....	147
Ride Phase Roadway Obstacles .....	149
Ride Phase Simulation Plots .....	152
Quarter Vehicle Results – Point Contact Follower.....	153
Quarter Vehicle Results – Ring Contact Follower .....	157
Quarter Vehicle Results – Constant Footprint Model.....	161
Quarter Vehicle Results – Adaptive Footprint Model .....	165
Quarter Vehicle Results – Two Point Follower Rigid Ring Model.....	170
Quarter Vehicle Results – Five Point Follower Rigid Ring Model .....	174
Ride Phase Results - Analysis.....	178
Ride Phase Peak Chassis Acceleration Objective Metrics .....	178
Ride Phase Peak Spindle Force Objective Metrics.....	182
Ride Phase Impulse Metric .....	185
Ride Phase Objective Metric Analysis .....	188

Tire Model Selection.....	196
Recommendations for Future Work.....	198
APPENDICES .....	200
A. Single Point Follower Simulink Model .....	201
Description.....	201
Single Spring and Point Follower with Mass at Wheel Center .....	202
Two Spring and Point Follower with Effective Summit Mass.....	206
B. Ring Follower Simulink Model.....	211
Description.....	211
Ring Follower Obstacle Filtering.....	218
C. Constant Footprint Simulink Model.....	225
D. Adaptive Footprint Simulink Model.....	239
Overview of the Adaptive Footprint Model.....	239
Derivation of the Dynamic Portion of the Adaptive Footprint Model..	251
E. Two Point Follower Rigid Ring Software.....	262
Two Point Rigid Ring Matlab MAIN Code.....	262
Two Point Rigid Ring Matlab Support Code.....	269
Two Point Rigid Ring Simulink Diagrams.....	279
F. Development of the Roadway Smooth Bump and Cleat Obstacles .....	297
Spatial Frequency Analysis.....	297
Development of the Sinusoidal Bump Obstacle .....	301
Development of the Rectangular Cleat .....	306
G. Future Simulation Improvements.....	314
Modifications to the Constant Footprint Model.....	314
FTire Simulated Contact Patch Length.....	317
REFERENCES .....	322



## LIST OF TABLES

Table	Page
Table 3.1: Longitudinal Offset of Effective Plane Elements in the 5 Point Follower .....	55
Table 4.1: Tire and Quarter Vehicle Model Parameters .....	55
Table 5.1: Cleat Phase Configurations for Fixed Spindle Lab Test .....	100
Table 5.2: Cleat Phase Tire Model Ranking via Spindle Force Objective Metrics .....	55
Table 6.1: Ride Phase Tire Model Ranking via Chassis Acceleration Metrics .....	189
Table 6.2: Ride Phase Tire Model Ranking via Wheel Spindle Force Metrics .....	192
Table 6.3: Ride Phase Tire Model Ranking Overview .....	194

## LIST OF FIGURES

Figure	Page
Figure 2.1: Location of the Principal Tire Structural Components .....	22
Figure 2.2: Point vs. Rigid Ring Contact Models.....	24
Figure 2.3: Fixed vs. Adaptive Footprint Tire Models .....	26
Figure 2.4: Single Point Follower “Simple” vs. “Equivalent Summit Mass” Models .....	28
Figure 2.5: Two Dimensional Embodiment of El-Gindy’s Rigid Ring Tire Model [2]...	30
Figure 2.6: Flexible Tire Ring Model FTire with Representative Spring/Dampers [10] .	32
Figure 3.1: Seven Degree-of-Freedom Rigid Ring Tire Model.....	37
Figure 3.2: Free Body Diagram for the Rim in the Z Axis Direction.....	39
Figure 3.3: Free Body Diagram for the Rim in the X Axis Direction .....	40
Figure 3.4: Free Body Diagram for the Rim in the Rotational Theta Direction.....	41
Figure 3.5: Free Body Diagram for the Rigid Ring in the Z Direction .....	43
Figure 3.6: Free Body Diagram for the Rigid Ring in the X Direction.....	45
Figure 3.7: Free Body Diagram for the Rigid Ring in the Theta ( $\theta$ ) Direction .....	46
Figure 3.8: Free Body Diagram for the Tread Block in the Z Direction .....	48
Figure 3.9: Free Body Diagram for the Tread Block in the X Direction.....	50
Figure 3.10: Free Body Diagram for the Tread Block in the Theta ( $\theta$ ) Direction.....	51
Figure 3.11: Effective Plane Elements in the Five Point Follower Rigid Ring Model .....	54
Figure 3.12: Physical Representation of Five vs. Two Point Contact Follower.....	56
Figure 3.13: Transfer of Contact Patch Tread Element Forces to the Rigid Ring.....	59
Figure 4.1: Investigation Process Flow Chart.....	61

List of Figures (Continued)

Figure	Page
Figure 4.2: Laboratory Road Wheel Test Machinery .....	64
Figure 4.3: Tire/Vehicle Model Implementation in Simulink .....	69
Figure 4.4: MatLab Simulink: Top Level for Single Point Contact Tire Model.....	74
Figure 4.5: MatLab Simulink: Point Contact Model Z Spindle Force Subsystem .....	76
Figure 4.6: Tire/Vehicle Model Implementation using SIMPACK and FTire.....	78
Figure 4.7: Quarter Vehicle Car Model Topology – Masses, Constraints, and Forces ....	83
Figure 4.8: Views of Quarter Vehicle Car Model as Implemented in SIMPACK .....	84
Figure 4.9: Example Tread Patterns Fitted to Modern Production Vehicles.....	91
Figure 4.10: Various Longitudinal Tire Stiffness Values.....	92
Figure 5.1: Vertical Test Spindle and Horizontal Road Wheel .....	98
Figure 5.2: Point Contact Follower – 8 Kph Fixed Spindle Results – Road Wheel Cleat	99
Figure 5.3: Generation of Longitudinal Spindle Force.....	101
Figure 5.4: Road Wheel Tire and Cleat Engagement Distance .....	103
Figure 5.5: Matrices of Spindle Force Characteristics Plots for Load and Speed .....	105
Figure 5.6: “Simple” Single Point Contact Follower Traversing a Sinusoidal Cleat .....	108
Figure 5.7: “Sinusoidal Equivalent” Model of a Rectangular Cleat.....	109
Figure 5.8: “Equivalent Summit Mass” Single Point Contact - Sinusoidal Cleat .....	110
Figure 5.9: “Simple” Point Contact Follower Traversing a Trapezoidal Cleat .....	111
Figure 5.10: “Equivalent Summit Mass” Point Contact Traversing Trapezoidal Cleat .	112
Figure 5.11: “Simple” Ring Contact Follower - Sinusoidal Cleat.....	115
Figure 5.12: “Equivalent Summit Mass” Ring Contact Follower - Sinusoidal Cleat.....	116

List of Figures (Continued)

Figure	Page
Figure 5.13: “Simple” Ring Contact Follower - Rectangular Cleat .....	117
Figure 5.14: “Equivalent Summit Mass” Ring Contact Follower - Rectangular Cleat ..	118
Figure 5.15: “Simple” Constant Footprint - Sinusoidal Cleat .....	120
Figure 5.16: “Equivalent Summit Mass” Constant Footprint - Sinusoidal Cleat .....	121
Figure 5.17: “Simple” Constant Footprint – Rectangular Cleat .....	122
Figure 5.18: “Equivalent Summit Mass” Constant Footprint – Rectangular Cleat .....	123
Figure 5.19: Adaptive Footprint Model - Sinusoidal Cleat .....	126
Figure 5.20: Adaptive Footprint Model - Rectangular Cleat.....	127
Figure 5.21: Two Point Rigid Ring Model – Sinusoidal Cleat.....	130
Figure 5.22: Two Point Rigid Ring Model – Rectangular Cleat .....	131
:Figure 5.23: Five Point Rigid Ring Model – Sinusoidal Cleat.....	133
Figure 5.24: Five Point Rigid Ring Model – Rectangular Cleat.....	134
Figure 5.25: Cosin FTire SIMPACK Automotive Plus MBS – Sinusoidal Cleat .....	135
Figure 5.26: Cosin FTire and SIMPACK Automotive Plus MBS – Rectangular Cleat.	136
Figure 5.27: Normalized Peak Spindle Force for Sinusoidal Cleat.....	139
Figure 5.28: Normalized Peak Spindle Force for Rectangular Cleat.....	140
Figure 5.29: Normalized Peak Spindle Forces for Sinus Cleat .....	143
Figure 6.1: Quarter Vehicle with Simple Point Follower Tire Traversing a Bump .....	150
Figure 6.2: Quarter Model Forces and Accelerations vs. Time .....	151
Figure 6.3: Chassis Accelerations – Point Contact Model Traversing a Cleat.....	153
Figure 6.4: Spindle Forces – Point Contact Model Traversing a Cleat .....	154

List of Figures (Continued)

Figure	Page
Figure 6.5: Chassis Accelerations – Point Contact Model Traversing a Bump.....	155
Figure 6.6: Spindle Forces – Point Contact Model Traversing a Bump.....	156
Figure 6.7: Chassis Accelerations – Ring Contact Model Traversing a Cleat.....	157
Figure 6.8: Spindle Forces – Ring Contact Model Traversing a Cleat.....	158
Figure 6.9: Chassis Accelerations – Ring Contact Model Traversing a Bump .....	159
Figure 6.10: Spindle Forces – Ring Contact Model Traversing a Bump.....	160
Figure 6.11: Chassis Accelerations – Constant Footprint Model Traversing a Cleat.....	161
Figure 6.12: Spindle Forces – Constant Footprint Model Traversing a Cleat .....	162
Figure 6.13: Chassis Accelerations – Constant Footprint Model Traversing a Bump ...	163
Figure 6.14: Spindle Forces – Constant Footprint Model Traversing a Bump.....	164
Figure 6.15: Chassis Accelerations – Adaptive Footprint Model Traversing a Cleat ....	166
Figure 6.16: Spindle Forces – Adaptive Footprint Model Traversing a Cleat.....	167
Figure 6.17: Chassis Accelerations – Adaptive Footprint Model Traversing a Bump...	168
Figure 6.18: Spindle Forces – Adaptive Footprint Model Traversing a Bump .....	169
Figure 6.19: Chassis Accelerations – Two Point Rigid Ring Model Traversing a Cleat	170
Figure 6.20: Spindle Forces – Two Point Rigid Ring Model Traversing a Cleat.....	171
Figure 6.21: Chassis Accelerations – Two Point Rigid Ring Model Traversing Bump.	172
Figure 6.22: Spindle Forces – Two Point Rigid Ring Model Traversing a Bump .....	173
Figure 6.23: Chassis Accelerations – Five Point Rigid Ring Model Traversing a Cleat	174
Figure 6.24: Spindle Forces – Five Point Rigid Ring Model Traversing a Cleat.....	175
Figure 6.25: Chassis Accelerations – Five Point Rigid Ring Model Traversing Bump.	176

List of Figures (Continued)

Figure	Page
Figure 6.26: Spindle Forces – Five Point Rigid Ring Model Traversing a Bump.....	177
Figure 6.27: Peak Chassis Accelerations - Sinusoidal Cleat Simulation.....	179
Figure 6.28: Peak Chassis Accelerations – Parking Bump Simulation .....	180
Figure 6.29: Spindle Force Metrics - Sinusoidal Cleat Simulation .....	183
Figure 6.30: Spindle Force Metrics – Parking Bump Simulation.....	184

## EXPLANATION OF SYMBOLS

$\alpha$	Obstacle engagement angle, referenced from horizontal ( $rad$ )
$a$	One half contact patch length ( $m$ )
$C_{axle}$	Vehicle suspension damping ( $Nm - sec/rad$ )
$C_{tire\_t}$	Tire sidewall torsional viscous damping ( $Nm - sec/rad$ )
$C_{tread\_cr}$	Tire tread block circumferential viscous damping ( $N - sec/m$ )
$C_{tread\_vr}$	Tire tread block radial viscous damping ( $N - sec/m$ )
$F_{resist}$	Tire aerodynamic and rolling resistance drag ( $N$ )
$F_{trac}$	Longitudinal tire traction ( $N$ )
$F_{norm}$	Normal force on the tread blocks in the contact patch ( $N$ )
$F_x$	Longitudinal tire spindle force ( $N$ )
$F_z$	Vertical tire spindle force ( $N$ )
$H$	Obstacle height ( $m$ )
$I_{bead}$	Rotational moment of inertia of the tire bead ( $kg \cdot m^2$ )
$I_{rim}$	Rotational moment of inertia of the rim ( $kg \cdot m^2$ )
$I_{sys}$	Multi-Body Simulation (MBS) ground reference system
$I_{tread}$	Rotational moment of inertia of the tread block ( $kg \cdot m^2$ )
$K_{axle\_z}$	Suspension spring rate ( $kg/m$ )

$K_{\text{tire}_x}$	Tire carcass longitudinal spring rate $\left(\frac{kg}{m}\right)$
$K_{\text{tire}_z}$	Tire carcass vertical spring rate $\left(\frac{kg}{m}\right)$
$K_{\text{tire}_\theta}$	Tire sidewall torsional spring rate $\left(\frac{Nm}{rad}\right)$
$K_{\text{tread}_{cr}}$	Tread block circumferential spring rate $\left(\frac{kg}{m}\right)$
$K_{\text{tread}_{vr}}$	Tread block radial spring rate $\left(\frac{kg}{m}\right)$
L	Obstacle length in the direction of wheel travel ( $m$ )
$\mu$	Coefficient of friction $\left(\frac{N}{N}\right)$
$M_{\text{axle}}$	Mass of one-half of the vehicle axle ( $kg$ )
MBS	Multi-Body Simulation
$M_{\text{car}}$	Mass of one-quarter of the car ( $kg$ )
$M_{\text{driveline}}$	Drive moment applied to the wheel rim ( $Nm$ )
$M_{\text{effective}_{rim}}$	Mass of the rim plus one-half the mass of the tire sidewall ( $kg$ )
MOI	Moment of Inertia
$M_{\text{rim}}$	Mass of the rim ( $kg$ )
$\omega$	Rotational velocity of the rim $\left(\frac{rad}{sec}\right)$
$R_{\text{effective}}$	Rolling radius of the tire/wheel assembly ( $m$ )
$\theta_{\text{rim}}$	Rotational position of the rim ( $rad$ )
$\theta_{\text{ring}}$	Rotational position of the tire rigid ring ( $rad$ )
$\theta_{\text{tread}}$	Rotation angle of the tread block relative to horizontal ( $rad$ )



$x_{\text{axle}}$	Longitudinal position of the axle ( $m$ )
$x_{\text{car}}$	Longitudinal position of the car chassis ( $m$ )
$x_{\text{ground}}$	Longitudinal position along the ground reference plane ( $m$ )
$x_{\text{rim}}$	Longitudinal position of the wheel rim ( $m$ )
$x_{\text{ring}}$	Longitudinal position of the tire rigid ring (summit) ( $m$ )
$x_{\text{spindle\_force}}$	Longitudinal spindle force ( $N$ )
$x_{\text{tread}}$	Longitudinal position of the tire tread block ( $m$ )
$z_{\text{axle}}$	Vertical position of the vehicle axle ( $m$ )
$z_{\text{car}}$	Vertical position of the vehicle chassis, or sprung mass ( $m$ )
$z_{\text{dot\_axle}}$	Vertical velocity of the vehicle axle ( $m/\text{sec}$ )
$z_{\text{dot\_road}}$	Vertical rate of the tread block due traversal of the obstacle ( $m/\text{sec}$ )
$z_{\text{tread}}$	Vertical position of the tire tread block ( $m$ )
$z_{\text{rim}}$	Vertical position of the axle ( $m$ )
$z_{\text{ring}}$	Vertical position of the tire rigid ring ( $m$ )
$z_{\text{road}}$	Vertical position of road contact due to the obstacle ( $m$ )
$z_{\text{spindle\_force}}$	Vertical spindle force ( $N$ )
$z_{\text{tread}}$	Vertical position of tread block ( $m$ )

# CHAPTER 1

## INTRODUCTION

### Research Motivation and Problem Statement

Fierce competition and over-capacity in the automotive industry mandate constant product innovation in an attempt to differentiate one manufacturer's product from another. This results in the reduction of the lifecycle of the vehicle models [1] and drives the manufacturers to different product design philosophies and design tools, as one would expect. As seen from the perspective of an outside component supplier, however, the generalized product design process itself seems at least globally similar in methodology and consists of:

- product functional specifications based upon customer expectations and marketing (the voice of the customer). These include passenger layout, interior volume, carrying and towing capacity, fuel economy, acceleration and braking performance, cost, etc.
- basic product design specifications that dictate the overall vehicle configuration, including:
  - chassis layout (2 door / 4 door / lift-back, etc.)
  - chassis construction (body on frame, monocoque, composite monocoque/subframe, chassis material selection, etc.)
  - power train specifications (engine type and displacement, basic drive line configuration such as front wheel drive, rear wheel drive, or all wheel drive, etc.)

- suspension and steering system configurations, including
  - independent or semi-independent, strut vs. control arm vs. multi-link, etc.
  - rack and pinion vs. recirculating ball steering gear
  - power steering boost system (mechanically or electrically-driven hydraulic power assist, electrical power assist, and various boost assist control strategies)
  - forward/rearward steering gear placement relative to the wheel spindle, spindle control arm configuration, etc.

Besides the design of the components themselves, business considerations such as the availability of existing off-the-shelf components, cost and other manufacturing and packaging constraints dictate many of the chassis, steering, and suspension components and their layout. These components are either specified and designed or selected from existing designs from the onset of the vehicle development process in an effort to satisfy the final vehicle performance specifications while achieving the lowest possible final cost. Many of the vehicle-manufactured components in the chassis, suspension and steering system are therefore necessarily fixed or “frozen” early in the development process in order to ensure subsystem compatibility and manufacturability. This leaves a significant portion of the final performance adjustments to bolt-on components that are tuned specifically for the vehicle manufacturer. Tires, shock absorbers, suspension bushings, and anti-roll bars are examples of bolt-on components that are able to directly influence performance compromises inherent in the frozen chassis, suspension, and steering system design. Manufacturers depend upon these bolt-on components to achieve

the final degree of tuning with minimum disruption as the vehicle design approaches production.

A wide array of performances is continuously being influenced either deliberately or unintentionally throughout the vehicle design process. These performances include:

- noise and vibration (both airborne and structure borne),
- road isolation and comfort
- steady-state and transient chassis handling (in both the linear and non-linear regimes)
- on-center steering performance and feel

All of these performance issues are greatly influenced by the design or tuning of bolt-on components that do not significantly impact the manufacturing process of the vehicle.

One simple example of this is the influence of anti-roll bars on the vehicle steady-state under steer coefficient. The anti-roll bars (sometimes called sway bars, roll bars, stabilizer bars, or anti-sway bars) directly influence the relative proportioning of the vertical load transferred between the inside and outside tires of the front and rear axles during cornering. Because the tire's ability to generate cornering force for a given slip angle is not linear with respect to vertical load, adjusting the rate of load transfer via the anti-roll bars will influence the relative rate of slip that is generated at the front and rear axles. Differences in the relative rate of slip angle change between the front and rear axles over a range of lateral acceleration is what determines the vehicle understeer characteristics, a first order handling parameter. This example illustrates that the vehicle manufacturer can, by varying the characteristics of a single bolt-on component, adjust the

final steady-state vehicle under steer characteristics for a given chassis, suspension, and steering system configuration whose design has long since been frozen for production.

The tire, by virtue of its position as the sole interface between the road surface and the vehicle suspension, is one of the key bolt-on components fitted during the vehicle assembly process. The tire is unique in that it can provide a final degree of tuning for virtually all of the integrated vehicle ride, comfort, handling, traction and noise performances. Vehicle manufacturers recognize this and therefore press tire manufacturers into a performance tuning role. Consequently, tire manufacturers employ a variety of predictive modeling tools to assist in these tuning roles in which they will be asked to participate.

One of the performance factors that continues to challenge designers is that of vehicle longitudinal and vertical ride comfort. Tire tuning for comfort can be particularly important for integrated tire/vehicle tuning as absorbing and damping the effect of traversing roadway obstacles depends heavily on the combination of both tire and chassis/suspension characteristics. Since the vehicle design characteristics that can significantly affect ride comfort are frequently frozen before final vehicle tuning and design release, the tire's role is of great importance to the final satisfactory ride and comfort performance of the vehicle.

One can better understand the comfort tuning options available to the vehicle designer by examining the available tuning parameters in the vertical and horizontal direction. For the vertical component of ride comfort, the principal chassis and suspension tuning parameters include:

- suspension vertical spring rate

- low and high-speed shock absorber damping characteristics
- suspension vertical friction (hysteresis)
- suspension bushing stiffness, damping, and hysteresis principally for those bushings located:
  - at the end of the shock absorber or strut attachment points
  - between the suspension components and the chassis frame or sub frame

As suspension travel is oriented vertically, there are more options for suspension ride tuning in the vertical direction. However, vertical road perturbations are accompanied by some corresponding longitudinal force component which must also be absorbed by the tire/vehicle system. In the horizontal direction, the principal chassis and suspension tuning parameters for ride comfort is suspension longitudinal compliance, consisting of:

- stiffness, damping, and hysteresis associated with bushings located principally between the suspension components and the chassis frame or sub frame and
- kinematic reaction (fore/aft movement of the wheel spindle upon vertical displacement of the spindle as it traverses the road perturbation)

Since the roadway perturbances must be accommodated by the chassis after passing through the tire, the tire's transfer function between the roadway and suspension:

- has a first order effect on ride and comfort performance
- provides the vehicle manufacturer with additional integrated tire/vehicle tuning possibilities that may be particularly important in the horizontal

direction, where longitudinal suspension tuning is limited in both options and range.

The transfer function between the roadway and the wheel spindle as a tire traverses an obstacle, necessary to evaluate longitudinal and vertical ride comfort as well as predicting vehicle suspension loadings, is a subject of ongoing research. Because the tire is a complex integration of natural and synthetic rubber polymers, metallic and non-mettalic cords and composite laminar structures, the transmission of forces between the tire contact patch and the vehicle spindle due to:

- lateral forces as a result of tire slip angle and tire camber angle relative to a smooth roadway surface, or
- the generation of longitudinal braking or driving forces as a result of a differential interface velocity between the tire tread band and the roadway surface, or
- the generation of longitudinal and vertical forces as the tire traverses a roadway obstacle

is highly non-linear and dependent upon the solicitation frequency and amplitude of inputs at the tire contact patch. Therefore accurate modeling and prediction of the generated tire forces and force transfer between the tire contact patch and the wheel spindle is complex even when examined for the most simple tire solicitations. In order to obtain useful vehicle simulation results, vehicle manufacturers use a myriad of techniques to represent the tire forces:

- representative statistical data from on-track analytical test machines and instrumented test hubs,

- indoor laboratory force and moment measurement machines,
- modal and FEA models

Recognizing some of the specific development needs of both vehicle manufacturers and tire manufacturers for ride comfort modeling, it was postulated that examination of simple tire models could result in the development of a more utilitarian tire model that could aid tire manufacturers bridge the gap between:

- complex non-linear models, such as
  1. FEA tire models, which require numerous complex inputs, such as anisotropic nonlinear material properties
  2. sophisticated multi-body simulation (MBS) tire models, which require extensive laboratory testing to characterize and optimize the model parameters and validation testing to verify their performance
  3. modal substructure modeling, which again requires sophisticated test measurement and careful validation of performance over the intended regime of interest
- and elementary tire models (consisting of simple linear spring and dampers)

A simplified tire model that could incorporate parameters that were easily measurable with standard laboratory tire tests could improve the ability of tire companies to work with vehicle manufacturers to optimize ride and comfort performance tuning with the tire as the vehicle passes through its final stages of prototyping. It could also help tire companies to better diagnose ride issues associated with integrated tire/vehicle ride comfort performance in order to better tune their tires.



This investigation examines a spectrum of tire models, ranging from an array of simple linear tire models that are used for initial ride comfort tuning, to several more complicated rigid ring tire models, and finally to a sophisticated commercially-available multi-body simulation of a flexible ring tire model, FTire. The purpose of this investigation is to better understand limitations and advantages inherent with the different types of tire models for ride comfort modeling. The goal is to better serve integrated tire/vehicle tire design by establishing general guidelines for applying the various tire models. Steps to implement this investigation will include:

1. Develop an understanding of tire model selection criteria for use with integrated tire/vehicle ride/comfort modeling
2. Develop a method for evaluating the ride comfort tire model parameters either by measuring physical tires in a laboratory environment or by simulating the tire properties in an FEA development environment. Determining the ride comfort tire model parameters using existing physical tires should:
  - a. use simple and readily-available non-destructive machine test methods
  - b. emphasize speed and the understanding of potential relative performance differences between tires (e.g. the physical testing and examination of competitor tires, where FEA tire models are not available)
3. Validate some of the tire model and parameter measurement methods by comparing results from laboratory fixed spindle road wheel cleat testing, and a commercial, flexible-ring tire model, FTire (in a multi-body simulation package SIMPACK).

### Background and Literature Review

Simply stated, the functions of tires on ground vehicles are to support the weight of the vehicle, provide longitudinal and lateral tractive forces to accelerate and decelerate the vehicle, and help cushion the vehicle from the effects of road surface irregularities in order to improve driver and passenger ride comfort [2]. Interestingly, the invention of the pneumatic tire was not for improving its vehicle weight capacity or increasing traction or handling, but for improved ride comfort. This is evidenced by the patent filed in France in 1846 by Robert William Thompson, the inventor of the pneumatic tire, which stated that his tire was inflated with air so that the wheels presented “a cushion of air to the ground, rail or track on which they run.”

The need for pneumatic tire models to provide the transfer function between the irregular roadway surface and the vehicle in order to predict vehicle ride performance has long been recognized. Gough and Jones [3] developed rigorous experimental testing of pneumatic tires as early as 1952. Lippman [4] extended Gough’s contention in the early 60’s that a tire rotating about a spindle of fixed height and slowly traversing an obstacle whose width is much shorter than the length of the tire contact patch would result in distinct characteristic signatures for vertical and longitudinal force. This research introduced the distinction between 1) point contact models, which assumed that all of the tire vertical tire force was the result of a single point which followed the terrain contours precisely, and 2) enveloping models, which take into account spatial frequency filtering due to contact patch length and mitigation of the peak vertical forces due to physical deformation within the contact patch.

Captain et al [5] summarized the state of the art for tire comfort models in 1974 as part of their research for the Army-Tank Automotive Command. Their work provides a succinct summary of the following basic tire models

1. the simple point contact model
2. a rigid tread band model (a point model which takes into account spatial path frequency filtering)
3. a fixed footprint model (constant contact patch area)
4. an adaptive footprint model (tire contact conforms to the terrain and the contact patch area changes with vertical deflection)

Later on Kisilowski et al [6] and Zegelaar [7] provided summaries of various enveloping models, the latter as late as 1998. These summaries include more complex enveloping models, including flexible ring and sophisticated radial / inter-radial spring models that represent degrees of freedom which are orders of magnitude greater than earlier models and require numerically more powerful computers. Enveloping models were further advanced by Guo and Liu [8], who include distributed vertical stiffness over the length of the contact patch, and flexible roller terrain following. Schmeitz [9] also discusses various enveloping models as well as distinguishing between “static” and “dynamic” tire models, the latter of which take into account tire mode shapes. Schmeitz subsequently describes applications of these semi-empirical “dynamic” tire models for traversing road profiles, his model using an interesting approach for obstacle envelopment by utilization of tandem ellipses or “cams” (one each representing the front and rear of the tire contact patch, respectively) to describe the envelopment of perturbances by an effective road plane surface. Gipser [10] developed a multi-

bodysimulation approach for a flexible ring model, representing the composite lamina in the summit belt package as consecutive mass/spring elements forming a series of circumferential hoops positioned parallel and laterally across the tread span.

The use of tire models in multi-body vehicle simulations (MBS) for up-front computer aided engineering (CAE) drives the development of many of the tire models. Eichberger and Schittenhelm [11] describe the classification of tire models as either simple (based upon spring/damper representation) or approximation (based upon mathematical modeling of tire forces from measured force and moment behaviors). They address the selection of appropriate tire models for vehicle MBS for the performance of interest, the amplitude of the vehicle oscillation, and the frequency of the vehicle oscillation. Lugner et al [12] describe three dynamic tire models for MBS simulations: FTire (including both flexible and non-flexible summit belt configurations), RMOD-K (a detailed finite element model of the actual tire structure), and SWIFT (a hybrid model using both empirical force fitting and the physical modeling of the belt package ring).

This investigation will provide another point of comparison among the multitude of continuously evolving tire models. FTire, developed by Dr. Michael Gipser and marketed under Cosin Inc. is implemented with SIMPACK Automotive Plus MBS software, developed by Intec as one of the industry standards for multibody ground vehicle simulation. FTire will be compared to laboratory measurements and simulation results from other tire models to explore the gain in model fidelity using this current state-of-the-art model and the resultant improvement on vehicle comfort modeling.

### Outline of Thesis

Chapter 1 provides a general introduction to this thesis. In this chapter, background information is provided, including the motivation behind the thesis research and a framework of how research of this type is relevant as it pertains to the overall integration of the tire as a subsystem in the tire/vehicle design process. In addition, the objectives of the thesis are outlined. To complete the introduction, a brief review of some of the relevant literature is presented.

The ride comfort tire models used in this investigation are discussed in Chapter 2. These models cover a range schemes to account for obstacle envelopment within the tire contact patch, from basic single-point terrain following to the more sophisticated terrain-adaptive footprint models. These models also cover different schemes for accounting for the tire dynamics that occur between the tire contact patch and the wheel spindle and which modify the spindle forces transmitted to the vehicle suspension.

The two point contact follower rigid ring model is derived in Chapter 3. The derivation starts using the basic assumptions of the rigid ring model developed by Mustafa El-Gindy [2]. The model is further developed to include a two-point contact terrain follower to emulate the tire contact patch. A brief overview of using laboratory test results to provide the tire model parameters is provided. Finally, the two-point contact rigid ring model is extended to a five point contact patch model.

In Chapter 4, implementation of the models for simulation is discussed. The use of MatLab Simulink for conducting simulation of both fixed-spindle laboratory road wheel cleat testing and quarter vehicle modeling is explained. In this chapter, a brief

overview is given of the implementation of SIMPACK multi-body (MBS) simulation tool by Intec, Inc. and Cosin FTire.

Chapter 5 consists of simulation results for the fixed-spindle height laboratory road wheel test using the range of tire models presented in Chapter 4. The validation of the model against laboratory testing is presented.

In Chapter 6, the tire models are attached to a simple quarter vehicle model. Simulation results are presented for traversing two different obstacles – a short cleat of the same dimension that was used in the fixed spindle laboratory test, and a parking lot speed bump. The tire models are compared not only for their accuracy relative to the commercial FTire model, but also for their suitability based upon their functional capability, range of applicability, and ease of use. Finally, a summary of the research findings is presented and future research topics are identified.

## CHAPTER 2

### RIDE COMFORT TIRE MODELS

#### Introduction

Because they are the sole link between the ground and the vehicle, the tires generate the majority of forces acting upon the vehicle (the other principal forces are due to aerodynamics). Therefore, some minimal representation of tire force generation is a primary requirement for modeling ground vehicle dynamics.

The tire is a complex assembly of a variety of visco-elastic polymer compounds as well as a number of orthotropic laminate composites embedded in a tensile structure. Consequently, tire force generation is non-linear and is a function of 1) operating conditions (environmental temperature, wear condition, operating pressure, characteristics of the ground surface and the terrain obstacles over which it must traverse) and 2) imposed solicitations (frequency and magnitude of loading, slip angle and camber). Consequently the development and appropriate application of tire models is an ongoing challenge with all but the most simple vehicle dynamics models.

The seven tire models that are used in this ride comfort investigation represent a wide range of models in terms of sophistication and use. The objective of developing these tire models is to gain an understanding of the limitations and suitability of the various models. This includes understanding the final objective of the integrated tire/vehicle model, the capabilities of the various tire models as well as the cost and

availability of data to determine the model parameters. These issues will ultimately determine the suitability and selection of the tire model for the simulation task at hand.



## Considerations for Selecting a Ride Comfort Tire Model

### Ride Comfort Tire Model Functional Requirements

Ride comfort tire models must reproduce the forces at the wheel spindle with sufficient accuracy such that the vehicle comfort metrics of the integrated tire/vehicle system can be predicted. For the two-dimensional case, these wheel spindle forces consist of vertical force, longitudinal force, and torsional moment about the wheel spin axis (driving or braking torque).

Even simple ride comfort models, such as a quarter vehicle model or a chassis pitch plane model, can provide insight into ride comfort modeling using only vertical spindle force inputs. For these classic chassis representations, a simple tire model which provides only vertical spindle forces via a point contact follower may be perfectly adequate for those instances where the terrain or obstacle being traversed has a wavelength greater than the length of the tire contact patch. Conversely, this same point contact follower may not be able to adequately predict vertical wheel spindle forces when the wavelength of the terrain or obstacle is less than the length of the contact patch. This is because the point contact follower has no provision for emulating the complex mechanical interaction which occurs when the tire contact patch encounters and then envelopes or “drapes” over short obstacles within the length of the contact patch. In addition, the ride metrics themselves need also be considered. Vertical ride comfort, as measured by vertical chassis acceleration, benefits from the high frequency filtering of

spindle forces via the compliant suspension system and the suspension and chassis masses. Horizontal ride comfort, as measured by horizontal chassis acceleration, does not benefit as much from this filtering effect as there is relatively little longitudinal compliance in the suspension system.

Vehicle ride comfort testing can be quite complex, as the tire/vehicle system must be evaluated over a wide range of obstacle types. For example, obstacles exist not only above the roadway plane (rectangular or square-edged cleats, bumps, etc.), but also below the roadway plane in the form of depressions (“potholes”). Obstacles such as cleats have short wavelengths which mimic impulse type inputs. Obstacles such as parking lot speed bumps and the longer roadway speed “humps” have long wavelengths. Another type of obstacle mimics step inputs. Step-up and step-down obstacles are a frequent occurrence on concrete interstate highways due to the uneven settling or shifting of concrete slabs.

Faced with such a wide variety of obstacles, vehicle and tire manufacturers have necessarily relied upon a number of standard obstacles upon which to base their ride comfort performance. The tire’s ability to absorb and dampen the impulse energy of relatively small obstacles and mitigate its effect at transmitting forces to the wheel spindle is a frequent measure of tire ride performance. This is the “enveloping power,” or the ability of the tire contact patch to deflect down, around, and envelop the obstacle, thereby reducing the peak forces at the tire center. Testing on rectangular, triangular, or rounded cleats of various dimensions that are shorter than the length of the tire contact patch are almost universally used as part of a measure of the tire’s ability to provide good ride comfort. Likewise, a tire’s ability to mitigate inputs from larger obstacles is also an

important ride performance characteristic. The tire carcass must be able to deflect over obstacles whose lengths are longer than the contact patch, thereby contributing to the total suspension compliance and helping the suspension isolate the sprung mass and improve ride comfort. Obstacles such as parking lot “speed bumps” have sufficiently long wavelength and height to measure the tire’s ride performance in this regime of operation.

Because vehicle testing uses both short and long wavelength obstacles to evaluate tire ride performance, this investigation will include simulations of both a rectangular cleat and a parking lot bump when evaluating the suitability of the seven tire ride comfort models. These two obstacles represent opposite ends of the range of wavelength and amplitude characteristics, but do not include the family of obstacles which represent “potholes” (depressions below the roadway median plane).

#### Ride Comfort Tire Model Implementation Considerations

It is important that tire ride comfort models be easy to implement. As with any modeling endeavor, testing to determine key tire characteristics and calculating the tire model parameters must be straightforward and inexpensive. The time required to integrate the tire model with existing or future vehicle ride models must also be considered. Despite the continuing increase in numerical computational power, tire models which require low computational overhead still possess distinct advantages - this is especially important if one of the goals is to support real-time driving simulators or projects involving “hardware in the loop” controllers. Costs and complexities associated

with establishing and maintaining simulation model code and software licensing requirements are all important factors that should be considered when selecting a tire model.

## Investigated Tire Models

### Overview of Tire Models

The intention of this investigation is to determine the suitability of tire models for ride comfort simulations and to examine the considerations for selecting the appropriate tire model. With the exception of the combination of the commercial software model - Cosin FTire model running with Intec SIMPACK Automotive Plus MBS software – all of tire models developed for this investigation consist of combinations of masses and linear springs and damping elements. The more complex and sophisticated models, such as modal or FEA models are not included in this investigation.

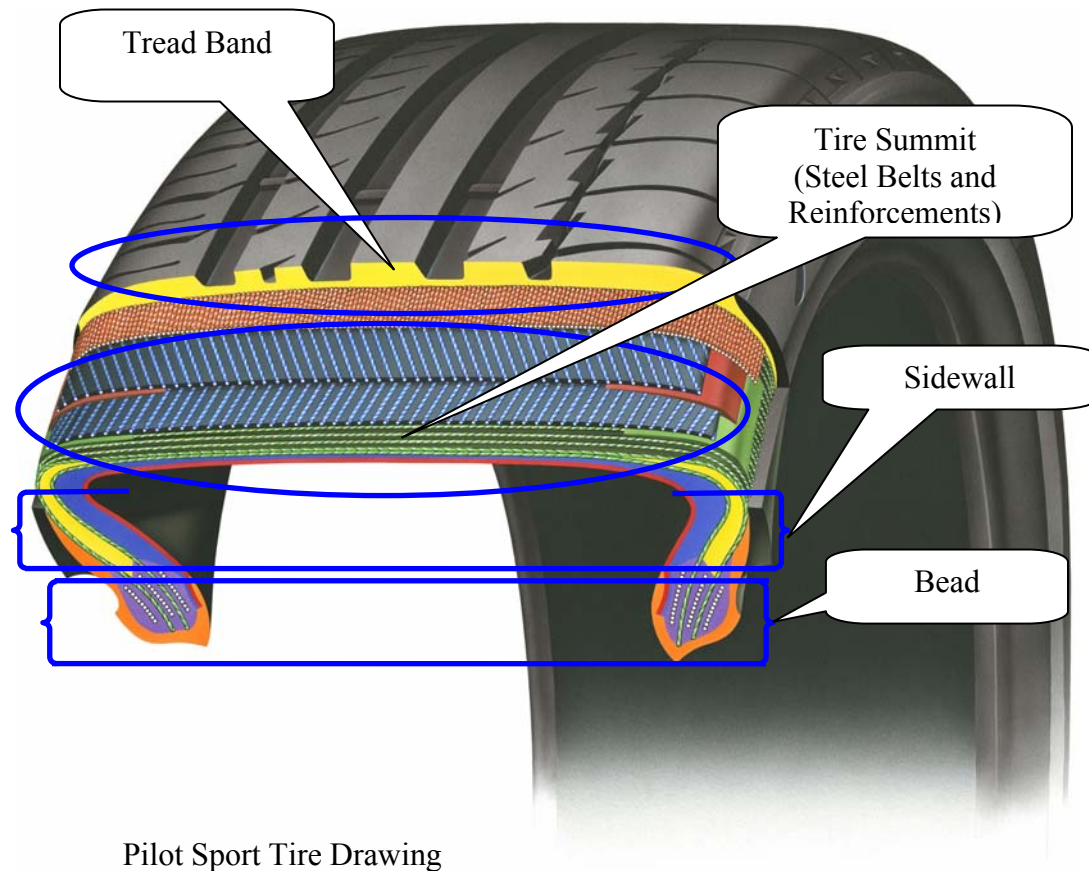
The tire models developed in this investigation use different strategies for modeling

- longitudinal driving and braking forces in the contact patch
- spindle forces as a result tire carcass deformation
- interactions of the tire and the terrain or obstacles at the tire/ground interface within the contact patch, such as the envelopment or “draping” of the contact patch over an obstacle whose length is considerably shorter than that of the contact patch

The first four tire models that are investigated consist of a common scheme to emulate how the tire carcass transmits forces between the tire contact patch and the wheel spindle – a simple spring, mass and damper system. However, each of these four “spring”

tire models differ significantly in how they emulate the interactions between the tire and the ground within the contact patch.

The next two tire models emulate the tire carcass as a rigid ring connected to the wheel spindle by springs and dampers. These two “rigid ring” tire models assume that the tire summit mass – the steel belt package and reinforcing material under the tread - can be modeled by an annular ring suspended on the inner circumference by springs representing the tire carcass and on the outer circumference by tread blocks. Because the tire summit ring is considered to be rigid, these models assume that a tread band model will be able to adequately represent the interaction between the terrain or obstacle and the tire contact patch without depending on flexibility in the tire summit ring. Figure 2.1 illustrates the location of the tread band, “rigid” summit ring, sidewall, and bead area.



Pilot Sport Tire Drawing  
Source: [www.Michelin.com](http://www.Michelin.com)

Figure 2.1: Location of the Principal Tire Structural Components

The seventh and last tire model considered is the Cosin FTire model, which models the tire summit as a flexible ring. The flexible summit ring consists of a series of rigid elements (bodies) arranged in a cylindrical shape. Combined with a sophisticated tread model, this model represents an industry standard for MBS modeling. Cosin FTire, along with other commercial tire models (such as TNO SWIFT) are capable of providing

high fidelity tire force modeling if they are provided with necessary quantities of tire test data spanning a wide range of laboratory test methods and test conditions.

### Spring-Type Ride Comfort Tire Models

The quest to understand the suitability of different analytical tire models in order to select an appropriate model for vehicle comfort simulations is not new. Khushroo M. Captain, et al [5] proposed several models for use with vehicle ride simulation modeling for the Army Tank Automotive Command, and they provide a basis for the first four of the seven categories of models used in this investigation. These first four categories of spring-type tire models consisted of (from most simple to most sophisticated):

1. Point contact follower
2. Ring adaptation of the point contact follower
3. Fixed footprint
4. Adaptive footprint

A basic schematic of the first two models, designed to illustrate and contrast their differences, is illustrated in Figure 2.2.



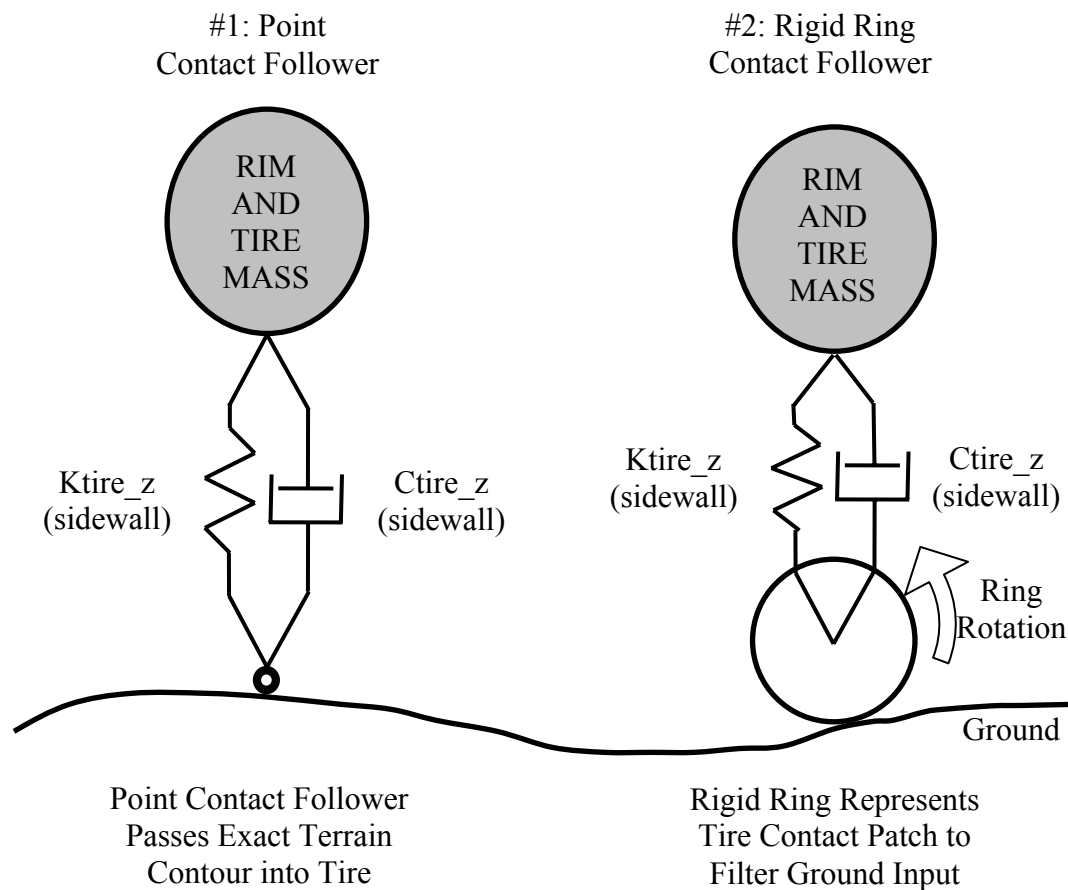


Figure 2.2: Point vs. Rigid Ring Contact Models

The rigid ring terrain follower for the second spring type tire model described by Captain et al originally used a follower ring of radius equal to that of the free radius of the tire. This is potentially the best choice for a very stiff tire (for example a commercial truck tire) traversing rugged terrain with irregularities of size roughly equivalent in magnitude to the diameter of the tire. However, this diameter does not mimic the filtering effect that occurs when the flexible contact patch of a conventional passenger tire

traverses normal obstacles. Consequently, the radius of the rigid ring terrain follower was chosen equal to one-half the length of the contact patch when evaluating this model.

The third and fourth spring-type tire models invoke compliance in the tire model at the tire/ground interface to model the enveloping power of the tire contact patch. The third model is the fixed footprint. The fixed footprint assumes that the contact patch maintains a constant footprint area, and that the vertical stiffness of the tire is distributed evenly along the length of the contact patch. The fourth model is the adaptive footprint. The adaptive footprint allows the area of the contact patch to vary as necessary to support the wheel spindle loads. The tire carcass stiffness is distributed equally and radially around the tire circumference. These two models are illustrated in Figure 2.3.

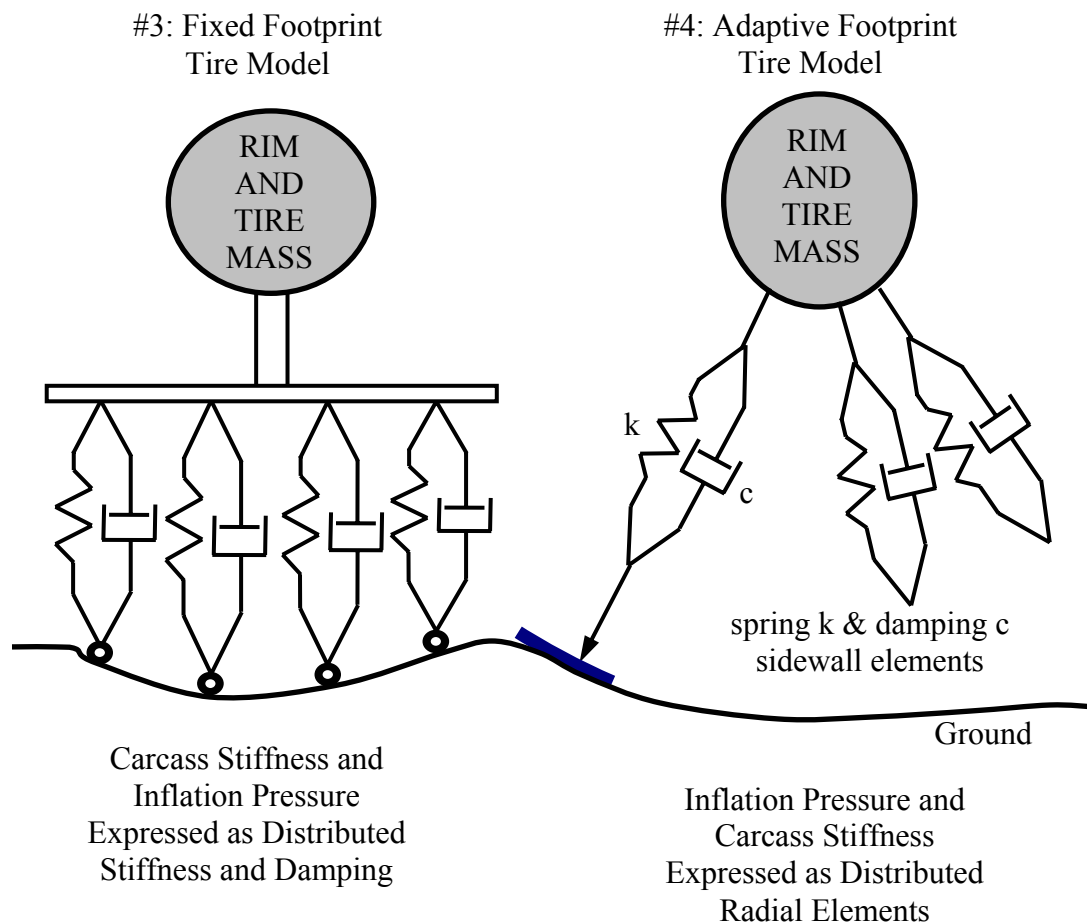


Figure 2.3: Fixed vs. Adaptive Footprint Tire Models

#### Adaptation of Spring Tire Models for Fixed Spindle Testing

It should be noted that these first four model spring-type models were used by Captain et al to conduct vehicle ride investigations of low to moderate frequencies and moderate to high amplitudes for military vehicles. Therefore the models were not intended to model the higher-frequency internal dynamics associated with the mass or structural properties of the tires themselves – the tire mass properties were simply applied to the center of the steel wheel or rim attached to the spindle. Since the primary focus was

the ability of the tire model to provide reasonable representations of spindle forces to the suspension and chassis system as the tire traversed and enveloped various terrains, it was also a reasonable assumption for the tire carcass model to consist exclusively of various arrangements of linear springs and dampers. Because any high frequency modes of the tire would be effectively filtered by relatively simple vehicle ride models – there were, for example, no chassis or suspension bushings – there was no need to model internal tire masses associated with tire modal frequencies. Instead of concentrating on modeling internal tire masses and structures, the spring-type models focused on different strategies for modeling the ability of the tire to envelop varying terrain and obstacles within the contact patch.

For this investigation, the performance of each tire model is determined by its comparison to a laboratory road wheel cleat test. The test consists of a “road” wheel to which a small rectangular cleat is affixed. Provisions are made for mounting the tire so that it remains at a fixed height above the road wheel. The road wheel rotates under the tire and sensors in the tire mounting spindle record the forces transmitted to the spindle as the cleat passes through the contact patch.

Since our output metrics of interest consist of spindle forces, there is no vertical low-pass filtering effect associated with the relatively simple vehicle models described by Captain. Therefore it was considered necessary to provide a representation of the tire sidewall, summit belt package, and tread masses in order to provide a simple representation for internal tire dynamics. The developments of these tire models, first in the “simple” original form as described by Captain, and then in their modified

“equivalent summit mass” form (with an equivalent tire sidewall and summit tread mass, as illustrated in Figure 2.4) are provided in the Appendices.

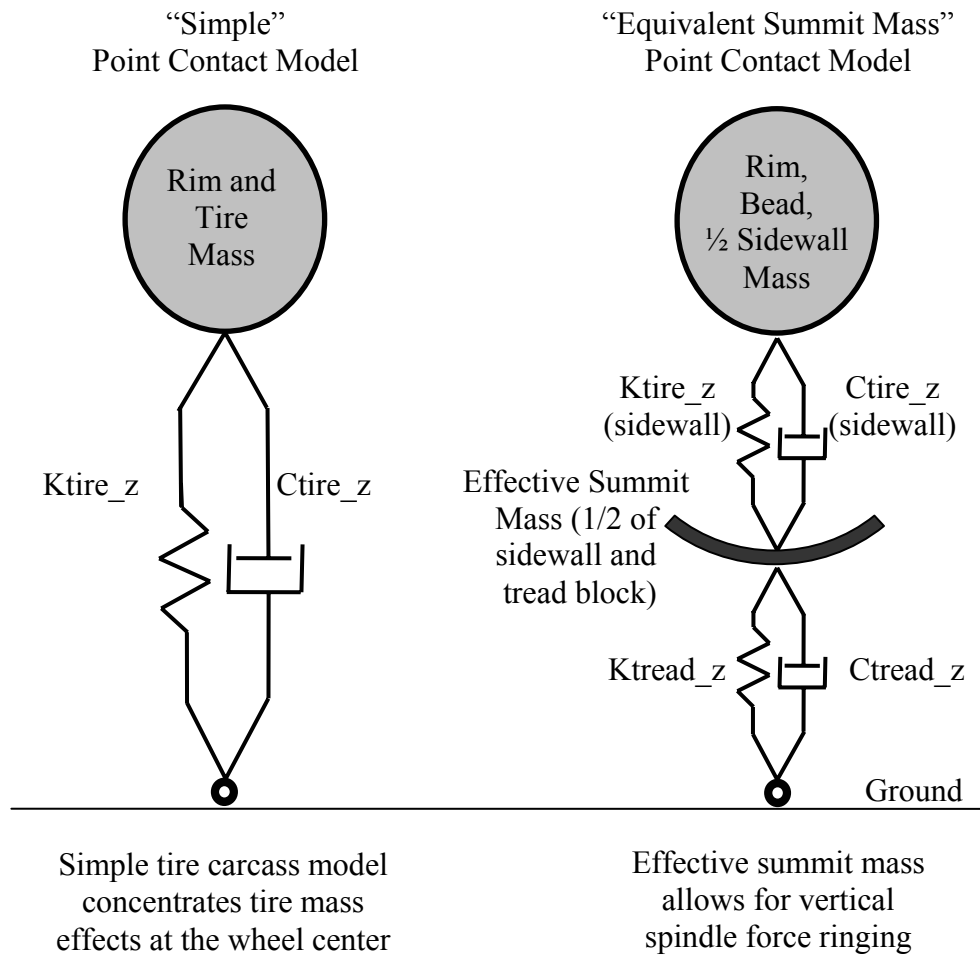


Figure 2.4: Single Point Follower “Simple” vs. “Equivalent Summit Mass” Models

Despite their relative simplicity, these first four tire models have been successfully utilized for some time, especially for first order tuning of vehicles for low frequency vertical ride comfort (less than approximately 50 Hz). It is only when more

precise and accurate predictive models are required – for example, when conducting road load (fatigue modeling of suspension components) or vibration modeling at frequencies at or above the first modal longitudinal frequency (typically 20 to 30 Hz) or first modal vertical frequency (typically 60 – 70 Hz) - that these models may prove to be inadequate.

#### Two Point Contact, Rigid Ring, Ride Comfort Tire Model

The fifth model considered for this investigation is an extension of the rigid ring model proposed by Moustafa El-Gindy and under development at the Pennsylvania State University Applied Research Laboratory [2]. This rigid ring model was developed to provide not only in-plane (X-Z vertical plane) spindle forces, but also 3-D out of plane dynamic forces. The intention was to replace a more detailed but computationally-intensive FEA model with a simpler rigid ring model that would allow faster simulation speeds while still maintaining adequate spindle force fidelity for ride, comfort, and vehicle durability modeling

A tire summit typically consists of two or more steel “ply” belts forming a composite structure underneath the tread band. These steel lamina create a structure which is stiff in comparison to other areas of the tire, such as the tire carcass and tread band. The rigid ring model assumes that the summit is completely rigid, and the enveloping properties of the tire, wherein the tire contact patch “drapes” over short wavelength obstacles in the roadway, can be incorporated into the tread block and sidewall models. A schematic of this model is shown in Figure 2.5, below.

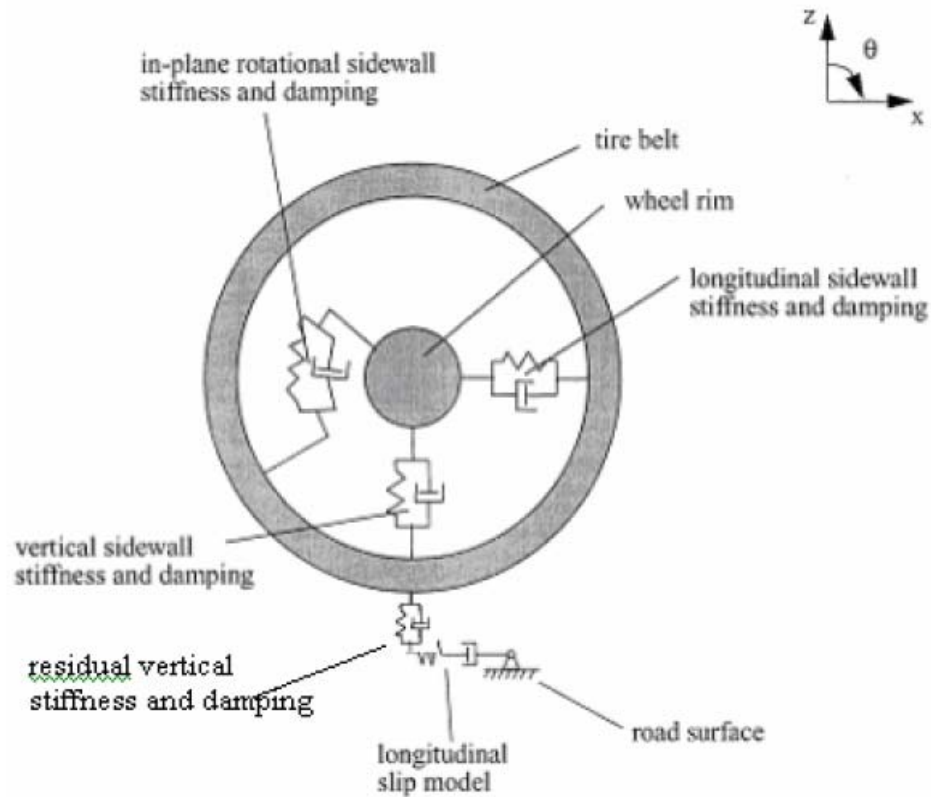


Figure 2.5: Two Dimensional Embodiment of El-Gindy's Rigid Ring Tire Model [2]

Since a comparison of the tire models for ride comfort modeling is the principal theme of this investigation, the rigid ring model was derived only for longitudinal and vertical forces in the vertical plane. This two dimensional model was, however, modified to include a two point contact patch follower to better emulate the enveloping characteristics of the tire contact patch, and a more extensive longitudinal traction force model for improved driving and braking force fidelity.

### Five Point Contact Follower Rigid Ring Ride Comfort Tire Model

The sixth tire model that was developed is an extension of the of the previous two point contact, rigid ring model. The five point contact follower model divides the single contact patch plane previously defined by the two point contact follower into four equal-length consecutive contact patch plane segments. The intention of using the four elements defined by the five point contact follower is to provide higher fidelity of normal forces across the length of the contact patch. Since the traction forces are not linear with vertical force, the average traction forces developed by the four segments should be more accurate than the traction force developed by a single average segment.

### Cosin FTire and Intec SIMPACK MBS Automotive Plus

The seventh and final model used in this investigation is a combination of two commercially-available software packages – SIMPACK Multi-Body Simulation Software by Intec Corporation and FTire flexible ring tire model by Cosin. These two software packages represent the state-of-the-art in multi-body simulation (MBS) programs. SIMPACK is used for a wide range of commercial MBS applications, and has become accepted as a standard amongst many commercial vehicle manufacturers. FTire is also a 3D multi-body simulation model that is specific to tire applications. FTire represents the stiffness of the tire summit by a series of flexible concentric hoops spanning along the spin axis of the tire. As shown in Figure 2.6, this series of flexible hoops consist of mass elements connected by tunable springs and dampers designed to mimic the functionality



of the physical tire summit structure. FTire has been highly developed such that the MBS parameters needed in the model are automatically optimized when tire test data is imported into the model. These two MBS programs interface such that the SIMPACK MBS chassis and suspension system inputs and outputs (wheel spindle forces, wheel plane positions) are continuously exchanged with FTire during the simulation.

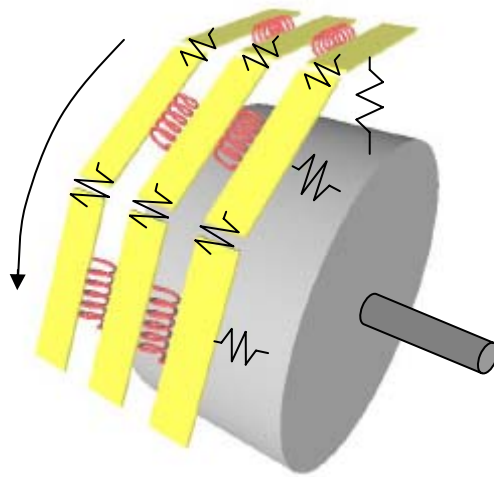


Figure 2.6: Flexible Tire Ring Model FTire with Representative Spring/Dampers [10]

## CHAPTER 3

### DERIVATION OF THE RIGID RING TIRE MODELS

#### Introduction

The tire model developed within this chapter is associated with a class of tire models known as rigid ring models. This class of models represents the tire carcass as a non-deformable hoop, or rigid ring, as the principal mass element between the ground and the wheel spindle. The particular rigid ring model that is developed here is based upon the following major characteristics:

- a multi-point ground follower is used to define the interactions between the tire contact patch and the terrain
- one (in the simplest embodiment) or multiple tread mass elements are used to represent the mass of the tire tread within the contact patch
- a rigid ring is used to represent the mass of the metallic tread bands making up the composite laminate structure in the tire summit just beneath the tread blocks
- a bead mass is used to represent that portion of tire metallic reinforcement and rubber that anchors the tire to the wheel rim, and can be associated as an integral component with the wheel rim to which the tire is mounted
- a sidewall mass is used to represent the mass of the tire carcass structure joining the rigid ring at the tire summit and the bead mass anchored at the tire/wheel interface.

The model is initially developed by representing the tread band in the contact patch as a plane defined by two points – a leading path follower at the front of the contact patch, and a trailing path follower at the rear, or exit of the contact patch. The two point follower model is further developed into a five point follower model. Using five point followers effectively splits the previously-defined single contact patch ground plane into four parts – two effective planes ahead and two effective planes behind the midpoint of the contact patch. Increasing the number and reducing the length of each effective plane increases the resolution of the interactions which take place within the contact patch at the tire/ground interface. The greater resolution is intended to allow the tire model to accommodate shorter-wavelength roadway obstacles as well as to allow more local definition of the tire tread block and ground interface forces, thereby increasing the accuracy of the net longitudinal driving/braking traction forces. These forces are calculated by a non-linear tire traction model between the contact patch elements and the roadway.

This new embodiment is an extension of rigid ring tire models developed by Mustafa El Gindy et al [2] , which included the effects of tire flexibility and nonlinear traction modeling, and lateral force generation (cornering forces developed by steering). This extension is limited in its current form to improvements ‘in plane’ of the tire wheel assembly, i.e., in the vertical and longitudinal coordinates and not in the lateral direction. These improvements include the use of an effective tread block mass and use multiple point contact patch following to improve both the traction modeling of the tire within the contact patch and to better represent the coupling between the tread components and the

rigid ring in the summit. One additional consideration for developing the improved model is its suitability for using simple standard laboratory tests to measure the required lumped parameters for vertical, longitudinal, and torsional sidewall stiffness as well as tread, rigid ring, and bead/sidewall mass elements.

The equations of motion for the tire model were derived using Newton's Method. For simplicity, only the stiffness terms are included in the derivations. This temporary simplification is possible as the spring and damping elements function in parallel, making the derivation of the damping elements the same as the derivation of the spring elements. Once the equations for the spring elements are derived, the damping elements are then added by inspection with the only notable difference being that the forces for the damping elements are functions of relative velocities between their associated masses as opposed to their relative positions.

The two point follower version of this rigid ring model is characterized by having seven degrees of freedom within three component masses:

1. the tire brake, rim, and bead assembly
2. the rigid ring, consisting of the tire summit belt package and the tread mass not associated with the tire contact patch (i.e., that amount of the tread ring not in contact with the ground)
3. the tread mass associated with the contact patch

The sidewall mass, although not a principal contributor to the tire's total mass, is apportioned equally between the brake/rim/bead assembly and the rigid ring assembly. This approximation is not unreasonable given that the tire sidewall is 1) of relatively

small mass compared to the tire bead, rigid ring, and tread masses, and 2) typically of fairly constant cross thickness about the tire equator. For more specialized tire constructions, such as low-profile performance tires of low aspect ratio, tires with metallic products in their sidewall, and run-flat tires with thick sidewall constructions, the sidewall mass can be re-apportioned between the bead area and the tire summit (rigid ring) as appropriate.

The seven degrees of freedom within the three mass rigid ring models are represented as follows:

- the tire bead, rim and axle assembly in both the vertical  $z$  direction ( $Z_{rim}$ ) and the longitudinal  $x$  direction ( $X_{rim}$ ),
- the tire bead and rim assembly in the spin axis rotation direction ( $\theta_{rim}$ ),
- the tire rigid ring assembly (representing the tire belt package in the tire summit region) in vertical  $z$  direction ( $Z_{ring}$ ), longitudinal  $x$  direction ( $X_{ring}$ ), and theta rotation directions ( $\theta_{ring}$ ).
- the tread block in contact with the ground only in the longitudinal  $x$  direction ( $X_{tread}$ ), as the  $z$  location ( $Z_{tread}$ ) and the rotation angle of the tread block ( $\theta_{tread}$ ) are dictated by obstacle height as a function of the  $x$  position of the contact point followers at the leading and trailing edge of the contact patch.

In all derivations for the tire model, positive deflection is assumed to be upward positive for  $z$ , forward to the left positive for  $x$ , and counterclockwise positive for rotation theta when viewed from the left hand side (positive  $x$  is pointing to the left). Refer to Figure 3.1 for a visual representation of the degrees of freedom and the dimensions of the

rigid ring tire model and the two-point follower representing the contact patch enveloping the road surface irregularities.

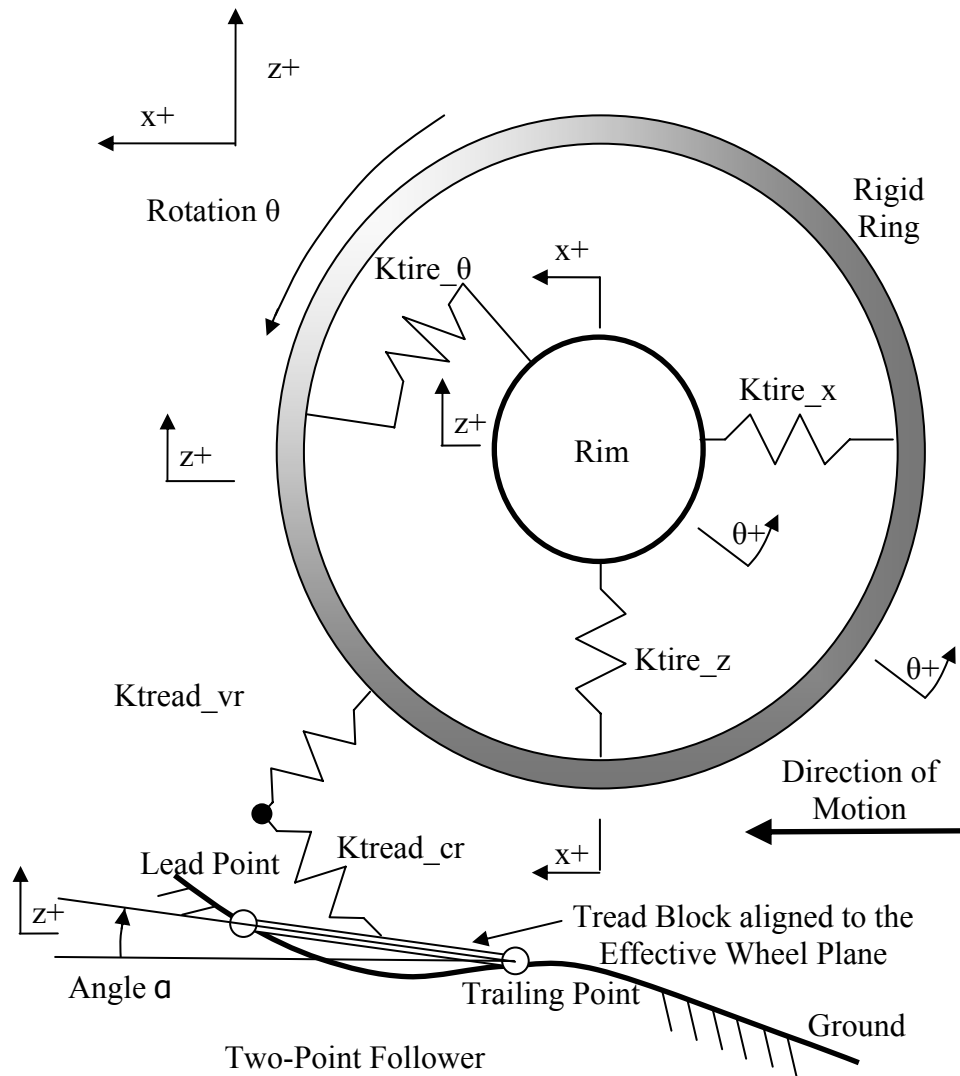


Figure 3.1: Seven Degree-of-Freedom Rigid Ring Tire Model

### Equations of Motion for the Two Point Follower Rigid Ring Tire Model

The equations of motion are derived using Newton's Method – defining a set of coordinates, drawing an appropriate free body diagram for each of the masses and then solving for the equations of motion directly. This is done for each mass, and each degree of freedom associated with the mass, in turn. Note that the equations of motion could also have just as easily been performed using Hamilton's Principle or the Lagrangian approach. These lend themselves to systems having many degrees of freedom or when most of the forces are derived from potential functions.

Selecting the rim as the first mass and addressing the degree of freedom in  $z$ , we define the rim mass as the mass of the rim itself plus the associated brake disk (or drum) and axle, the tire bead, and one half of the sidewall mass (the sidewall mass is divided equally between the tire bead and the tire summit). Note that the appropriate definitions for the rim mass will depend upon the degree of freedom that is being analyzed and will be defined for each degree of freedom - the mass properties associated with the tire bead, wheel, brake disk and axle are all appropriate for the equation of motion in the vertical direction  $z$ , but including the axle mass property is not appropriate for the equation of motion about the spin axis. Next, the free body diagram of the rim is drawn showing the forces on the rim as displacements from the static equilibrium condition and the dynamic forces on the body due to acceleration. See Figure 3.2:

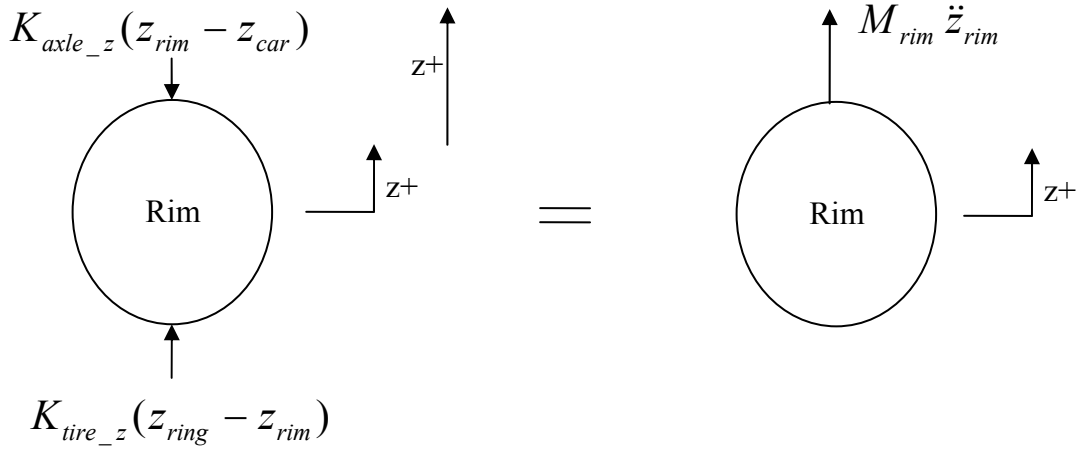


Figure 3.2: Free Body Diagram for the Rim in the Z Axis Direction

Writing the forces in the z direction positive upwards yields:

$$-k_{axle\_z}(z_{rim} - z_{car}) + k_{tire\_z}(-z_{rim} + z_{ring}) = M_{rim}\ddot{z}_{rim} \quad (3.1)$$

Rearranging and solving for the vertical acceleration yields:

$$\ddot{z}_{rim} = -\frac{1}{M_{rim}} \{k_{axle\_z}(z_{rim} - z_{car}) + k_{tire\_z}(z_{rim} - z_{ring})\} \quad (3.2)$$

Adding the damping coefficients produces the final equation for the vertical degree of freedom:

$$\ddot{z}_{rim} = -\frac{1}{M_{rim}} \{k_{axle\_z}(z_{rim} - z_{car}) + c_{axle\_z}(\dot{z}_{rim} - \dot{z}_{car}) + k_{tire\_z}(z_{rim} - z_{ring}) + c_{tire\_z}(\dot{z}_{rim} - \dot{z}_{ring})\} \quad (3.3)$$

Proceeding with the equation of motion of the rim in x, we note that the car chassis mass is included in the x degree of freedom and that the rim, axle, and car



represent the mass in the x direction along with the tire bead mass and one-half of the sidewall mass. The free body diagram is annotated accordingly and the equation of motion is solved as follows.

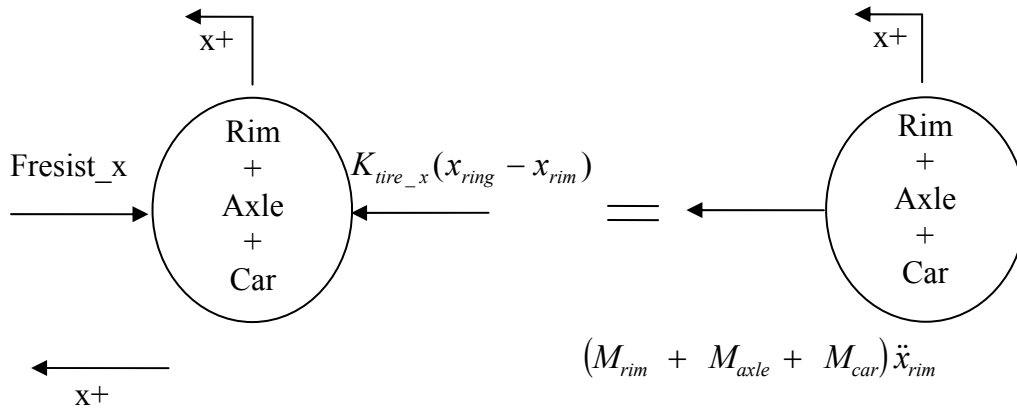


Figure 3.3: Free Body Diagram for the Rim in the X Axis Direction

Writing the forces in the x direction positive to the left as shown in Figure 3.3 and defining the mass of the rim to represent the total effective mass of the rim, the axle, and the car along with the appropriate portions of the tire model mass yields:

$$+k_{tire\_x}(-x_{rim} + x_{ring}) - F_{resist\_x} = M_{effective\_rim} \ddot{x}_{rim} \quad (3.4)$$

As stated previously, the mass properties of the car and the axle are taken into account by the effective rim mass term.

The force term  $F_{resist\_x}$  represents the summation of aerodynamic drag and the overall rolling resistance. In this case, the overall resistance to forward motion due to driveline bearing drag and the tire rolling resistance is implemented as nonlinear function look-up tables and embedded in the MatLab Simulink software. In this way, empirical data for different drive line frictional losses and tire rolling resistance on different

surfaces (concrete, rough or sealed asphalt, etc.) can be introduced into the simulation as desired.

Adding the damping term for the tire longitudinal sidewall stiffness and solving for the longitudinal acceleration yields:

$$\ddot{x}_{rim} = -\frac{1}{M_{effective\_rim}} \left\{ k_{tire\_x} (x_{rim} - x_{ring}) + C_{tire\_x} (\dot{x}_{rim} - \dot{x}_{ring}) + F_{resist\_x} \right\} \quad (3.5)$$

Proceeding with the third and final equation of motion for the rim, the free body diagram associated with the rotation about the spin axis theta is shown in Figure 3.4.

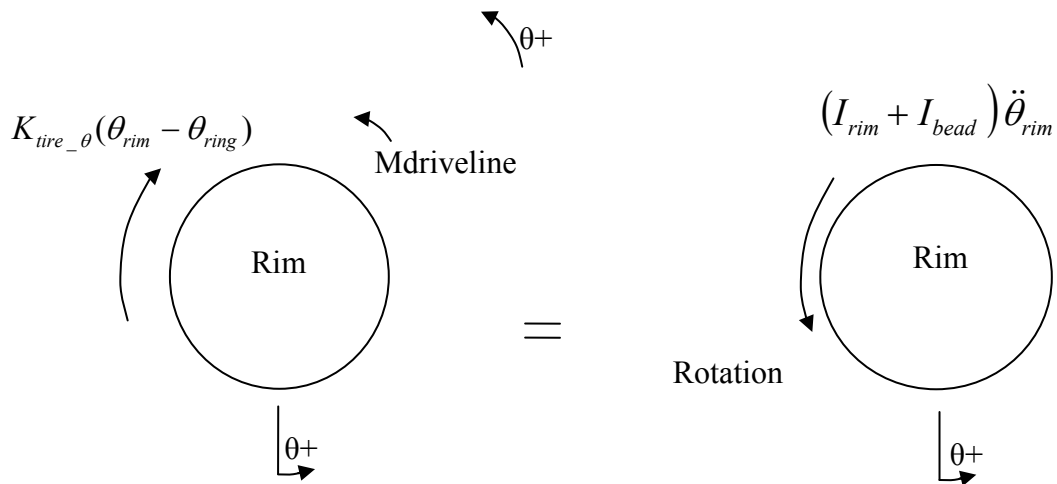


Figure 3.4: Free Body Diagram for the Rim in the Rotational Theta Direction

Defining theta to be positive counterclockwise (driving the car forward in x positive) and defining the rotational moment of inertia of the rim to include the contribution from both the rim and tire bead, the sum of the moments yields:

$$-k_{tire\_theta} (\theta_{rim} - \theta_{ring}) + M_{driveline} = (I_{rim} + I_{bead}) \ddot{\theta}_{rim} \quad (3.6)$$

Adding the damping term for the tire sidewall torsional stiffness and solving for the rotational acceleration yields:

$$\ddot{\theta}_{rim} = -\frac{1}{I_{rim} + I_{bead}} \left\{ k_{tire\_theta} (\theta_{rim} - \theta_{ring}) + C_{tire\_theta} (\dot{\theta}_{rim} - \dot{\theta}_{ring}) - M_{driveline} \right\} \quad (3.7)$$

Selecting the rigid ring as the second mass, we first define the ring mass as the mass of the tire summit (consisting of the belt plies underneath the tread band) and that portion of the tread band outside the tire contact patch, plus any additional mass associated with that portion of the tire sidewall. The three degrees of freedom associated with the ring are in the vertical z, longitudinal x and rotational theta directions. As with the development of the equations of motion for the rim, a set of free body diagrams is drawn for each mass or inertia and the equations of motion are derived. Proceeding with the equation of motion of the ring in z, we draw the diagrams in Figure 3.5 showing the dynamic forces on the body as a displacement from the equilibrium condition:

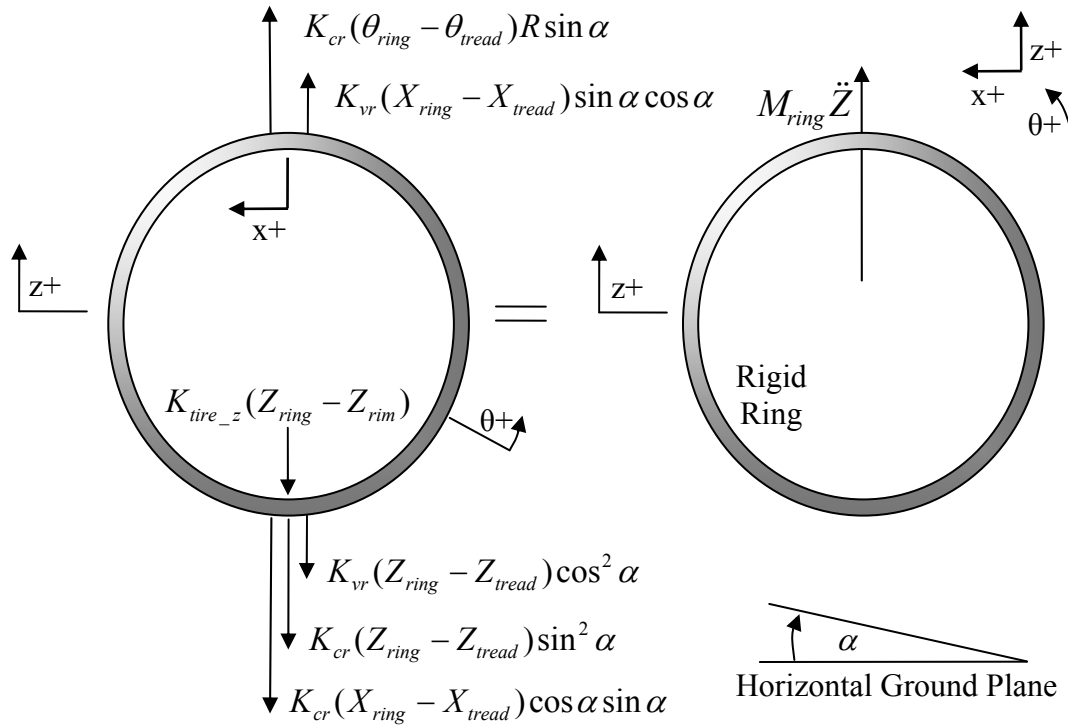


Figure 3.5: Free Body Diagram for the Rigid Ring in the Z Direction

Summing the forces in the z direction and taking into account the angle of incidence with the ground plane, angle  $\alpha$ , yields the following equation:

$$\begin{aligned}
 & -k_{tire\_z}(Z_{ring} - Z_{rim}) \\
 & -k_{vr}(Z_{ring} - Z_{tread})\cos\alpha\cos\alpha \\
 & +k_{vr}(X_{ring} - X_{tread})\sin\alpha\cos\alpha \\
 & -k_{cr}(Z_{ring} - Z_{tread})\sin\alpha\sin\alpha \\
 & -k_{cr}(X_{ring} - X_{tread})\cos\alpha\sin\alpha \\
 & +k_{cr}(\theta_{ring} - \theta_{tread})R\sin\alpha \\
 & = M_{ring}\ddot{Z}_{ring}
 \end{aligned} \tag{3.8}$$

Adding the damping terms for the tire vertical sidewall stiffness and for the circumferential and radial components of tread element stiffness and solving for the vertical acceleration yields:

$$\ddot{Z}_{ring} = \frac{-1}{M_{ring}} \left\{ \begin{array}{l} k_{tire\_z} (Z_{ring} - Z_{rim}) + c_{tire\_z} (\dot{Z}_{ring} - \dot{Z}_{rim}) + \\ k_{vr} (Z_{ring} - Z_{tread}) \cos^2 \alpha + c_{vr} (\dot{Z}_{ring} - \dot{Z}_{tread}) \cos^2 \alpha - \\ k_{vr} (X_{ring} - X_{tread}) \sin \alpha \cos \alpha - c_{vr} (\dot{X}_{ring} - \dot{X}_{tread}) \sin \alpha \cos \alpha + \\ k_{cr} (Z_{ring} - Z_{tread}) \sin^2 \alpha + c_{cr} (\dot{Z}_{ring} - \dot{Z}_{tread}) \sin^2 \alpha + \\ k_{cr} (X_{ring} - X_{tread}) \cos \alpha \sin \alpha + c_{cr} (\dot{X}_{ring} - \dot{X}_{tread}) \cos \alpha \sin \alpha - \\ k_{cr} (\theta_{ring} - \theta_{tread}) R \sin \alpha - c_{cr} (\dot{\theta}_{ring} - \dot{\theta}_{tread}) R \sin \alpha \end{array} \right\}$$

Equation (3.9)

Here, the longitudinal position  $x$  of the rim is equivalent to the longitudinal position of either the axle or the car. The effective height of the ground plane is determined by the position in  $x$  of the ring and the contour of the ground designated by the tread contact point followers.

Proceeding with the equation of motion of the ring in  $x$ , the free body diagram is drawn and annotated accordingly in Figure 3.6. The equation of motion for the ring in  $x$  is solved as follows.

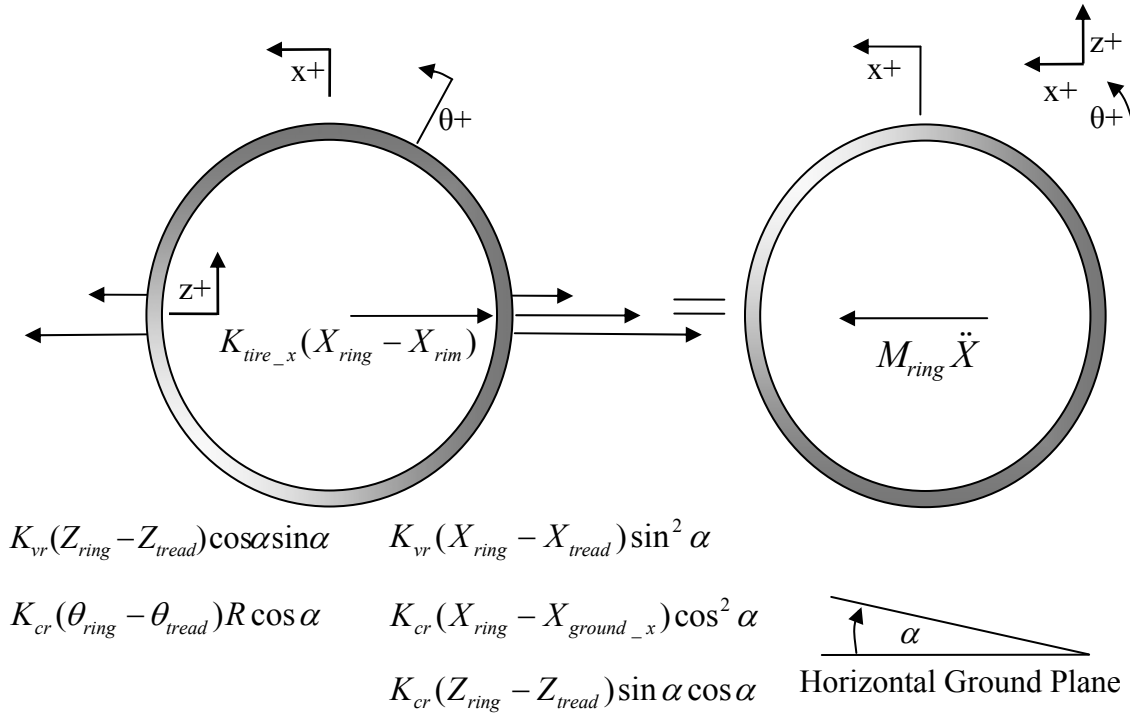


Figure 3.6: Free Body Diagram for the Rigid Ring in the X Direction

Summing the forces in the x direction positive to the left yields:

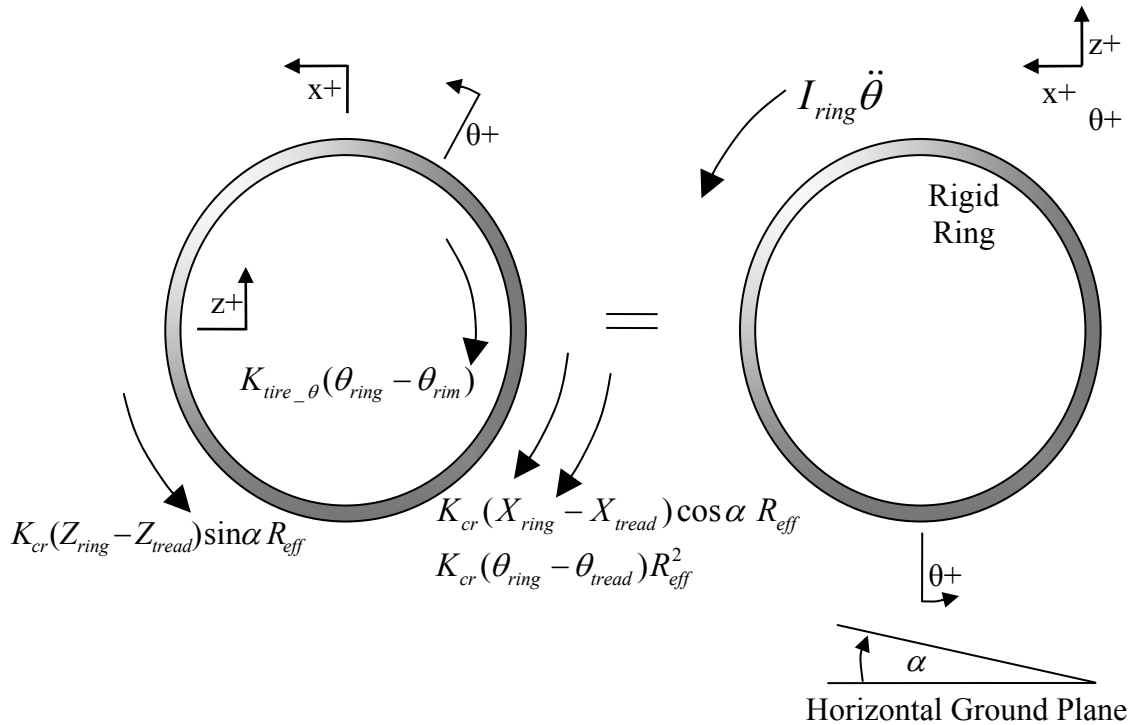
$$\begin{aligned}
 & -k_{tire\_x}(X_{ring} - X_{rim}) \\
 & -k_{vr}(X_{ring} - X_{tread})\sin^2\alpha \\
 & +k_{vr}(Z_{ring} - Z_{tread})\cos\alpha\sin\alpha \\
 & -k_{cr}(X_{ring} - X_{ground\_x})\cos^2\alpha \\
 & -k_{cr}(Z_{ring} - Z_{tread})\sin\alpha\cos\alpha \\
 & +k_{cr}(\theta_{ring} - \theta_{tread})R\cos\alpha \\
 & = M_{ring}\ddot{X}_{ring}
 \end{aligned} \tag{3.10}$$

Adding the damping terms for the tire longitudinal sidewall stiffness and for the circumferential and radial components of tread element stiffness yields:

$$\ddot{X}_{ring} = \frac{-1}{M_{ring}} \left\{ \begin{array}{l} k_{tire\_x} (X_{ring} - X_{rim}) + c_{tire\_x} (\dot{X}_{ring} - \dot{X}_{rim}) + \\ k_{vr} (X_{ring} - X_{tread}) \sin^2 \alpha + c_{vr} (\dot{X}_{ring} - \dot{X}_{tread}) \sin^2 \alpha - \\ k_{vr} (Z_{ring} - Z_{tread}) \cos \alpha \sin \alpha - c_{vr} (\dot{Z}_{ring} - \dot{Z}_{tread}) \cos \alpha \sin \alpha + \\ k_{cr} (X_{ring} - X_{tread}) \cos^2 \alpha + c_{cr} (\dot{X}_{ring} - \dot{X}_{tread}) \cos^2 \alpha + \\ k_{cr} (Z_{ring} - Z_{tread}) \sin \alpha \cos \alpha + c_{cr} (\dot{Z}_{ring} - \dot{Z}_{tread}) \sin \alpha \cos \alpha - \\ k_{cr} (\theta_{ring} - \theta_{tread}) R \cos \alpha - c_{cr} (\dot{\theta}_{ring} - \dot{\theta}_{tread}) R \cos \alpha \end{array} \right\}$$

Equation (3.11)

Proceeding with the third and final equation of motion for the rigid ring, the free body diagram associated with the rotation about the spin axis theta is shown in Figure 3.7.

Figure 3.7: Free Body Diagram for the Rigid Ring in the Theta ( $\theta$ ) Direction

Defining theta to be positive counterclockwise (driving the car forward in the positive x direction) and defining the rotational moment of inertia of the ring to include the contribution from both the tire tread summit belts, the tread mass outside the contact patch, and the portion of the sidewall attributable to the tire summit, the sum of the moments yields:

$$\begin{aligned}
& -k_{tire\_theta} (\theta_{ring} - \theta_{rim}) \\
& + k_{cr} (X_{ring} - X_{tread}) \cos \alpha R_{eff} \\
& - k_{cr} (Z_{ring} - Z_{tread}) \sin \alpha R_{eff} \\
& - k_{cr} (\theta_{ring} - \theta_{tread}) R_{eff}^2 \\
& = I_{ring} \ddot{\theta}_{ring}
\end{aligned} \tag{3.12}$$

Adding the damping terms for the tire sidewall torsional stiffness and for the circumferential and radial components of tread element stiffness yields:

$$\ddot{\theta}_{ring} = \frac{-1}{I_{ring}} \left[ \begin{aligned} & k_{tire\_theta} (\theta_{ring} - \theta_{rim}) + c_{tire\_theta} (\dot{\theta}_{ring} - \dot{\theta}_{rim}) - \\ & k_{cr} (X_{ring} - X_{tread}) \cos \alpha R_{eff} - c_{cr} (\dot{X}_{ring} - \dot{X}_{tread}) \cos \alpha R_{eff} + \\ & k_{cr} (Z_{ring} - Z_{tread}) \sin \alpha R_{eff} + c_{cr} (\dot{Z}_{ring} - \dot{Z}_{tread}) \sin \alpha R_{eff} + \\ & k_{cr} (\theta_{ring} - \theta_{tread}) R_{eff}^2 + c_{cr} (\dot{\theta}_{ring} - \dot{\theta}_{tread}) R_{eff}^2 \end{aligned} \right] \tag{3.13}$$

Selecting the tread element as the third mass, we first define the tread mass as the mass of the tire tread band residing within the contact patch. The three degrees of freedom associated with the tread mass are in the vertical z, longitudinal x and rotational theta directions. As with the development of the equations of motion for the rim and the ring, a set of free body diagrams is drawn for each degree of freedom and the equations of motion for each degree of freedom are solved for in turn. Proceeding with the equation



of motion for the tread in  $z$ , we draw the diagrams showing the dynamic forces on the body as a displacement from the equilibrium condition in Figure 3.8:

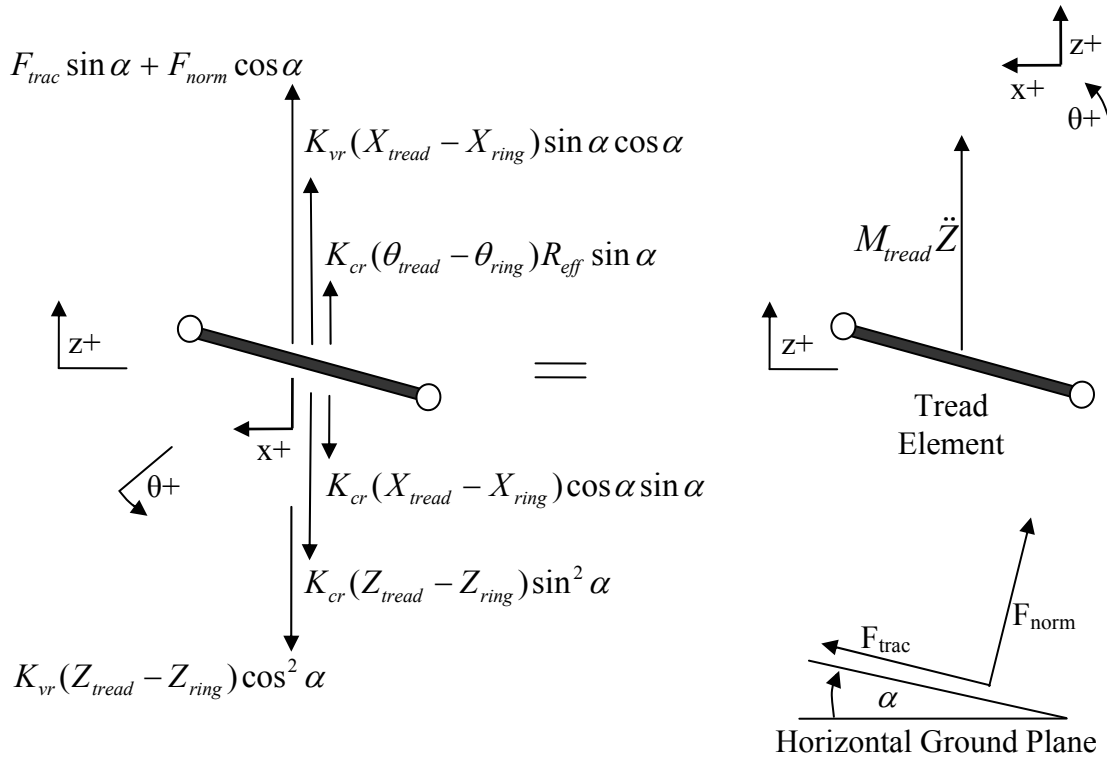


Figure 3.8: Free Body Diagram for the Tread Block in the  $Z$  Direction

Summing the forces in the  $z$  direction yields the following equation:

$$\begin{aligned}
 & + F_{trac} \sin \alpha + F_{norm} \cos \alpha \\
 & - k_{vr} (Z_{tread} - Z_{ring}) \cos^2 \alpha \\
 & + k_{vr} (X_{tread} - X_{ring}) \sin \alpha \cos \alpha \\
 & - k_{cr} (Z_{tread} - Z_{ring}) \sin^2 \alpha \\
 & - k_{cr} (X_{tread} - X_{ring}) \cos \alpha \sin \alpha \\
 & + k_{cr} (\theta_{tread} - \theta_{ring}) R_{eff} \sin \alpha \\
 & = M_{tread} \ddot{Z}_{tread}
 \end{aligned} \tag{3.14}$$

In equation 3.14 the normal force is the combination of the normal forces between the ground surface and the tread block due to the static quarter weight of the vehicle and the spring displacement and velocity damping between the ring and the tread block normal to the effective ground plane. Adding damping terms associated with the circumferential and radial components of tread element stiffness yields:

$$\ddot{Z}_{tread} = \frac{-1}{M_{tread}} \left\{ \begin{array}{l} -F_{trac} \sin \alpha - F_{norm} \cos \alpha + \\ k_{vr} (Z_{tread} - Z_{ring}) \cos^2 \alpha + c_{vr} (\dot{Z}_{tread} - \dot{Z}_{ring}) \cos^2 \alpha - \\ k_{vr} (X_{tread} - X_{ring}) \sin \alpha \cos \alpha - c_{vr} (\dot{X}_{tread} - \dot{X}_{ring}) \sin \alpha \cos \alpha + \\ k_{cr} (Z_{tread} - Z_{ring}) \sin^2 \alpha + c_{cr} (\dot{Z}_{tread} - \dot{Z}_{ring}) \sin^2 \alpha + \\ k_{cr} (X_{tread} - X_{ring}) \cos \alpha \sin \alpha + c_{cr} (\dot{X}_{tread} - \dot{X}_{ring}) \cos \alpha \sin \alpha - \\ k_{cr} (\theta_{tread} - \theta_{ring}) R_{eff} \sin \alpha - c_{cr} (\dot{\theta}_{tread} - \dot{\theta}_{ring}) R_{eff} \sin \alpha \end{array} \right\} \quad (3.15)$$

Proceeding with the equation of motion of the tread block in x, the free body diagram is annotated accordingly as shown in Figure 3.9 and the equation of motion is solved as follows:

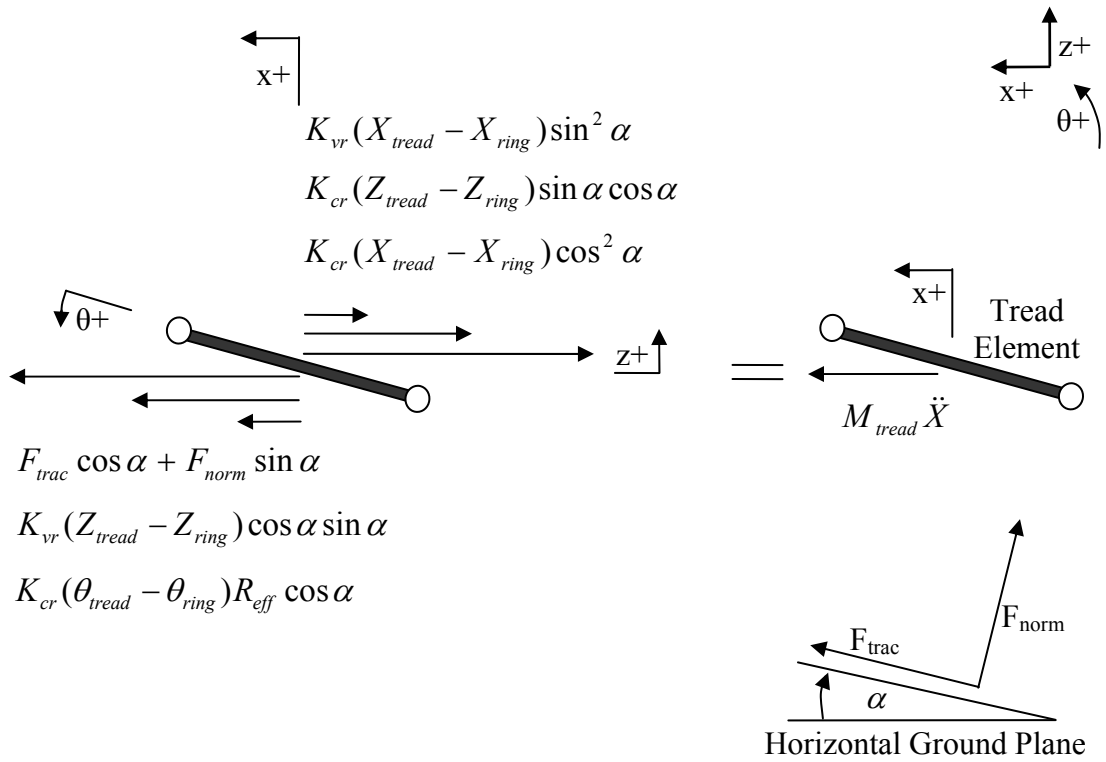


Figure 3.9: Free Body Diagram for the Tread Block in the X Direction

Summing the forces in the x direction positive to the left yields the following equation:

$$\begin{aligned}
 &+ F_{trac} \cos \alpha + F_{norm} \sin \alpha \\
 &+ k_{vr} (Z_{tread} - Z_{ring}) \cos \alpha \sin \alpha \\
 &- k_{vr} (X_{tread} - X_{ring}) \sin^2 \alpha \\
 &- k_{cr} (Z_{tread} - Z_{ring}) \sin \alpha \cos \alpha \\
 &- k_{cr} (X_{tread} - X_{ring}) \cos^2 \alpha \\
 &+ k_{cr} (\theta_{tread} - \theta_{ring}) R_{eff} \cos \alpha \\
 &= M_{tread} \ddot{X}_{tread}
 \end{aligned} \tag{3.16}$$

Adding the damping terms for the circumferential and radial components of tread element stiffness and solving for acceleration of the tread block in x yields:

$$\ddot{X}_{tread} = \frac{-1}{M_{tread}} \left\{ \begin{array}{l} -F_{trac} \cos \alpha + F_{norm} \sin \alpha - \\ k_{vr} (Z_{tread} - Z_{ring}) \cos \alpha \sin \alpha - c_{vr} (\dot{Z}_{tread} - \dot{Z}_{ring}) \cos \alpha \sin \alpha + \\ k_{vr} (X_{tread} - X_{ring}) \sin^2 \alpha + c_{vr} (\dot{X}_{tread} - \dot{X}_{ring}) \sin^2 \alpha + \\ k_{cr} (Z_{tread} - Z_{ring}) \sin \alpha \cos \alpha + c_{cr} (\dot{Z}_{tread} - \dot{Z}_{ring}) \sin \alpha \cos \alpha + \\ k_{cr} (X_{tread} - X_{ring}) \cos^2 \alpha + c_{cr} (\dot{X}_{tread} - \dot{X}_{ring}) \cos^2 \alpha - \\ k_{cr} (\theta_{tread} - \theta_{ring}) R_{eff} \cos \alpha - c_{cr} (\dot{\theta}_{tread} - \dot{\theta}_{ring}) R_{eff} \cos \alpha \end{array} \right\} \quad (3.17)$$

Proceeding with the third and final equation of motion for the tread block, the free body diagram associated with the rotation about the spin axis theta is shown in Figure 3.10.

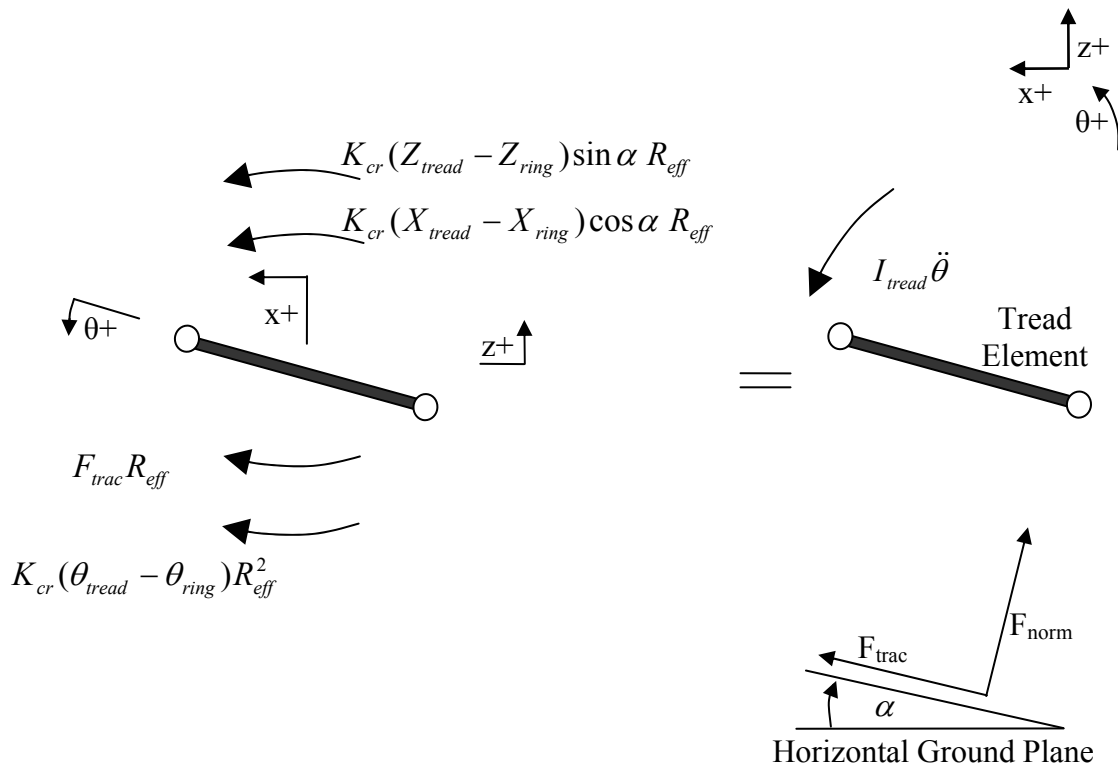


Figure 3.10: Free Body Diagram for the Tread Block in the Theta ( $\theta$ ) Direction

Defining theta to be positive counterclockwise and defining the rotational moment of inertia of the tread block to be that associated with the portion of the tread within the contact patch the sum of the moments about the tire spin axis yields:

$$\begin{aligned}
& -F_{trac} R_{eff} \\
& + k_{cr} (Z_{tread} - Z_{ring}) \sin \alpha R_{eff} \\
& + k_{cr} (X_{tread} - X_{ring}) \cos \alpha R_{eff} \\
& - k_{cr} (\theta_{tread} - \theta_{ring}) R_{eff}^2 \\
& = I_{tread} \ddot{\theta}_{tread}
\end{aligned} \tag{3.18}$$

Adding the damping terms for the circumferential and radial components of tread element stiffness yields:

$$\ddot{\theta}_{tread} = \frac{-1}{I_{tread}} \left\{ \begin{array}{l} F_{trac} R_{eff} - \\ k_{cr} (Z_{tread} - Z_{ring}) \sin \alpha R_{eff} - c_{cr} (\dot{Z}_{tread} - \dot{Z}_{ring}) \sin \alpha R_{eff} - \\ k_{cr} (X_{tread} - X_{ring}) \cos \alpha R_{eff} - c_{cr} (\dot{X}_{tread} - \dot{X}_{ring}) \cos \alpha R_{eff} + \\ k_{cr} (\theta_{tread} - \theta_{ring}) R_{eff}^2 + c_{cr} (\dot{\theta}_{tread} - \dot{\theta}_{ring}) R_{eff}^2 \end{array} \right\} \tag{3.19}$$

This completes the third and final equation of motion for the tread block within the contact patch.

The equations of motion for all three masses complete the new tire model on the most elementary level.

### Extending from a Two Point to a Five Point Follower for the Rigid Ring

The transformation of the rigid ring model from a two point follower configuration to a five point follower divides the effective plane of the tire contact patch into four equal effective planes. The principal advantages associated with breaking the single ground plane into multiple planes include:

- the discretized plane provides higher fidelity in regards to the spatial frequency content associated with both the vertical characteristic of the obstacle as well as the rotational angle of each discretized plane as it travels over the obstacle
- the sum of the longitudinal traction forces for all of the discretized planes provides for greater accuracy than one average plane due to the nonlinear characteristic of the tire traction model
- the shorter length associated with the multiple planes increases the spatial frequency response of the model, allowing the model to perform with either shorter wavelength obstacles or faster vehicle speeds

The development of the five point follower can be addressed by first defining the tread ring and the positions of each of the four effective segments within the contact patch. This is illustrated in Fig 3.11.

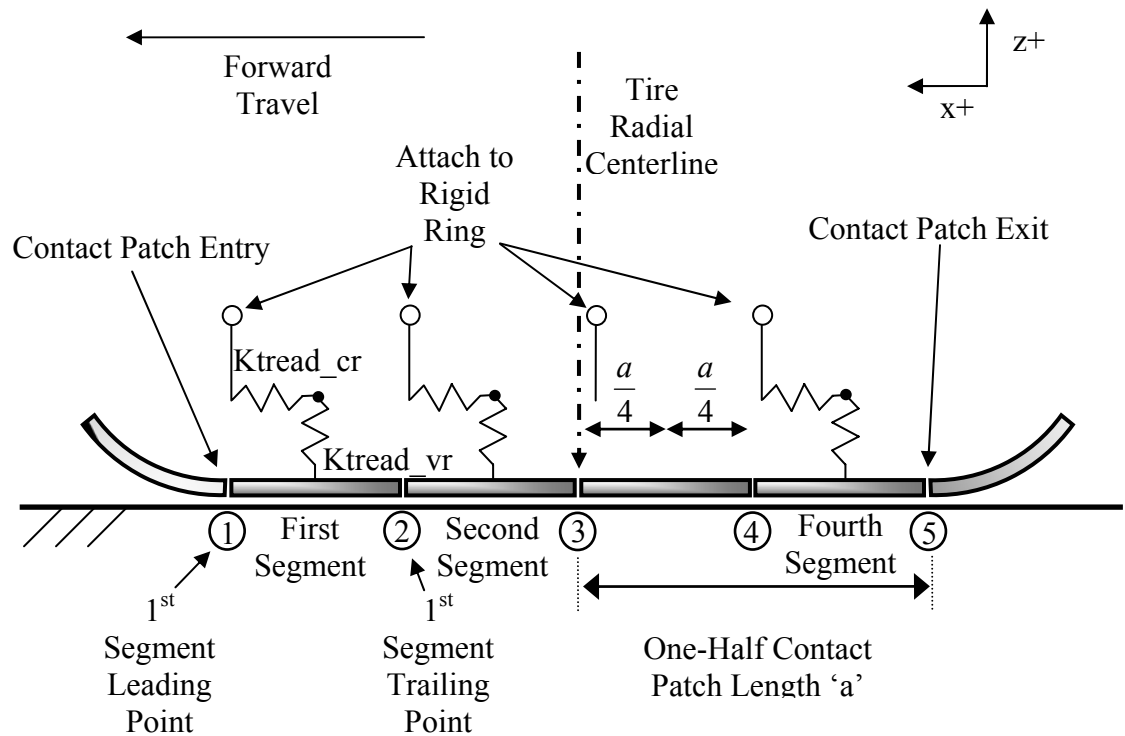


Figure 3.11: Effective Plane Elements in the Five Point Follower Rigid Ring Model

The definition of the longitudinal offset for each of the four tread blocks is generated based upon the center of its effective plane length in the contact patch. With 'a' being defined as one-half of the contact patch length, the length of each of the four effective planes is  $\frac{1}{2} a$ . The position of each effective plane segment relative to the midpoint of the contact patch,  $X_{tread}$ , is therefore defined as in Table 3.1, below:

Table 3.1: Longitudinal Offset of Effective Plane Elements in the 5 Point Follower

Tread Segment	Longitudinal Offset
1 <sup>st</sup> Segment (‘Leading’ segment at the entry point of the contact patch)	Lead Point = $X_{\text{tread}} + (1)a$ Mid Point = $X_{\text{tread}} + (\frac{3}{4})a$ Trail Point = $X_{\text{tread}} + (\frac{1}{2})a$
2nd Segment (Segment immediately in front of the contact patch midpoint)	Lead Point = $X_{\text{tread}} + (\frac{1}{2})a$ Mid Point = $X_{\text{tread}} + (\frac{1}{4})a$ Trail Point = $X_{\text{tread}}$
3rd Segment (Segment immediately behind the contact patch midpoint)	Lead Point = $X_{\text{tread}}$ Mid Point = $X_{\text{tread}} - (\frac{1}{4})a$ Trail Point = $X_{\text{tread}} - (\frac{1}{2})a$
4th Segment (‘Trailing’ segment at the exit point of the contact patch)	Lead Point = $X_{\text{tread}} - (\frac{1}{2})a$ Mid Point = $X_{\text{tread}} - (\frac{3}{4})a$ Trail Point = $X_{\text{tread}} - (1)a$
Note: The mass, spring rate, and damping rate attributed to each separate tread segment are assumed to be equal to one-quarter that of the entire contiguous tread segment within the contact patch.	

The MatLab Simulink model uses a look-up table to provide a continuous function for the vertical position of any defined roadway obstacle as a function of longitudinal position on the ground. By using the offsets defined in Table 3.1, the Simulink model can then:

1. obtain the vertical position for each of the five point followers
2. calculate the mean vertical position for each of the four effective planes
3. calculate the angle of engagement for each of the four effective planes

and use this information when performing the time step integration as the tire model traverses the obstacle.

The previously discussed advantages of the five point follower model (four segments, each represented by an effective plane) as opposed to the two point follower model (single segment represented by a single effective plane) is perhaps most easily conveyed by the illustration in Fig 3.12 below:



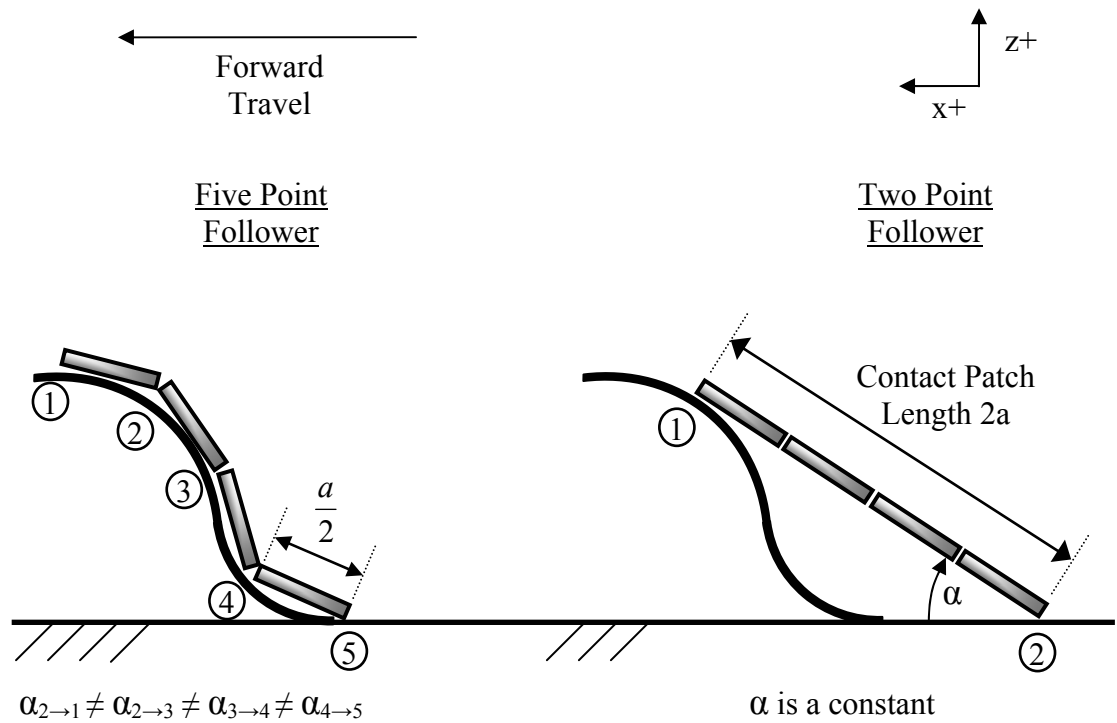


Figure 3.12: Physical Representation of Five vs. Two Point Contact Follower

For any given obstacle, the increased resolution of the five point follower quadruples the information available for calculating the forces generated by the contact patch – instead of one normal force value in the contact patch, there are four values, instead of one angle of obstacle engagement  $\alpha$  there are four angles, etc. An adequate resolution within the contact patch is important for two general reasons:

- the engagement of the spatial frequency of the obstacle (the greater the division within the contact patch, the shorter the wavelength obstacle that can be reasonably modeled) and

- the more accurate the modeling of the non-linear traction forces within the contact patch, including greater resolution of the normal forces as well as the angle at which the normal forces react.

The latter point is important as this not only improves the traction model, but also more accurately represents the generation of longitudinal forces as the tire engages the obstacle and exits the obstacle. The enveloping power of the tread is also more accurately modeled as it traverses an obstacle with a length shorter than that of the total contact patch length.

Just as there are limitations associated with the use of a two point follower and a single effective contact plane, there are also limitations with too great a number of contact patch elements. These disadvantages become increasingly troublesome when the obstacle contains high spatial frequency content and the effective plane segments in the contact patch are short, resulting in modeled angles of obstacle engagement that are greater than can be realized in a physical tire of given radius and summit construction stiffness.

- The shorter the length of each effective plane element, the greater the angle of obstacle engagement, angle  $\alpha$ . This is without regard to the limitation of the tread block to physically be pliable enough to conform to the rapid changes in obstacle height. In a real tire, the bending stiffness associated with the tread band and the tire summit will not allow the tire to 'drape' completely over high frequency or 'jagged' obstacle asperities. The result is that the modeled

tire will generate traction forces with greater efficiency (erroneously higher) than can be realized in an actual tire.

- The greater the angle of obstacle engagement, angle  $\alpha$ , the greater the portion of modeled longitudinal inertial forces acting normal to the tread block. This results in modeled traction forces (parallel to the tread block) which are greater than traction forces normally associated with the physical tire. This is because the traction model is based upon an analytical model derived from a single complete contact patch plane being tested on a homogenous surface.
- There is error caused by the lack of modeling of the bending rigidity between the consecutive effective plane segments. It is a common accepted assumption that the effect of the bending stiffness as the tire enters and exits the contact patch is negligible in comparison to the effect of other measured compliances. However, combining the bending stiffnesses at the entry and exit of the contact patch with the bending stiffnesses between the consecutive plane segments within the contact patch may no longer be negligible, especially with large differences in segment engagement angles.

It can be concluded that this tire model is appropriate for obstacles of intermediate length, and that the most appropriate number of follower elements needs to be determined based not only upon the physical characteristics of the obstacle being traversed, but also the length of the tire contact patch (principally determined by inflation pressure and normal static load, but also to a lesser degree the tire construction parameters).

Because the rigid summit ring does not deflect, the application of forces on the rigid ring can be applied without restriction as to the circumferential position at which those forces are applied. The application of the simple displacement offsets described in Table 3.1 can therefore be applied to each of the four tread segments and allow the re-use of the code for generating the tread block effective plane and engagement angle  $\alpha$ , greatly simplifying the software. The effect as the contact patch engages the front side of a sinusoidal obstacle, as in Fig. 3.12 is shown conceptually in Fig 3.13.

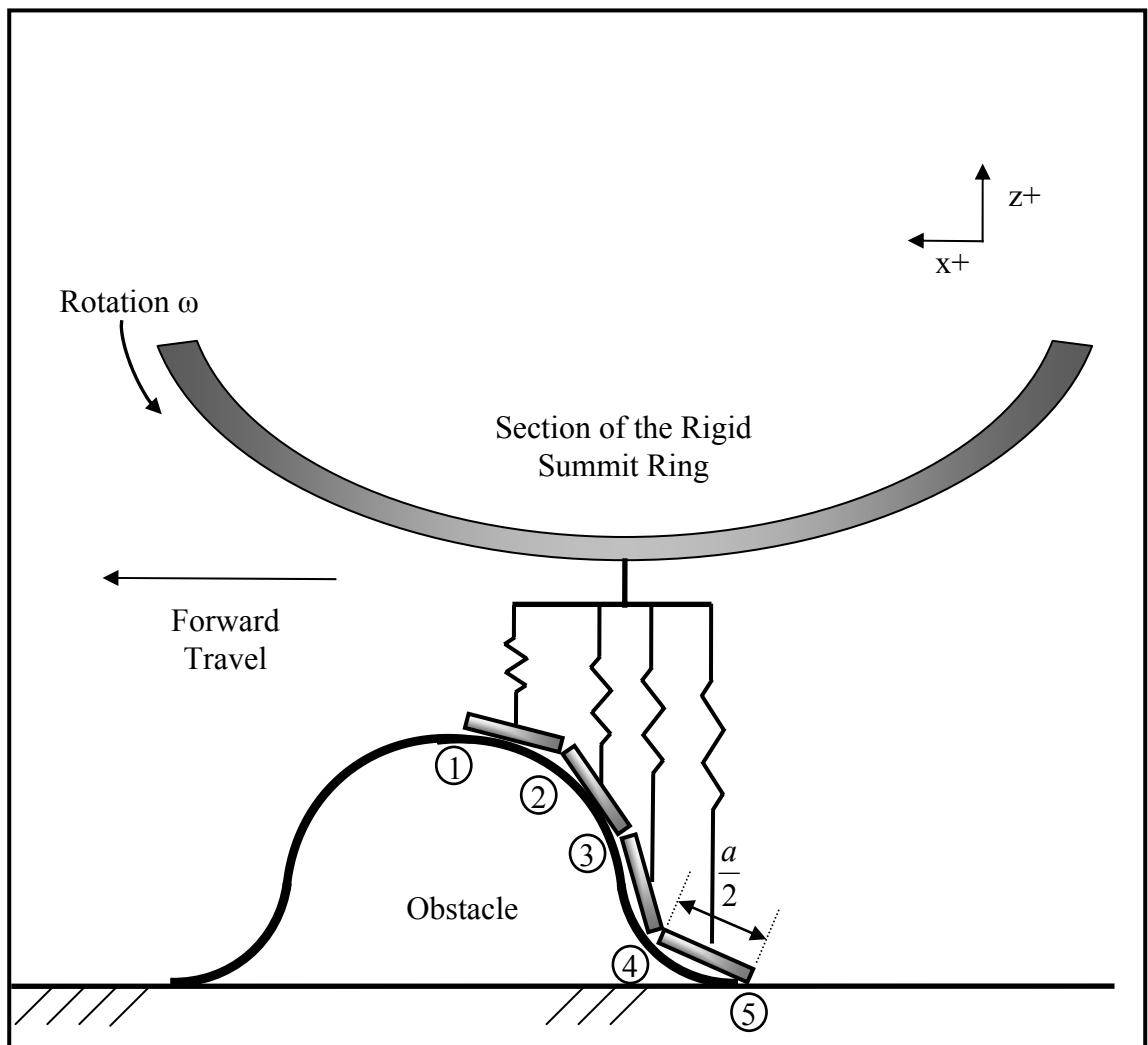


Figure 3.13: Transfer of Contact Patch Tread Element Forces to the Rigid Ring

## CHAPTER 4

### CONDUCTING THE INVESTIGATION OF THE TIRE MODEL

#### Introduction

The overall goal of this work is to develop an understanding of basic tire models used in ride comfort simulations. This will permit more informed decisions as to the selection of tire models for integrated tire/vehicle ride modeling. This is accomplished in two distinct and separate phases. The first phase concentrates on the development of the tire models and comparing simulation results to laboratory measurements of a tire running over a small cleat test cleat attached to test drum. This first phase, or “Cleat” phase, consists of:

- the development of the tire models themselves,
- implementing them in MatLab Simulink
- implementing commercial tire model Cosin FTire in Intec SIMPACK Automotive Plus MBS
- comparing the results against the laboratory road wheel cleat test.

The second phase consists of combining the tire models developed in the Cleat Phase with a simple quarter vehicle ride model. In this Ride Phase, simulations of the integrated quarter vehicle and tire model are performed over two obstacles:

- a sinusoidal equivalent of the 9.5 mm tall and 19 mm long rectangular road wheel cleat
- a sinusoidal parking lot bump measuring 4 inches high and 12 inches long

in order to assess the effect of the tire model with respect to ride comfort performance.

The investigative process is illustrated graphically in Figure 4.1.

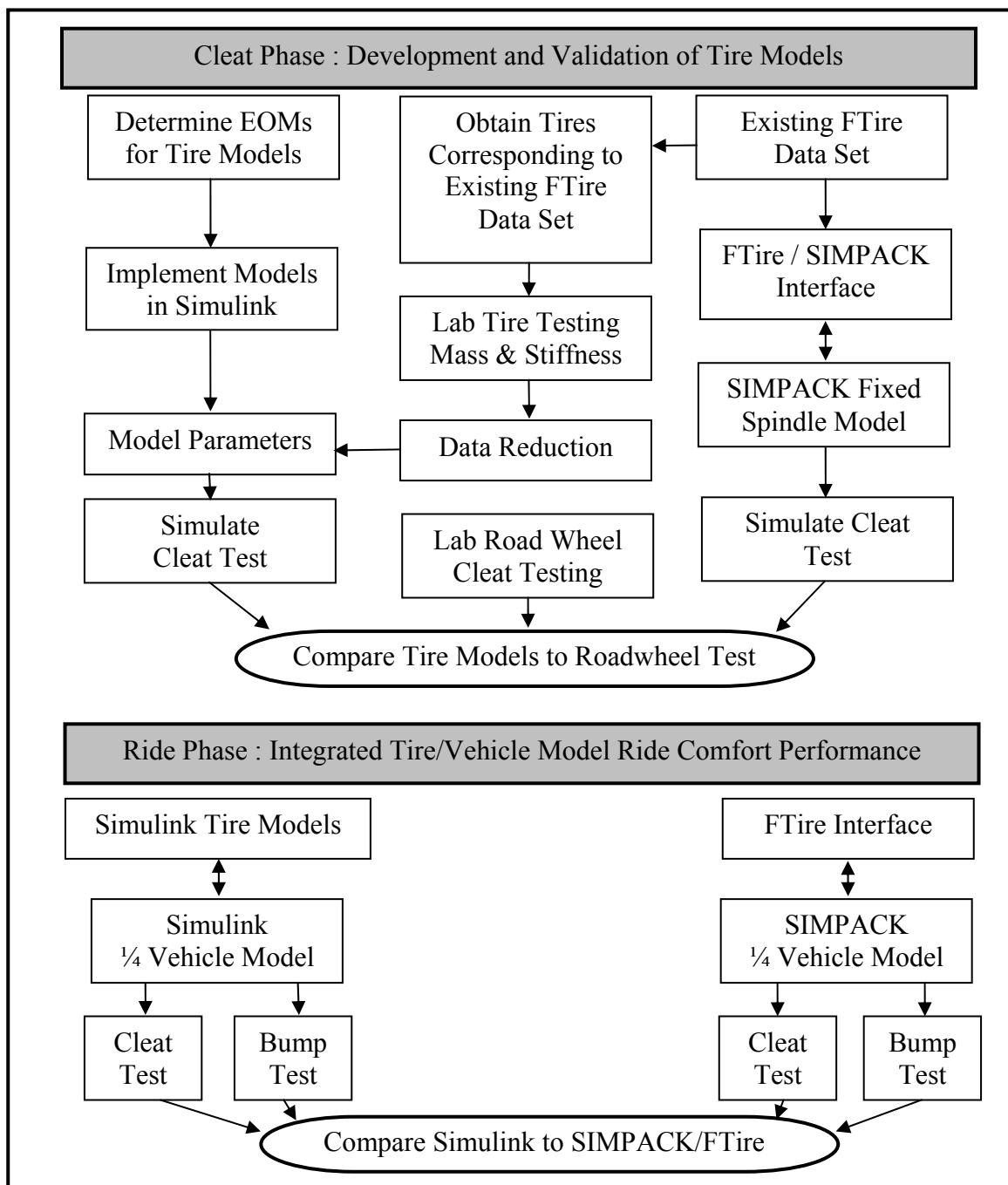


Figure 4.1: Investigation Process Flow Chart

There are several fundamental considerations which were addressed when forming the investigation implementation strategy. One of the issues is the need to validate the tire models that were developed. Although the commercially-available tire model Cosin FTire and simulation package Intec SIMPACK Automotive Plus MBS are thoroughly tested and accepted as validated models in the vehicle industry, laboratory measurements provide not only an absolute comparison but also offer an invaluable “real world” perspective. Also, comparing simulated tire model performance against a laboratory tire test provides a direct means to evaluate tire model performance metrics per se.

## Cleat Phase – Laboratory Measurement to Validate Tire Models

### Simulation Software

Two different simulation paths were utilized. In one simulation path, the equations of motion for the six tire models that were developed are implemented in MatLab Simulink software. In the second simulation path a seventh tire model – Cosin FTire (Flexible Ring Tire Model) was implemented in SIMPACK Automotive Plus. The simulations from all seven models are compared to the measured results from the laboratory road wheel cleat test. The MatLab Simulink path is shown on the left side and the Cosin FTire path is shown on the right side of Figure 4.1.

### Laboratory Tests

In this test, the tire is loaded against a road wheel to which a single rectangular cleat is affixed. The test hub is locked in place such that the spindle height is constant throughout the test. The road wheel drives the test tire and the instrumented test hub records the wheel spindle forces as the free-rolling tire passes over the road wheel cleat. The equipment is illustrated in Figure 4.2.



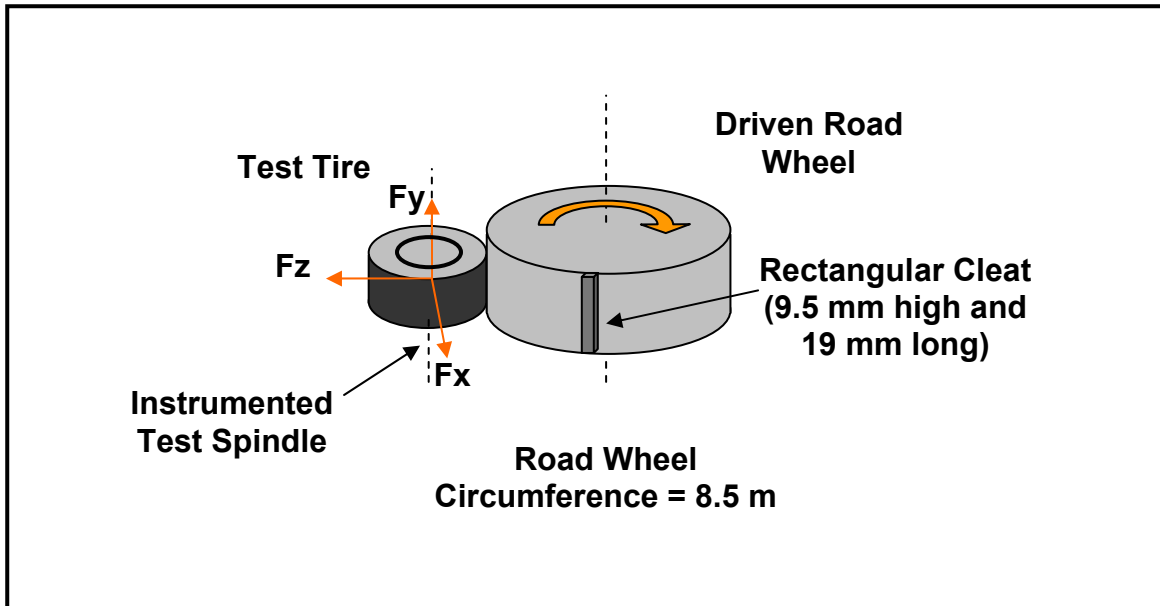


Figure 4.2: Laboratory Road Wheel Test Machinery

The Michelin Americas Research Company (MARC) instrumented spindle road wheel used for the road wheel cleat test is typically reserved for measuring dynamic high-speed tire uniformity. This presented several challenges:

1. As uniformity force measurements require great precision, the maximum operating ranges of the wheel spindle transducers are limited to the largest loads anticipated during tire uniformity measurement. This limits the maximum size of the cleats so as not to over-range the spindle force transducers. As a consequence, only one relatively small road wheel cleat of rectangular cross section – 9.5 mm tall and 19 mm wide – was available for use. This prevented the use of a range of input excitations into the tire, and the one input that was relatively small in magnitude. Having a variety of cleat sizes with larger dimensions would have allowed the investigation to better

compare the various tire models under different operating conditions and in operating ranges that may have been more useful for ride comfort performance.

2. The Michelin precision high-speed uniformity road wheel is 8.5 meters in circumference and is designed to operate in a test speed range between 10 and 200 Kph. This prevents testing at the slower speeds needed to confirm the tire compliance characteristics, such as the change in vertical compliance as the cleat first enters, then traverses, and finally exits the contact patch. The lowest solicitation speed of which the machine is capable is 8 Kph (2.22 m/sec), which is already fast enough to excite the internal tire dynamics as the cleat passes through the contact patch, as evidenced by “ringing” of the spindle forces. For the test tire in question, a European (non P-metric) 245/45ZR18 Michelin Pilot Sport 2, the contact patch length (the length of the tire which remains in continuous contact with the ground) is approximately 0.158 meters at the test conditions of 2.0 bar inflation pressure and 5,780 N vertical load. The total time that the tire engages the cleat (neglecting the curvature of the roadway drum and the height of the cleat) is only 71 msec at 8 Kph. So although this precision road wheel machine is ideally suited for measuring tire uniformity and tire vibration modes that occur at high speeds, it is not optimized for operating in a manner that would be used for validating tire ride comfort models. Ideally, testing would commence using very slow speeds – perhaps 1 Kph or even slower - to first verify the tire compliance without any

significant dynamic effects before increasing speed to verify the internal tire dynamic effects.

These limitations on road wheel cleat testing do not allow for ideal data sets with which to validate the tire model simulations. However, the data are adequate such that the relative merits of the various tire models can be explored and provide insight into tire functionality which exceeds that which could be obtained through simulations alone.

The simulated waveforms and the normalized peak spindle forces obtained from the simulation outputs of all seven tire models are compared to the laboratory test results. These results are expected to confirm that the most sophisticated tire model will perform with the greatest fidelity, and will subsequently be used as a reference for the simulations in the second phase of the investigation, the “Ride” phase.

#### Testing for Tire Model Parameters

A means was needed to provide data for the tire model parameters. This was accomplished by utilizing Michelin’s machine test facility. The tire tests were chosen on the basis of testing ease, speed, and cost. The testing consisted of:

1. Static stiffness testing in longitudinal (x-axis), lateral (y-axis) and vertical (z-axis) directions at multiple inflation pressures.
2. Moment of inertia testing about the spin axis for both the tire and the test wheel used with the road wheel cleat test

3. Tire weight and measurement of standard “Omega” cuts to determine the relative mass and moment of inertia contributions of the tire components to the tire bead area, the sidewall, the summit package, and the tread.

These test and measurements, as well as the numerical techniques for determining the relative contributions of tire sidewall and tread compliance needed for the Simulink models, are detailed in the appendices.

### Development of Tire Models in Simulink

The six types of tire models that were developed for this investigation were implemented using MATLAB Simulink. Once the two software development tools were defined, a strategy for implementing the various tire/laboratory road wheel (Clead Phase) and tire/vehicle model (Ride Phase) was needed.

#### Implementation Strategy

The implementation strategy of the MatLab Simulink modeling process is illustrated in Figure 4.3.

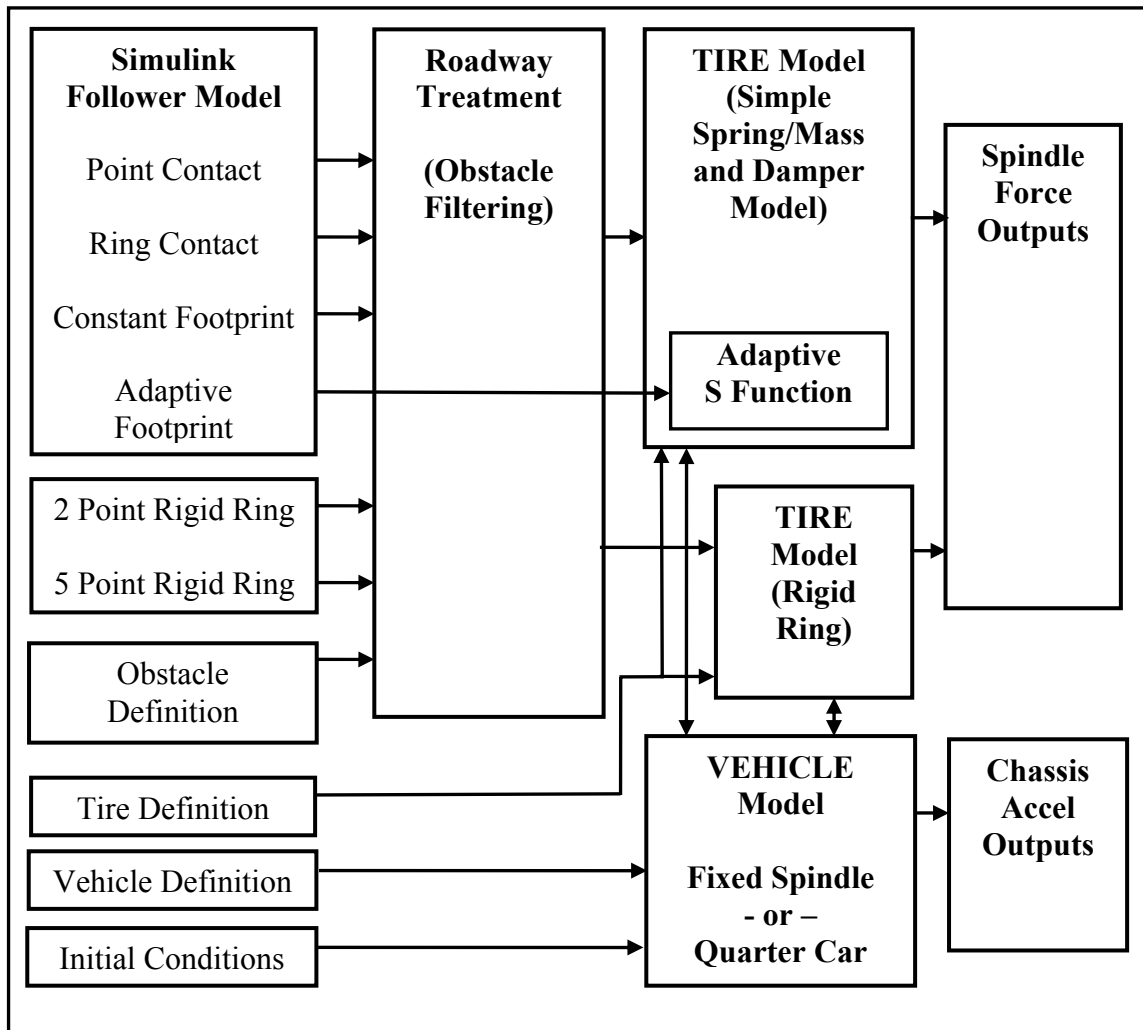


Figure 4.3: Tire/Vehicle Model Implementation in Simulink

For the Simulink models, all six tire models can be implemented using only three “core” tire carcass representations. The fundamental differences in the first three models – the point contact, the ring contact, and the constant footprint model – lie only in the way that the roadway obstacle displacement is presented to the tire carcass model.

## Obstacle “Conditioning”

Each of these three models use an obstacle conditioning algorithm in which the effective height, length, and geometry of the obstacle is modified. The resulting longitudinal position vs. displacement and effective contact patch engagement angle is passed to the tire carcass model. These input conditioning schemes are described in detail in the appendices, but the general implementation and their characteristic effect is as follows:

- The point contact follower emulates the rectangular cleat by first conditioning the rectangular road wheel cleat, transforming the rectangular obstacle shape into a sinusoidal input that maintains both:
  - identical peak input height (9.5 mm) and
  - identical area under the height vs. distance curve.

The resulting sinusoidal input is passed to the tire carcass model.

- The ring follower conditioning scheme is slightly more complex than the single point contact follower. The ring follower input conditioning is characterized by 1) maintaining the obstacle’s peak input amplitude in the vertical direction and 2) increasing the obstacle’s wavelength. The resulting input waveform is passed to the identical tire carcass model that was used for the single point contact follower.
- The constant footprint conditioning averages the obstacle height of the obstacle by enveloping it mathematically, thereby lowering the effective obstacle height

and increasing its wavelength. The resulting input signature is also passed to the identical tire carcass model that was used for the case of the single point contact follower.

- Because the adaptive footprint model uses radial carcass elements, its implementation was more complex and was best performed by writing a specific Simulink model that contained an embedded MatLab function. This function carries out a numerical integration of the vertical and fore/aft tire spindle force contributions attributed to each of the radial spring element deflections. The adaptive footprint model lengthens the obstacle wavelength due to the contact patch length, which will vary as a function of total static and dynamic vertical load.

The two point rigid ring model and the five point rigid ring model are significantly more complex than the previous four models. These two models account for the tread mass in the contact patch separately from the summit (rigid ring) mass. In addition, the static and normal dynamic forces in the tread elements are used with a traction model to generate longitudinal force based upon a longitudinal sliding friction model. The two point follower and five point follower schemes are both executed using similar code, the only difference being that the five point model represents the contact patch as four individual segments interacting independently with the traction model and the rigid ring as opposed to a single contact patch element for the two point model. Although not utilized in this investigation, these tire models provide the capability of generating driving and braking longitudinal force at the contact patch, making them suitable for studies involving



driveline accelerating torque and braking decelerating torque. The overall effect of the input conditioning for the two point and five point models is to mitigate the height of the obstacle as it is enveloped within the contact patch.

### Implementation of the Tire Models in Simulink

The approach for implementing the tire models in Simulink is straightforward and is performed as follows:

1. The tire model is defined (using simple linear second order equivalent mass/spring/damper systems).
2. The free body diagrams are drawn for each degree of freedom.
3. The equations of motion are written for each of the coordinates.
4. The roadway obstacle and the algorithm for the tire envelopment model is generated, i.e., the amplitude of the obstacle vertical input as a function of longitudinal wheel displacement  $x$ .
5. the enveloping model (single point follower, ring follower, constant footprint, adaptive footprint, 2 point follower, or 5 point follower) is written such that the obstacle is filtered as a function of longitudinal position.
6. auxiliary functions, such as inputting constants for the various lumped tire model parameters, initial conditions, traction model (in the case of the rigid ring models), etc. are written and incorporated into the Simulink model via MatLab 'm' scripts.

The process is detailed for each of the Simulink models in the appendices. An example of the Simulink code for the most basic tire model – the single contact point follower – is illustrated in Figure 4.4.

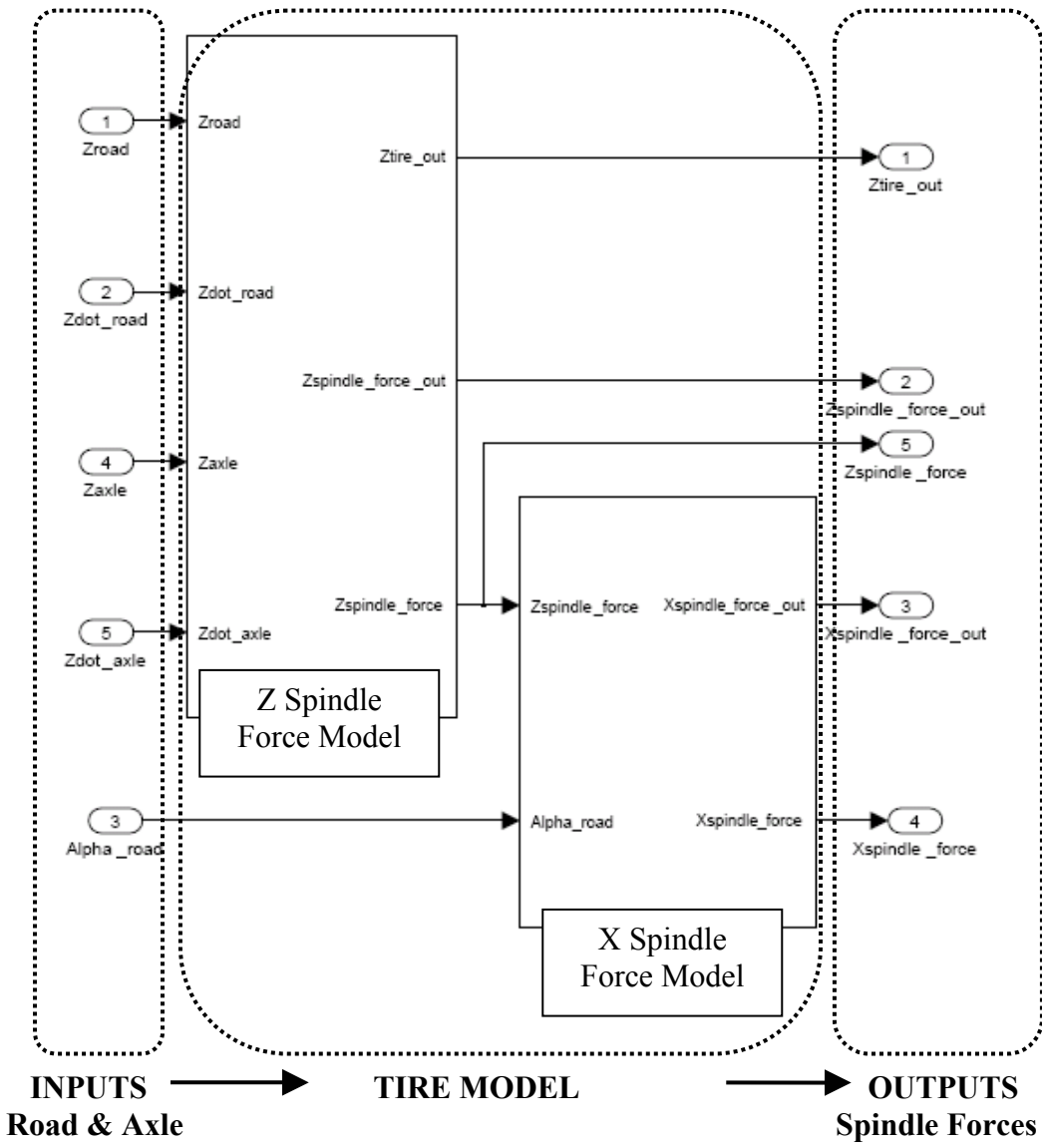


Figure 4.4: MatLab Simulink: Top Level for Single Point Contact Tire Model. The direction of signal flow in Simulink can of course be arbitrary. In this particular instance, the inputs to the tire model as shown in the left blue box, and include the Z position of the roadway obstacle (Zroad) and its instantaneous rate (Zdot\_road), and the

position of the axle or wheel center ( $Z_{axle}$ ) and its instantaneous rate ( $\dot{Z}_{axle}$ ). The fifth and final input to this tire model is the angle of incidence, or the angle between horizontal and the tangent to the obstacle ( $\alpha_{road}$ ). The outputs for the Simulink module are the vertical and horizontal spindle forces ( $Z_{spindle\_force}$  and  $X_{spindle\_force}$ , respectively). The additional two output ports for the spindle forces ( $Z_{spindle\_force\_out}$  and  $X_{spindle\_force\_out}$ ) are used to make the output forces available in the MatLab workspace.

The subsystem for the Z spindle position and force model is shown in Figure 4.5. As an ordinary second order differential equation, there are two integration blocks and a summation of forces which act upon the mass of the effective tire mass.

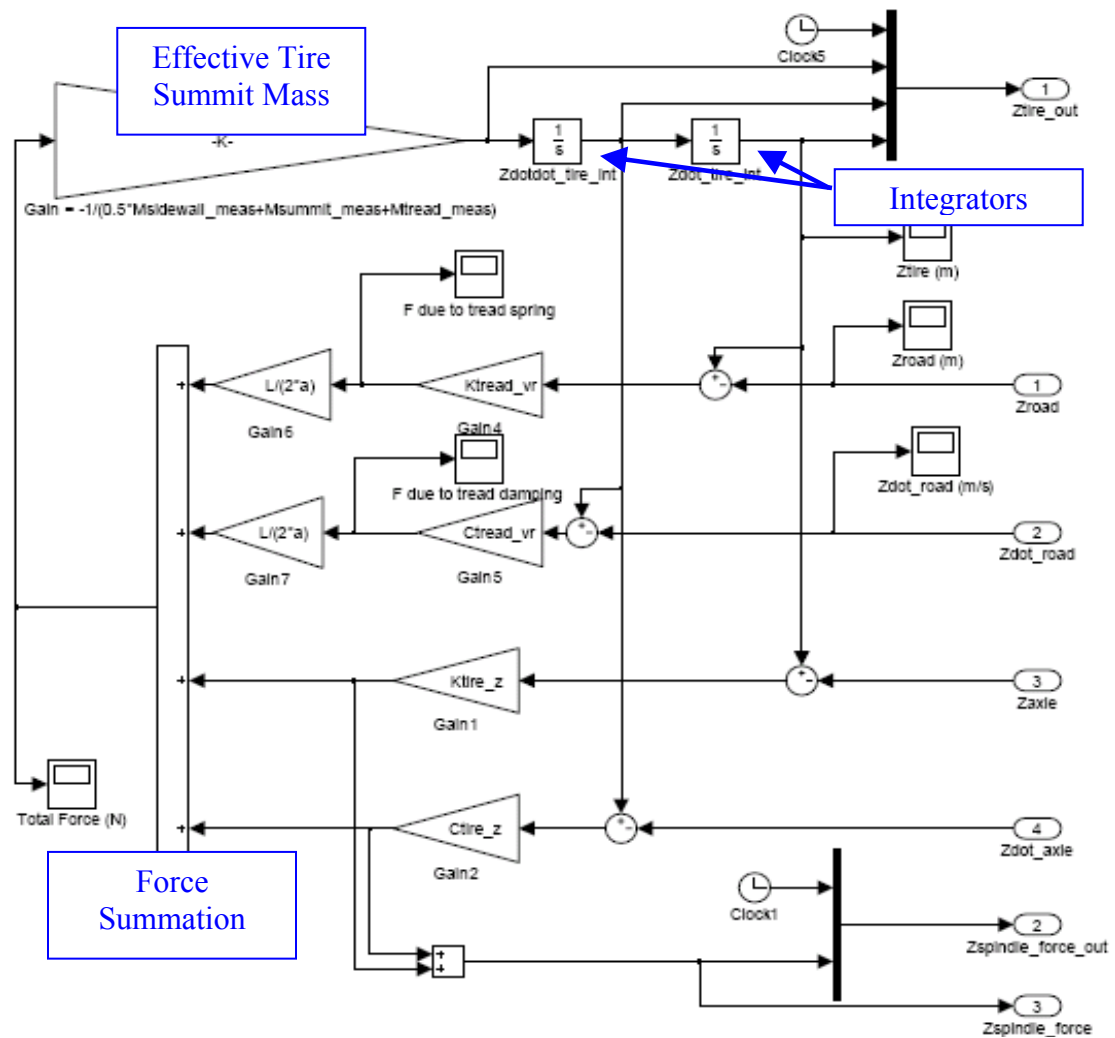


Figure 4.5: MatLab Simulink: Point Contact Model Z Spindle Force Subsystem

### Development of the FTire and Simulink Combined Model

The overall implementation scheme for the FTire model in SIMPACK is similar to but distinctly separate from the implementation of the Simulink models. As with a myriad of other analytical and statistical tire models, FTire is designed to be incorporated into a vehicle model via an interface that allows for the exchange of:

1. Tire solicitation, as imposed by the steering and suspension and the prevailing state of the vehicle. Tire solicitation includes the imposed tire slip angle, camber angle, vertical spindle load, and percent of driving or braking slip at the tire/ground interface.
2. Resulting tire force and moments, as returned to the steering and suspension system as a result of the imposed tire solicitation. These tire forces and moments include lateral force, driving or braking torque, and overturning moment as a result from the interaction between the tire and the ground at the tire/ground interface.

Therefore, suitable MBS software was needed to provide the vehicle interface required by FTire. The software selected to represent the vehicle (or, for the simulation of our laboratory road wheel test, the laboratory road wheel and spindle) is Intec SIMPACK Automotive Plus MBS.

The same data that was used to generate the simulation initial conditions, vehicle parameters, and obstacle characteristics are transferred into the FTire and SIMPACK

simulation files so that the outputs can be compared directly with that obtained from MatLab Simulink. The overall implementation of the MBS simulation is illustrated in Figure 4.6.

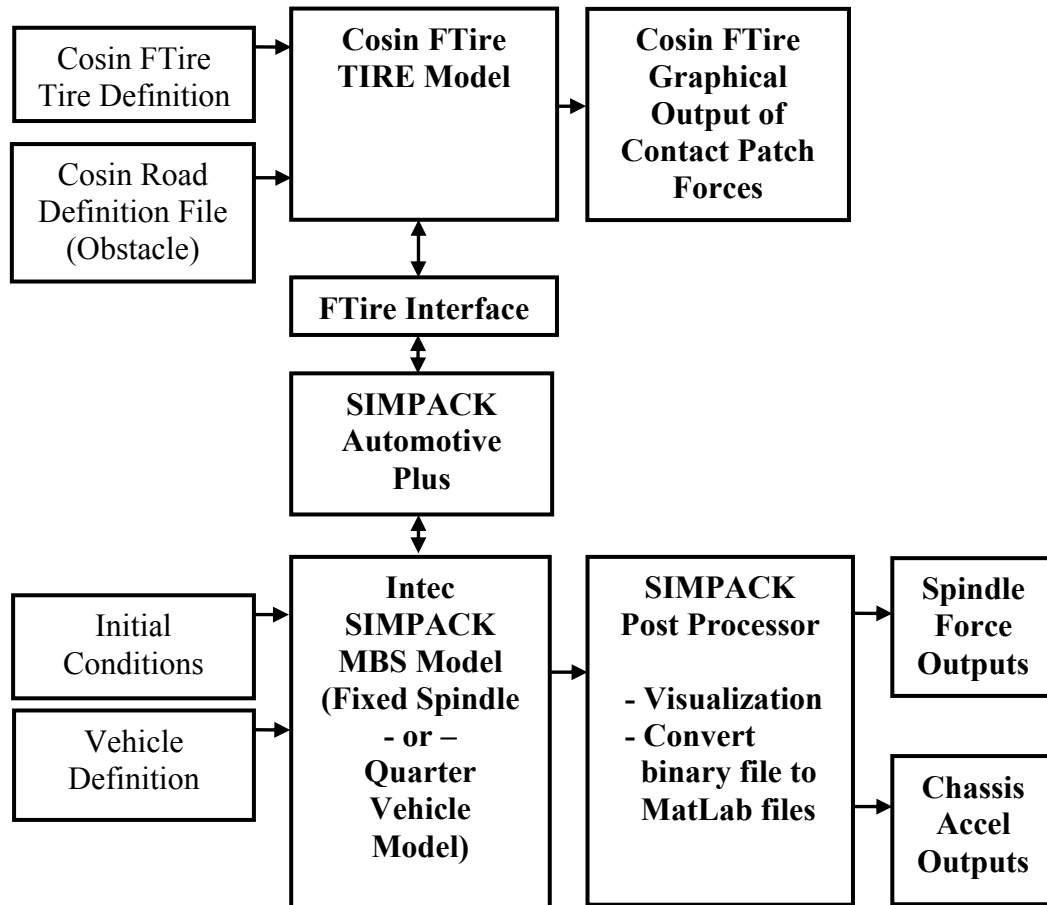


Figure 4.6: Tire/Vehicle Model Implementation using SIMPACK and FTire

FTire is a multi-body simulation model that models the tire summit belt package as a series of mass elements interconnected by nonlinear springs and dampers. The resolution of the mass elements is defined such that the global material characteristics of the composite belt structure are well represented functionally. However, they are not so

finely defined as to require the extensive material property characterization associated with finite element mesh models. The value of FTire is that it is sufficiently complex to capture relatively short wavelength phenomena, such as enveloping a cleat in the tire contact patch. It also provides frequency resolution beyond what can be obtained using mass/spring/damper models such as rigid ring models without requiring the increased computational power associated with FEA codes. FTire is sufficiently accurate that it is used in a variety of vehicle dynamic modeling software suites for such tasks as basic chassis dynamics in the linear operating regime, nonlinear handling such as emergency avoidance and safety maneuvers, ride comfort modeling, and generating road load characteristics for suspension endurance studies.



### Implementation of the Tire Models in SIMPACK Vehicle Plus

The intent of this investigation is not to explain the science of multi-body simulations (MBS) but to merely contrast that this approach, necessary for implementing the Cosin FTire model in SIMPACK Automotive Plus, is quite different than that required for modeling mechanical systems via other analytical and modeling methodologies. Although both MatLab Simulink and SIMPACK MBS approach use time step numerical integration solvers, the mechanical systems are defined using different techniques. Simulink requires that the mathematics inherent with the model be understood and the equations of motion written explicitly. In MatLab, the equations of motion are implemented directly in the code. In MatLab Simulink, the equations of motion are constructed as a block diagram in the graphical user interface. The SIMPACK MBS software does not require that the equations of motion be derived. Rather, the software relies upon the characterization of the physical model by the 1) mass properties of the components, 2) the constraints which exist between the mass components, and 3) any forces that are applied to the masses. The equations of motion are inherent in the kinematic chains which result from the system of masses, constraints, and external forces.

Construction and implantation of the FTire model in SIMPACK involves the following steps:

1. FTire is one of a number of tire models which can be implemented via the tire model interfaces already built into the SIMPACK software. Tire models (or for that matter, any force model) can also interface directly to SIMPACK.
2. The remainder of the physical system is constructed in the SIMPACK MBS software. For this investigation simple fixed spindle and quarter vehicle models were constructed. Using SIMPACK's Automotive Plus toolbox provides a comprehensive interface to pre-existing tire models, and automates a number of functions common to automotive modeling (routines which convert vehicle and suspension states into tire solicitations, driver models, speed controllers, etc.).
3. For the Cosin FTire model, an array of testing is required to populate the FTire model via an FTire "workbench." The software is designed to optimize the FTire parameters, and accepts a wide range of testing methods.
4. The Cosin FTire requires a road definition file to describe the roadway path in 3D and has a number of tools for customizing pre-defined roadway obstacles, generating obstacle functions, or importing pre-recorded roadway characteristic files. Cosin FTire is not compatible with the SIMPACK Automotive Plus roadway files.
5. The MBS is launched via the SIMPACK user interface. The Automotive Plus toolbox passes the vehicle state from the SIMPACK MBS vehicle model to the FTire model. The FTire model uses the road definition file and the imposed vehicle state to determine the generated wheel spindle forces and moments. The

Automotive Plus FTire model interface returns these spindle forces and moments back to the vehicle simulation in order to carry out the time step integration.

6. After the simulation is complete, time histories of position, velocity, force, etc. for both the FTire and SIMPACK model are saved as a SIMPACK binary output file. The binary output file can be analyzed by the SIMPACK post processor. Alternatively, the post processor can export selected simulation results to a variety of common formats, including MatLab arrays.

For this investigation, a quarter car MBS vehicle was built using SIMPACK's Automotive Plus toolkit. For the Cleat Phase laboratory road wheel simulation, the wheel spindle height of the quarter vehicle model was constrained to a height above the ground plane which would correspond to the desired static vertical tire load. For the quarter vehicle model simulation in the Ride Phase, the constraint was simply removed. The topology for the MBS model that was developed for the quarter vehicle is shown in Figure 4.7.

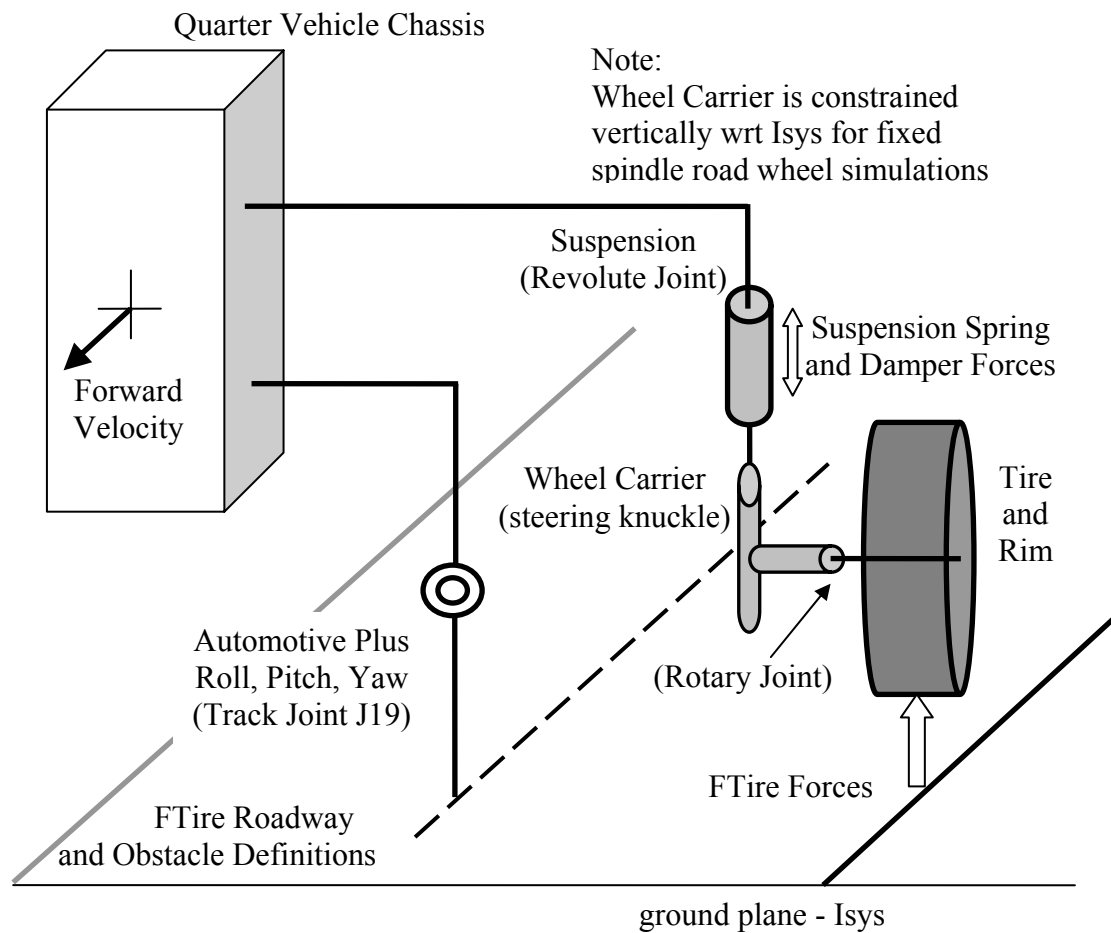


Figure 4.7: Quarter Vehicle Car Model Topology – Masses, Constraints, and Forces

This topology is equivalent to the classic quarter vehicle ride comfort model. The quarter vehicle ride model, as implemented in SIMPACK, is shown in Figure 4.8. Values used to generate the quarter vehicle ride model were obtained from a vehicle study performed at Michelin Americas Research Company[16] and are included in Table 4.1.

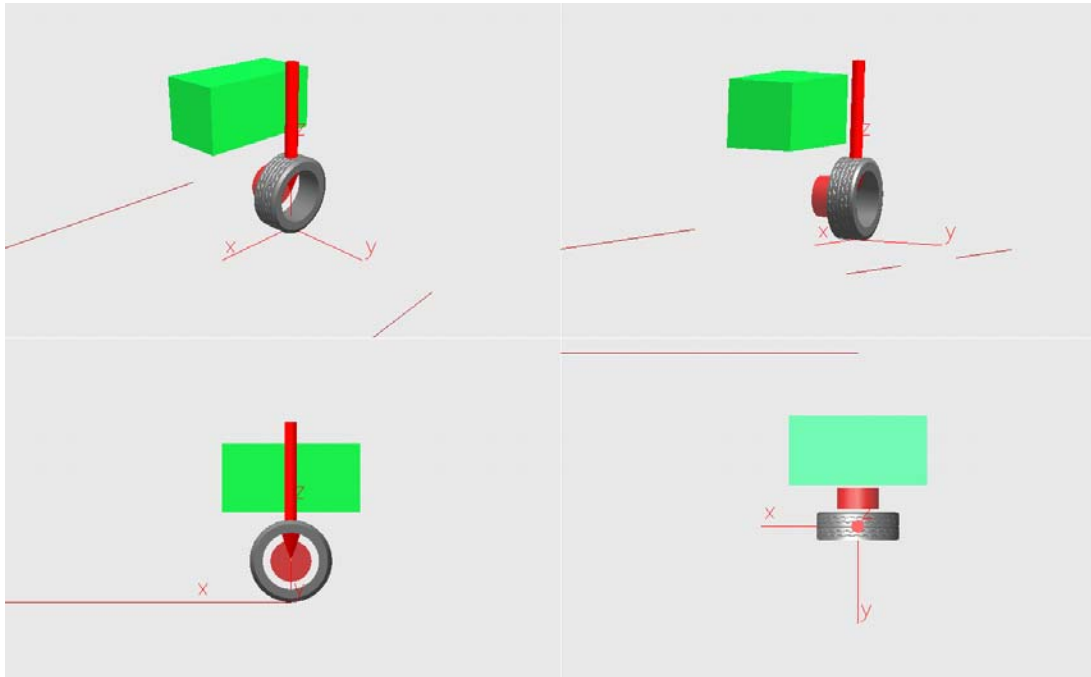


Figure 4.8: Views of Quarter Vehicle Car Model as Implemented in SIMPACK

Table 4.1: Tire and Quarter Vehicle Model Parameters

Variable Descriptor	Value	Units	Variable
Tire aspect ratio (section height to width ratio)	45	%	%
Tire contact patch length	0.158	m	CPL_pneu
Area contact between tire and ground	44.8	in <sup>2</sup>	CP_Area_in2
Quarter car average suspension viscous damping	2950	N sec/m	Caxle
Tire sidewall rotation damping about the axle spin axis	72.1	Nm sec/rad	Ctire_theta
Tire sidewall fixed spindle longitudinal damping	1354	N sec/m	Ctire_x
Tire sidewall vertical damping	209	N sec/m	Ctire_z
Circumferential damping coefficient of tread blocks	2693	N sec/m	Ctread_cr
Vertical damping coefficient of tread blocks	1775	N sec/m	Ctread_vr
MOI of tire bead structure incl. sidewall component	0.23	Kg m <sup>2</sup>	Ibead
Moment of inertia of tire bead structure	0.15	Kg m <sup>2</sup>	Ibead_meas
Moment of inertia of the wheel about the spin axis	0.73	Kg m <sup>2</sup>	Irim

Moment of inertia of the tire sidewall structure	0.91	Kg m <sup>2</sup>	Iring
Moment of inertia of the tire sidewall	0.16	Kg m <sup>2</sup>	Isidewall_meas
Moment of inertia of the tire summit structure	0.63	Kg m <sup>2</sup>	Isummit_meas
Total moment of inertia of the tire about the spin axis	1.16	Kg m <sup>2</sup>	Itire
Moment of inertia of the tread band	0.017	Kg m <sup>2</sup>	Itread
Moment of inertia of the tread band outside of the tire contact patch associated with the rigid summit ring	0.222	Kg m <sup>2</sup>	Itread_meas
Average suspension vertical wheel rate	31675	Kg m <sup>2</sup>	Kaxle
Tire sidewall rotational spring rate	60057	Nm/rad	Ktire_theta
Tire sidewall longitudinal spring rate	1354447	N/m	Ktire_x
Tire sidewall vertical spring rate	261347	N/m	Ktire_z
Tread block circumferential damping	2692900	N/m	Ktread_cr
Tread block radial damping	1775149	N/m	Ktread_vr
Axle mass for one-quarter vehicle	23.8	Kg	Maxle
Moment of inertia of tire bead structure	3.15	Kg	Mbead
MOI of tire bead structure incl. sidewall component	2.25	Kg	Mbead_meas
Quarter vehicle total mass	589	Kg	Mcar
Driving torque at the wheel spindle	0	Kg	Mdrive
Moment of inertia of the wheel about the spin axis	17.3	Kg	Mrim
Moment of inertia of the tire sidewall structure	8.61	Kg	Mring
Moment of inertia of the tire sidewall	1.80	Kg	Msidewall_meas
Sprung chassis mass of one-quarter vehicle	536	Kg	Msprung
Moment of inertia of the tire summit structure	5.87	Kg	Msummit_meas
Mass of tire	11.9	Kg	Mtire
Mass of the tread band in the contact patch	0.15	Kg	Mtread
Total mass of the tread band around the tire circ.	1.99	Kg	Mtead_meas
Rolling tread width	0.183	m	RTW
Effective Rolling Radius	0.3292	m	Reff
Rim diameter	18	in	Rim
Section Width	0.245	m	SW
Quarter Vehicle Mass	589	Kg	Spindle_mass
Tire inflation pressure in Pascals	200	kPa	Tire_press_kPa

Tire inflation pressure in psi	29	Lbf/in <sup>2</sup>	Tire_press psi
One-half contact patch length	0.0789	m	a
Fraction of tire circumference in the tire contact patch	0.0763	N/A	frac_CP

### Ride Phase – Ride Comfort Predictions of Quarter Vehicle Models

In the Ride Phase, simulations are conducted by incorporating the tire models into a simple quarter vehicle model. For MatLab Simulink, this consists of generating the equations of motion for a representative quarter model vehicle and applying them via block diagrams. For Cosin FTire and SIMPACK MBS software, a quarter-vehicle MBS model is created and implemented in SIMPACK Automotive Plus. These models are then exercised over:

- the rectangular laboratory road wheel test cleat – this size was chosen as it provides a means of easily verifying the expected mitigation in peak vertical spindle forces due to the suspension compliance, and
- a typical parking lot speed bump.

Since no on-vehicle measurements are available, the tire model simulation metrics are normalized to the SIMPACK MBS software running the Cosin FTire. A comparison of the simulation vs. laboratory test results of all tire models in the Cleat Phase confirmed that the Cosin FTire model provided the best model fidelity, as was expected – Cosin FTire has many additional degrees of freedom and requires considerably more test data input to generate the tire model. Consequently, it was possible to assume that the combined integrated SIMPACK MBS and Cosin FTire model could represent the “control vehicle” to which all other simulation results are compared.



The normalized metrics of the integrated tire/vehicle models are compared to those of the SIMPACK MBS and Cosin FTire control vehicle determine for obstacles of:

- short wavelength compared to the contact patch – the 9.5 mm high by 19 mm long rectangular cleat (representing a spatial interaction length of only approximately 1/8 times the length of the tire contact patch) , and
- long wavelength compared to the tire contact patch - the sinusoidal-shaped parking lot bump measuring 4 inches high and 12 inches long (representing a spatial interaction of approximately 1.9 times the length of the contact patch).

Having two distinct obstacles that are fundamentally both 1) much shorter and 2) much longer than that of the contact patch is important, as a primary factor for determining the suitability of a tire model for tire/vehicle simulation will be its ability to correctly emulate contact patch envelopment of a roadway obstacle.

### Tire Selection and Tire Modeling Considerations

There were numerous considerations when selecting a tire with which to conduct this investigation of tire models for ride comfort simulations.

1. The data set that is required to populate the algorithms to generate an FTire model is extensive and beyond the resources of this investigation. Therefore, an available FTire model which had already been created was provided by Michelin Americas Research Company's European research headquarters in Ladoux, France. Since the FTire model was generated for a low aspect ratio summer performance tire, it presented challenges to the modeling effort that would not be anticipated when modeling more generic passenger car or light truck all-season tires. For example, the relatively stiff summit structure of this tire consists of not only the normal working steel ply lamina, but also:
  - a. extensive reinforcing material consisting of circumferentially-wrapped nylon belts, at a zero degree angle, over the two steel belt composite in the summit (generically referred to as a zero degree cap ply).
  - b. additional circumferential Kevlar cord over the zero degree cap ply.

These two structural reinforcements reduce the summit compliance, which aids the assumption that the summit structure is a rigid ring. However, the reinforcements also increase the shear stiffness at the base of the tread band,

making the representative bulk stiffness more difficult to capture using the conventional battery of tire rigidity testing at our disposal.

In addition to the greater summit stiffness of performance all-season tires, performance tire treads can be stiffer than all season or all terrain tires, despite the use of softer, more hysteretic rubber compounds. This greater tread band stiffness is due to:

- larger tread blocks with shorter tread depth
- lack of grooving in existing tread blocks
- lack of tread blocks in the center ribs, replaced by solid or nearly solid ribs

To illustrate the potential for a wide range of longitudinal and vertical tread block stiffnesses, three different tread patterns are illustrated in Figure 4.9. The tread pattern at the top of the figure is for the handling-oriented performance handling tire that was used in this investigation. This pattern consists of solid ribs or large tread blocks of reduced height (shallow tread depth) to increase the rigidity in the contact patch. The tread pattern in the middle is that of a typical all-season tire. This tread pattern consists of closely-spaced but distinct tread blocks of moderate height (moderate tread depth). Under moderate to severe longitudinal shear forces, such as those that occur under forceful braking, the small lateral grooves and tread blocks come into contact with one another and their mutual reinforcement increases the longitudinal tread block rigidity. This tread sculpture is less rigid than the sport tire, but typically offers better resistance to

hydroplaning, improved snow performance and comfort over the handling performance tire. The tread pattern at the bottom of the figure comes from an all-terrain tire that would be found on light trucks or utility vehicles that are occasionally tasked with driving off of paved roads. The tread blocks are widely spaced and do not have any possibility of interlocking and reinforcing each other during moderate to severe driving or braking forces. These tread blocks have the deepest tread depth to improve snow and mud traction performance.

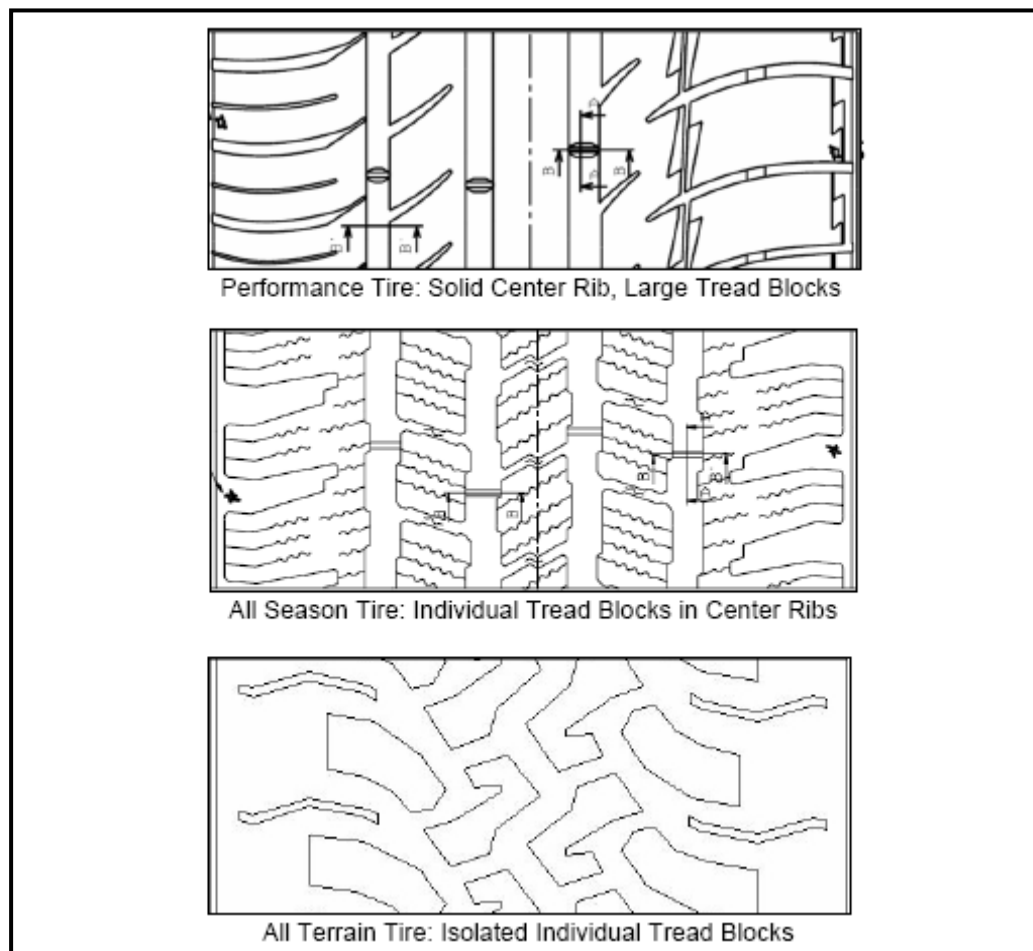


Figure 4.9: Example Tread Patterns Fitted to Modern Production Vehicles

The combined effect of geometry and structural differences in pneumatic tires can result in a wide range of longitudinal stiffness characteristics. This is evident by comparing tire longitudinal stiffness values versus inflation pressure for different classes of tires and constructions, as illustrated in Figure 4.10.

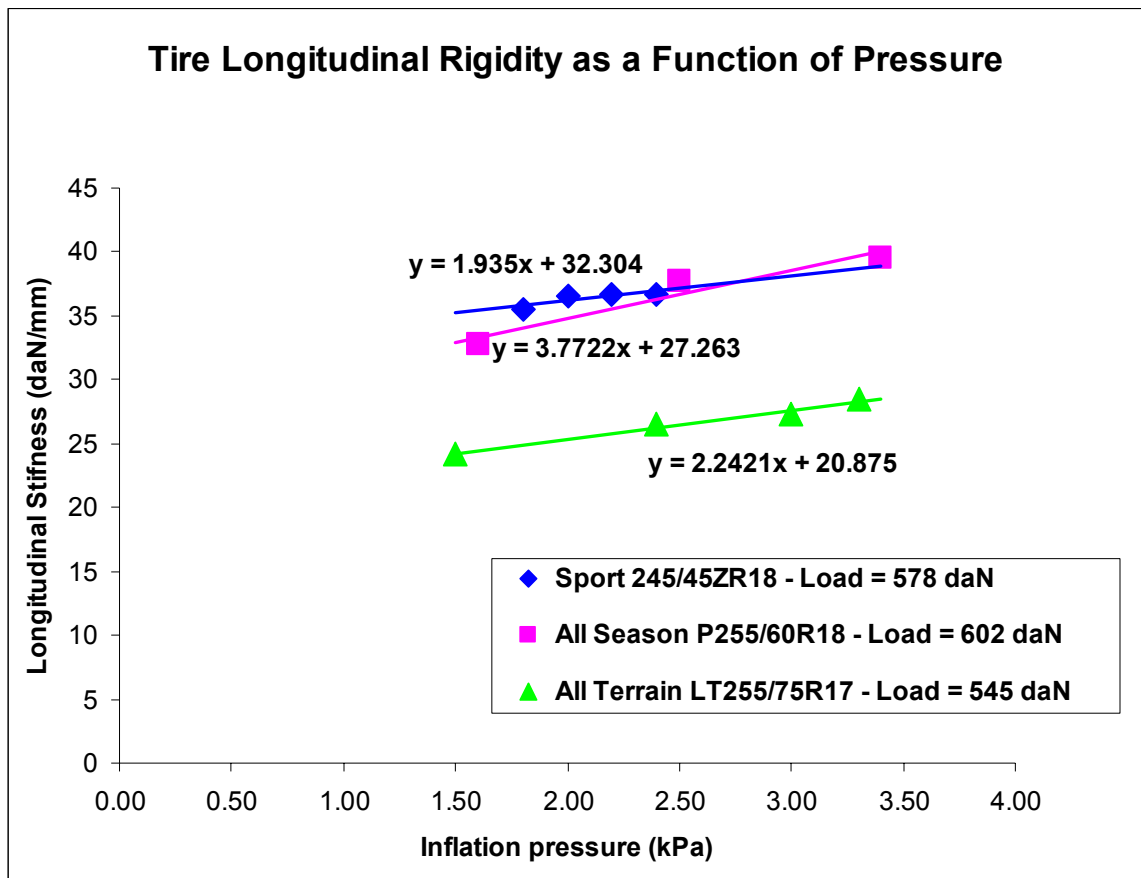


Figure 4.10: Various Longitudinal Tire Stiffness Values

In general, many factors contribute to the longitudinal stiffness characteristics of pneumatic tires. Being able to first measure and then model these static stiffness characteristics is the first step in developing the tire ride model. Verification that the dynamic characteristics of the tire are adequate for ride comfort modeling would then be the next step.

2. The FTire model parameters are extensive and are generated by an FTire “Workbench,” which optimizes a wide variety of test data. The optimization routines in FTire are designed to manage the over-constraints imposed by multiple sets of tire test and testing conditions, but the internal criteria for resolving these over-constraints are neither available nor visible to the end user. The original FTire tire data file supplied by Ladoux was not numerically stable when loaded into the combined FTire and SIMPACK MBS vehicle simulation software. After an extensive inspection of the existing data file, the intermediate pressure from a set of three vertical deflection tests was removed, and a numerically-stable composite tire/vehicle model was achieved.
3. The curvature of the road wheel was neglected in the road wheel cleat simulations. However, the radius of the curvature of the road wheel will affect the vertical force characteristic to some extent as the cleat traverses the contact patch. Specifically, a non-infinite radius of curvature will result in:
  - a. The cleat engaging the contact patch at an angle.
  - b. The tire having greater vertical deflection at the center of the contact patch than if the tire was loaded on a flat surface. This affects the contribution of the vertical structural stiffness in the contact patch. The magnitude of the structural effect will be less for tires having relatively high sidewalls, such as a conventional passenger tire, but greater for tires with low sidewalls, such as performance tires. The structural effect will be more pronounced with self-supporting “zero pressure” run flat or extended mobility tires, all

of which have more structural sidewall rigidity than conventional pneumatic tires.

The relative importance of these effects will depend upon the tire itself as well as the radius of the road wheel. However, these effects of these differences are considered to be both 1) reasonably small and 2) consistent amongst all of the models. Therefore, they were not considered in this investigation.

## CHAPTER 5

### RESULTS OF FIXED SPINDLE, CLEAT PHASE

#### Introduction

The general purpose of the investigation is to determine the suitability of a range of tire models for integrated tire/vehicle comfort simulations. This was accomplished using a two-phase approach:

1. The Cleat Phase was a comparison of the spindle force fidelity of the seven different tire models versus results obtained from laboratory tests. One simulation model was Cosin FTire, a commercially-available flexible ring tire model implemented in SIMPACK Automotive Plus. This model was expected to compare the best with test results, as it is the most complex model and requires the greatest amount of testing data to obtain the tire model parameters.
2. The Ride Phase was the implementation of all tire models in a quarter vehicle comfort model. Since instrumented vehicle results were not available, the results of the simulations using Cosin FTire and SIMPACK were used as the reference. The metrics for judging simulation fidelity in this case were peak longitudinal and vertical acceleration of the chassis as the quarter vehicle model traversed two obstacles – the same small cleat used in the road wheel test, and a parking lot bump. These two obstacles respectively have wavelengths that are shorter and longer than the tire contact patch. The cleat



solicits the enveloping characteristics of the tire's contact patch whereas the parking lot bump solicits the carcass deflections.

This chapter (Chapter 5) describes the first phase of the investigation, which is the comparison of the spindle force fidelity of the seven different tire models versus results obtained from laboratory tests. The next chapter (Chapter 6) will describe the second phase of the investigation, which is the comparison of the tire models when they are integrated with a quarter vehicle model.

### Cleat Phase Results – Fixed Spindle Road Wheel Investigation

In the Cleat Phase, the results of the tire model simulations are compared to test results. The road wheel cleat test is conducted at eight kilometers per hour and the spindle height is fixed after establishing the static vertical tire load. In the case of the 245/45R18 summer performance test tire, a load of 589 kg (which is the maximum rated load at 180 kPa or 26 psi inflation pressure) was selected, with a corresponding 200 kPa (or 29 psi) inflation pressure. This load/pressure combination represents a typical maximum expected tire load at the lowest anticipated, vehicle placard, cold inflation pressure. The test cleat consists of a steel bar of rectangular cross section attached to the road wheel such that the longest dimension of the bar is perpendicular to the direction of travel. The rectangular cross section is 9.5 mm high and 19 mm wide (obstacle length of 19 mm). An overview of the physical layout of the Michelin Americas Research Company test apparatus used to obtain the spindle force data is shown in Figure 5.1.

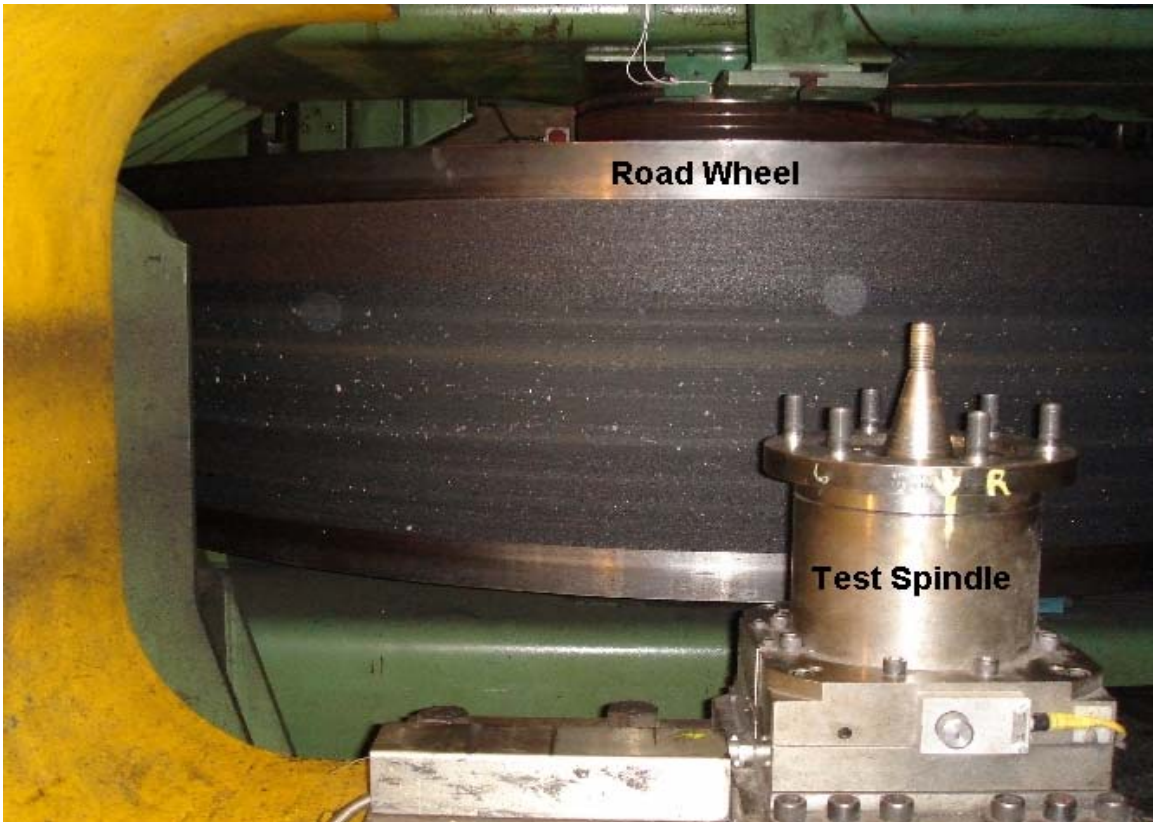


Figure 5.1: Vertical Test Spindle and Horizontal Road Wheel

This comparison testing for the Cleat Phase is analyzed by plotting the simulated vertical and longitudinal spindle forces versus longitudinal road wheel distance and then overlaying the measured laboratory road wheel spindle forces for each of the tire models. As an example, the results for the fixed spindle test for the single point contact follower are shown in Figure 5.2.

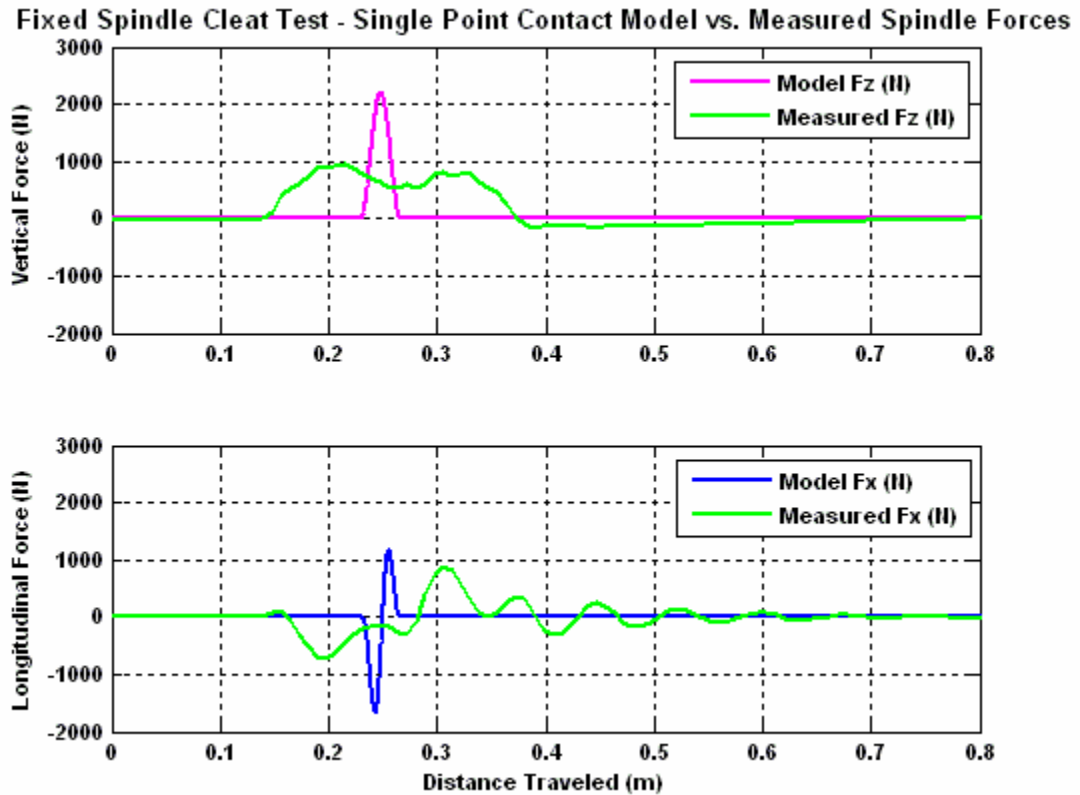


Figure 5.2: Point Contact Follower – 8 Kph Fixed Spindle Results – Road Wheel Cleat

The intention is to first examine the simulated spindle force vs. distance plots in order to understand the characteristic “signatures” of the models and how they compare to the corresponding laboratory data. Then, the maximum amplitudes of the vertical and longitudinal simulated spindle forces are normalized to the values obtained from the test measurements. This allows the models to be compared objectively against the test data and each other.

In the Cleat Phase, two different configurations for the first three models (single point contact follower, ring contact follower, and constant footprint) were developed:

1. A “Simple Spring” configuration, in which the tire/wheel mass is concentrated at the wheel hub, and

2. An “Equivalent Summit Mass” configuration, in which the equivalent mass of the tire summit belt package has an additional degree of freedom in the vertical direction. Although the exact physics are not mimicked using this approach, it does allow the summit mass to oscillate in a manner similar to what is observed when actual tires are tested on a road wheel with cleats.

The various tire models that were studied in the Cleat Phase investigation and their basic configurations are listed in Table 5.1.

Table 5.1 Cleat Phase Configurations for Fixed Spindle Lab Test

<b>Tire Model</b>	<b>Configuration</b>	<b>Cleat</b>	<b>Comment</b>
Single Point Contact (“1 Pt”)	Simple Spring (“K”)	Sinusoid	The rectangular cleat is represented by a trapezoid of equal cross sectional area
“	“	Rectangular	
“	Summit Mass (“KM”)	Sinusoid	
“	“	Rectangular	
Ring Follower Contact (“Ring”)	Simple Spring	Sinusoid	Ring follower may have one or two points of contact
“	“	Rectangular	
“	Summit Mass	Sinusoid	
“	“	Rectangular	
Constant Footprint (“Const”)	Simple Spring	Sinusoid	Footprint area stays constant. Vertical force is distributed in contact area.
“	“	Rectangular	
“	Summit Mass	Sinusoid	
“	“	Rectangular	
Adaptive Footprint (“Adapt”)	Simple Spring	Sinusoid	No logical summit mass configuration
“	“	Rectangular	
2 Point Follower Rigid Ring (“2 Pt”)	N/A	Sinusoid	Model developed for this investigation
“	“	Rectangular	
5 Point Follower Rigid Ring (“5 Pt”)	N/A	Sinusoid	Contact patch represented by 4 segments
“	“	Rectangular	
Cosin FTire and SIMPACK (“FT”)	N/A	Sinusoid	Commercial Multi-Body Simulation (MBS) Software
“	“	Rectangular	

Note that the sinusoidal cleat consists of one complete sine wave which has the following characteristics:

1. identical peak-to-peak amplitude as the height of the rectangular road wheel cleat
2. length which is twice that of the rectangular road wheel cleat
3. identical area as the rectangular road wheel cleat
4. has continuous first and second derivatives

A generally-accepted assumption for simple tire models is that the resultant spindle force vector is normal to the obstacle surface, as shown in Figure 5.3.

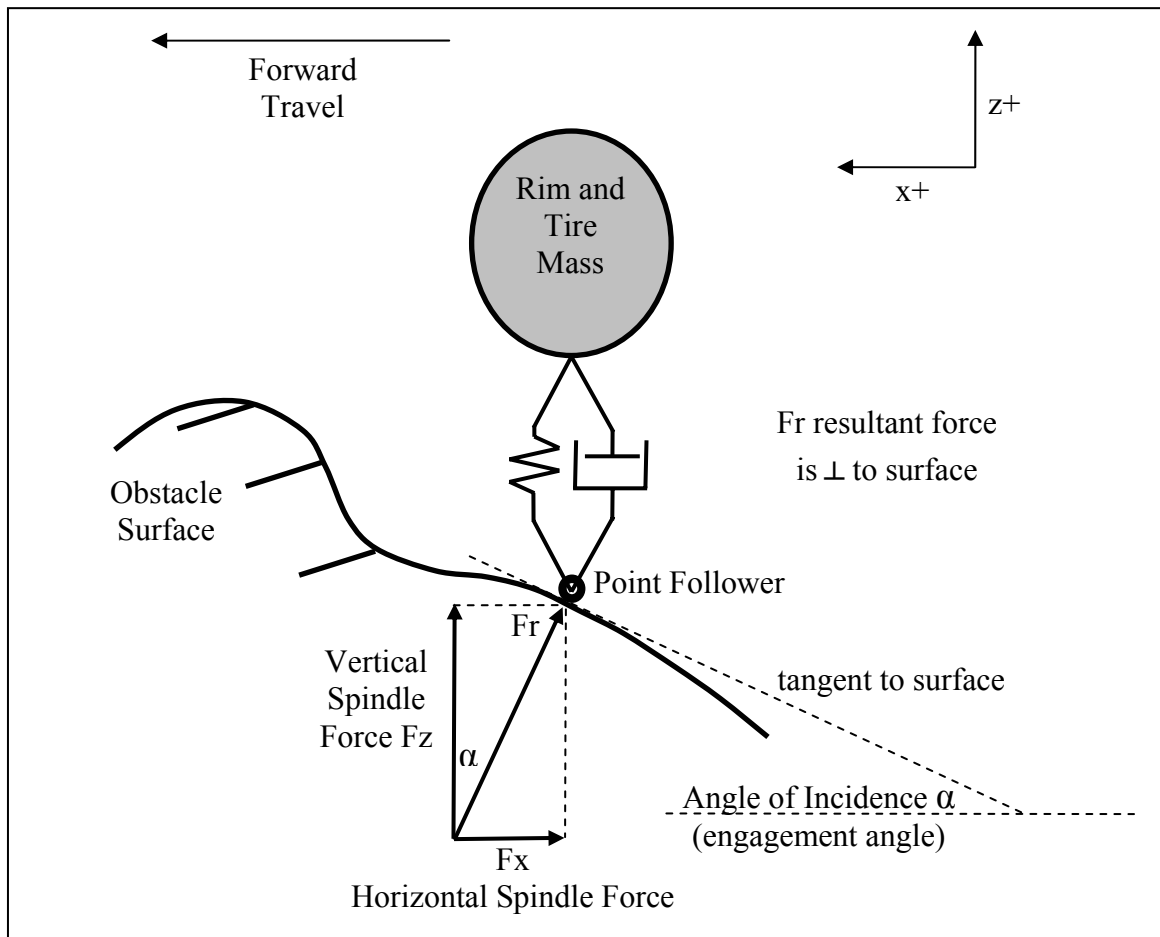


Figure 5.3: Generation of Longitudinal Spindle Force

However, if the obstacle is of a true rectangular nature, a point follower cannot provide a defined longitudinal force component. One solution is to approximate the cleat as a trapezoid of equal height and area as the rectangular cleat. In this investigation, the trapezoidal representation of the cleat rectangular cross section was created by arbitrarily adding 5% of the cleat length to the base of the trapezoid and subtracting 5% of the cleat length from the top of the trapezoid.

Simulating all of the tire model configurations as listed in Table 5.1 will produce a total of 40 vertical and horizontal spindle force graphs for the Cleat Phase investigation. As the goal of this investigation is to determine the suitability of applying various types of tire models to integrated tire/vehicle comfort modeling, a practical approach is needed to clarify and summarize the simulation results. Therefore summary bar charts of each tire model's ability to accurately predict two of the most simple yet potentially most informative metrics – peak vertical and peak longitudinal spindle forces – are developed in order to provide concise objective summaries of relative performance of the tire models compared to the laboratory results.

#### Fixed Spindle Road Wheel Cleat Testing

For the Cleat Phase investigation, the road wheel cleat test is the standard to which all of the fixed spindle simulation results will be compared. Therefore, it is important to be familiar with the general characteristics of the spindle forces generated by the test. This can be accomplished by examining the spindle force wave forms that result when the tire encounters a rectangular test cleat. Figure 5.4 shows the test tire engaging the cleat and the resultant spindle forces as a function of distance. The physical length of

the rectangular cleat on the drum - 19 mm – is shorter than the distance the tire is actually engaged with the cleat because the cleat must pass beneath the entire length of the contact patch (approximately 160 mm). Another factor is the geometry of the cleat and the loaded tire. As the tire approaches the cleat, the cleat contacts the exterior of the tread band prior to the cleat actually entering the contact patch. The cleat remains in contact with the tire until after the cleat exits the contact patch and finally clears the exterior of the tread band. The higher the cleat and the larger the tire radius, the greater the increase in total cleat engagement distance.

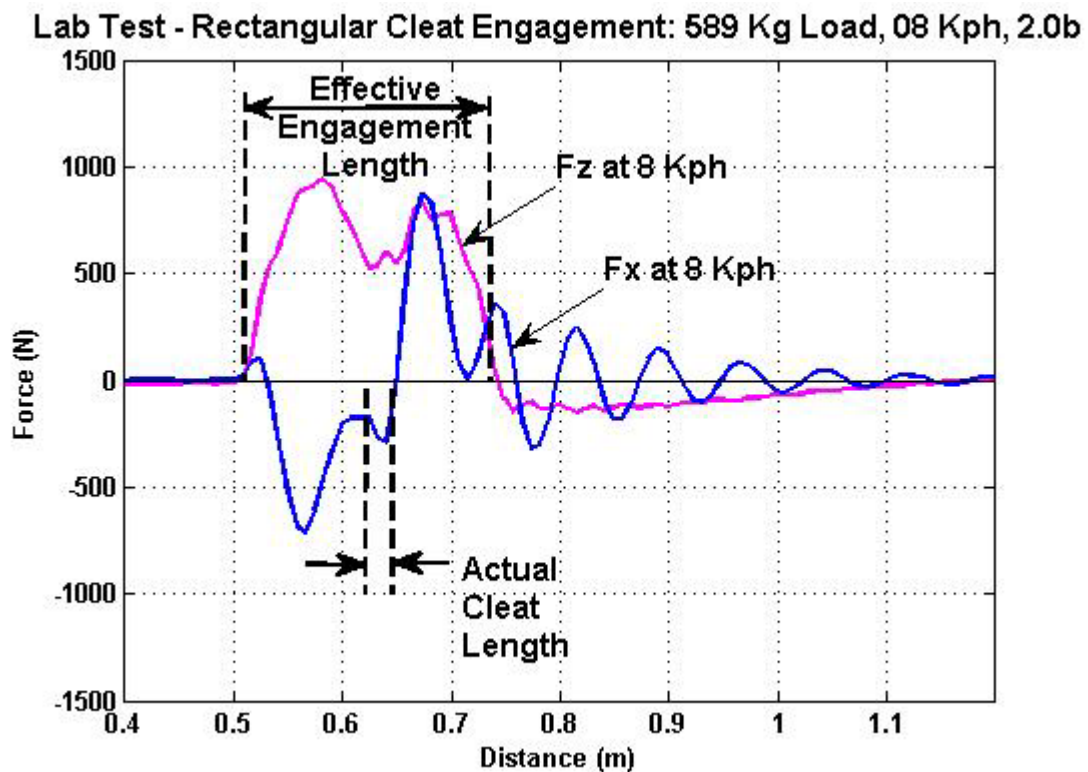


Figure 5.4: Road Wheel Tire and Cleat Engagement Distance

Even though the tire is:

- traveling relatively slowly at 2.22 meters per second
- traversing a cleat that is only 9.5 mm high and 19 mm in length



- operating at a relatively low inflation pressure of 2.0 bars

the tire oscillations are clearly evident. This ringing is indicative of not only the low damping present in modern tire constructions and materials, but also the presence of a complex sequence of energy transfer and storage within the tire itself - and the potential for complex energy transfer between the tire and the vehicle suspension.

#### Load and Speed Effects on Laboratory Road Wheel Cleat Tests

Because this investigation involves multiple types and variations on tire models as well as several obstacle types, investigating multiple speed, load, and pressure conditions was relegated to future work. However, it is beneficial to examine the relationship between the tire test speed and tire test load conditions at least on a rudimentary level.

The net effect of speed and load on the response of a tire as it encounters a cleat obstacle are the result of multiple competing mechanisms in the tire. Using only experimental road wheel cleat data, as shown in Figure 5.5, one can examine general trends in fixed spindle forces for our study tire.

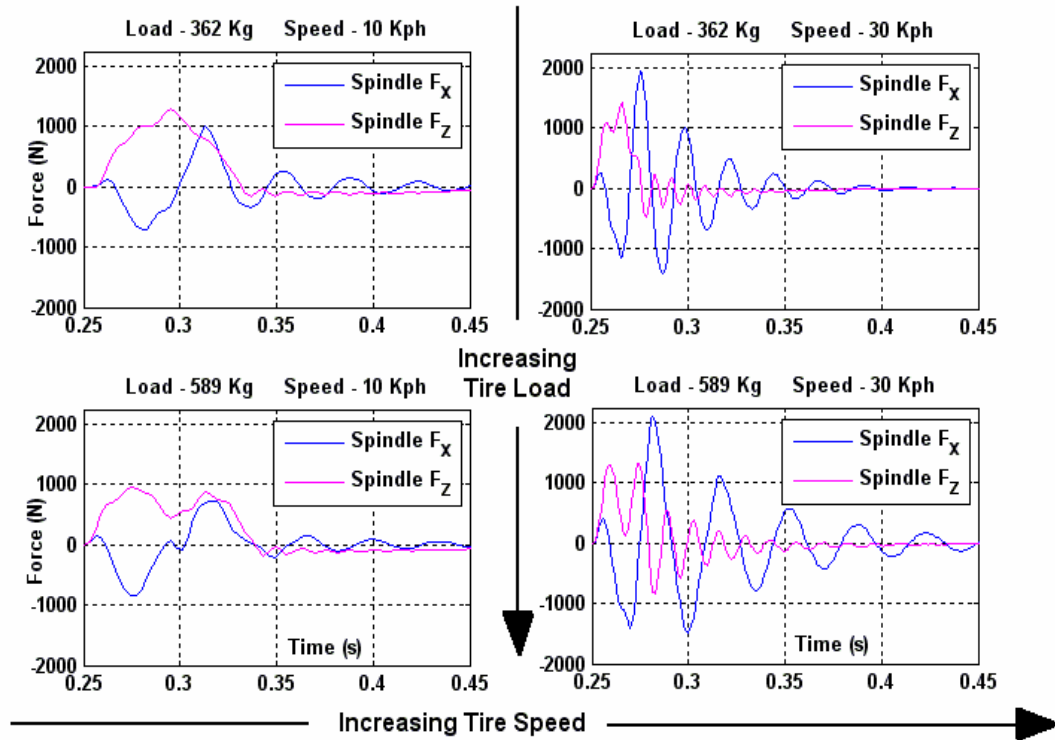


Figure 5.5: Matrices of Spindle Force Characteristics Plots for Load and Speed

Some general trends include:

- The characteristic shape of the vertical spindle force as the cleat traverses the contact patch evolves as a function of tire load – concave down to concave up – as the load is increased.
- Peak vertical spindle force decreases as load increases.
- Peak vertical spindle force increases as tire speed increases
- Despite a 63% increase in load when going from the low to the high vertical static load test conditions, the tire’s resonant vertical spindle frequency remains relatively constant at approximately 73 Hz. This is expected, as the distributed mass properties and structural stiffness remain essentially constant

Similarly, one can look for general trends in the horizontal spindle forces:

- The characteristic shape of the horizontal spindle force as the cleat traverses the contact patch generally does not evolve significantly as a function of tire load with one exception: there are local maxima and minima at the low speed and high load condition that occur as the cleat traverses across the centerline of the contact patch ( $t=0.3$  seconds).
- The peak horizontal spindle force is lower at the high load condition
- The peak horizontal spindle force increases with speed
- As with the resonant frequency of the vertical spindle force, the resonant frequency of the horizontal force is a weak function of tire load and speed. However, a higher torsional structural stiffness as the contact patch length increases with load may account for the higher resonant frequency at the higher vertical load condition (approximately 29 Hz for the 589 kg load and 26 Hz for the 362 kg load condition).

Greater analysis of tire characteristics will require more sophisticated modeling, such as substructure modal analysis, and are beyond the intention of this tire model investigation.

### Fixed Spindle Results – Point Contact Follower

The first three models that were implemented in MATLAB Simulink – the point contact follower, the ring contact follower, and the constant footprint tire models - were developed both as 1) simple “spring” models, where the tire mass was concentrated at the wheel spindle, and 2) “equivalent summit mass” models, where the tire summit mass was modeled between the tread blocks and the tire sidewall such that the additional degree of freedom would allow the tire to generate a vertical mode, a characteristic of pneumatic tires. Unless this additional degree of freedom is added, the simple models degenerate into terrain following with a simple spring / damper system transmitting forces between the terrain and the wheel spindle. The fourth model that was implemented in MatLab Simulink – the adaptive footprint model – was not developed with an equivalent tire summit mass, as the radial force elements would require a mass element not unlike that of a rigid ring. The two point contact follower and five point contact follower rigid ring models already contain an equivalent summit mass with a vertical degree of freedom, as does the flexible ring FTire model.

In order to best develop an understanding of how well the simulations perform relative to the laboratory measurements, the graph of the spindle force curves is presented first. Visually comparing the spindle force signatures as the tire models traverse an obstacle and comparing them to the measured laboratory results is an effective way to subjectively evaluate tire model performance. The metrics for each model – peak spindle vertical and horizontal forces – are captured, normalized to the laboratory road wheel

cleat test, and presented later as bar charts in order to provide a more objective means of comparing tire model performance.

The vertical and horizontal spindle forces generated by the point contact model are graphed as functions of position along with the laboratory road wheel. Figure 5.6 shows the results for the “simple” tire model as it traverses the “sinusoidal equivalent” of the rectangular laboratory road wheel cleat. Figure 5.7 depicts the “sinusoidal equivalent” of the rectangular cleat of height  $H$  and length  $L$  that was used in this investigation – details of its derivation are in the appendices.

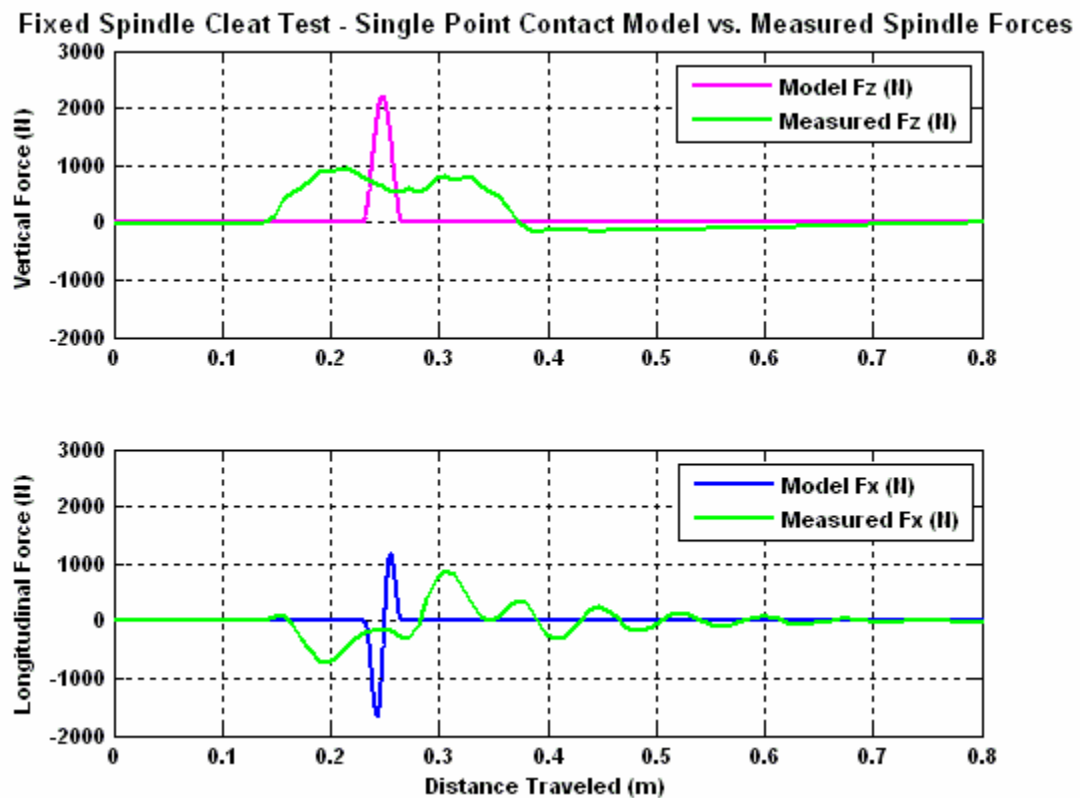


Figure 5.6: “Simple” Single Point Contact Follower Traversing a Sinusoidal Cleat

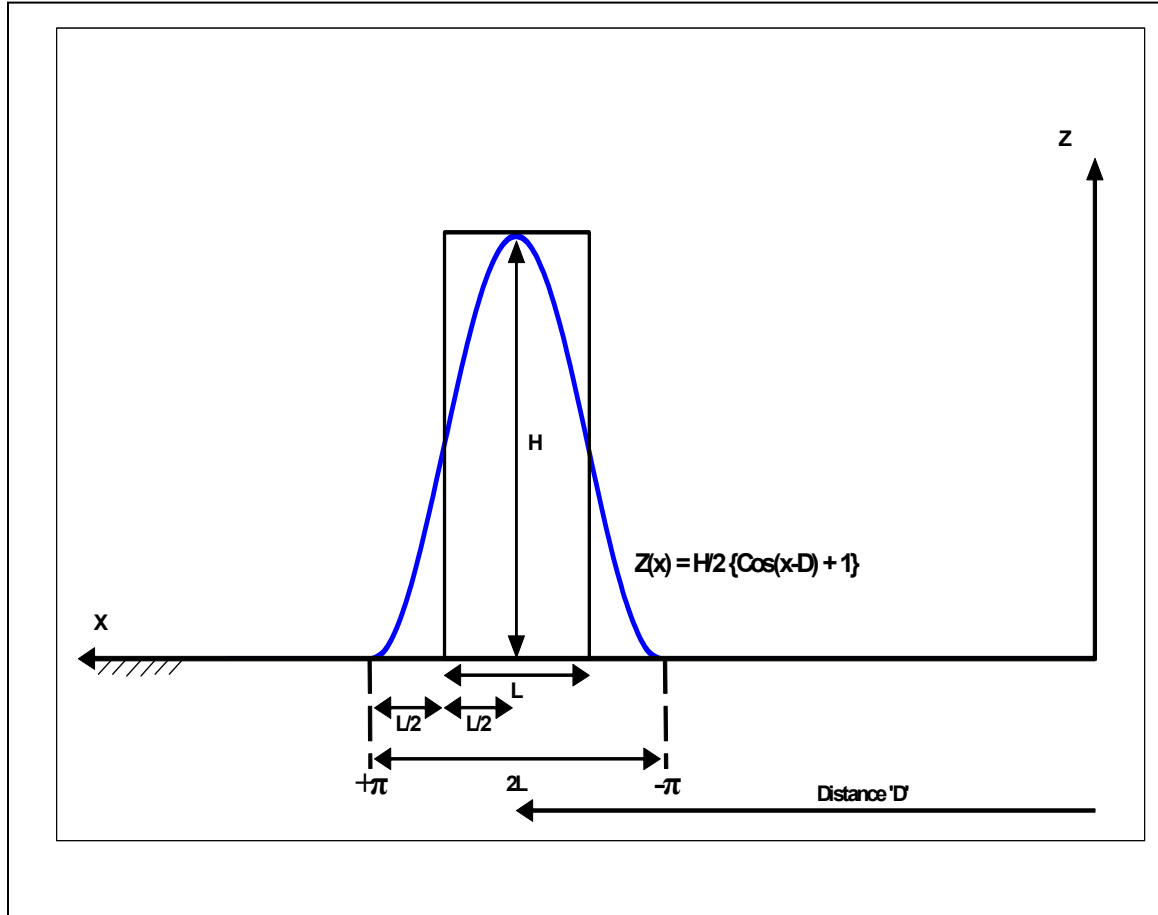


Figure 5.7: “Sinusoidal Equivalent” Model of a Rectangular Cleat

The Simulink point contact model presents a reasonable approximation of the peak vertical and horizontal spindle forces. As expected, the duration of the spindle force is too short (as there is no longitudinal contact patch through which the cleat traverses) and there are no force oscillations as there is no mass between the spindle and the single point contact follower – the tire mass is concentrated at the wheel rim.

The Simulink results for the “equivalent summit mass” exhibit the expected vertical ringing as shown in Figure 5.8. Since there is no longitudinal degree of freedom in the single point model, there is no visible ringing for the longitudinal spindle forces.

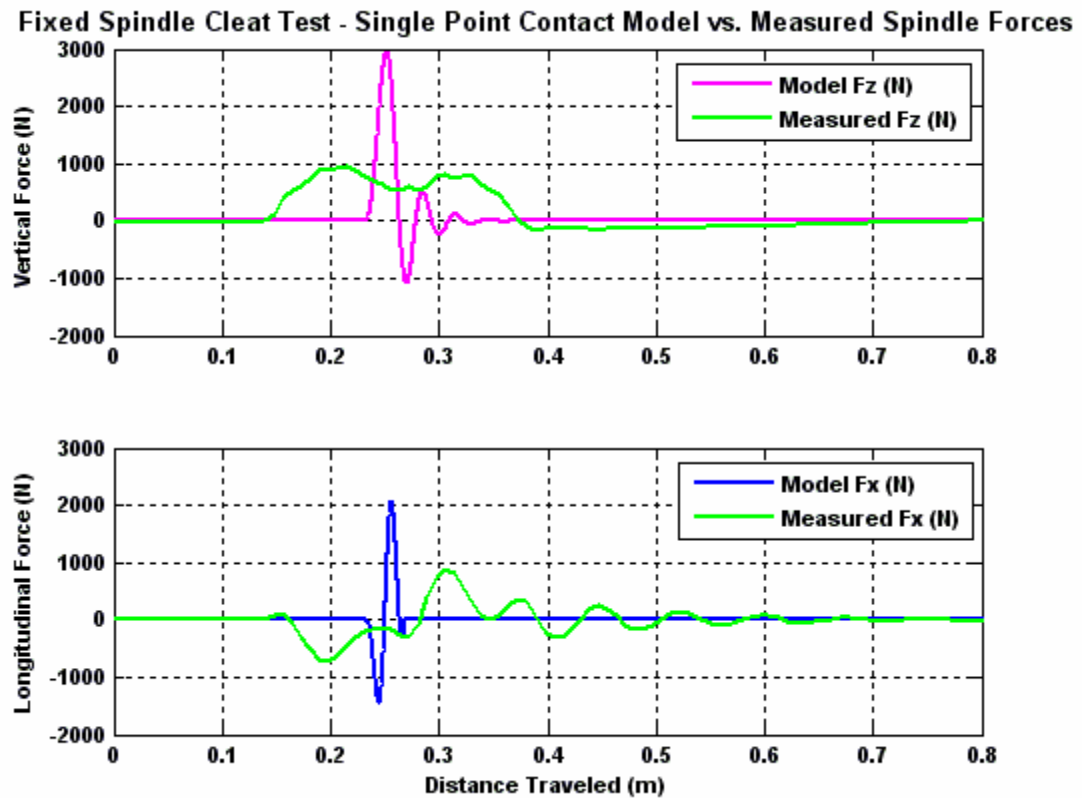


Figure 5.8: “Equivalent Summit Mass” Single Point Contact - Sinusoidal Cleat

Calculating the horizontal forces for a point contact follower traversing a rectangular cleat poses a unique problem – there is no defined obstacle slope with which to calculate horizontal forces. Therefore, a trapezoidal approximation of the rectangular cleat is used. The results for the “simple” point contact model are shown in Figure 5.9.

Fixed Spindle Cleat Test - Single Point Contact Model Traversing a Rectangular Cleat

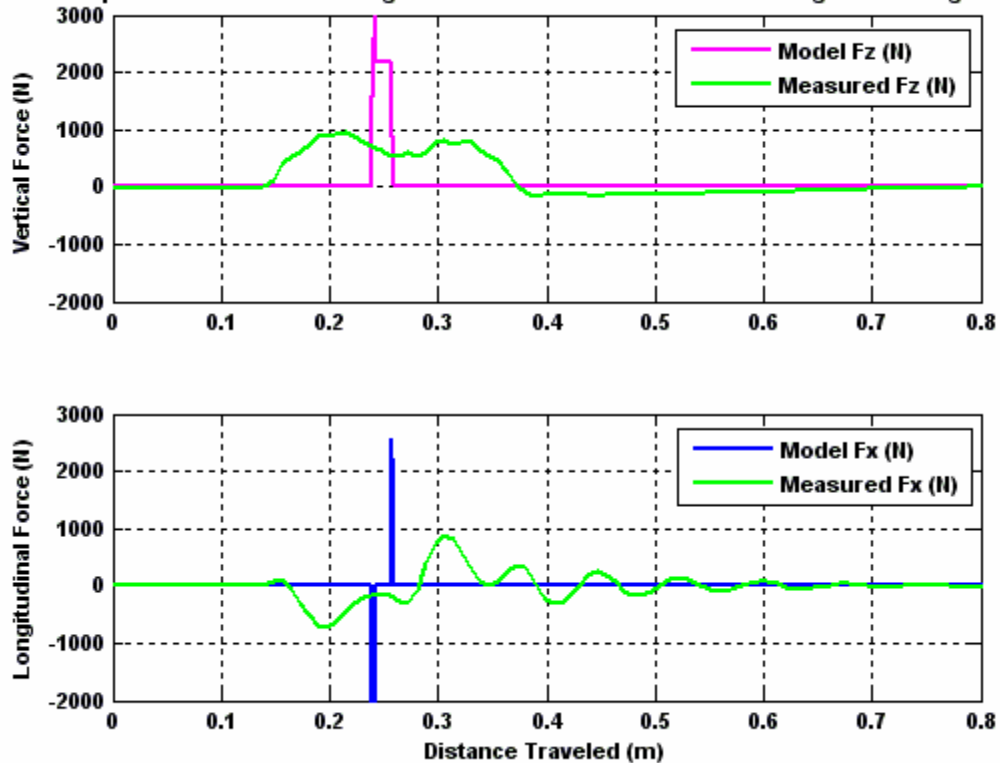


Figure 5.9: “Simple” Point Contact Follower Traversing a Trapezoidal Cleat

The positive vertical force spike for the rectangular cleat is the result of the large change in velocity as the single point contact travels vertically up the positive slope of the trapezoid approximation of the rectangular cleat. Figure 5.10 shows the simulation results for the same obstacle being traversed by the point contact model with the “equivalent summit mass.” Note that force oscillations afforded by the additional vertical degree of freedom effectively mask the shape of the obstacle for this obstacle wavelength and simulation speed (eight kilometers per hour).



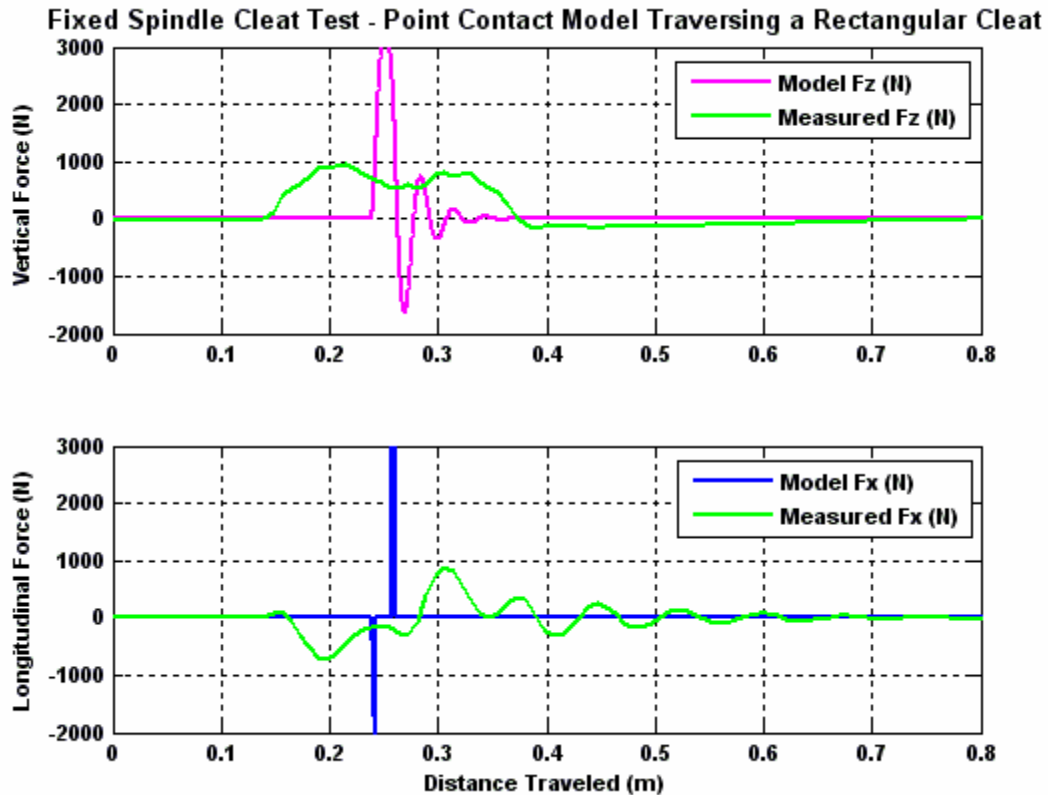


Figure 5.10: “Equivalent Summit Mass” Point Contact Traversing a Trapezoidal Cleat

Several observations can be made concerning the point contact model as it simulates traversing a trapezoidal cleat:

- The peak vertical and horizontal forces for both the “simple” and “equivalent summit mass” models are greater than the measured forces.
- Although the damping coefficients in tires is very small – damping coefficients in the order of 0.05 are not atypical - the rapid change in vertical velocity as the follower encounters the side of the trapezoid may cause the model to over-estimate the vertical spindle forces.

One concern that is unique to the simulation of tire models as they traverse a rectangular cleat is the instantaneous change in vertical velocity (or at least a change that is more rapid than can be reasonably expected for the actual physical system) can cause

numerical issues in the time step integration process of the simulation itself. Thus, simulating the traversal of a rectangular cleat with nothing more than a point contact follower must be done with care not only from a modeling perspective, but may also cause unpredictable model behavior from a numerical simulation perspective.

### Fixed Spindle Results – Ring Contact Follower

The ring contact follower model is identical to the single point contact follower model in every way with the exception of the follower geometry – the ring follower uses a circular ring to define the input into the tire model instead of a single point. The intention of the ring follower is to emulate the filtering effect that occurs when the tire contact patch “window averages” the ground undulations along the length of the contact patch. The effects of using the ring contact follower are:

- for positive obstacles (those obstacles which protrude above the roadway ground plane)
  - the magnitude of the vertical input is not mitigated (identical to the single point contact follower)
  - the effective obstacle wavelength is increased.
- for negative obstacles (“potholes”, or those obstacles which extend below the roadway ground plane)
  - the effective obstacle wavelength does not change
  - depending upon the ring follower and pothole geometry, the magnitude of the vertical input may be attenuated.

For this investigation, the radius of the contact ring was chosen to be one half the length of the contact patch. Criteria for selecting the radius of the ring contact follower and a discussion of the consequences of changing the radius are discussed in the appendices.

The vertical and horizontal spindle forces generated by the ring contact follower are illustrated in Figure 5.11. As the ring follower does not attenuate the magnitude of the vertical input imposed by the cleat, the peak vertical spindle force for the “simple” tire model as it traverses the sinusoidal equivalent of the rectangular laboratory road wheel cleat are almost identical between the single point contact and the ring contact follower models. However, there is an 1) increase in the input wavelength and a resulting 2) decrease in the obstacle angle which results when the ring contact follower engages the obstacle. The change in the obstacle engagement geometry emulates the obstacle wavelength filtering which occurs in the tire contact patch.

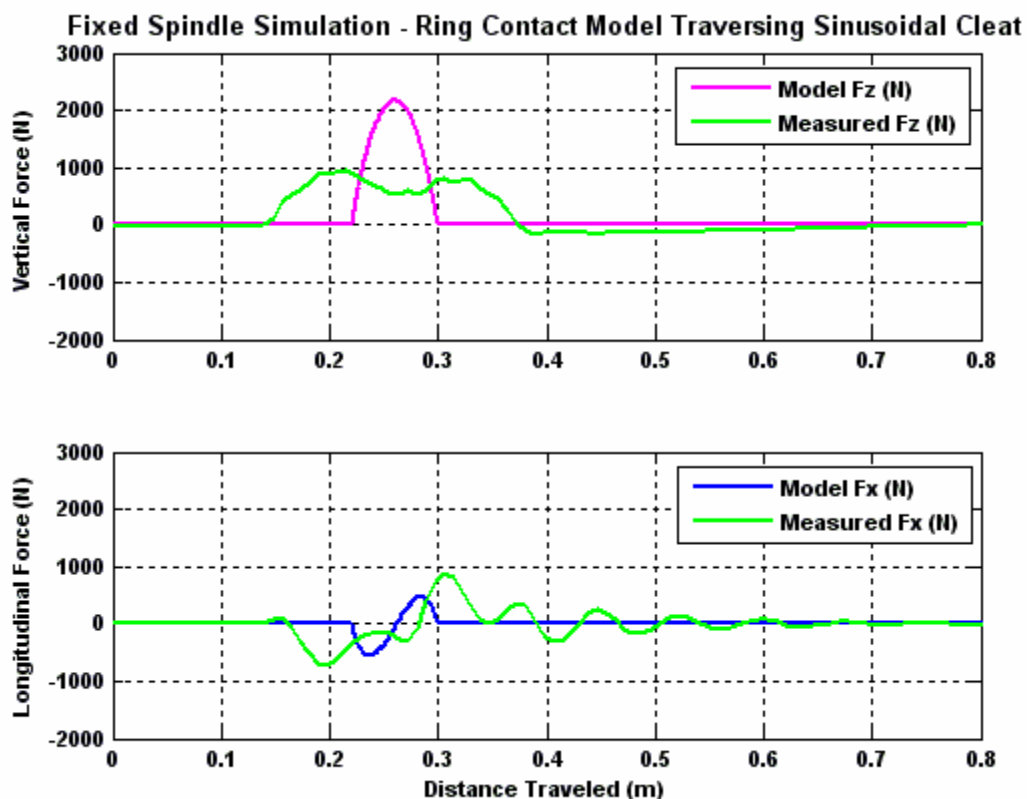


Figure 5.11: “Simple” Ring Contact Follower - Sinusoidal Cleat

The results for the “equivalent summit mass” are shown in Figure 5.12. These results include a higher overshoot in peak vertical force, and reduced horizontal spindle

forces. Although the “effective summit mass” model allows vertical oscillation, the overall simulation results are degraded for peak vertical and horizontal spindle force.

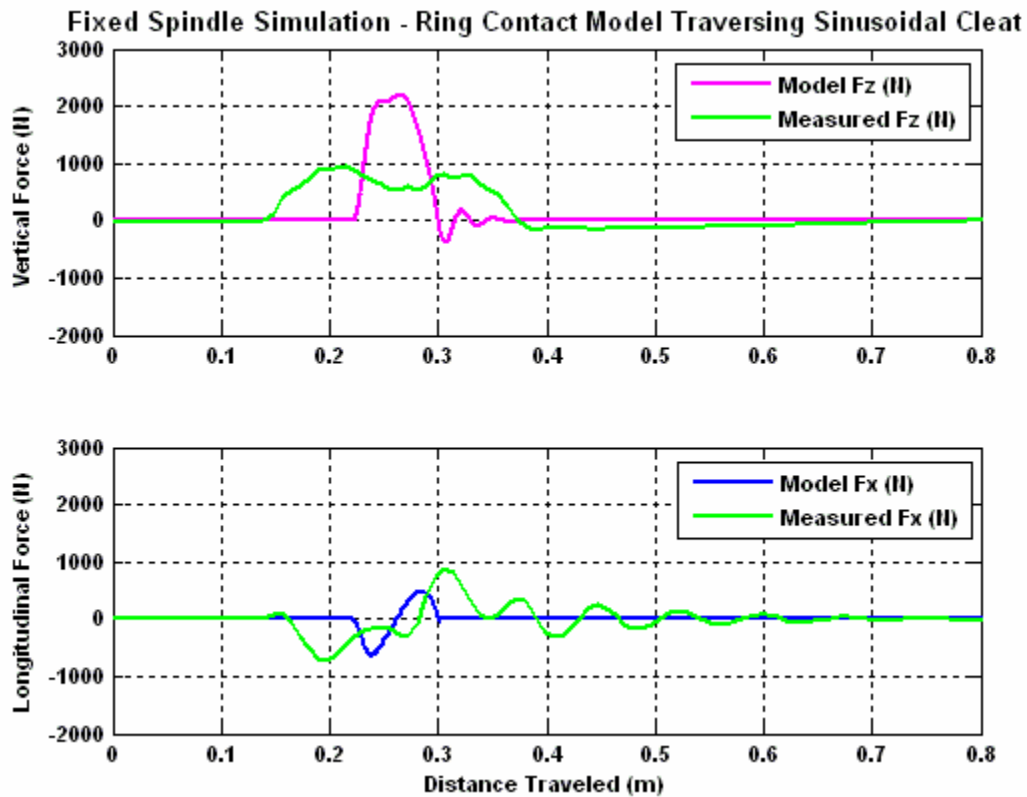


Figure 5.12: “Equivalent Summit Mass” Ring Contact Follower - Sinusoidal Cleat

Unlike the single point contact model, simulating a rectangular cleat with the ring contact follower does not require a trapezoidal approximation of the cleat. Figure 5.13 illustrates the “simple” ring contact follower model results, which shows significant improvement in spindle force simulation fidelity over that of the previous point contact model.

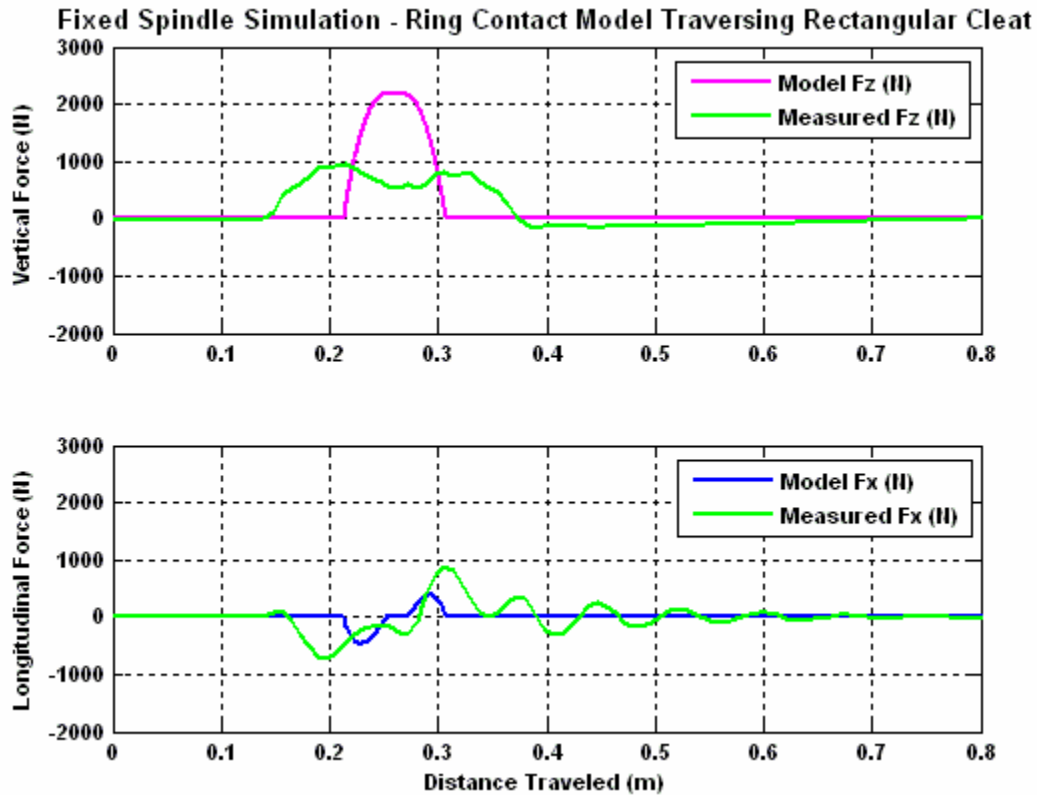


Figure 5.13: “Simple” Ring Contact Follower - Rectangular Cleat

The simulation of a rectangular cleat with a ring contact follower and the “equivalent summit mass” is shown in Figure 5.14. As with the comparison between the “simple” and the “equivalent summit mass” single point contact follower, the tradeoff for the extra degree of freedom with the summit mass and the resultant ability of the tire to “ring” does not appear to significantly improve spindle force simulation fidelity. Since the tire models are functional representations and do not emulate the physics of the pneumatic tire structure, the addition of an “equivalent summit mass” does not necessarily produce a better tire model.

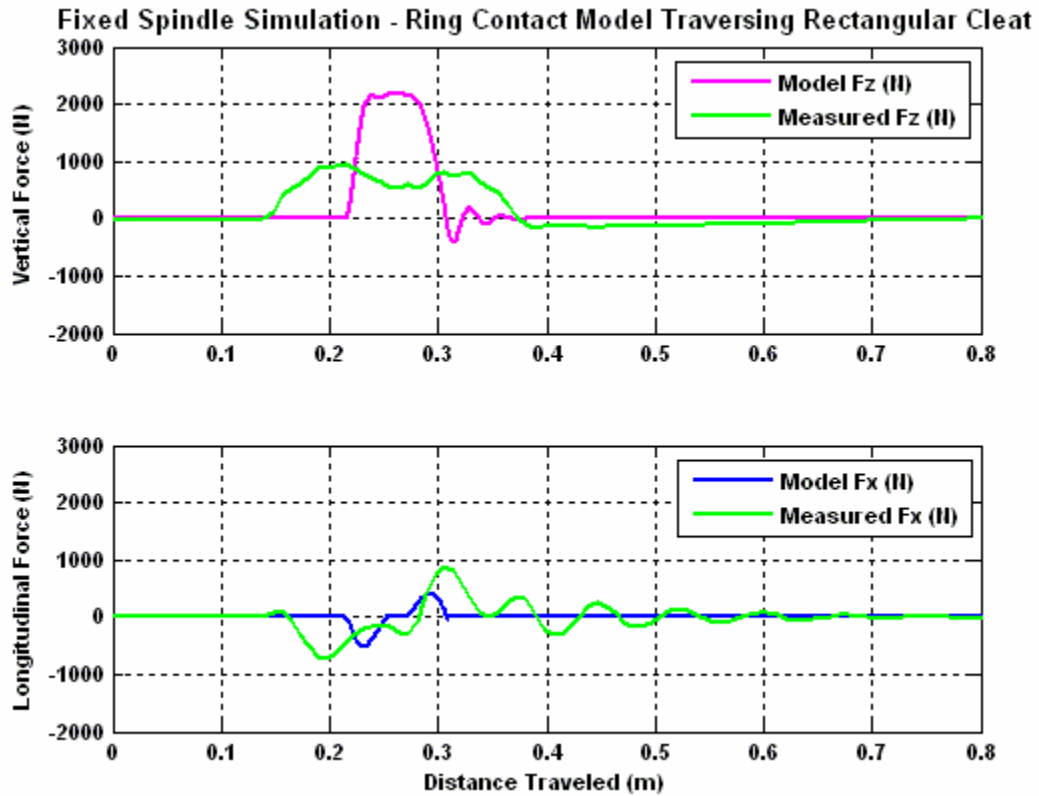


Figure 5.14: “Equivalent Summit Mass” Ring Contact Follower - Rectangular Cleat

The ring contact model has a distinct advantage over the single point contact follower – its ability to emulate the tire contact patch interaction with an obstacle by increasing the obstacle wavelength. It does this without preconditioning the obstacle (generating a sinusoidal or trapezoidal equivalent of the rectangular cleat). However, the rigid ring contact follower may require adjustment of the radius of the ring contact follower to optimize results, and the ring follower cannot emulate the “draping” envelopment of obstacles within the contact patch.

### Fixed Spindle Results – Constant Footprint Model

The constant footprint model is identical to the single point contact follower and the ring contact follower model with the exception of how the model emulates the interaction between the obstacle and the tire as the obstacle passes beneath the contact patch. The constant footprint model emulates this interaction by summing the forces generated when elements of equally-distributed vertical stiffness across the length of the contact patch are displaced vertically by the obstacle. Horizontal forces, as in the previous two models, are generated such that the resultant force vector is normal to the obstacle.

The filtering effect of the constant footprint model is such that the contact patch begins to develop vertical force as soon as the obstacle begins to enter the contact patch. Since 1) the vertical stiffness is evenly distributed along the length of the contact patch, and 2) the length of the contact patch is greater than the length of the cleat, the constant footprint model mimics both “draping” around an obstacle and increasing the effective wavelength of the obstacle.

The vertical and horizontal spindle forces generated by the “simple” constant footprint model as it traverses the sinusoidal equivalent of the rectangular cleat are shown in Figure 5.15. As anticipated, the vertical force is small due to the attenuation of the vertical input displacement and the horizontal forces are zero when the obstacle is “enveloped” within the footprint.



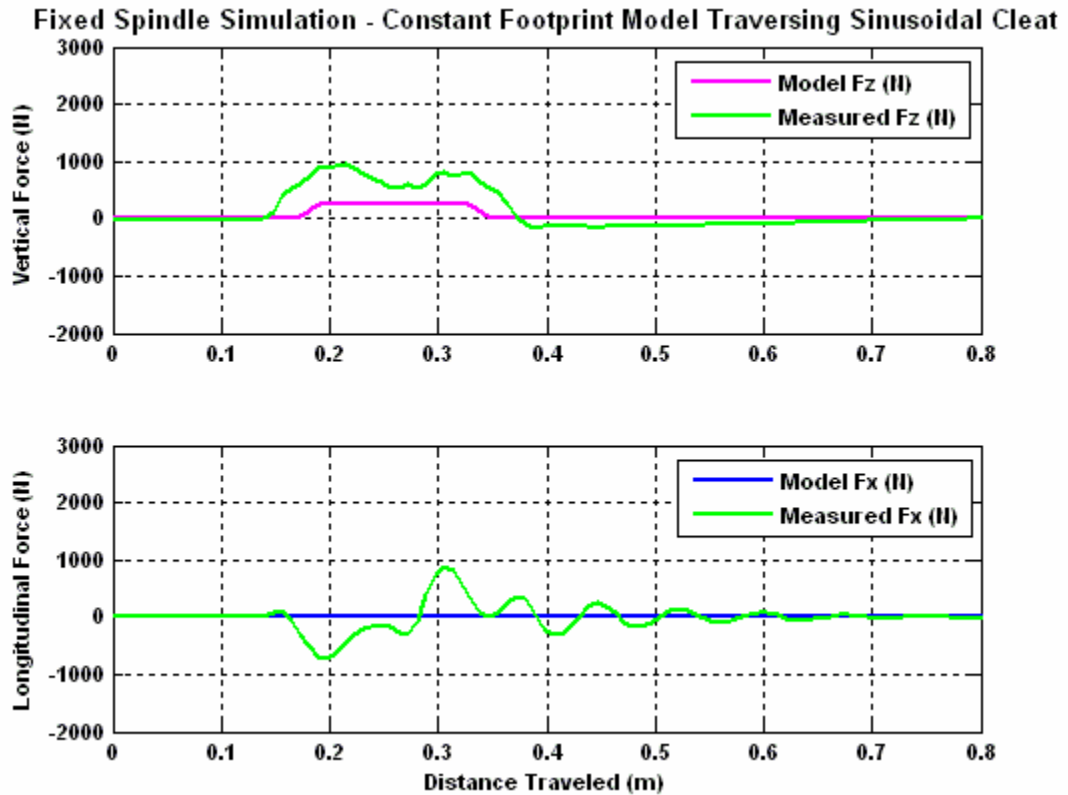


Figure 5.15: “Simple” Constant Footprint - Sinusoidal Cleat

The use of an equivalent summit mass model traversing the sinusoid cleat, and the resulting oscillations at both the beginning and end of obstacle engagement, are shown in Figure 5.16.

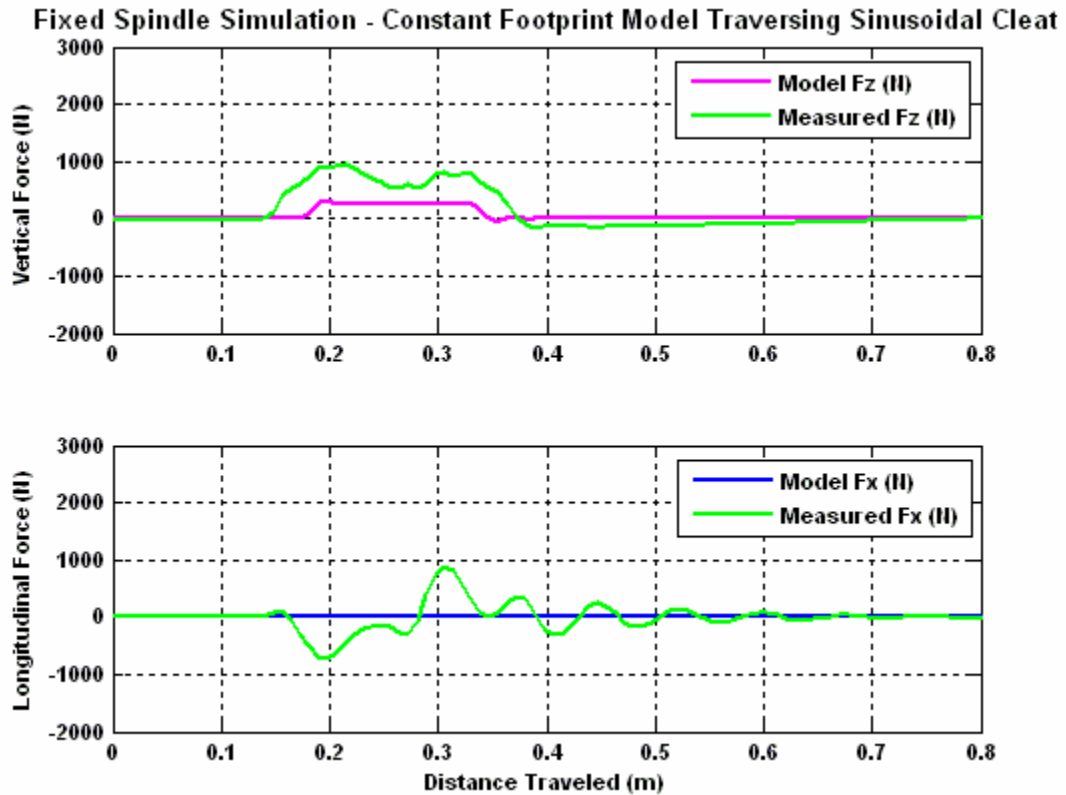


Figure 5.16: “Equivalent Summit Mass” Constant Footprint - Sinusoidal Cleat

The simulation results for the constant footprint model traversing the rectangular cleat are illustrated in Figures 5.17 and 5.18. The results indicate that there is no difference in the magnitudes of the vertical forces between the sinusoidal cleat and the rectangular cleat when the obstacles are fully enveloped ( $F_z = 260$  N). This is expected, as the areas under the curves for both obstacles are identical and the vertical stiffness of the tire is linear.

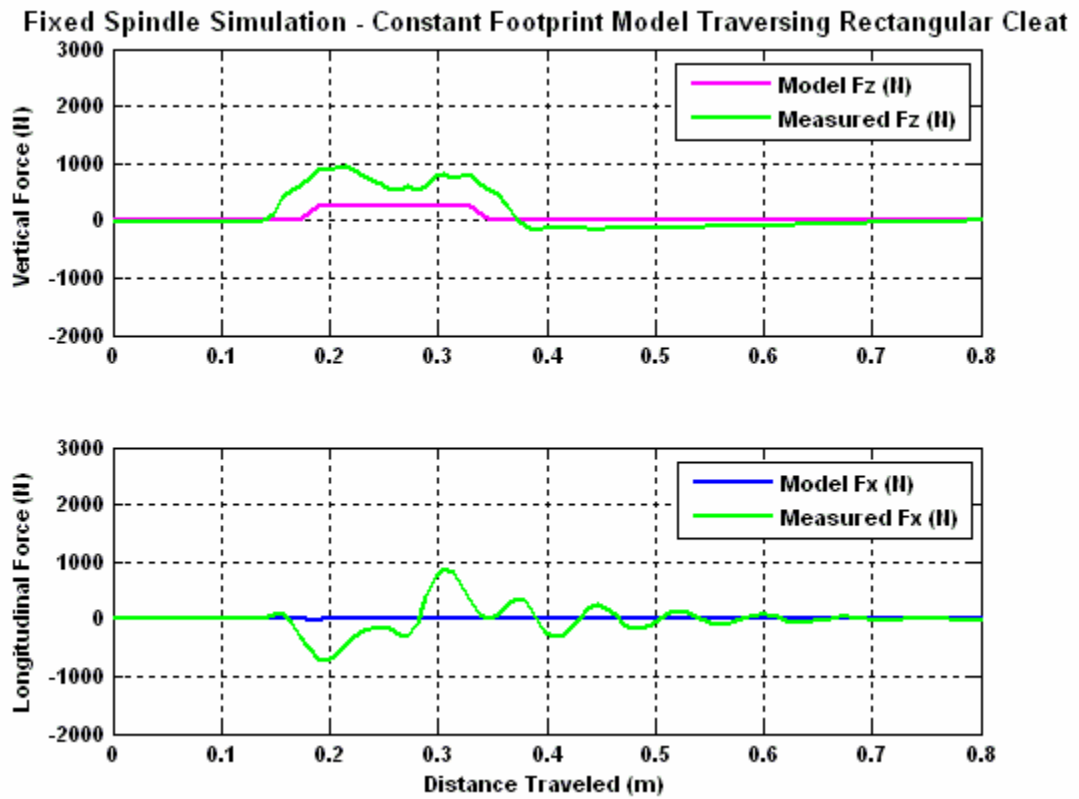


Figure 5.17: "Simple" Constant Footprint – Rectangular Cleat

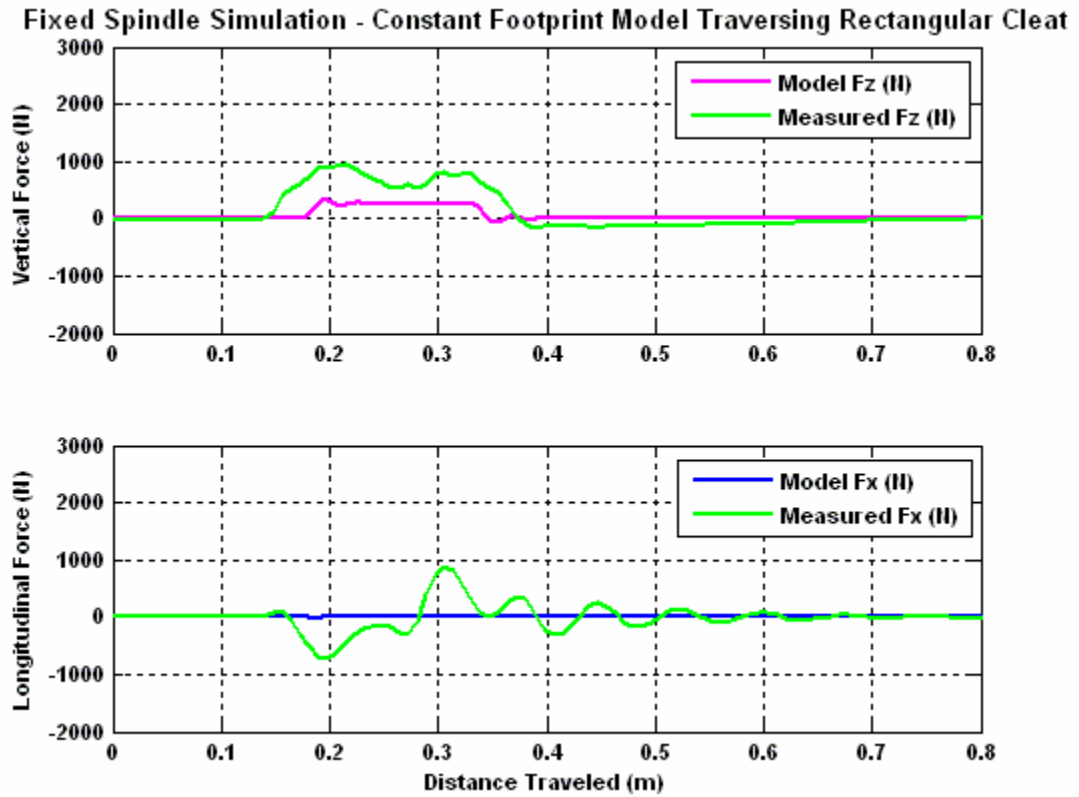


Figure 5.18: “Equivalent Summit Mass” Constant Footprint – Rectangular Cleat

### Fixed Spindle Results – Adaptive Footprint Model

The adaptive footprint model is a major departure from the previous three tire models (point contact follower, ring contact follower, and constant footprint) in that the horizontal spindle force is generated by horizontal deflection of the tire carcass. Because the model assumes that the tire carcass stiffness always lies radially outward from the center of the tire, any imposed deflection that is not parallel to the vertical centerline of the tire will result in a horizontal force component. The adaptive footprint model does not assume that the resultant spindle force remains normal to the obstacle surface.

The adaptive footprint model, as with the constant footprint model, does not take into account the bending stiffness or shear caused by localized deflection of the belt summit. This model will therefore also underestimate the tire spindle forces for objects that are shorter than the length of the contact patch.

Unlike previous models, the adaptive footprint does not lend itself well to the development of the “equivalent summit mass” variation. This is because deflection of the radial carcass elements develops longitudinal forces at the spindle and an equivalent summit mass would necessarily require either neglecting the horizontal force components or adding one (horizontal) or more (horizontal and rotational) degrees of freedom for the equivalent summit mass - at this point the adaptive footprint model becomes a rigid ring model.

The technique of obstacle filtering to obtain an equivalent obstacle profile cannot readily be applied to the adaptive footprint model because of the radial nature of the force and damping elements. Modeling is instead accomplished by use of an embedded

MatLab Simulink function. The Simulink function emulates the force generation within the contact patch for each simulation time step by first displacing the radial carcass stiffness elements inward to envelop the obstacle, and then summing the horizontal and vertical components of all the radial elements. This requires that the geometry of the obstacle either is passed to the embedded Simulink function during simulation or included in the function itself. Details of implementing this model are included in the appendices.

The simulated shapes of the fixed spindle forces for the adaptive footprint model traversing a sinusoidal cleat agree favorably with the test results. The vertical force plot in Figure 5.19 illustrates obstacle envelopment within the contact patch. The magnitude of the peak vertical force is similar to the test results, but the value of the vertical force when the obstacle is beneath the center of the contact patch is too low. The underestimation of the spindle forces is again due to the even distribution of the measured stiffness of the tire measured on a flat plate – there is no accounting for localized bending and shear stiffness in the model. The horizontal force plot exhibits the general characteristic shape of obstacle envelopment, (less the initial driving force at the entry of contact patch at distance equal to 0.12 meters). The horizontal force values, as with previous models, are underestimated.

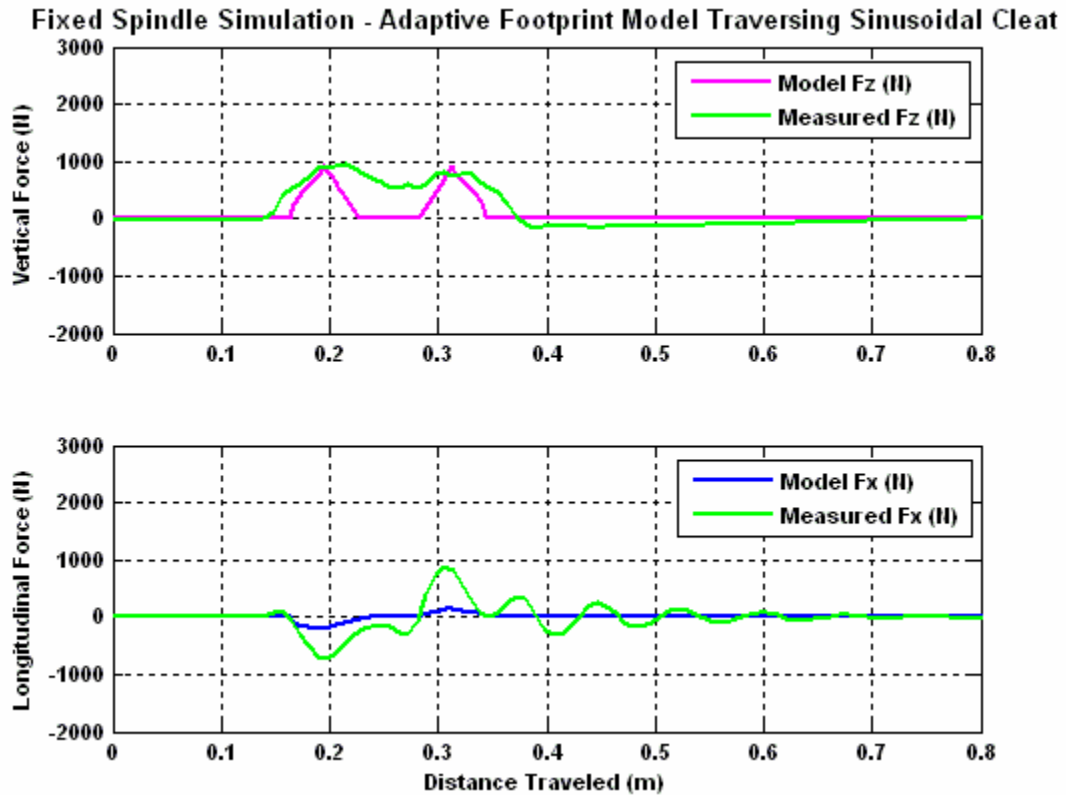


Figure 5.19: Adaptive Footprint Model - Sinusoidal Cleat

The fixed spindle simulation results for traversing a rectangular cleat are shown in Figure 5.20. The adaptive footprint model again provides for a favorable vertical force vs. distance signature. The reduced horizontal force is due to the rectangular cleat length being half the length of the sinusoidal equivalent. The larger peak vertical forces are the result of the step vertical input in displacement as the radial tread elements engage the cleat as a step input.

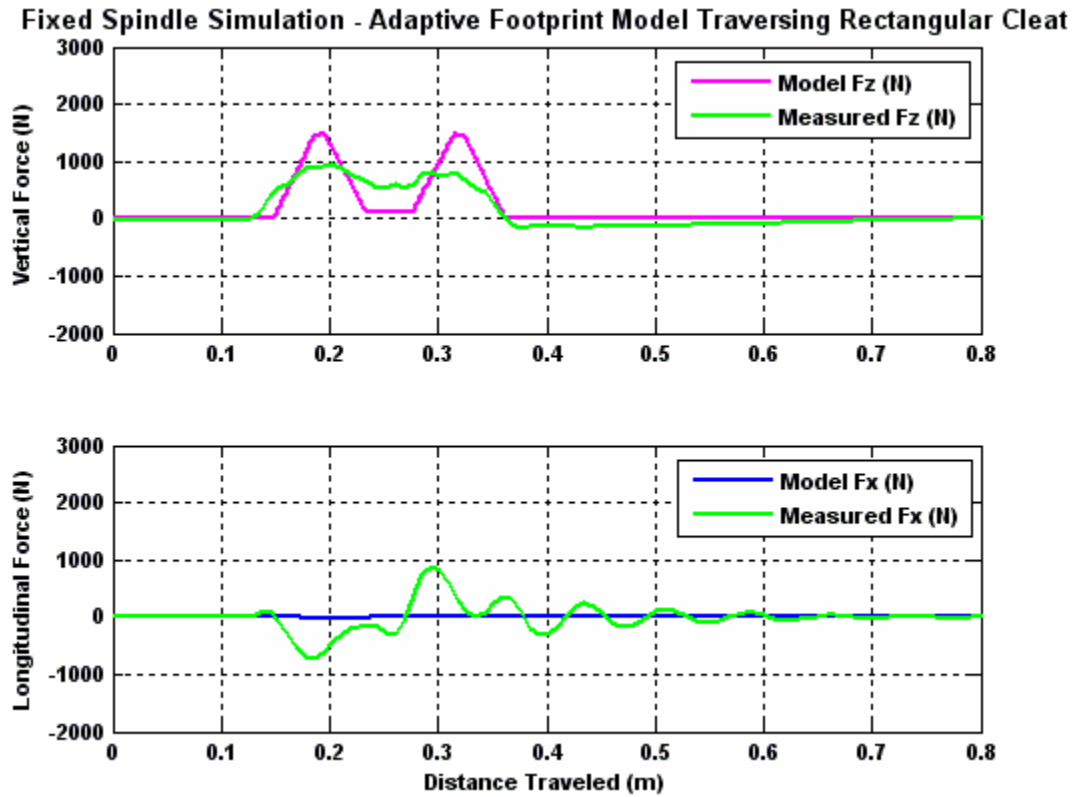


Figure 5.20: Adaptive Footprint Model - Rectangular Cleat



### Fixed Spindle Results – Two Point Follower Rigid Ring Model

The two point follower rigid ring model is an adaptation of a model proposed by El-Gindy et al [2]. The rigid ring model assumes that the summit mass can be modeled as a rigid ring between the tread elements and the tire carcass. The tire carcass is assumed to have bulk equivalent stiffness along the horizontal, vertical, and tire spin axes between the wheel hub and the rigid summit ring mass. The tread blocks are assumed to have radial and circumferential stiffness between the rigid summit ring mass and the ground. In the case of the two point follower, the contact patch is assumed to have a constant length with its position – vertical, horizontal, and rotational – defined by two single point contact followers. The first of two point contact followers is located at the entry of the contact patch. The second point contact follower is located at the exit. The resulting contact patch “plane” (or line, in the case of this 2D model) reacts with the ground, generating normal forces perpendicular to the plane. The relative translational velocity at the interface between the contact patch plane and the ground, combined with the normal forces, generates the driving and braking forces.

Although the rigid ring model is more complex than the earlier models, it does have some inherent advantages:

- The rigid ring is the “equivalent summit mass”
- The rigid ring has the ability to transmit driving and braking torque between the wheel hub, rigid ring, and the tread blocks, thereby enabling the rigid ring model to interact with vehicle driveline and/or braking components

- If driving or braking traction is to be modeled, the rigid ring model uses a conventional  $\mu$ /slip friction model that can be adjusted to match various track surfaces

The simplifying assumption that the summit mass can be modeled as a rigid ring does present several shortcomings:

- The contact patch or tread summit model must be able to adequately represent contact patch envelopment for obstacles which have wavelengths significantly shorter than the length of the contact patch. This model falls short because “abrupt obstacles” such as tall narrow cleats deflect the tire summit, violating the rigid ring assumption.
- The two point follower can emulate obstacle envelopment, but there are no provisions which account for bending and shear forces due to the locally-imposed deflections in the tread band.

The results for the two point contact follower rigid ring model traversing a sinusoidal equivalent of the road wheel test cleat is shown in Figure 5.21. Several observations can be made regarding the general behavior of the model as it traverses a sinusoidal cleat. The two point contact patch follower provides for obstacle envelopment similar to the constant footprint and the adaptive footprint tire models. However, the lack of bending stiffness or shear stresses between the leading and trailing point contact followers results in the underestimation of the vertical force generation when the obstacle is fully enveloped by the contact patch. The model also underestimates the longitudinal spindle forces. However, the model does reproduce the horizontal inertial spindle reaction forces when the cleat enters the contact patch (+50N). Previous models are

incapable of modeling this force. Finally, the oscillation of the horizontal spindle force following the cleat exit at the contact patch appears to be modeled accurately. The measured horizontal spindle force oscillates at approximately 28.9 Hz whereas the modeled force oscillates at approximately 27.3 Hz.

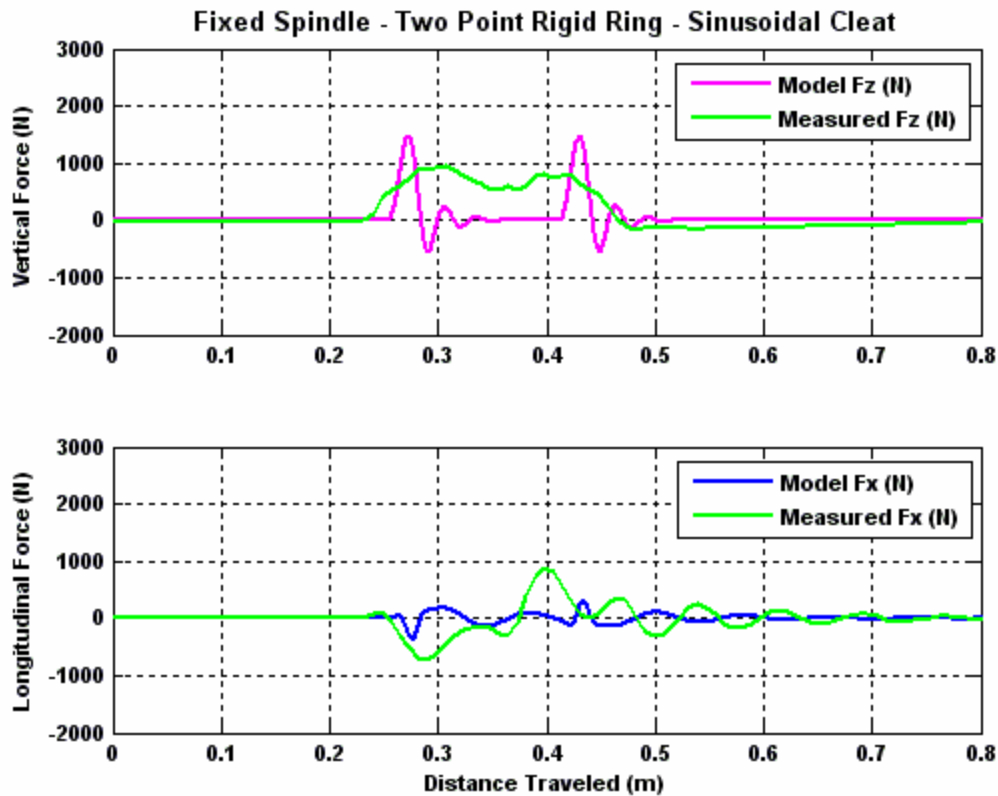


Figure 5.21: Two Point Rigid Ring Model – Sinusoidal Cleat

The results for the two point rigid ring model traversing the rectangular cleat are shown in Figure 5.22. The simulation results for traversing a rectangular cleat are similar to the results when the model traverses a sinusoidal cleat. The unfiltered vertical input as the rectangular cleat enters the contact patch results in higher peak vertical and horizontal spindle forces of 19% and 75%, respectively. In addition, the initial driving force as the cleat enters the contact patch is more prominent.

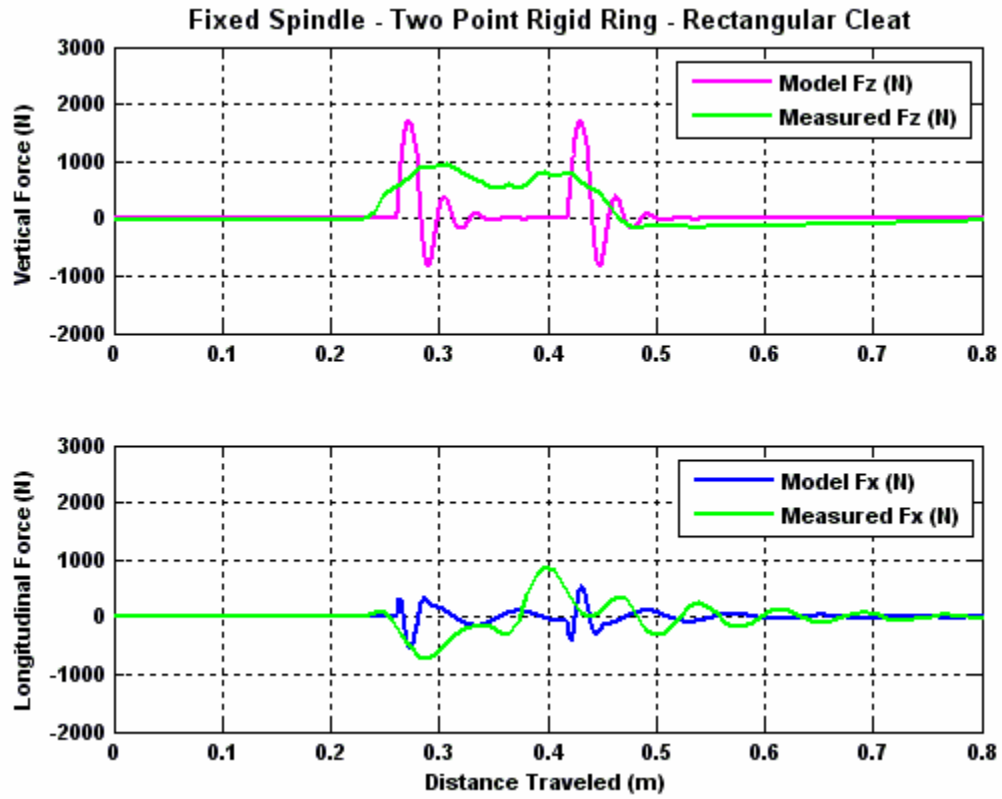


Figure 5.22: Two Point Rigid Ring Model – Rectangular Cleat

### Fixed Spindle Results – Five Point Follower Rigid Ring Model

The five point follower rigid ring model is a refinement of the two point follower rigid ring model. Using the five point rigid ring model to develop four individual contact planes – two elements in front and two elements behind the center of the contact patch – is intended to increase the model fidelity by providing greater resolution of forces developed in the contact patch. This is especially important because:

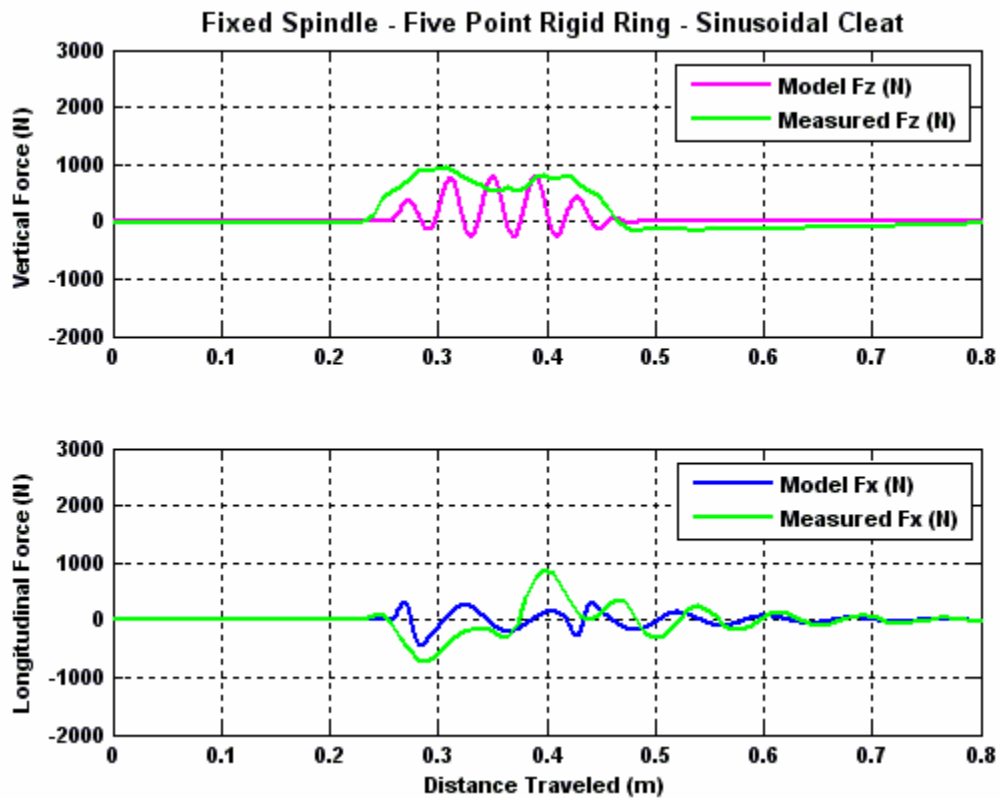
- the contact patch traction model is highly nonlinear, therefore averaging the normal forces across the entire length of the contact patch will not provide as accurate a traction model if the normal forces were calculated separately based upon each individual plane segments
- Increasing the number of plane segments in the contact patch should increase the precision of obstacle envelopment and provide a better model of obstacle wavelength filtering.

The results of increasing the number of element planes in the contact patch can be seen in Figure 5.23. The modeled peak spindle forces better mimic the measured forces than the two point contact model. However, the force developed by each individual contact patch segment as it is displaced over the cleat introduces an oscillatory vertical spindle force that is not present in the measured force. Potential solutions to reduce this artificial vertical oscillatory force could include:

- increase the number of elements within the contact patch so that there would be multiple contact plane elements interacting simultaneously with the obstacle, or

- modeling the bending moments and shear forces between the individual contact plane elements, thus mitigating the vertical displacement differences between the elements when a single element encounters the cleat.

With the exception of FTire, the modeled horizontal spindle forces of the five point follower rigid ring model are closer in magnitude and have better waveform fidelity than any of the other models investigated.



:Figure 5.23: Five Point Rigid Ring Model – Sinusoidal Cleat

The forces for the rectangular cleat are shown in Figure 5.24. The modeled and measured peak vertical forces are within a few percent of each other. Simulations using the rectangular cleat in place of the sinusoidal cleat required approximately five times the computational time, and there are indications of solver convergence issues at 0.28 and 0.38 meters. Several Simulink solvers and tolerances were used but the relatively long

simulation time was not resolved. An intermediate solution may be to use the trapezoidal equivalent cleat that was used for the single point contact follower model.

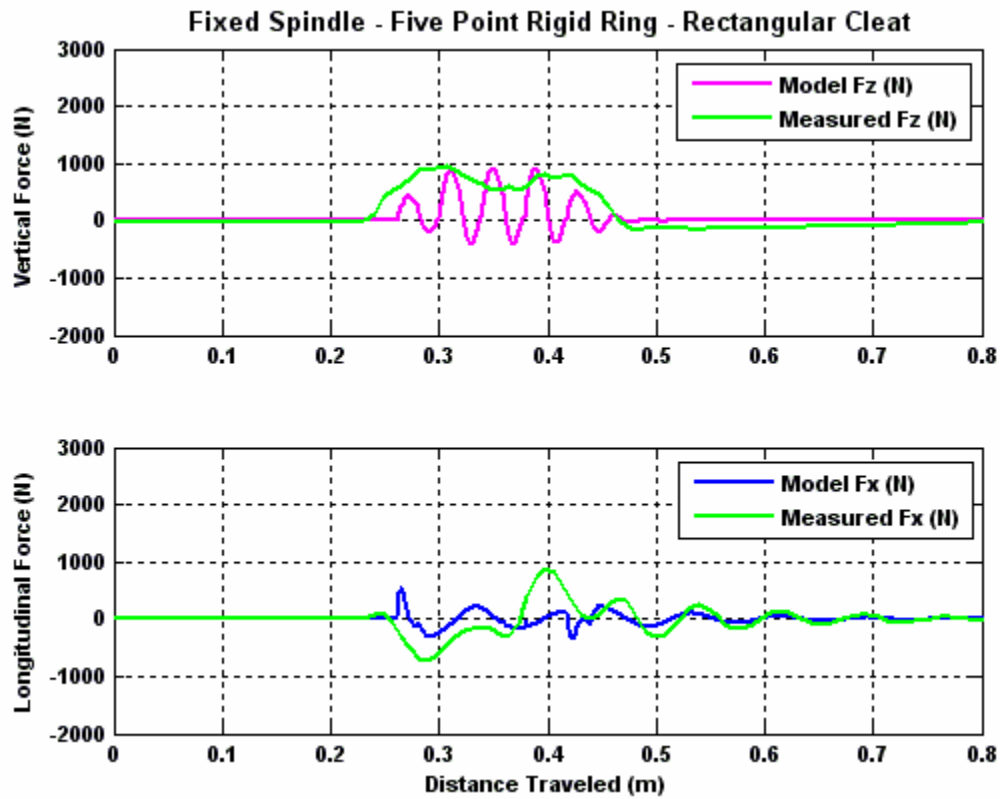


Figure 5.24: Five Point Rigid Ring Model – Rectangular Cleat

### Fixed Spindle Results – Cosin FTire and SIMPACK MBS

The Cosin FTire model running in conjunction with the SIMPACK Automotive Plus MBS software is the seventh and last simulation to be examined. The results of the simulations for the 1) sinusoidal cleat equivalent and the 2) rectangular cleat are shown in Figures 5.25 and 5.26.

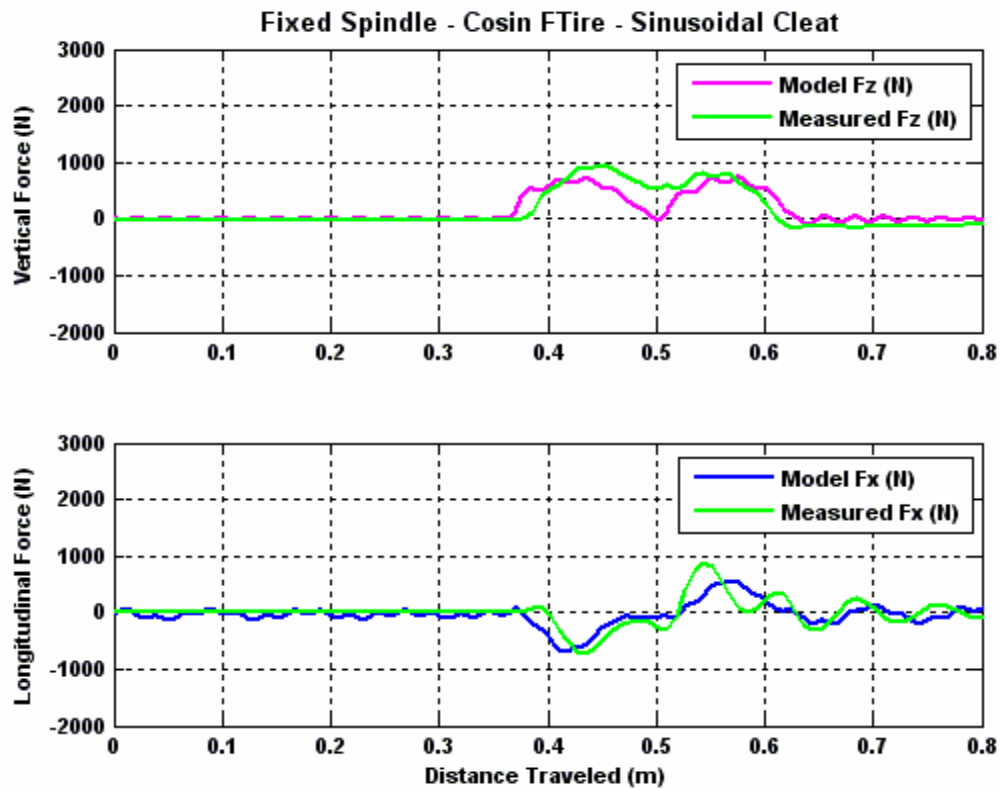


Figure 5.25: Cosin FTire SIMPACK Automotive Plus MBS – Sinusoidal Cleat



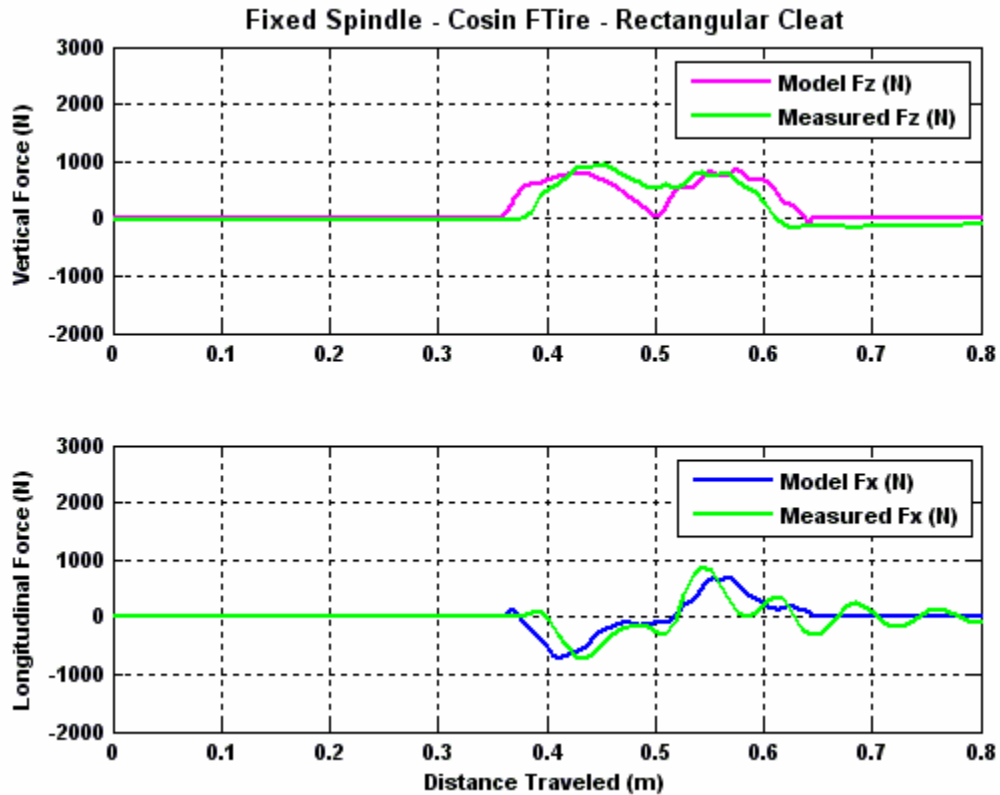


Figure 5.26: Cosin FTire and SIMPACK Automotive Plus MBS – Rectangular Cleat

Several observations are:

- The FTire produced excellent fidelity for both the vertical and the horizontal forces.
- Just as with the adaptive footprint model, the modeled vertical spindle force of the FTire model is too low – almost zero - as the cleat passes through the center of the contact patch.
- Small spindle force oscillations, especially visible in the longitudinal spindle force graph of Figure 5.13, are occasionally present in FTire simulations. This may be caused by the time-step integration error tolerance present in all MBS models. Although SIMPACK MBS provides a wide array of integration

schemes, attempts to eliminate the small spindle force oscillations were not always successful and may require the assistance of an expert user.

- FTire results were not significantly affected by using a sinusoidal cleat to emulate a rectangular cleat, causing only a slight reduction in peak spindle forces – the spindle force signatures are almost identical, as would be expected with test data.

### FTire Simulation Considerations

Although the simpler models developed and implemented for this report are able to rival the commercial software suite in terms of peak spindle force metrics, visual examination of the force traces indicate that the commercial software produces the highest model fidelity. The fidelity does, however, come at a cost:

- The FTire model requires additional tire testing to provide sufficient data to generate the FTire file. For example, tire vertical stiffness test measurements on test cleats as well as the standard flat surface are obviously needed to characterize the bending stiffness of the flexible summit belt package in the flexible ring tire model.
- Use of the FTire model requires not only the data reduction and simulation software, but also requires a period of learning and familiarization
- FTire is not a stand-alone simulation – it requires implementation with any number of vehicle modeling software packages. The SIMPACK Automotive Plus MBS software was intuitive, well-documented, and provided a well-

integrated environment for generating the MBS road wheel and quarter vehicle models, integrating the FTire model, performing simulations, and conducting post-processing.

- Although the simulation time is expected to be much shorter than can be expected with any FEA tire simulations, the FTire simulations do require the longest simulation time of all models tested in this investigation.
- FTire does provide for graphic presentation of forces developed in the contact patch and SIMPACK MBS provides graphic outputs for the MBS models. However, the FTire and SIMPACK MBS output graphics are not integrated and cannot be generated or viewed as a single integrated graphic or movie.
- Some functional characteristics of the FTire model cannot easily be parameterized. For example, reducing tread depth would increase the tread block rigidity. However, this parameter could not be changed in the FTire data set directly – either new tires must be built, tested, and the new test data processed in FTire, or the new test data must be approximated by some external means and reprocessed in FTire.

## Cleat Phase Results – Analysis

### Cleat Phase Peak Spindle Force Objective Metrics

Two objective output metrics were selected – peak spindle vertical force,  $F_z$ , and peak horizontal force,  $F_x$ . The spindle force metrics were normalized relative to the cleat test so that a value greater than one indicates that the magnitude of the peak force is greater than that obtained in the lab. The results for the simulations using the sinusoidal cleat are shown in Figure 5.27. The results for simulations using a square cleat (or the trapezoid equivalent, in the case of the point contact and constant footprint models) are shown in Figure 5.28.

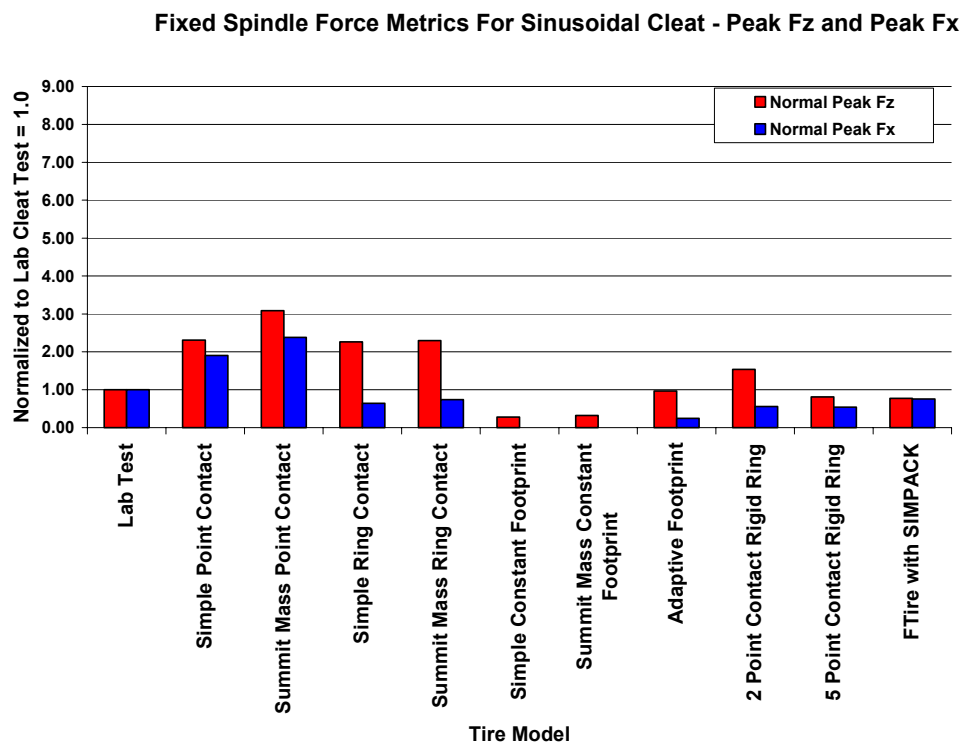


Figure 5.27: Normalized Peak Spindle Force for Sinusoidal Cleat

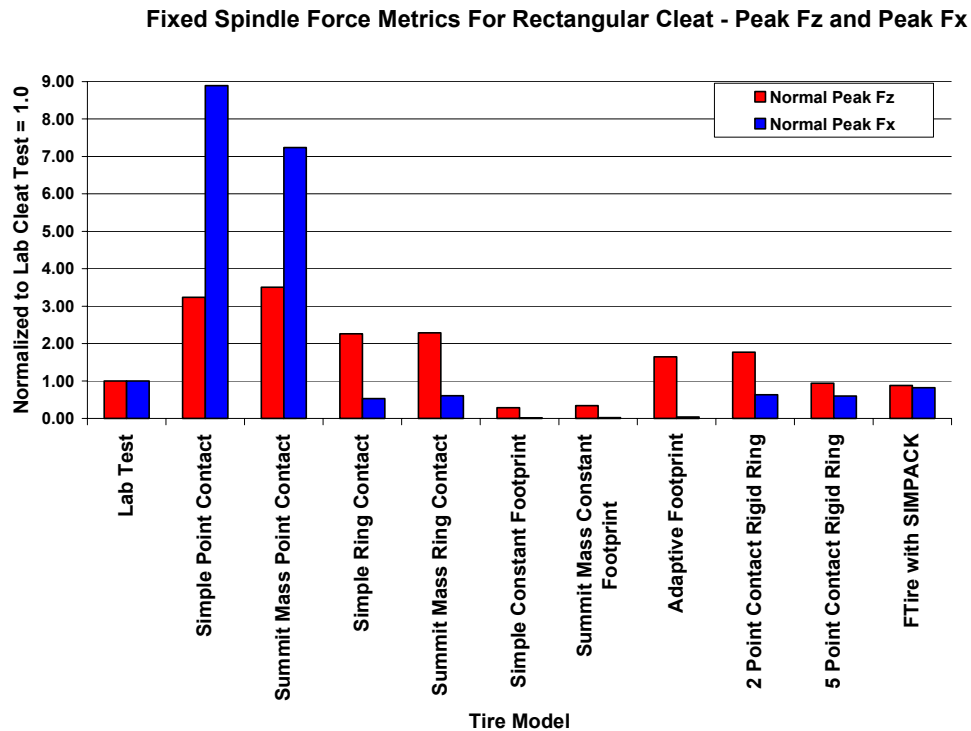


Figure 5.28: Normalized Peak Spindle Force for Rectangular Cleat

Several conclusions that can be drawn from examining the objective metrics include:

- Converting (or “pre-conditioning”) the cleat from a rectangular profile to the sinusoidal equivalent improved the MatLab simulation results in all cases.
- Adding the “equivalent summit mass” as an additional degree of freedom in the vertical direction did not improve the tire model performance.
- The simplest model – the point contact follower without any equivalent mass – consistently overestimates both Fz and Fx. However, the normalized values for both Fz and Fx when traversing the sinusoidal cleat are relatively close to one another (2.31 and 1.91, respectively). Since the model has consistent error in both Fz and Fx, the model may be useful for first-order ride comfort

investigations which place equal importance on the accurate prediction of these two inputs. It is important to note that the point contact model could only achieve this accuracy if the rectangular cleat was first converted into its sinusoidal equivalent. Although the peak force metrics for the point contact model are reasonable, the lack of any contact patch filtering will make the point contact model perform poorly where reproduction of the spindle force waveforms is required, especially for obstacles whose wavelengths are shorter than the tire contact patch length.

- The ring follower performed well and was less sensitive to the differences between the rectangular and sinusoidal cleat than the point contact follower due to the ring contact geometry increasing the wavelength of the obstacle and filtering the input. However, proper selection of the ring follower radius directly affects the performance of the obstacle wavelength filtering (see appendices for details). Although the ring model overestimated the peak vertical force (as expected, due to the lack of obstacle envelopment in the vertical direction), the model does provide horizontal obstacle wavelength filtering.
- The constant footprint model is the simplest model which emulates the mechanism for obstacle envelopment. However, the constant footprint model does not develop sufficient spindle force in either the vertical or the longitudinal direction. Longitudinal spindle force  $F_x$  was, as expected, close to zero, thus making the constant footprint model unsuitable for simulations requiring horizontal force modeling.

- Both the two point and the five point rigid ring models provided reasonable values for both vertical and horizontal peak spindle forces. The five point contact rigid ring model performed better than the two point version.
- Although the envelope around the vertical force trace appears to be acceptable, the five point model results contained force oscillations when the contact patch segment lengths interacted with the obstacle wavelength.
- The FTire results slightly underestimated the peak spindle forces, but provided the best spindle force accuracy of all the tire models.

Because the sinusoidal obstacle provided not only better spindle force fidelity, but also:

- slightly improved simulation times
- eliminated time step numerical integration issues

It was concluded that the sinusoidal equivalent of the rectangular cleat could be used in the remainder of the Cleat Phase objective metric analysis and for the entirety of the second or Ride Phase - quarter vehicle ride comfort simulations.

#### Cleat Phase Objective Metric Analysis

The objective metrics – peak magnitudes of the spindle forces in  $F_z$  and  $F_x$  - are normalized to the values obtained in the laboratory test. The tire models of interest are the “simple” models which do not use an “equivalent summit mass.” The obstacle of interest is the sinusoidal equivalent of the rectangular laboratory cleat. The results of these simulations are illustrated in Figure 5.29.

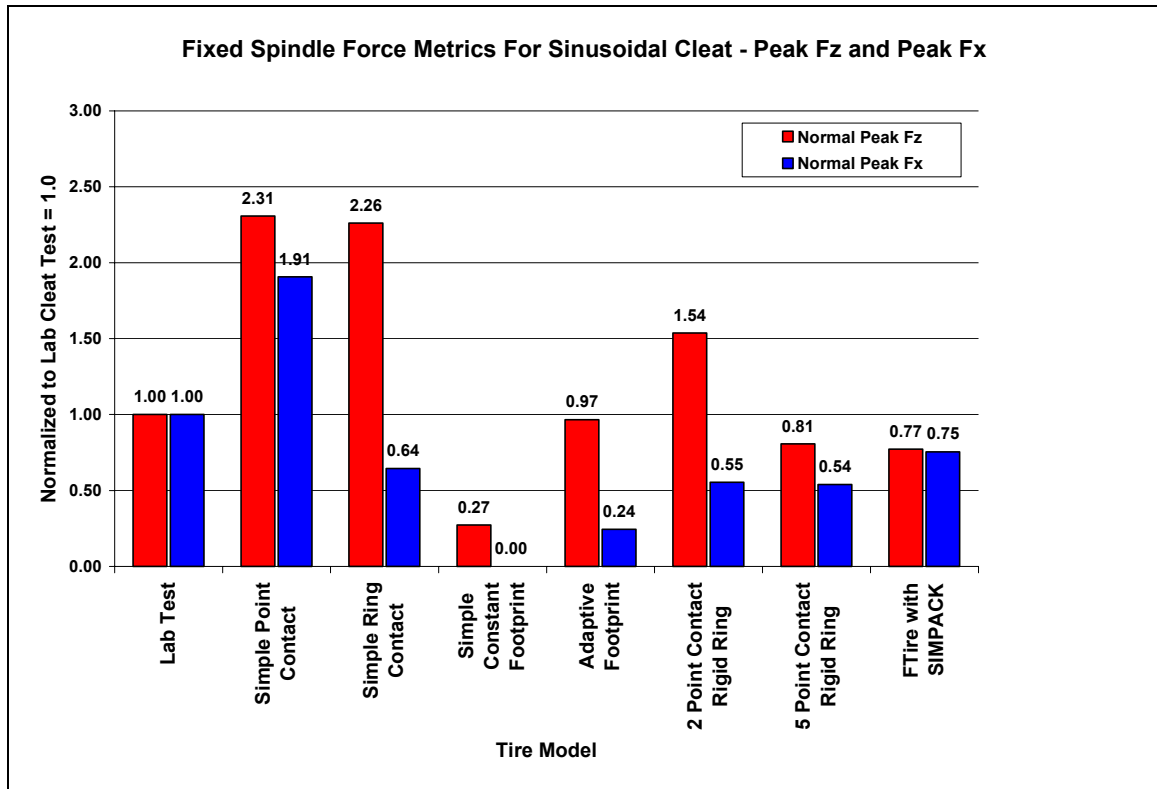


Figure 5.29: Normalized Peak Spindle Forces for Sinus Cleat

The objective metrics indicate that the FTire simulation is the most accurate model. However, other simpler models may be appropriate as they are less costly in terms of both testing requirements to obtain the model parameters and simulation time. Therefore, the model objective metrics need to be analyzed to determine which model will be most suitable for the ride comfort simulation task. This is accomplished by:

- Organizing the metrics in tabular format – in this case, peak Fz and peak Fx – for each of the tire models.
- Calculating the absolute value of the percent error for each metric.
- Ranking the models for each error metric, peak Fz and peak Fx, individually.



- Applying a weighting factor, if desired, to place a relative importance each of the two error metrics. Since the ride comfort model to which the tire models will be applied is not known, no weighting was used.
- Summing the weighted errors of the metrics in order to rank the overall performance of the tire models.

Table 5.2 is the result of this process for the fixed spindle peak force metrics.

Table 5.2 Cleat Phase Tire Model Ranking via Spindle Force Objective Metrics

Tire Model	Peak Fz Absolute Percent Error	Peak Fz Absolute Percent Error	Ranking		Model Overall Ranking
			Peak Fz	Peak Fx	
Lab Test (Reference)	0	0	0	0	0
Simple Point Contact	131	91	6	5	5
Simple Ring Contact	126	56	5	2	4
Simple Constant Footprint	270	>1000	7	7	7
Adaptive Footprint	3	317	1	6	6
Two Point Rigid Ring	54	81	4	3	3
Five Point Rigid Ring	23	85	2	4	2
FTire with SIMPACK	28	33	3	1	1

Several observations regarding the ranking of the seven tire models for simulating fixed spindle force generation include:

- All tire models were better at predicting the peak vertical forces than the peak horizontal forces.
- The adaptive footprint model achieved the highest performance ranking for predicting peak Fz, but second to last for peak Fx. For some ride comfort modeling tasks which do not require force modeling in the horizontal direction, the adaptive footprint model may provide a better cost / performance benefit ratio than FTire.

- The point contact model, widely used for first-order exploratory ride comfort modeling, does not perform well when used for obstacles whose wavelength is shorter than the tire contact patch length. For this model,
  - there is no mechanism to emulate contact patch envelopment; consequently, the point contact model does not mitigate peak vertical forces, and
  - there is no mechanism to emulate obstacle wavelength filtering that is inherent in normal tires.
- The ring contact model was ranked second for peak  $F_x$ , and higher than the point contact model for peak  $F_z$ . The ring model is almost as easy to implement as the single point contact model, but its ability to emulate the obstacle wavelength filtering allows it to perform reasonably for peak  $F_x$  without the additional complications of more sophisticated models. The ring contact model may be well suited for ride comfort studies that require higher accuracy in the horizontal direction and only moderate accuracy in the vertical direction.
- The five point rigid ring and the two point rigid ring models ranked second and third overall, respectively, ahead of all models but FTire.
- Although the sophisticated MBS tire model, FTire, did not rank highest for peak  $F_z$ , it achieved the highest overall ranking over the more simple tire models.

The Cleat Phase analysis indicates that the selection of a tire model will depend upon a number of factors, such as:

- The geometry of the obstacle relative to the tire (for example, the wavelength of the obstacle compared to the length of the contact patch and the height of the obstacle). This is because each model emulates obstacle wavelength filtering and contact patch envelopment differently.
- The intended application of the vehicle comfort model and the comfort issue being addressed. For example:
  - the adaptive footprint model achieved the highest ranking for peak  $F_z$ , and may be suitable for studies requiring accurate peak vertical load models
  - the ring contact model ranked second only to FTire for peak  $F_x$ , and may be suitable for studies which involve longitudinal suspension compliance.
- The peak force metrics analyzed here are most useful for predicting the shock loads on components (wheels, suspension components, etc.). However, fidelity of waveform (and consequently fidelity of impulse) will have the most effect on ride acceleration.

## CHAPTER 6

### RESULTS OF QUARTER VEHICLE, RIDE PHASE

#### Ride Phase Simulation Overview

In the Cleat Phase, the tire models were evaluated by comparing the peak vertical and horizontal spindle forces while traversing a cleat. The wheel spindle was fixed to a set height corresponding to an initial vertical load. For the Ride Phase, the tire models are integrated into a quarter vehicle model. The quarter vehicle model provides the same static load but allows the tire spindle height to change as part of the integrated tire/vehicle system. The metrics of interest for the Ride Phase are those which are of interest to ride comfort and chassis engineers:

- Peak vertical and horizontal chassis accelerations,  $A_z$  and  $A_x$ , respectively. These peak accelerations are useful metrics with which to study the effect of the different tire models on ride comfort predictions.
- Peak vertical and horizontal spindle forces,  $F_z$  and  $F_x$ , respectively. These peak forces are useful metrics with which to study the effect of the different tire models on “road load” predictions, used when designing wheel and suspension components.

The quarter vehicle model representing the integrated tire/vehicle system provides three additional degrees of freedom - 1) axle vertical, 2) chassis vertical, and 3) chassis horizontal. As the vehicle model does not contain longitudinal compliance, it is expected that the:

- integration of the horizontal spindle force  $F_x$  as a function of time will determine the final change in longitudinal velocity and
- peak longitudinal chassis acceleration  $A_x$  will be directly proportional to the peak longitudinal spindle force  $F_x$ .

Peak vertical spindle force  $F_z$  should correlate but not necessarily be proportional to peak chassis vertical acceleration metrics for most short wavelength obstacles. The vertical transmissibility which exists between the roadway obstacle input and the chassis acceleration output is complex as:

- the tire spindle forces are functions of the relative displacement and velocity between the tire spindle and the roadway obstacle, and
- vertical spindle position and velocity are based upon the time history of the spindle forces

As a result, the vertical chassis acceleration will depend upon the magnitude (height) of the obstacle as well the frequency (wavelength of the obstacle and the vehicle speed). In order to account for this magnitude and frequency dependence, the integrated tire/vehicle models will be simulated while traversing:

- an obstacle of relatively small vertical magnitude and short wavelength relative to the length of the contact patch – the 19 mm wide and 9.5 mm tall rectangular laboratory cleat previously tested, and
- an obstacle of relatively large vertical magnitude and long wavelength compared to the length of the contact patch – a 12 inch (0.305 m) long by 4 (0.102 m) high parking lot “speed bump”.

### Ride Phase Roadway Obstacles

Measuring peak acceleration values of a simple quarter vehicle model has the effect of inserting a series of low pass filters between the roadway obstacle and the chassis. Starting with the interface between the tire and the roadway:

1. All of the tire models (with the exception of the point contact follower) emulate some aspect of either:
  - a. obstacle wavelength filtering or
  - b. envelopment characteristics of a tire contact patch

These effects lower the frequency and amplitude of the imposed obstacle displacement.

2. The remaining high frequency displacements are further attenuated by the tire mass and damping before being passed as spindle forces into the vehicle suspension.
3. Once at the wheel spindle, high frequency content is again attenuated by the two degree of freedom quarter vehicle model, which acts as a low pass filter.

For the quarter vehicle model parameters used in this study, the modal frequencies obtained from eigenvalue analysis are:

- 13.2 Hz (vertical wheel hop) and
- 1.16Hz (vertical chassis heave)

The sinusoidal equivalent of the 19 mm long rectangular cleat entering the contact patch at eight kilometers per hour is equivalent to 58 Hz excitation – a frequency that is approaching the upper limits of the rigid ring frequency range. Therefore an additional

obstacle representing a longer wavelength (lower frequency) was needed to excite the tire/vehicle system at the opposite end of the intended input frequency spectrum. A common parking lot bump measuring 12 inches long and 4 inches high, used to slow vehicles down to walking speed in parking areas where there is high pedestrian traffic, was chosen. At eight kilometers per hour, this bump represents a 7.2 Hz input. Additional considerations regarding the selection of obstacle wavelength are given in the appendices.

The conversion of roadway obstacle input displacement into chassis acceleration via the tire model and suspension is illustrated in Figures 6.1 and 6.2. The upper graph of Figure 6.1 shows the obstacle geometry - in this case, the parking bump. The spindle forces that are generated as the simple point follower tire model encounters the obstacle are shown in the lower graph of Figure 6.1.

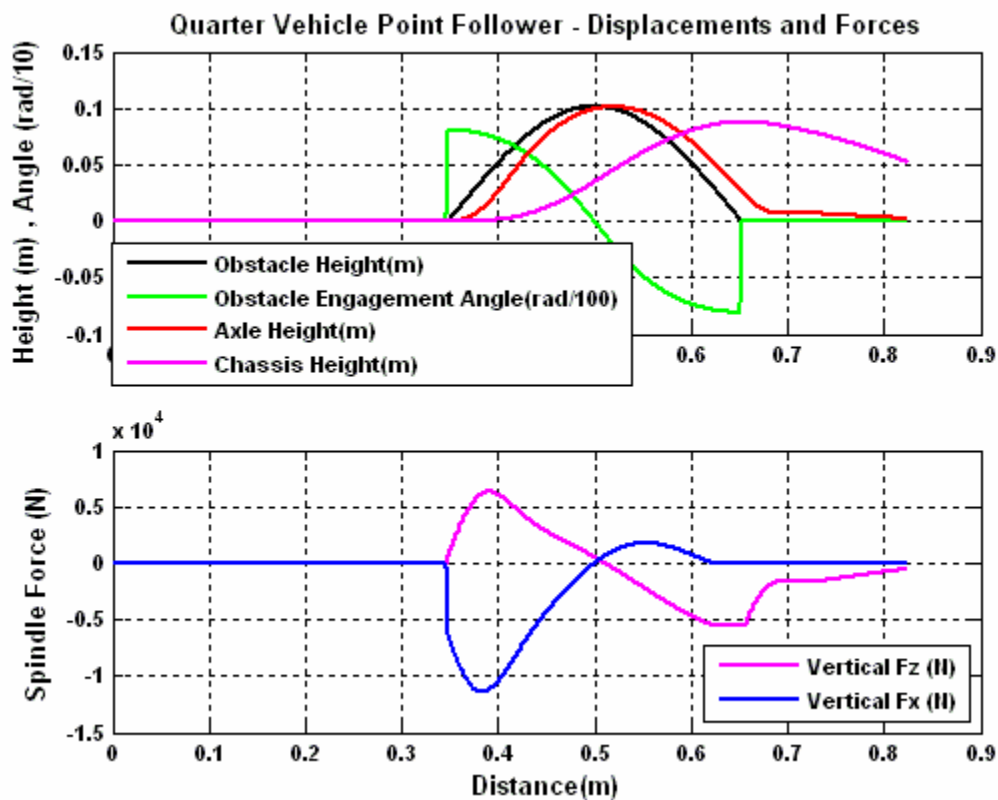


Figure 6.1: Quarter Vehicle with Simple Point Follower Tire Traversing a Bump

The upper graph of Figure 6.2 shows these same spindle forces plotted against time. The resulting vertical and longitudinal chassis accelerations are shown in the lower graph of Figure 6.2.

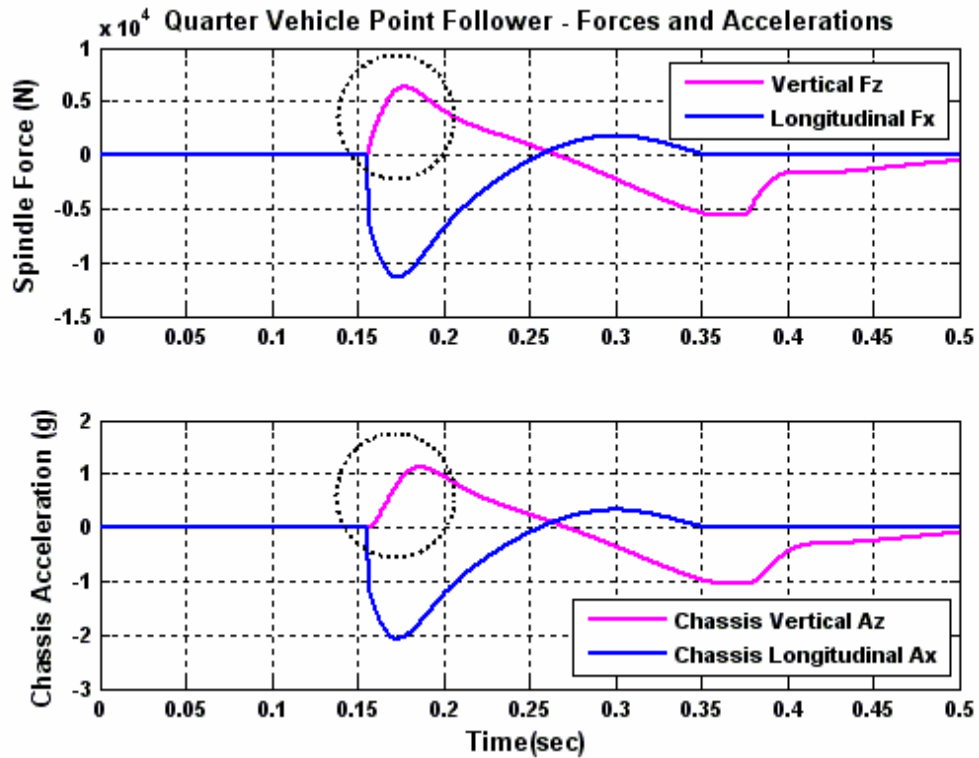


Figure 6.2: Quarter Model Forces and Accelerations vs. Time

As expected, longitudinal chassis acceleration  $A_x$  is proportional to the longitudinal tire forces  $F_x$  as there are no longitudinal degrees of freedom between the wheel carrier and chassis – it therefore accelerates longitudinally as if it were a single point mass.

Examination of the vertical spindle force  $F_z$  and vertical chassis acceleration  $A_z$  curves starting at time  $t = 0.155$  seconds illustrates that  $A_z$ , unlike  $A_x$ , is not proportional to the vertical spindle force  $F_z$ . The  $A_z$  curve displays characteristics of vibratory response associated with a mass/spring/damper system (sinusoidal response, phase delay) afforded



it by virtue of the vertical degree of freedom between the wheel carrier and the chassis mass.

### Ride Phase Simulation Plots

The objective metrics for the Ride Phase include both 1) vertical and longitudinal chassis accelerations and 2) vertical and longitudinal spindle forces. Therefore, each tire model will be evaluated first by inspecting four plots, one plot each containing a pair of vertical and longitudinal metrics. The four plots are examined in the following order:

1. chassis accelerations while traversing the sinusoidal cleat
2. wheel spindle forces while traversing the sinusoidal cleat
3. chassis accelerations while traversing the parking lot bump
4. wheel spindle forces while traversing the parking lot bump

In the Cleat Phase, the FTire model was proven to have the highest fidelity of all tire models when compared against the laboratory road wheel cleat measurements. Since no corresponding on-vehicle measurements were available for the Ride Phase, FTire will be used as the standard to which the other tire models will be compared. Subsequently, all tire model plots include an overlay of the FTire results.

### Quarter Vehicle Results – Point Contact Follower

The vertical and horizontal chassis accelerations,  $A_z$  and  $A_x$ , generated by the point contact model are graphed as functions of time along with the FTire results. Figure 6.3 shows the chassis accelerations for the “simple” tire model as it traverses the “sinusoidal equivalent” of the rectangular laboratory road wheel cleat. Figure 6.4 shows the spindle forces which generated the accelerations.

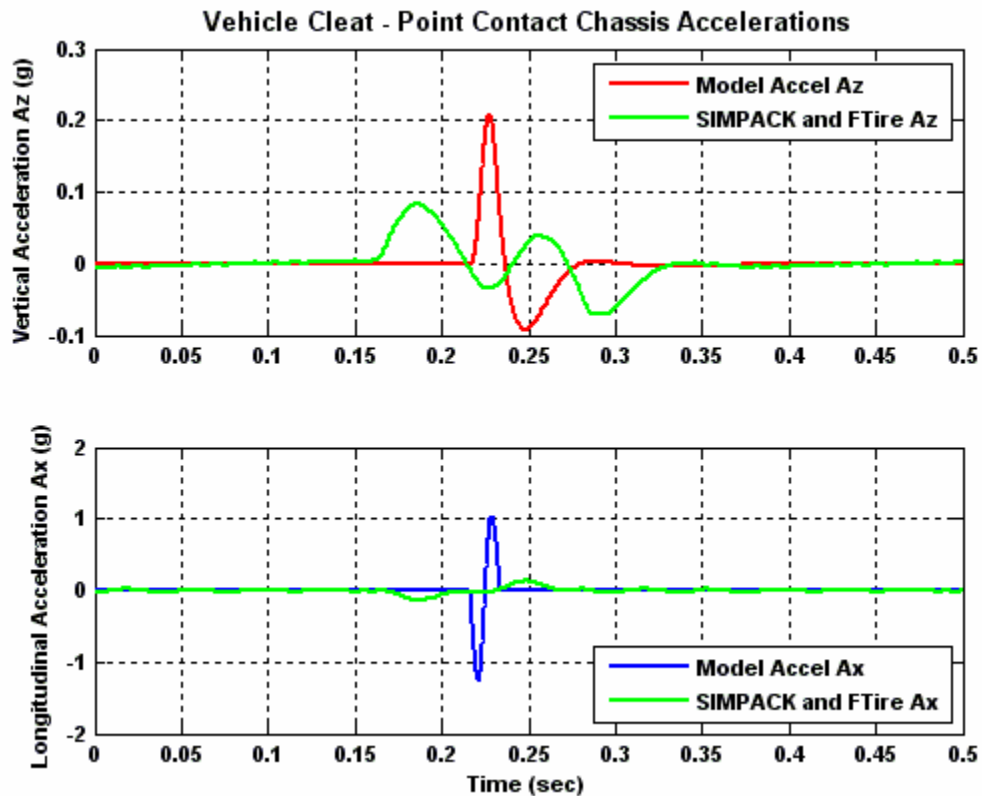


Figure 6.3: Chassis Accelerations – Point Contact Model Traversing a Cleat

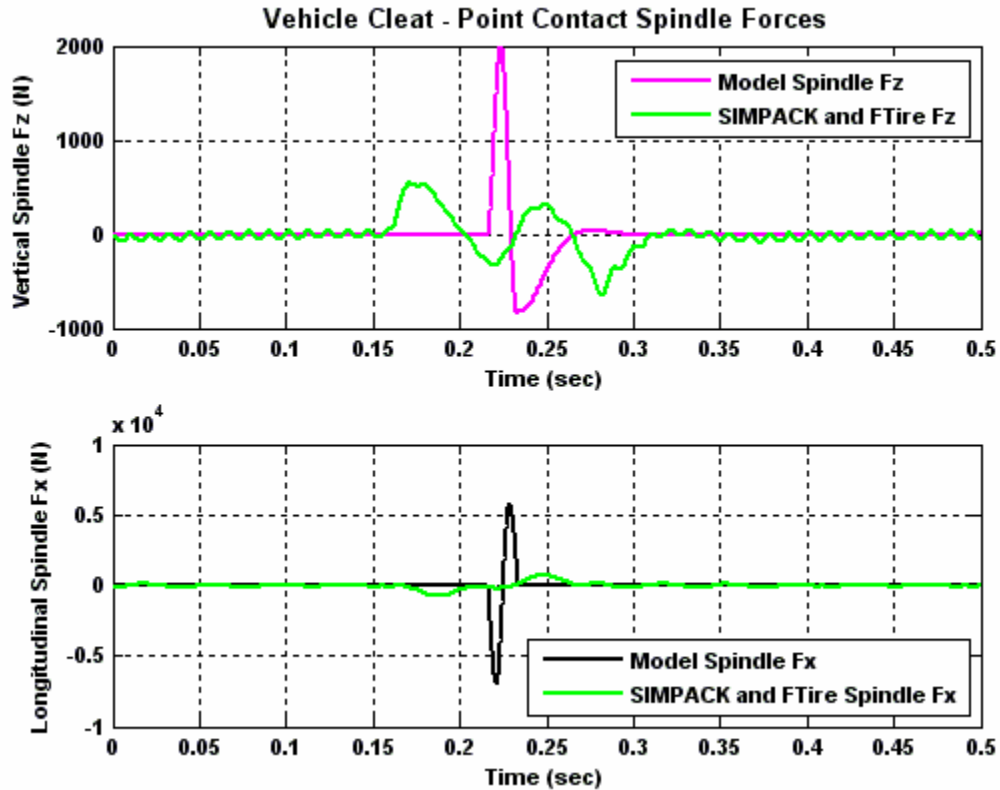


Figure 6.4: Spindle Forces – Point Contact Model Traversing a Cleat

As expected, the simulated tire spindle forces occur over a shorter time period than the FTire reference – this is because the point contact model has no provision for emulating either contact patch length or obstacle wavelength filtering.

Figure 6.5 shows the chassis accelerations for the “simple” tire model as it traverses the “parking bump,” a sinusoidal obstacle measuring 4 inches (101.6 mm) tall and 12 inches (304.8 mm) wide. Figure 6.6 shows the spindle forces which generated the accelerations.

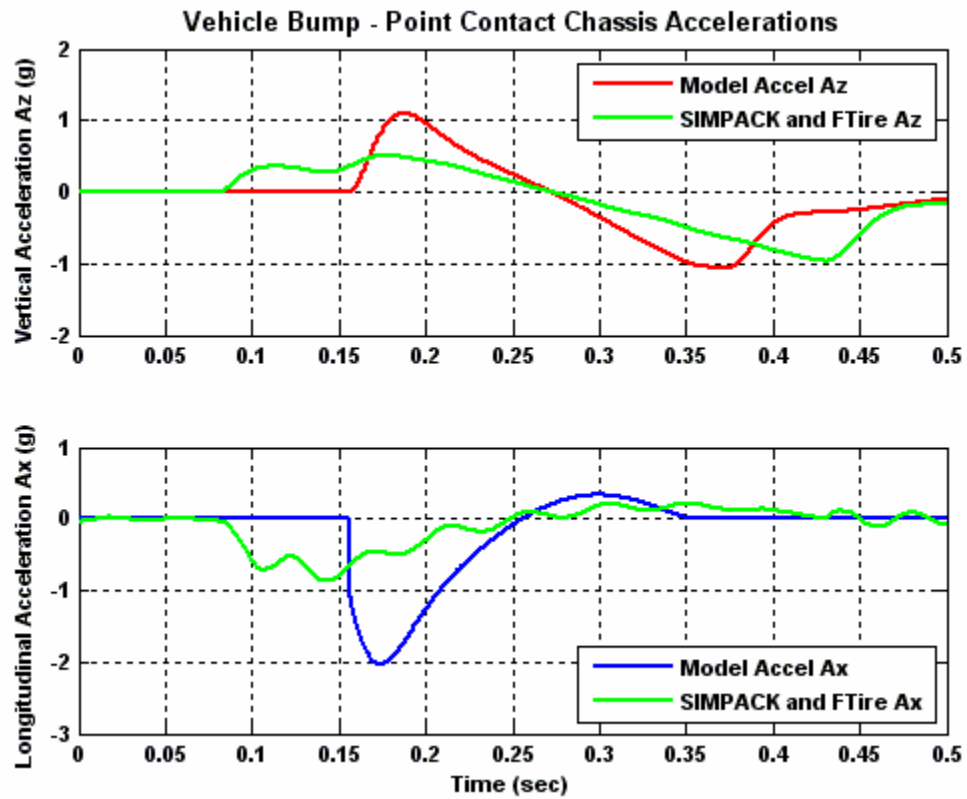


Figure 6.5: Chassis Accelerations – Point Contact Model Traversing a Bump

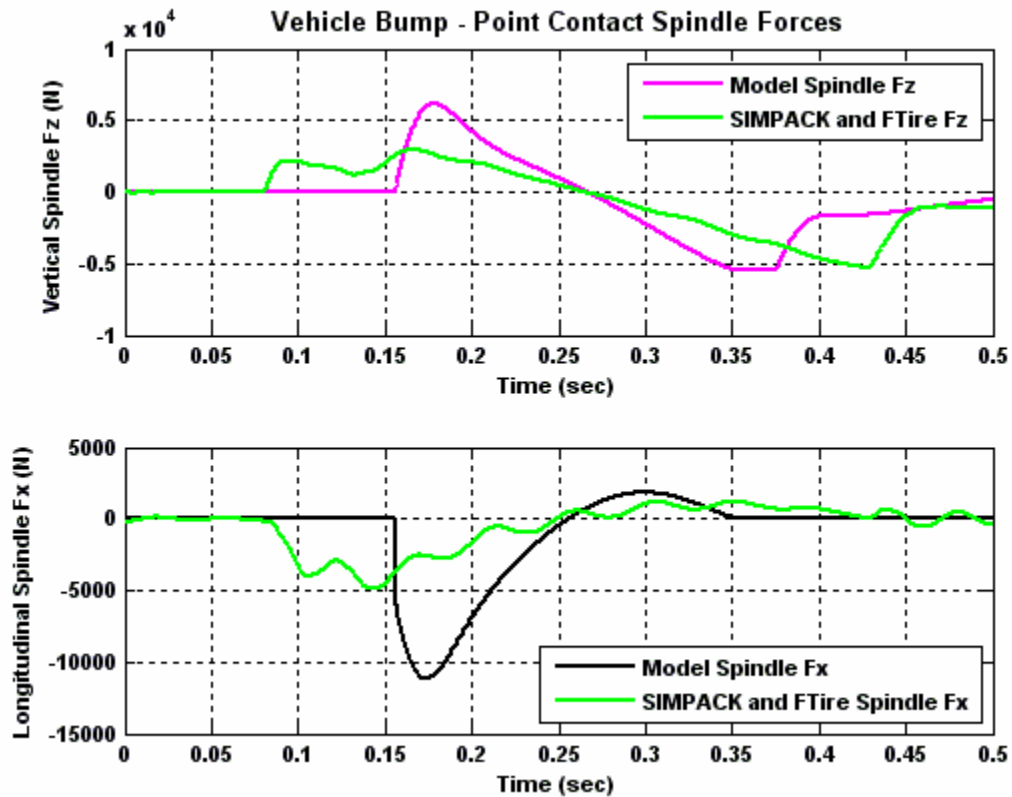


Figure 6.6: Spindle Forces – Point Contact Model Traversing a Bump

The spindle force waveform fidelity as the point contact model traverses the parking bump is better than when it traverses the cleat. The absence of obstacle wavelength filtering when using the point contact model is not as penalizing as when it is applied to long wavelength obstacles whose wavelength is greater than the tire contact patch length.

### Quarter Vehicle Results – Ring Contact Follower

The ring contact follower is similar to the point contact model, but the geometry of the ring contact follower interacting with the obstacle emulates the obstacle wavelength filtering that occurs in the tire contact patch. Figure 6.7 shows the chassis accelerations for the “simple” tire model as it traverses the “sinusoidal equivalent” of the rectangular laboratory road wheel cleat. Figure 6.8 shows the spindle forces which generated the accelerations.

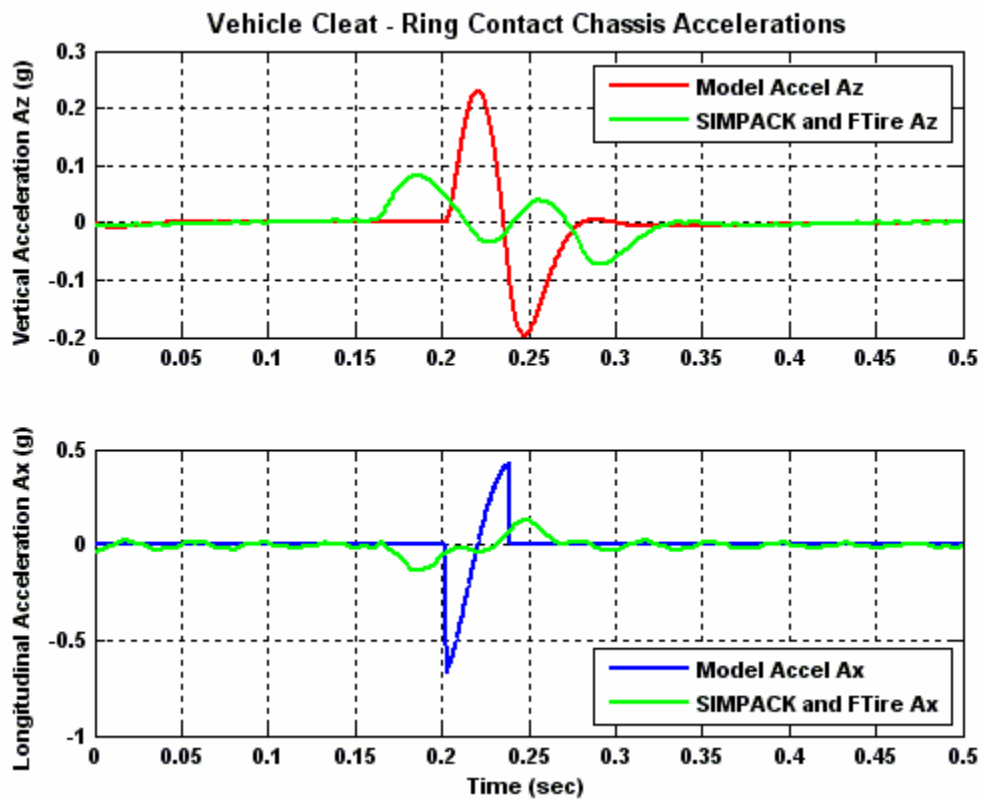


Figure 6.7: Chassis Accelerations – Ring Contact Model Traversing a Cleat

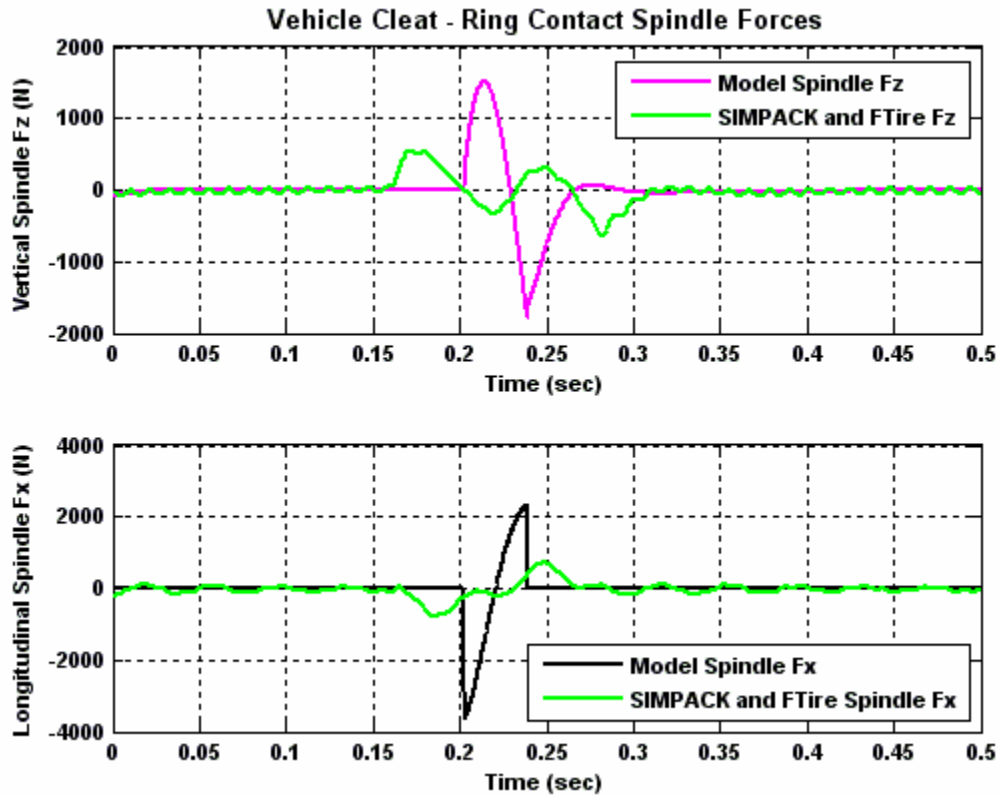


Figure 6.8: Spindle Forces – Ring Contact Model Traversing a Cleat

The simulated tire spindle forces occur over a shorter time period than the FTire reference, but longer than the point contact model. If the ride comfort simulations were expected to be used with obstacles of specific lengths, it would be possible to adjust the effective radius of the ring follower to better emulate obstacle wavelength filtering.

Figure 6.9 shows the chassis accelerations for the ring contact tire model as it traverses the bump, and spindle forces which generated the accelerations are shown in Figure 6.10.

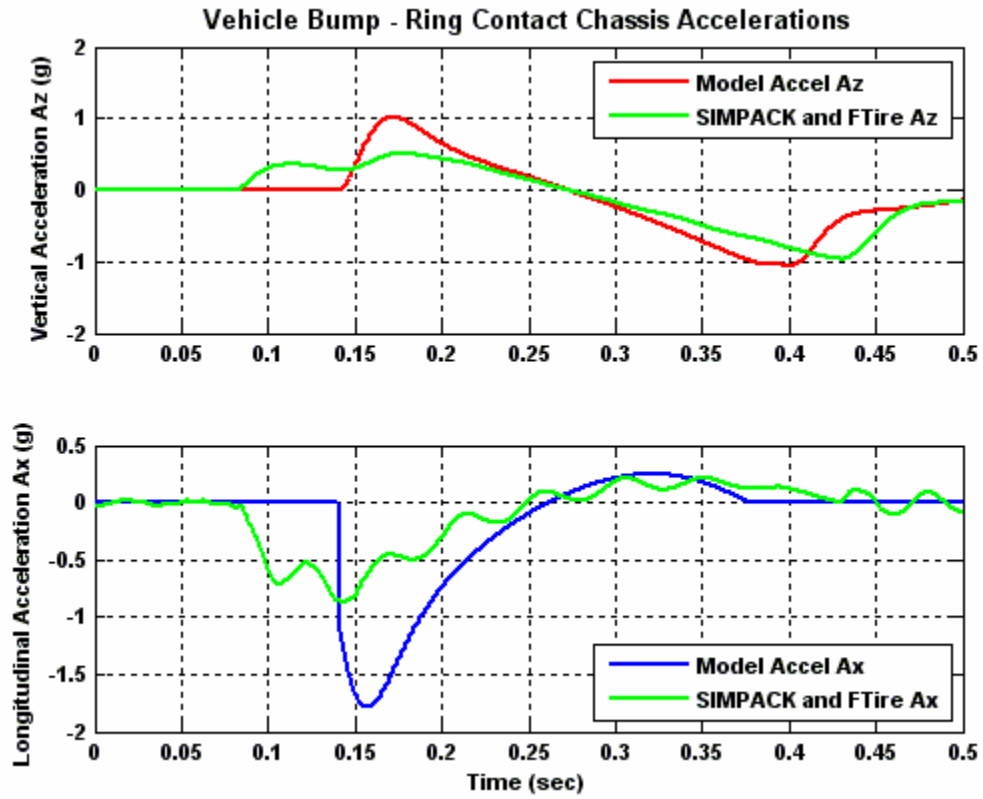


Figure 6.9: Chassis Accelerations – Ring Contact Model Traversing a Bump



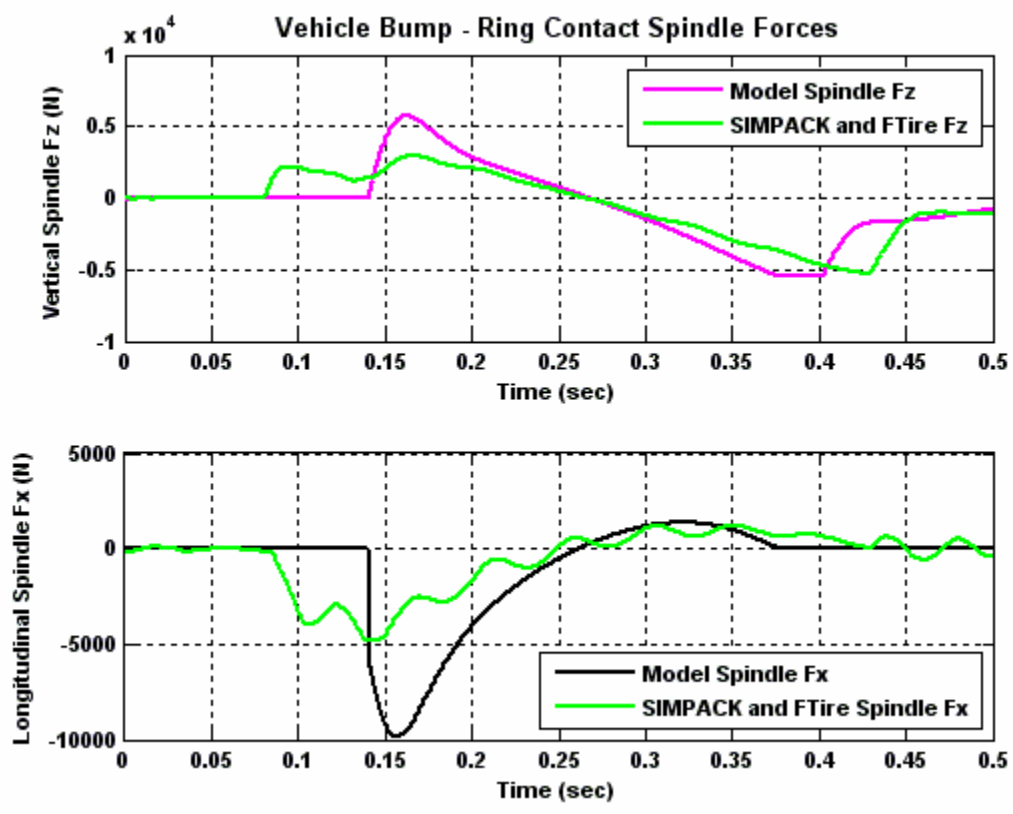


Figure 6.10: Spindle Forces – Ring Contact Model Traversing a Bump

### Quarter Vehicle Results – Constant Footprint Model

The constant footprint model is the first model which emulates both the obstacle wavelength filtering and envelopment characteristics of a pneumatic tire. Figure 6.11 shows the chassis accelerations for the constant footprint tire model as it traverses the sinusoidal equivalent of the cleat. Figure 6.12 shows the spindle forces which generated the accelerations.

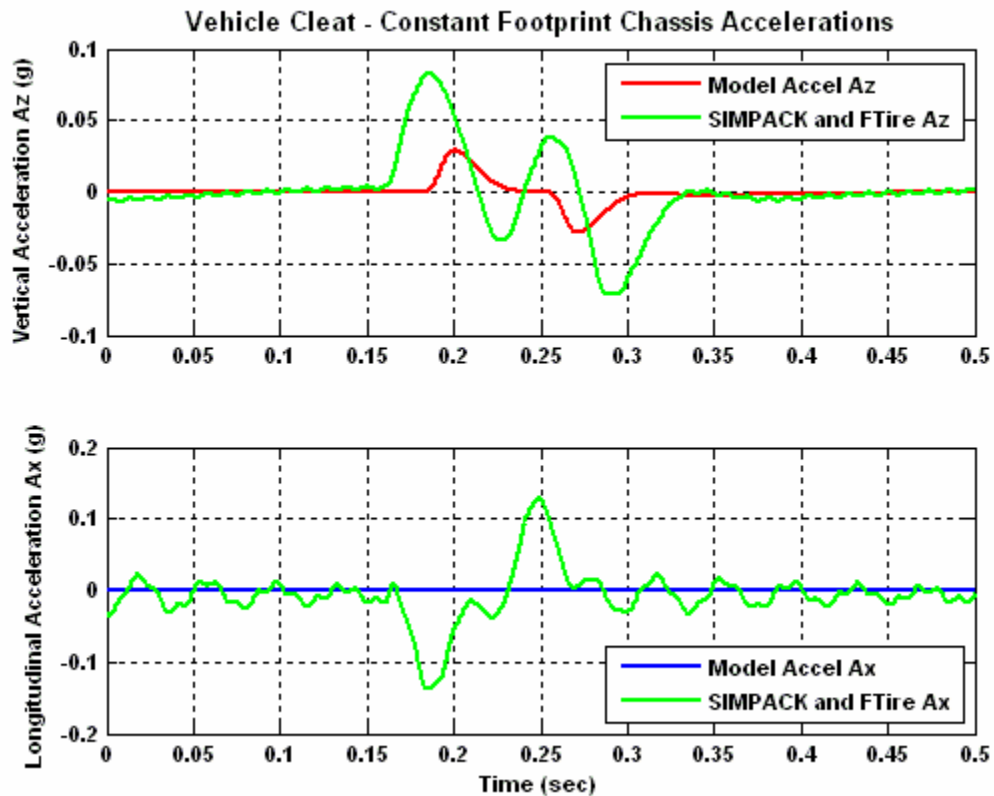


Figure 6.11: Chassis Accelerations – Constant Footprint Model Traversing a Cleat

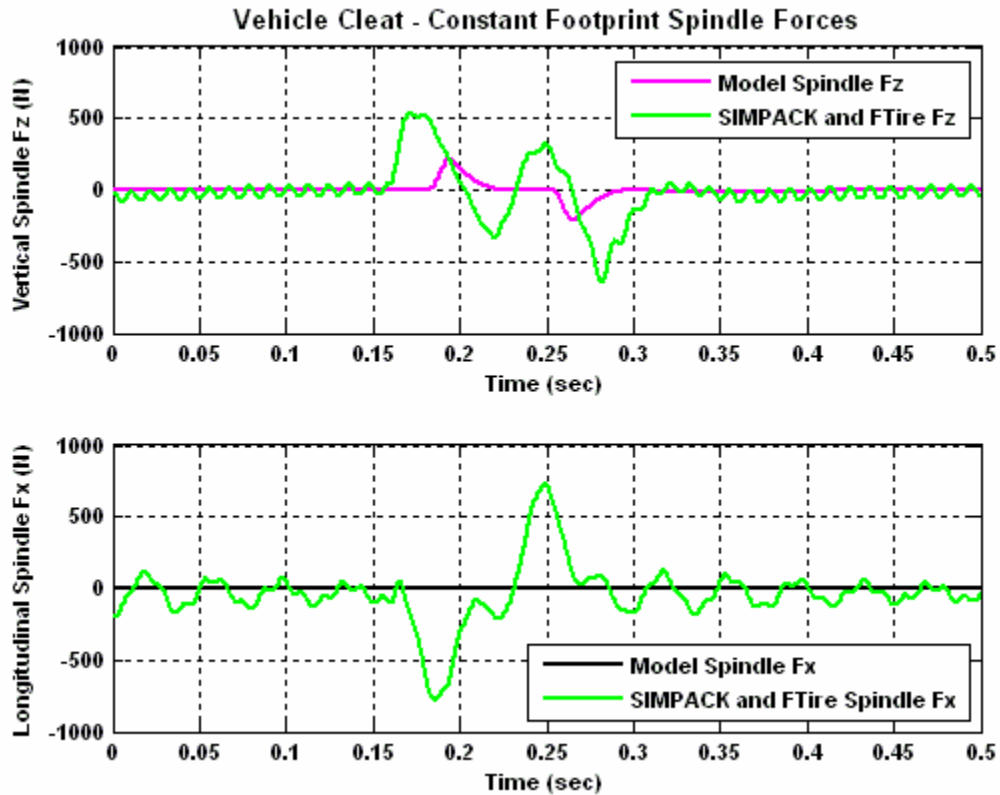


Figure 6.12: Spindle Forces – Constant Footprint Model Traversing a Cleat

The spindle forces generated by the constant footprint model show:

- obstacle wavelength filtering in the Fz trace, and
- lack of longitudinal force Fx

The constant footprint model is unable to generate longitudinal forces when traversing obstacles whose wavelength is shorter than the contact patch because the tire vertical stiffness is generated by vertical elements – there is no mechanism within the tire model for generating longitudinal force when the obstacle is enveloped within the contact patch.

Figure 6.13 shows the chassis accelerations for the constant footprint tire model as it traverses the bump, and spindle forces which generated the accelerations are shown in Figure 6.14.

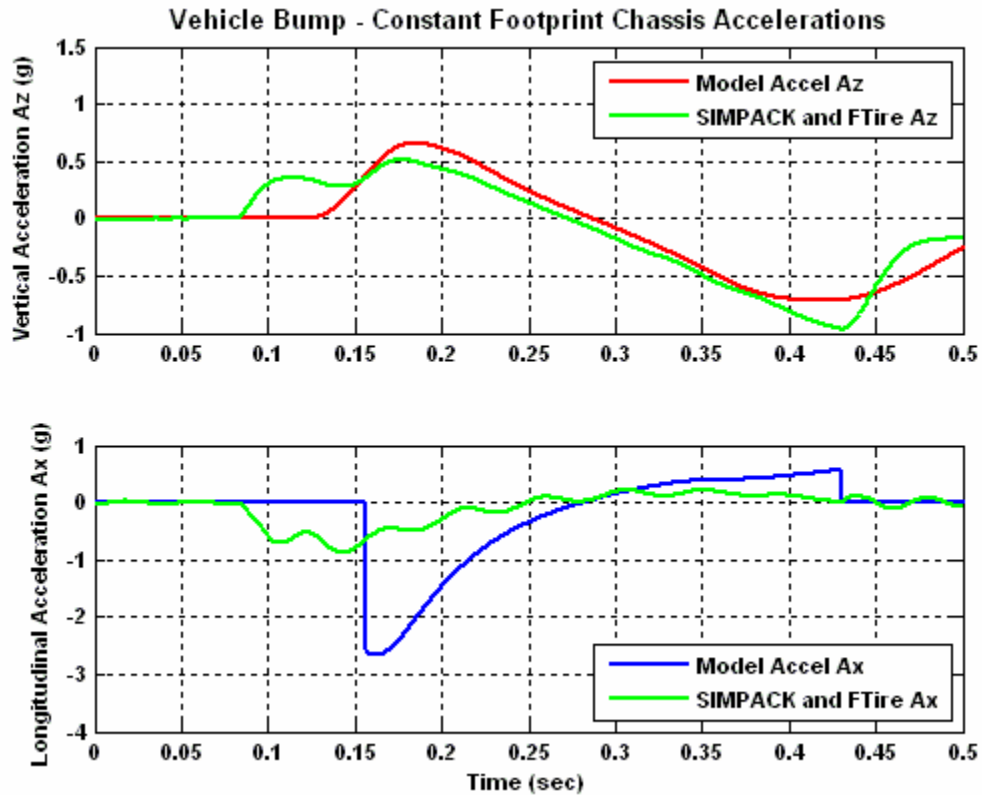


Figure 6.13: Chassis Accelerations – Constant Footprint Model Traversing a Bump

Unlike traversing the cleat obstacle, the constant footprint model does generate longitudinal force when traversing the parking bump. This is because the wavelength of the parking bump is long relative to the length of the footprint, generating an angle of incidence  $\alpha$  between the footprint and horizontal. Since the constant footprint model generates longitudinal spindle force  $F_x$  using the assumption that the resultant spindle force vector is always normal to the obstacle surface (perpendicular to angle of incidence  $\alpha$ ), the constant footprint model will generate longitudinal spindle forces when traversing obstacles with long wavelengths.

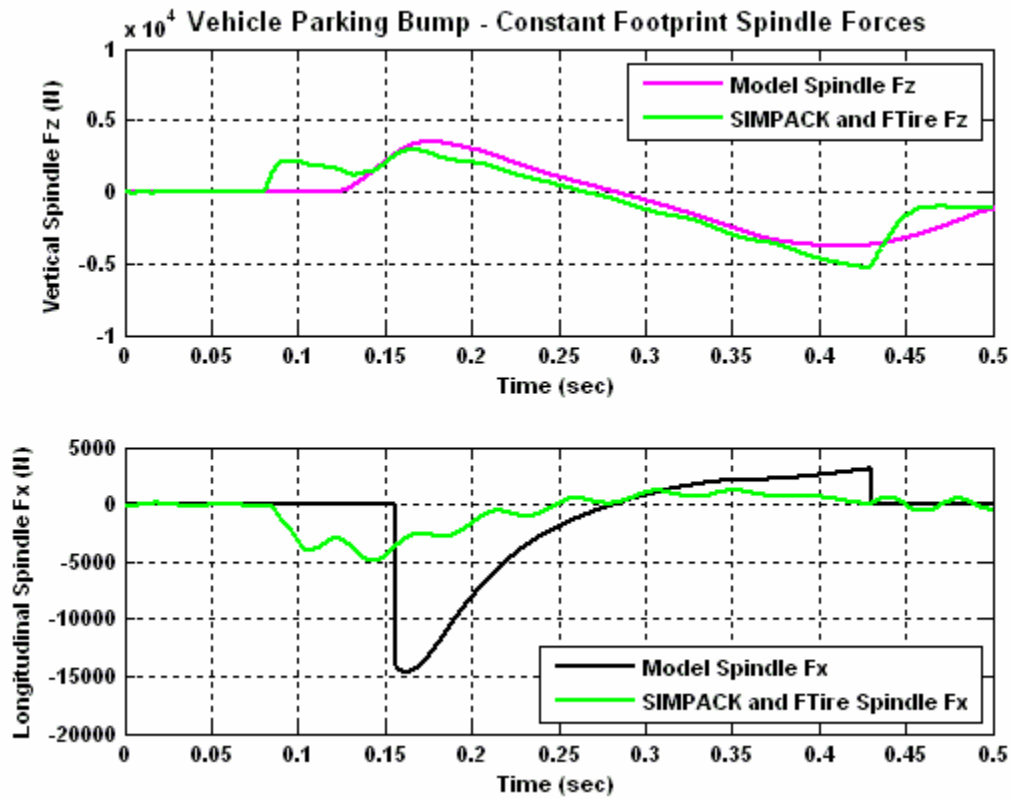


Figure 6.14: Spindle Forces – Constant Footprint Model Traversing a Bump

### Quarter Vehicle Results – Adaptive Footprint Model

The adaptive footprint model is similar to the constant footprint model in that it can emulate both the obstacle wavelength filtering and the envelopment characteristics of a pneumatic tire. The adaptive footprint, however, has two additional characteristics which improve model fidelity:

- the length of the contact patch varies in order to sustain the imposed vertical spindle load, and
- The force elements, instead of being aligned vertically, extend radially outward from the rim to the tread band – this feature allows the adaptive footprint model to develop longitudinal forces without requiring the previous assumption that the resultant of the tire spindle forces always acts perpendicular to the obstacle surface.

Figure 6.15 shows the chassis accelerations for the adaptive footprint tire model as it traverses the cleat. Figure 6.16 shows the spindle forces which generated the accelerations.

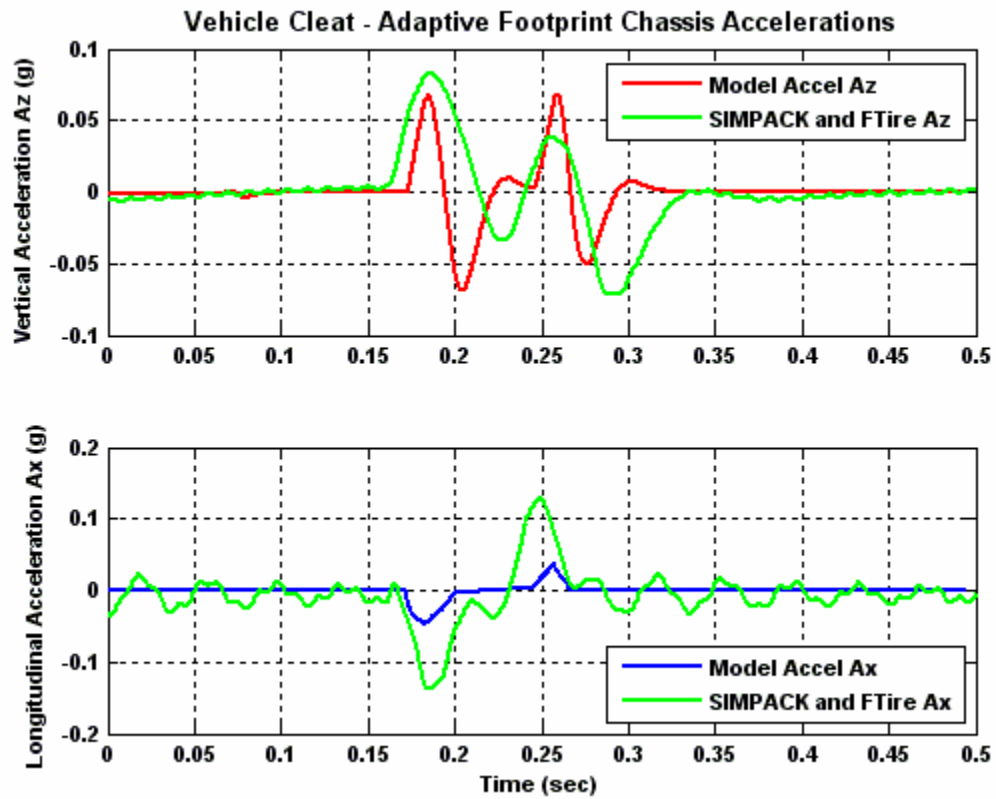


Figure 6.15: Chassis Accelerations – Adaptive Footprint Model Traversing a Cleat

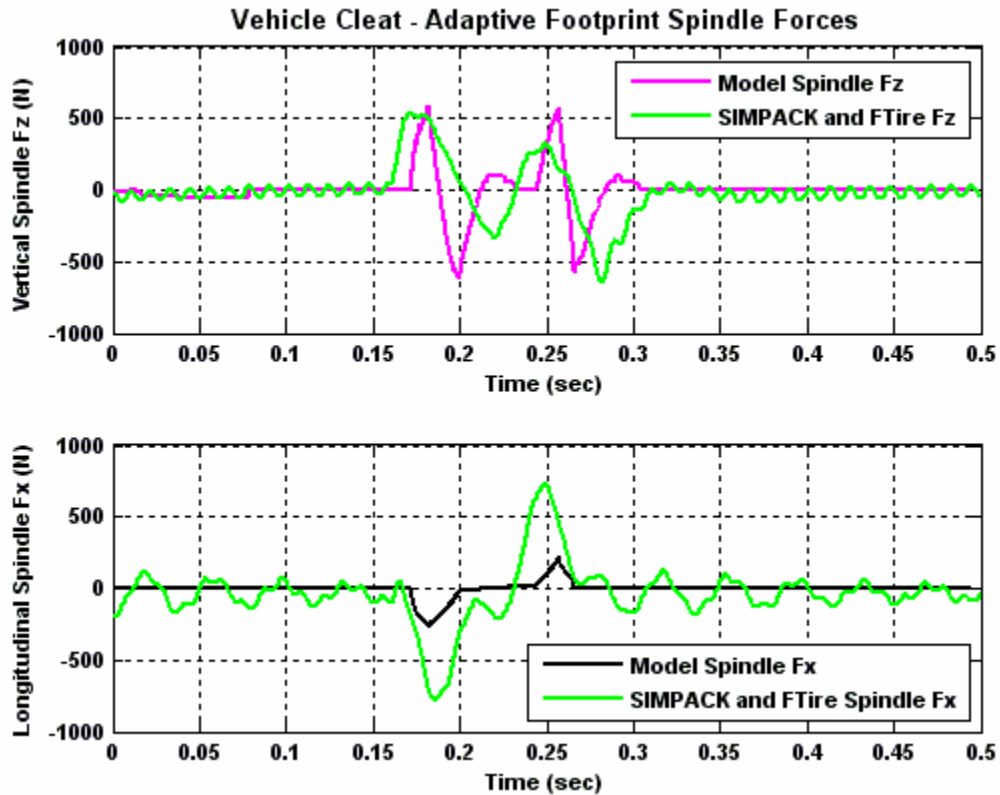


Figure 6.16: Spindle Forces – Adaptive Footprint Model Traversing a Cleat

Although the horizontal spindle forces generated by the adaptive footprint model still underestimate the FTire reference, the adaptive footprint model fidelity is highest of any of the previous models. Also, the engagement time between the tire and the cleat is closest to the FTire simulation due to the increase in contact patch length when the tire model encounters the obstacle.

Figure 6.17 shows the chassis accelerations for the adaptive footprint tire model as it traverses the bump, and spindle forces which generated the accelerations are shown in Figure 6.18. When encountering the parking bump, the vertical force is overestimated and – in contrast to the cleat obstacle - the contact patch length is subsequently too short.



The adaptive footprint force reaches a minimum force of approximately 5,300 N as the tire contact patch leaves the ground as a result of striking the parking lot bump.

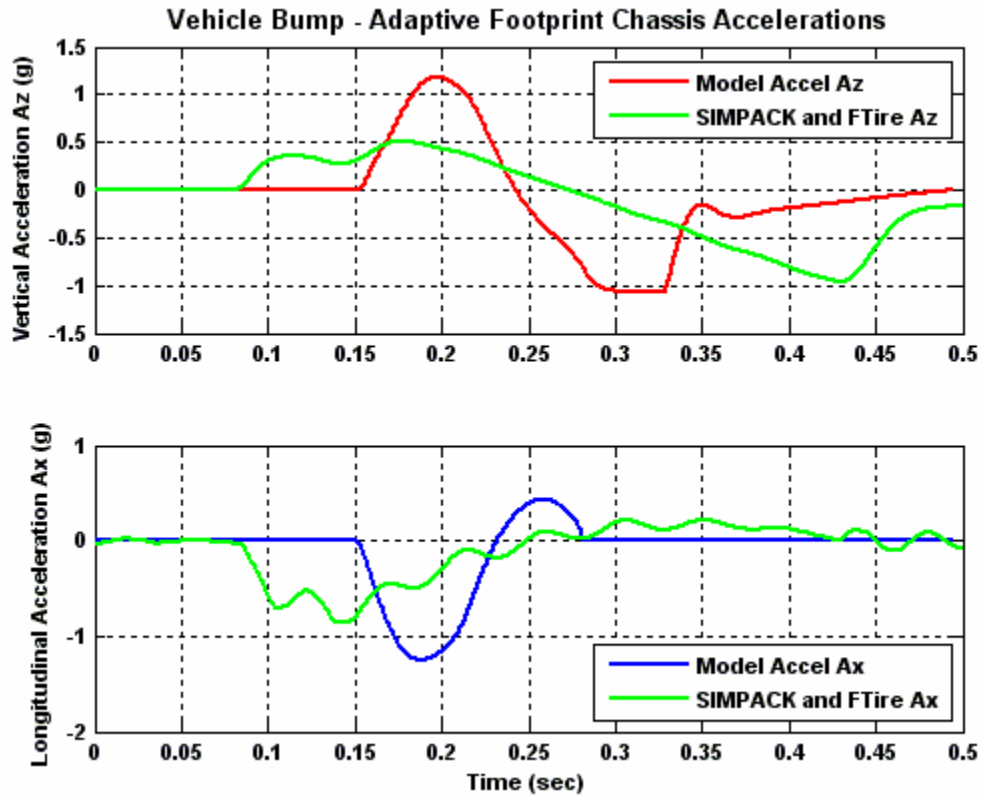


Figure 6.17: Chassis Accelerations – Adaptive Footprint Model Traversing a Bump

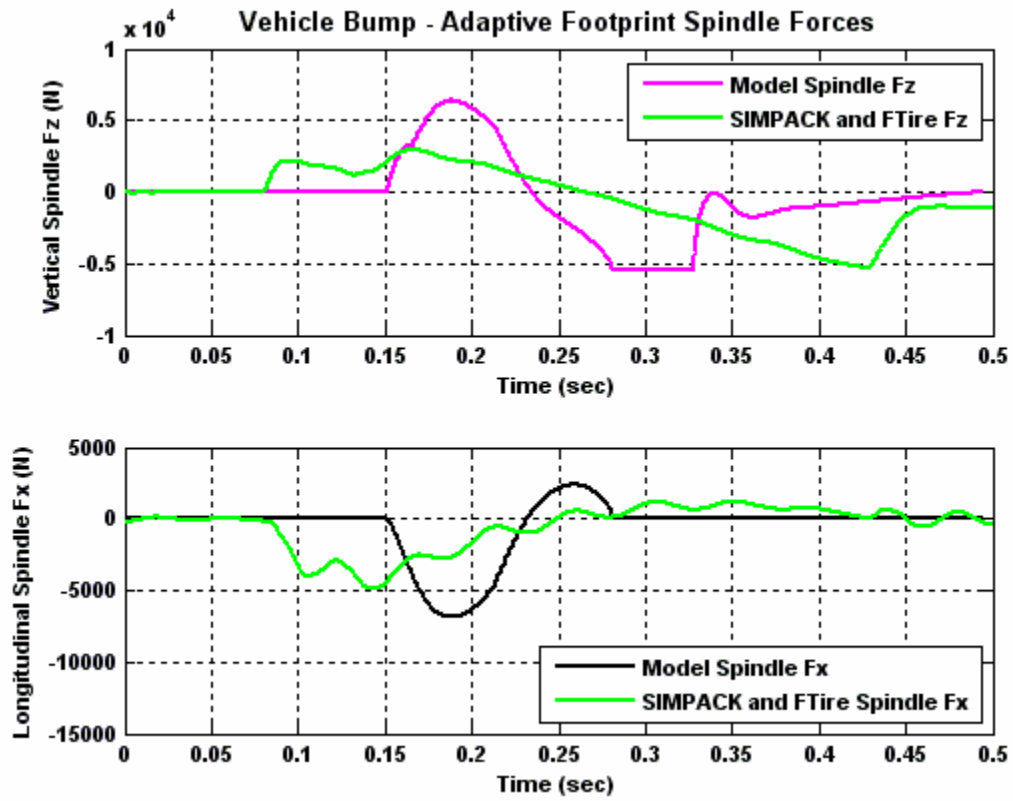


Figure 6.18: Spindle Forces – Adaptive Footprint Model Traversing a Bump

### Quarter Vehicle Results – Two Point Follower Rigid Ring Model

The two point rigid ring model emulates both the obstacle wavelength filtering and envelopment characteristics of a pneumatic tire using two point followers – one at the entrance and one at the exit of the contact patch. The rigid ring, representing the relatively inflexible and inextensible steel belts in the tire summit between the tread band and the tire sidewall, is intended to model tire internal dynamic modes. Figure 6.19 shows the chassis accelerations for the two point rigid ring tire model as it traverses the “sinusoidal equivalent” of the cleat. Figure 6.20 shows the spindle forces which generated the accelerations.

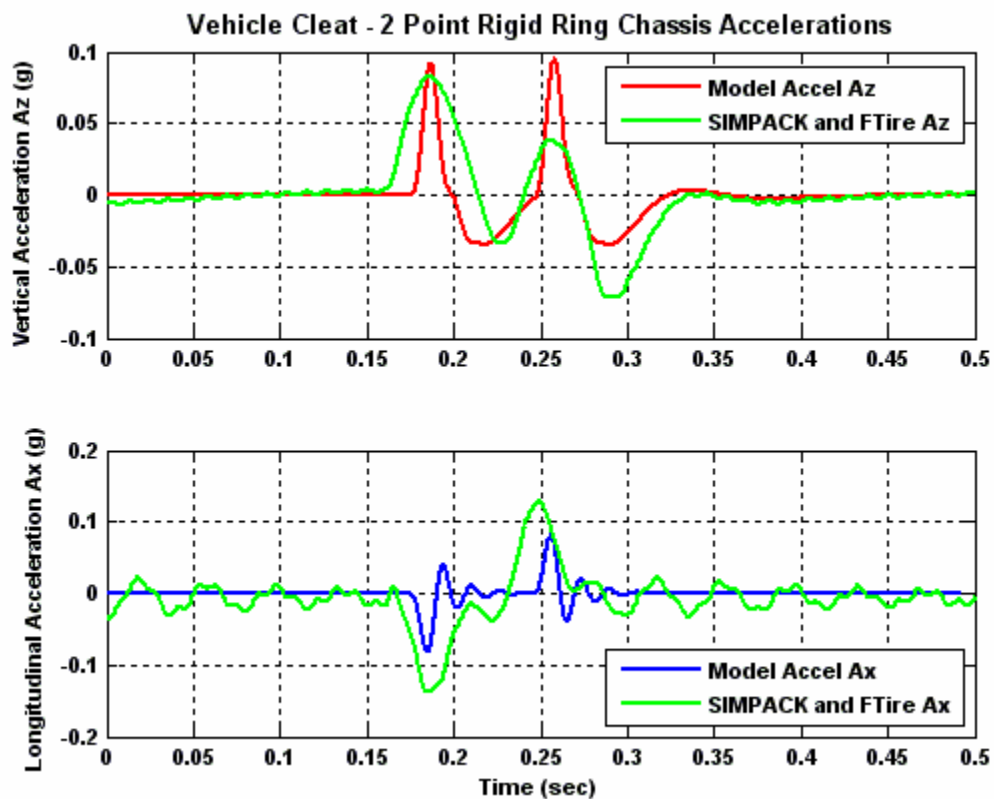


Figure 6.19: Chassis Accelerations – Two Point Rigid Ring Model Traversing a Cleat

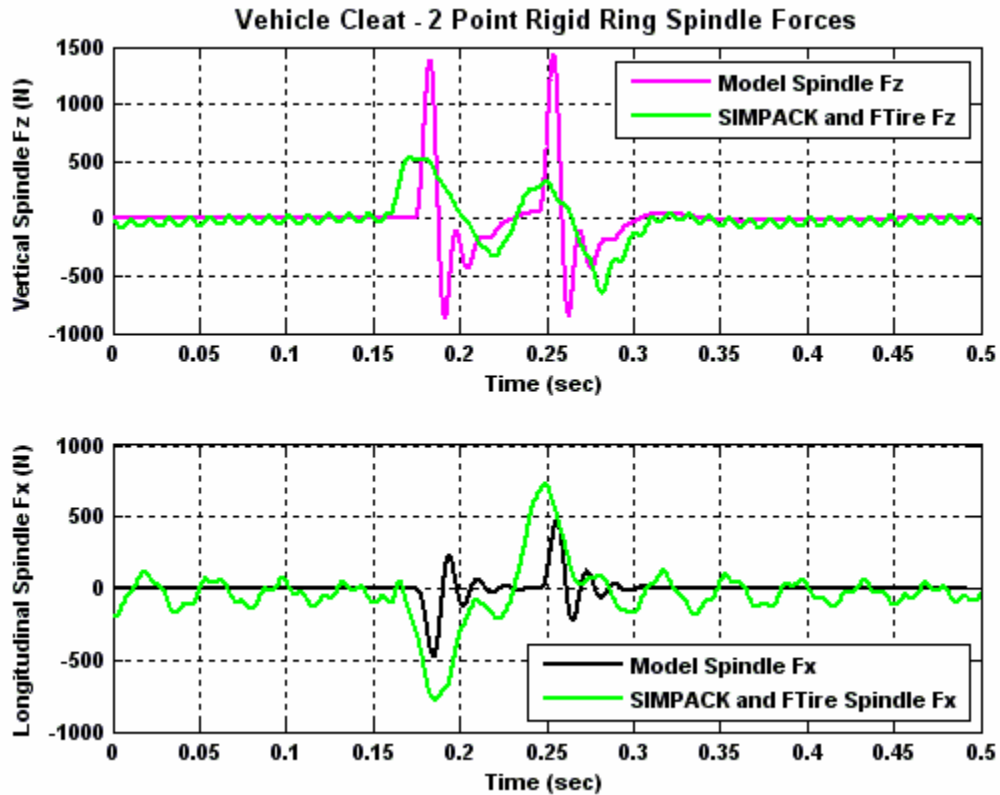


Figure 6.20: Spindle Forces – Two Point Rigid Ring Model Traversing a Cleat

The spindle forces generated by the two point rigid ring model clearly show internal “ringing” of the tire summit as the two point contact model engages, envelopes, and then disengages from the cleat.

Figure 6.21 shows the chassis accelerations for the two point rigid ring tire model as it traverses the bump. The ringing as the leading and trailing point followers engage and disengage from the bump are visible. The low pass filtering effect on vertical chassis acceleration  $A_z$  (due to the vertical degree of freedom in the chassis) contrasts sharply with the longitudinal chassis acceleration  $A_x$ . The spindle forces which generated the accelerations are shown in Figure 6.22.

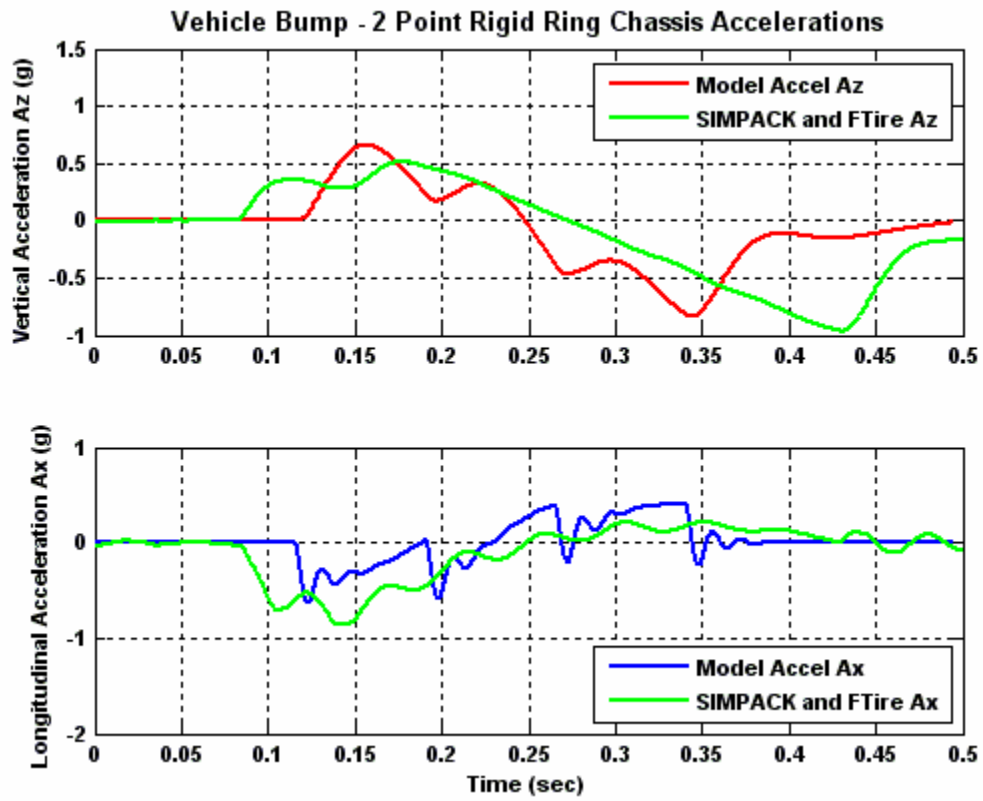


Figure 6.21: Chassis Accelerations – Two Point Rigid Ring Model Traversing a Bump

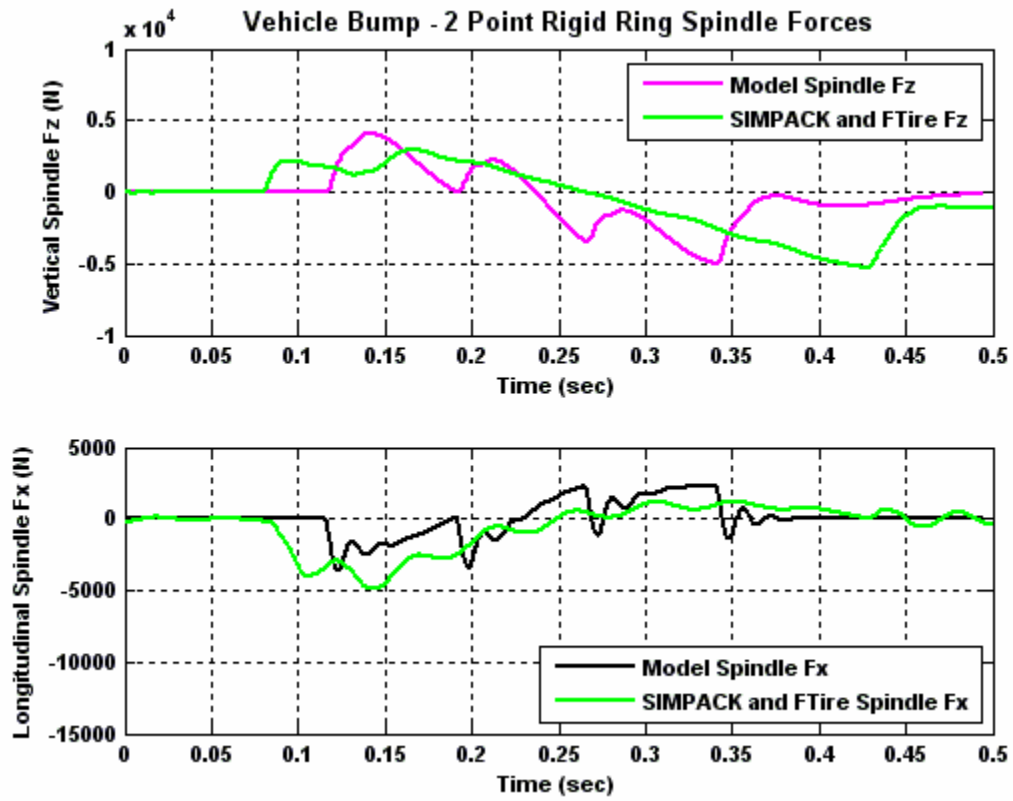


Figure 6.22: Spindle Forces – Two Point Rigid Ring Model Traversing a Bump

### Quarter Vehicle Results – Five Point Follower Rigid Ring Model

The five point rigid ring model is identical to the two point equivalent with the exception of the number of elements used to emulate the functions of the contact patch – four versus one. Figure 6.23 shows the chassis accelerations for the five point rigid ring tire model as it traverses the “sinusoidal equivalent” cleat. Figure 6.24 shows the spindle forces which generated the accelerations.

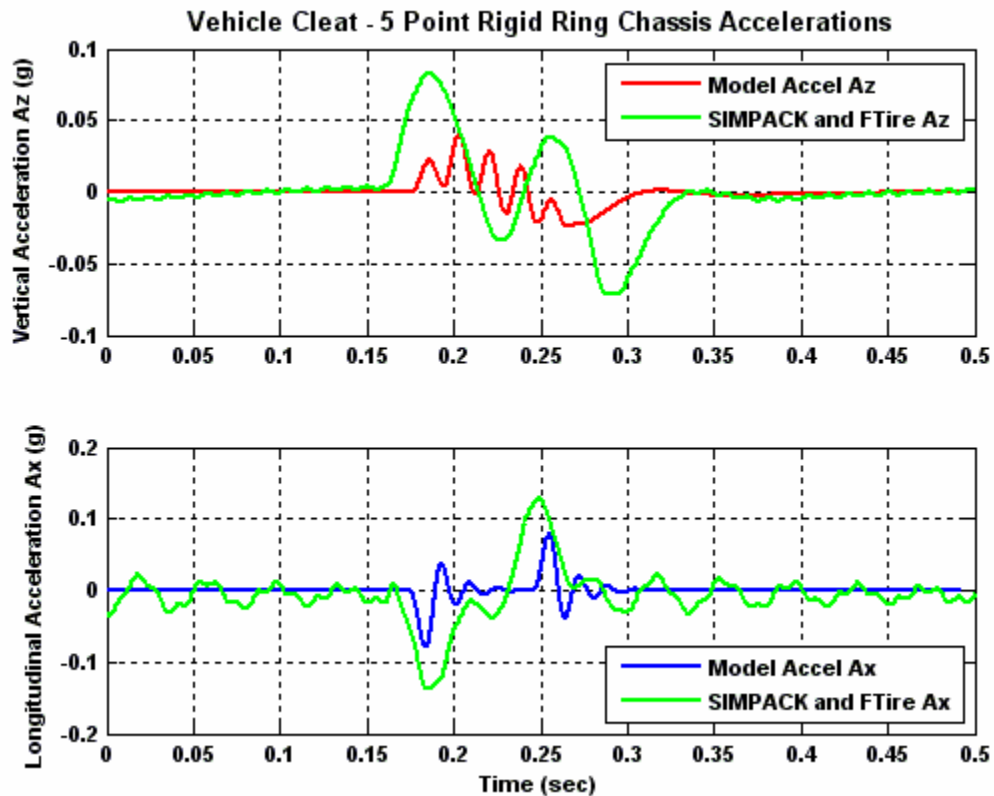


Figure 6.23: Chassis Accelerations – Five Point Rigid Ring Model Traversing a Cleat

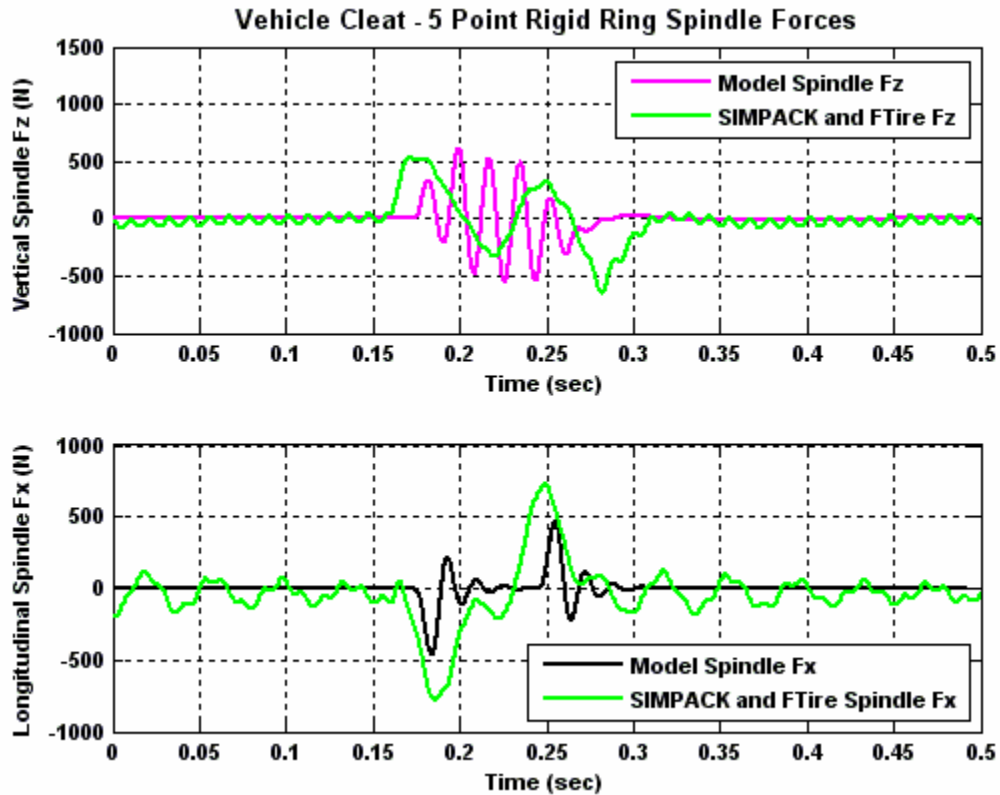


Figure 6.24: Spindle Forces – Five Point Rigid Ring Model Traversing a Cleat

The spindle forces generated by the five point rigid ring model show:

- vertical force oscillations as the four contact patch elements each individually envelop the cleat
- longitudinal force generation with tire dynamics due to “ringing” of the rigid ring

Any improvements afforded by the greater resolution in the contact patch - obtained by dividing the contact patch plane into four individual elements – appear to be offset by the lack of shear and bending moment stiffness between the plane elements. Bending stiffness, generated between the contact plane elements by:

- material properties in the tread band and tire summit, and
- tire inflation pressure (hoop stress)



would mitigate the angle of engagement  $\alpha$  of the individual plane elements and potentially improve the simulation results.

Figure 6.25 shows the chassis accelerations for the five point rigid ring model as it traverses the bump, and spindle forces which generated the accelerations are shown in Figure 6.26.

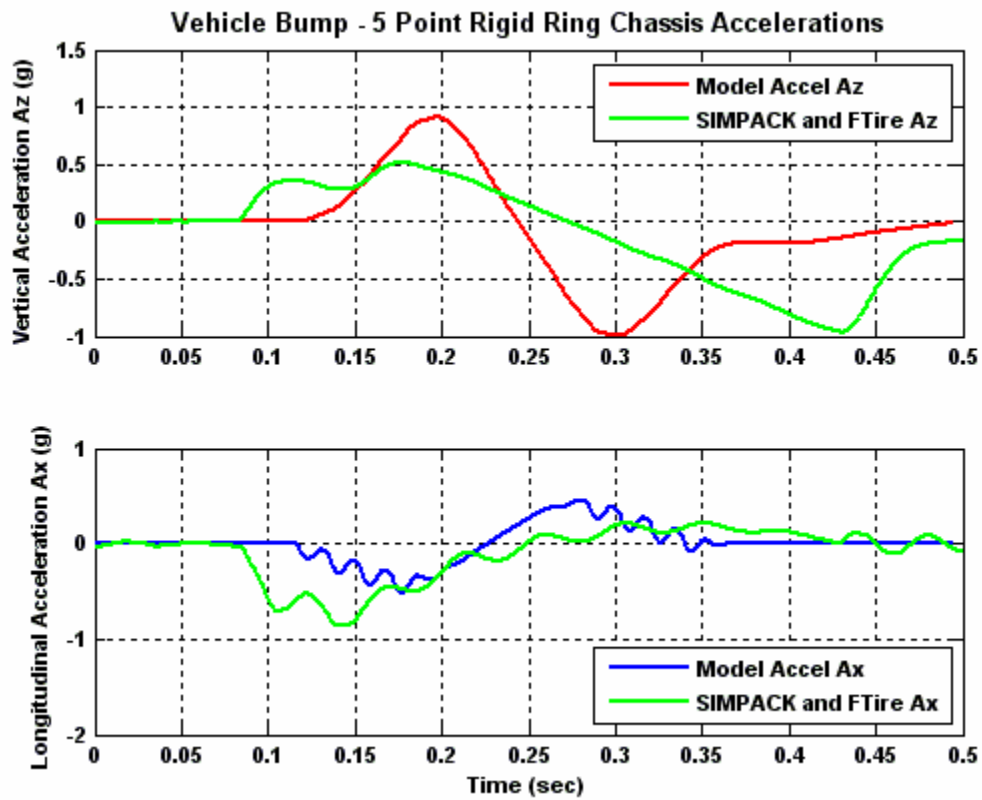


Figure 6.25: Chassis Accelerations – Five Point Rigid Ring Model Traversing a Bump

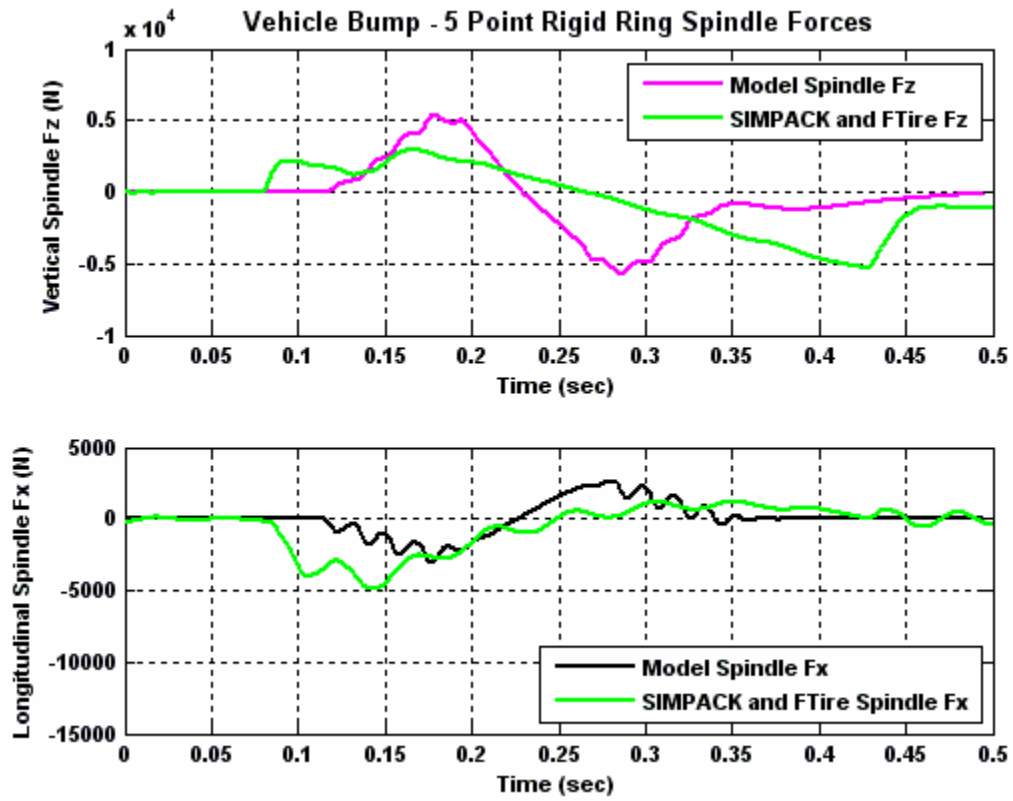


Figure 6.26: Spindle Forces – Five Point Rigid Ring Model Traversing a Bump

## Ride Phase Results - Analysis

### Ride Phase Peak Chassis Acceleration Objective Metrics

Two primary output metrics for vehicle ride – peak chassis vertical acceleration  $A_z$  and peak horizontal acceleration  $A_x$  - were evaluated for all tire models except for those three which used an “equivalent summit mass.” These three models were not used as the results from the Cleat Phase of the investigation concluded that adding an equivalent summit mass did not improve tire model performance. In addition, only simulations using the sinusoidal approximation of the rectangular cleat were used. This approach was chosen as the sinusoidal cleat provided better simulation results than the rectangular cleat during the Cleat Phase investigation.

Because on-vehicle measurements were not available, the peak chassis acceleration metrics for both the cleat and the bump were normalized to results obtained using FTire implemented in SIMPACK Automotive Plus MBS. Figure 6.27 compares the peak acceleration metrics for the cleat obstacle.

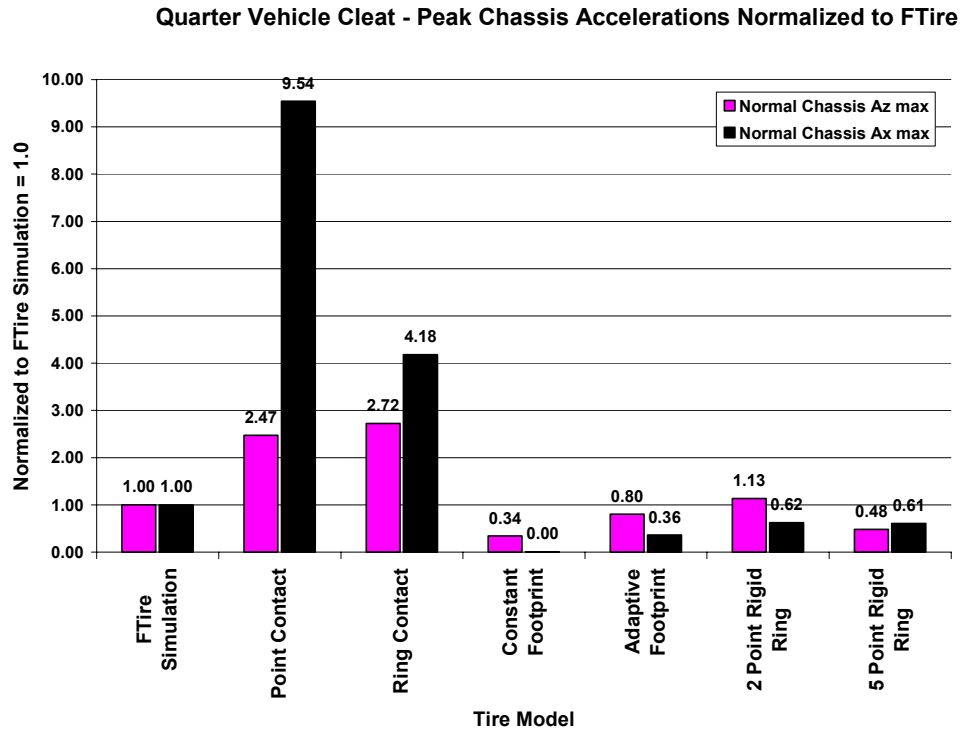


Figure 6.27: Peak Chassis Accelerations - Sinusoidal Cleat Simulation

Several conclusions can be drawn from the quarter car peak accelerations for the sinusoidal cleat (short wavelength relative to contact patch length) simulation:

- The point contact and the ring contact models do not emulate contact patch envelopment and therefore overestimate both vertical and horizontal accelerations.
- The constant footprint acceleration results were consistent with the fixed spindle force results in that the constant footprint model underestimates metrics in both the vertical and longitudinal directions.
- The distributed vertical spring rate of the constant footprint model emulates obstacle envelopment in the contact patch. However, the model does not take into account localized bending stiffnesses and therefore does not provide

enough vertical spindle force, as evidenced by the low peak vertical acceleration.

The quarter vehicle acceleration results support the general conclusion from the fixed spindle simulation results – the tire models which do not have mechanisms to emulate the obstacle wavelength filtering or the obstacle envelopment characteristics of a tire contact patch will perform poorly in those instances where the obstacle wavelength is shorter than that of the tire contact patch length.

The peak vertical and longitudinal acceleration results for the parking bump are summarized in Figure 6.28.

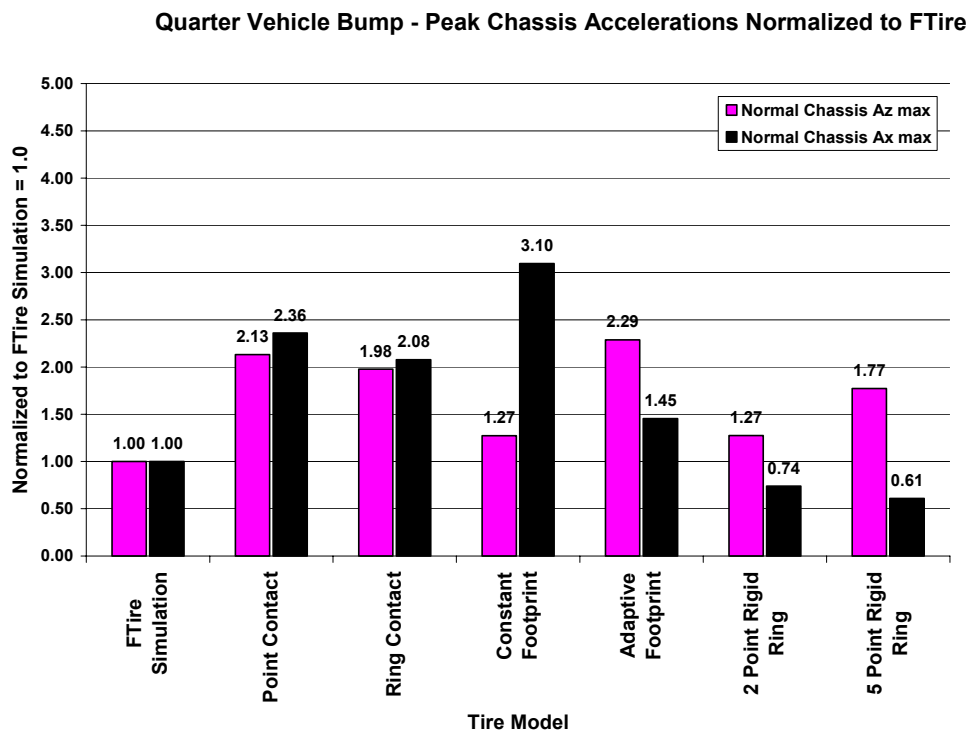


Figure 6.28: Peak Chassis Accelerations – Parking Bump Simulation

Several conclusions that can be drawn from the quarter car peak acceleration metrics for the parking bump (long wavelength relative to the contact patch length) simulation:

- The peak chassis accelerations are, with the exception of longitudinal acceleration for the two point and five point rigid ring models, consistently too high.
- The increased complexity of the five point rigid ring model does not appear to provide improvement over the less complex two point rigid ring model.
- The point contact and the ring contact models produced peak vertical acceleration values that are too high. This is because neither of these models is capable of emulating obstacle envelopment.
- With the exception of the two point and five point rigid ring models, all models overestimate longitudinal peak acceleration compared to FTire.
- If absolute values for peak acceleration are not a consideration (determining the relative changes between solutions is adequate) and the obstacle wavelength is long compared to the contact patch length:
  - The point contact model works consistently in that both  $A_z$  and  $A_x$  are overestimated by approximately the same amount.
  - The point contact model is extremely simple to implement.
  - The ring contact model provides improvement over the point contact model with little additional cost
- If longitudinal fidelity is not a consideration, the constant footprint model provides reasonable vertical fidelity for long wavelength obstacles while being relatively easy to implement in comparison with the adaptive footprint and rigid ring models.

- The rigid ring models provide adequate fidelity for both acceleration metrics but their added complexity over the simpler adaptive footprint model can only be justified if:
  - internal tire dynamics are important (upwards of approximately 70 to 100 Hz), or
  - driving/braking torque and traction modeling is needed.

Comparing the chassis acceleration metrics from Figures 6.27 and 6.28 indicates that the shorter wavelength cleat is more challenging than the longer wavelength parking bump. Some embodiment of both obstacle wavelength filtering and contact patch envelopment characteristics is needed in order for the models to perform adequately over a range of obstacle wavelengths and geometries, especially those obstacles whose wavelengths are shorter than the tire contact patch.

#### Ride Phase Peak Spindle Force Objective Metrics

Two additional ride metrics were investigated – peak vertical spindle force  $F_z$  and peak horizontal spindle force  $F_x$ . These forces were evaluated as they are of concern for designing wheel and suspension components to withstand anticipated “road loads” during vehicle operation.

Peak spindle forces in the vertical direction are positive (upward) as the vehicle traverses an obstacle protruding upwards from the road surface. Spindle forces in the horizontal direction, however, are first developed in the negative (braking) direction as the obstacle enters the contact patch and then in the positive direction (driving) as the obstacle exits the contact patch. The horizontal spindle force metric was defined as the

maximum magnitude of the rearward (braking direction) force that occurs as the vehicle encounters an obstacle.

Figures 6.29 and 6.30 compare the peak spindle forces for the quarter vehicle model as it traverses the sinusoidal cleat and the parking bump, respectively. As with the peak chassis acceleration metrics, on-vehicle measurements were not available, so the spindle force metrics were normalized to results obtained using FTire implemented in SIMPACK Automotive Plus MBS.

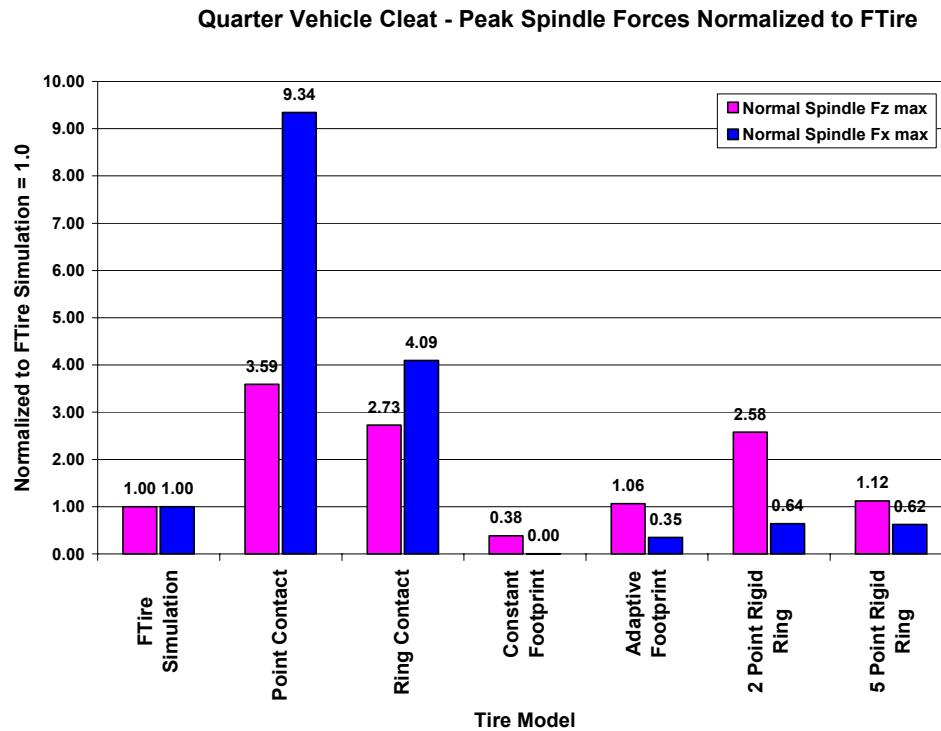


Figure 6.29: Spindle Force Metrics - Sinusoidal Cleat Simulation



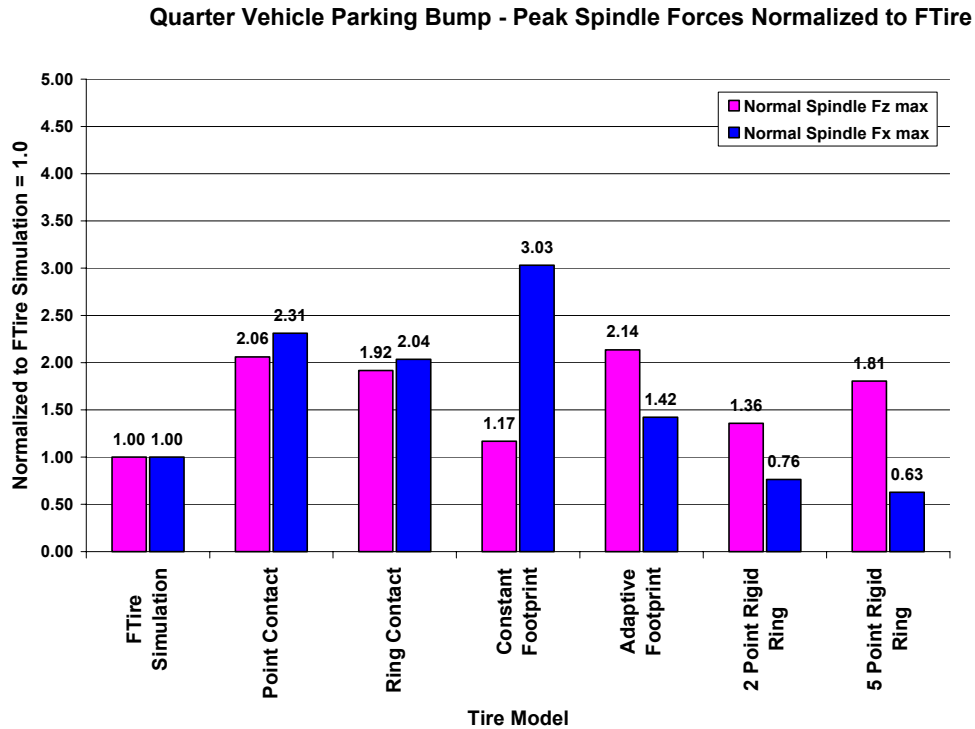


Figure 6.30: Spindle Force Metrics – Parking Bump Simulation

In general, the vertical and horizontal spindle force metrics correspond well to the acceleration metrics. Some general observations include:

- The five point rigid ring model provides the best overall result for the short wavelength cleat obstacle.
- The two point rigid ring model provides the best overall result for the long wavelength parking bump.
- The constant footprint model provided the best vertical spindle force fidelity for long wavelength parking bump but performed the worst for the longitudinal force metric.

The general conclusion that was reached using the chassis acceleration metrics is supported by the spindle force metrics - simulation of the shorter wavelength cleat is

more challenging than the longer wavelength parking bump and requires a more sophisticated tire model.

### Ride Phase Impulse Metric

In addition to the peak spindle force and peak chassis acceleration metrics, ride comfort response is also related to the complete time/history response of the chassis. Therefore, an objective means for comparing the shapes of the chassis acceleration curves was also desired.

The chassis frequency response is relatively slow (approximately 1.16 Hz) relative to the frequency associated with the forces developed by the tire/obstacle interaction. At eight kilometers per hour these frequencies are approximately 12.4 Hz for the cleat obstacle and 4.8 Hz for the parking bump, and they increase linearly with speed. Consequently, in many cases, it may be assumed that the tire forces can be considered as shock loads, or impulses, to the integrated system. It was therefore postulated that the vertical ride comfort could potentially be correlated to the impulse generated by the tire model as it encountered the obstacle..

The impulse applied to the chassis is the suspension force  $F(t)$  acting on the chassis over a given time period. Defining the time period:

- beginning just prior to the tire engaging the obstacle as  $t = 0^-$ , and
- ending just after the tire disengages from the obstacle as  $t = 0^+$

the impulse to the chassis can be expressed as:

$$J_{chassis} = \int_{t=0^-}^{t=0^+} F_{suspension}(t) dt \quad (6.1)$$

As the chassis mass is known, the principle of impulse-momentum can be applied to find the change in chassis vertical velocity due to impulse  $J_{chassis}$  as follows:

$$J_{chassis} = m_{chassis} \Delta \dot{z}_{chassis} = m_{chassis} (\dot{z}_{final} - \dot{z}_{initial}) \quad (6.2)$$

As the initial vertical chassis velocity is zero prior to the tire engaging the obstacle, equations 5.1 and 5.2 can be combined to yield:

$$\int_{t=0^-}^{t=0^+} F_{suspension}(t) dt = m_{chassis} (\dot{z}_{final}) \quad (6.3)$$

Equation 5.3 implies that the integrated time history of the suspension force on the chassis as a result of the tire spindle forces encountering the obstacle can be used to determine the chassis vertical velocity at the end of the impulse:

$$\dot{z}_{final} = \frac{\int_{t=0^-}^{t=0^+} F_{suspension}(t) dt}{m_{chassis}} \quad (6.4)$$

Assuming that the chassis was in equilibrium prior to the tire encountering the obstacle, the response of the chassis immediately following the impulse will depend solely upon the state of the chassis at time  $t = 0^+$ , starting with the initial conditions:

$$z_{chassis}(0) = z_{final}(t = 0^+) = 0,$$

$$\dot{z}_{chassis}(0) = \dot{z}_{final}(t = 0^+)$$

A similar argument may be made regarding the model response to the horizontal force,  $F_x$ . Consequently, impulse appears to be a key metric that could be used to assess the fidelity of the tire model.

An attempt was made to determine the fidelity of the tire models using an impulse metric as outlined above. However, this proved to be quite challenging as:

- The total longitudinal impulse was quite small – the time integral for the chassis forces (which are the same as the tire spindle forces) as a result of the tire model traversing the cleat obstacle:
  - was close to zero, and
  - varied according to the assumed rolling resistance value for the FTire reference model

As the impulse of the reference model was small and the impulse values of the other tire models were large, the resulting normalized longitudinal chassis metrics:

$$\text{Normalized Longitudinal Chassis Metric} = \frac{J_{Model}}{J_{FTire}} \quad (6.5)$$

were large, varied greatly, and were not particularly meaningful for comparison purposes.

- As the FTire “reference standard” took into account tire contact patch distortion and cleat geometry internal to the model, the ending time of the cleat impulse could not readily be determined as the cleat disengagement was hidden by the force oscillations. As a result, the exact impulse imposed by the cleat could not be determined.
- The initial longitudinal velocity for each simulation was eight kilometers per hour. However, the time period over which the impulse was calculated was different for each of the different tire models because:

- the geometry for the interaction between the tires was different for the various tire models
- the longitudinal position of the quarter vehicle model was unconstrained

As a result, use of the impulse metric did not prove satisfactory and is left as an area to be further explored in future work.

### Ride Phase Objective Metric Analysis

As with the Cleat Phase of the investigation, a summary of the objective criteria for the Ride Phase was needed to evaluate the overall performance of the tire models.

This was accomplished in a tabular manner similar to the Cleat Phase investigation, but substituting in turn each of two sets of objective metrics:

- peak chassis accelerations, and
- peak spindle forces

for each of two obstacles:

- the sinusoidal cleat, and
- the parking bump.

As the peak chassis acceleration metrics are primarily used for ride comfort and the peak spindle forces are primarily used for suspension durability, the data was grouped by metric. Accordingly, the results for the peak chassis accelerations for both the cleat and bump obstacle are summarized in Table 6.1 - the results for the peak spindle forces are summarized later in Table 6.2.

Table 6.1 Ride Phase Tire Model Ranking via Chassis Acceleration Metrics

<b>Chassis Peak Acceleration Metrics</b>						
<b>Tire Model</b>	<b>Chassis Peak Az % Error</b>	<b>Chassis Peak Ax % Error</b>	<b>Sum % Error</b>	<b>Ranking</b>		
				<b>Peak Az</b>	<b>Peak Ax</b>	<b>Overall</b>
<b>Cleat Obstacle (obstacle wavelength less than tire contact patch length)</b>						
Cosin FTire	0	0	N/A	N/A	N/A	N/A
Point Contact	147	854	1001	5	6	6
Ring Contact	172	318	490	6	5	5
Constant Footprint	66	99	165	4	4	4
Adaptive Footprint	20	64	84	2	3	2
Two Point Rigid Ring	13	38	51	1	1	1
Five Point Rigid Ring	52	39	91	3	2	3
<b>Parking Bump Obstacle (obstacle wavelength greater than contact patch length)</b>						
Cosin FTire	0	0	N/A	N/A	N/A	N/A
Point Contact	113	136	249	5	5	6
Ring Contact	98	108	206	4	4	4
Constant Footprint	27	210	237	2	6	5
Adaptive Footprint	129	45	174	6	3	3
Two Point Rigid Ring	27	26	53	1	1	1
Five Point Rigid Ring	77	39	116	3	2	2

Examination of the chassis acceleration metrics provides an overall picture of the tire model performance for chassis ride comfort while traversing both short and long wavelength obstacles. Some of the general conclusions include:

- The point contact and the ring contact models perform merely adequately for chassis peak acceleration metrics while traversing obstacles with long wavelengths. Error associated with the ring contact model, however, is better than the point contact model.
- The ring contact model improves the peak longitudinal chassis acceleration metric with minimum added modeling complexity. The ring model performs better than the point contact model due to its ability to emulate obstacle wavelength filtering – this is especially important with short wavelength obstacles. The ring model should be used instead of the point contact model for most instances and should be strongly considered when the study includes obstacles of short wavelength.
- The two point rigid ring model provides the highest performance in comparison to the FTire standard. The additional complexity of the five point rigid ring model does not appear to be warranted.
- The adaptive footprint model ranks second for short wavelength obstacles and appears to be a reasonable performance and cost compromise as long as tire braking and driving forces are not required.
- As the adaptive footprint and the two rigid ring models:
  1. provide means to emulate both wavelength filtering and obstacle envelopment, and
  2. develop longitudinal force without depending upon the resolution of the horizontal and vertical forces such that the resultant forces are always normal to the obstacle surface,

they appear to offer the best performance for a variety of obstacles if the FTire model is not available for use.

In order to determine a ranking of tire models for simulating peak wheel spindle forces for determining suspension “road loads”, Table 6.2 was created.



Table 6.2 Ride Phase Tire Model Ranking via Wheel Spindle Force Metrics

<b>Wheel Peak Spindle Force Metrics</b>						
<b>Tire Model</b>	<b>Chassis Peak Fz % Error</b>	<b>Chassis Peak Fx % Error</b>	<b>Sum % Error</b>	<b>Ranking</b>		
				<b>Peak Fz</b>	<b>Peak Fx</b>	<b>Overall</b>
<b>Cleat Obstacle (obstacle wavelength less than tire contact patch length)</b>						
Cosin FTire	0	0	N/A	N/A	N/A	N/A
Point Contact	259	834	1093	6	6	6
Ring Contact	173	309	482	5	5	5
Constant Footprint	62	99	161	3	4	3
Adaptive Footprint	6	65	71	1	3	2
Two Point Rigid Ring	158	36	194	4	1	4
Five Point Rigid Ring	12	38	50	2	2	1
<b>Parking Bump Obstacle (obstacle wavelength greater than contact patch length)</b>						
Cosin FTire	0	0	N/A	N/A	N/A	N/A
Point Contact	106	131	237	5	5	6
Ring Contact	92	104	196	4	4	4
Constant Footprint	17	203	220	1	6	5
Adaptive Footprint	114	42	156	6	3	3
Two Point Rigid Ring	36	24	60	2	1	1
Five Point Rigid Ring	81	37	118	3	2	2

In general, the spindle force metrics correlate well to the chassis acceleration metrics. It is clear from examination of the chassis acceleration and spindle force curves, comparison of the normalized metrics, and ranking of the results by percent error that:




- The intended use of the integrated tire/vehicle simulation model will dictate the suitability of the tire model.
- Simulations which require modeling of short wavelength obstacles are more demanding of the tire model than those simulations which model long wavelength obstacles. This is because obstacles whose wavelengths are shorter than the tire contact patch length solicit the tire's ability to:
  1. filter the obstacle wavelength
  2. envelope the obstacle within the contact patch

The most elementary models are not capable of emulating these tire characteristics and therefore should only be used for simulations which include long-wavelength obstacles.

For comparison purposes, Table 6.3 is a summary of tire model performance ranking for all of the metric/obstacle combinations investigated.

Table 6.3 Ride Phase Tire Model Ranking Overview

Tire Model	Cleat Obstacle				Parking Bump Obstacle			
	Accel Peak Az	Accel Peak Ax	Force Peak Fz	Force Peak Fx	Accel Peak Az	Accel Peak Ax	Force Peak Fz	Force Peak Fx
Cosin FTire	N/A	N/A	N/A	N/A	N/A	N/A	N/A	N/A
Point Contact	5	6	6	6	5	5	5	5
Ring Contact	6	5	5	5	4	4	4	4
Constant Footprint	4	4	3	4	2	6	1	6
Adaptive Footprint	2	3	1	3	6	3	6	3
Two Point Rigid Ring	1	1	4	1	1	1	2	1
Five Point Rigid Ring	3	2	2	2	3	2	3	2

Key:		1st or 2nd ranking
		3rd ranking
		4th ranking
		5th or 6th ranking

With the exception of the two point rigid ring model simulating peak spindle force Fz while traversing a cleat obstacle, the two point rigid ring model appears to perform best and remains robust for all simulation metrics. The five point rigid ring model also performs well, consistently ranking second or third.

The adaptive footprint model ranks both first and second for the cleat obstacle, but does not perform as well for the vertical metrics over the large parking bump. The constant footprint also does not appear to be sufficiently robust, and ranks slightly lower than the adaptive footprint model.

Finally, the point contact and ring contact models ranked the lowest. These models were not expected to perform well, as neither of them emulate the obstacle

envelopment characteristics of a tire. The obstacle wavelength filtering provided by the ring contact model does allow it to place ahead of the point contact model. The point and the ring contact models, while useful for simple ride comfort modeling, should only be used judiciously and with long wavelength obstacles. The ring contact model should be used in place of the point contact model whenever possible.

### Tire Model Selection

The tire models that were developed in this thesis can be applied to study the sensitivity of commonly-measured tire characteristics on simulated tire-spindle forces. However, the tensile pneumatic structure which makes up a modern automotive tire does not lend itself easily to lumped parameter modeling, as linear springs and dampers do not emulate well the physics of the radial carcass plies and the tire summit. When using lumped-parameter tire models, care is required to consider not only the operating condition of the tire that is being modeled, but also the size and shape of the obstacle relative to the contact patch size, tire section height, etc. Simple tire models can provide reasonable inputs for integrated tire/vehicle comfort modeling as long as the tire model is carefully considered and judiciously applied. In scenarios where tire frequency response of less than 50 Hz is adequate – often the case, since vehicle ride models act as low pass filters - these simple tire models may be adequate while being significantly less costly in terms of software licenses, testing to obtain tire model parameters, and computational requirements. Appropriate statistical commercial tire models, or other physical models such as Cosin FTire or TNO MF SWIFT tire model incorporated into SIMPACK Automotive Plus or other MBS software may be more costly, but their robustness – applicability and accuracy over a wide operating range of circumstances - may warrant their additional cost.

One advantage of the two point and five point rigid ring models developed in this investigation may lie in their ability to provide a reasonable compromise in model complexity and fidelity for 2D comfort modeling between full FEA or MBS tire models

and the simpler footprint models that were implemented in this investigation. A higher intrinsic value of the two point and five point rigid ring tire models is that they are capable of developing driving and braking forces at the contact patch from driving and braking moments at the wheel center. This capability is beyond the simple footprint models, but is less costly to implement than Cosin FTire. For example, these rigid ring models may be capable of supporting tire/vehicle drive line or braking vibration sensitivity studies for tire design characteristics such as such as tread circumferential compliance, sidewall damping, and traction parameters within the contact patch or tread circumferential compliance.

### Recommendations for Future Work

This investigation illustrates that the functionality of the tire can be encapsulated into three distinct areas:

1. transformation of roadway obstacles into contact patch deformations – the input amplitudes of short wavelength obstacles are attenuated and their effective wavelengths are increased.
2. transformation of contact patch deformations into spindle forces by the tire's tensile pneumatic carcass structure
3. generation of friction forces at the interface between the tire and the ground surface

When analyzing the use of a model, all three of these functions must be considered.

Future work could include isolating the model functional characteristics and attempting to better match them to their intended applications. For example, the rigid ring model provides internal tire dynamics, but its use of a two point or five point contact patch follower to emulate the tire contact patch may hinder it for some applications.

Functionally, it may be possible and advantageous to use the contact patch model concept from the adaptive footprint model instead of the two point or five pint follower, while retaining the rigid ring for the tire summit and sidewall dynamics.

Additional areas for future work include the following:

- Tire modeling in this investigation was limited to relatively low speeds (eight kilometers per hour). The ability of the tire models to deliver

sufficient fidelity when encountering different obstacle geometry at different speeds should be investigated.

- The height of the obstacle causes the tire to engage the obstacle in front of the contact patch, and to stay engaged after exiting the contact patch. Although the overall effect on chassis acceleration was assumed to be small and constant across the tire models that were developed for this investigation, including this geometry would improve agreement between the MatLab Simulink models and FTire in future work.
- The vehicle model can be upgraded to include two axles (pitch plane model) and longitudinal compliance. Both of these modifications will affect the chassis acceleration metrics.
- On-vehicle testing to verify the performance of the integrated tire/suspension/chassis system model.



## APPENDICES

## Appendix A

### A. Single Point Follower Simulink Model

#### Description

For developing first-order vehicle dynamics models, several approaches at tire modeling have been undertaken that have proven adequate for gaining insight into vehicle dynamic behavior, especially at steady-state or low solicitation frequencies and amplitude (close to the linear region of the systems, where the responses of simplified tire and vehicle models can be mathematically superimposed). For two dimensional vertical ride comfort modeling, a single point follower, or point contact model, can adequately represent the spring stiffness of the tire during encounters with common vertical obstacles of low amplitude and low frequency content, such as sinusoidal parking lot speed bumps or roadway depression irregularities (“potholes”). This type of tire model proves to be adequate because the force transfer function of the tire is relatively simple in this regime, and the principal component contributing to the chassis dynamics being studied is the suspension, and not the tire. The point follower model is the easiest model to implement, but can only adequately represents the transfer of spectral energy into the chassis at low frequencies (i.e., well below the 1<sup>st</sup> vertical modal modes of the tire, approximately 80 Hz for typical passenger car tires). The physical representation of the single point contact follower model is illustrated in figure A.1, below:

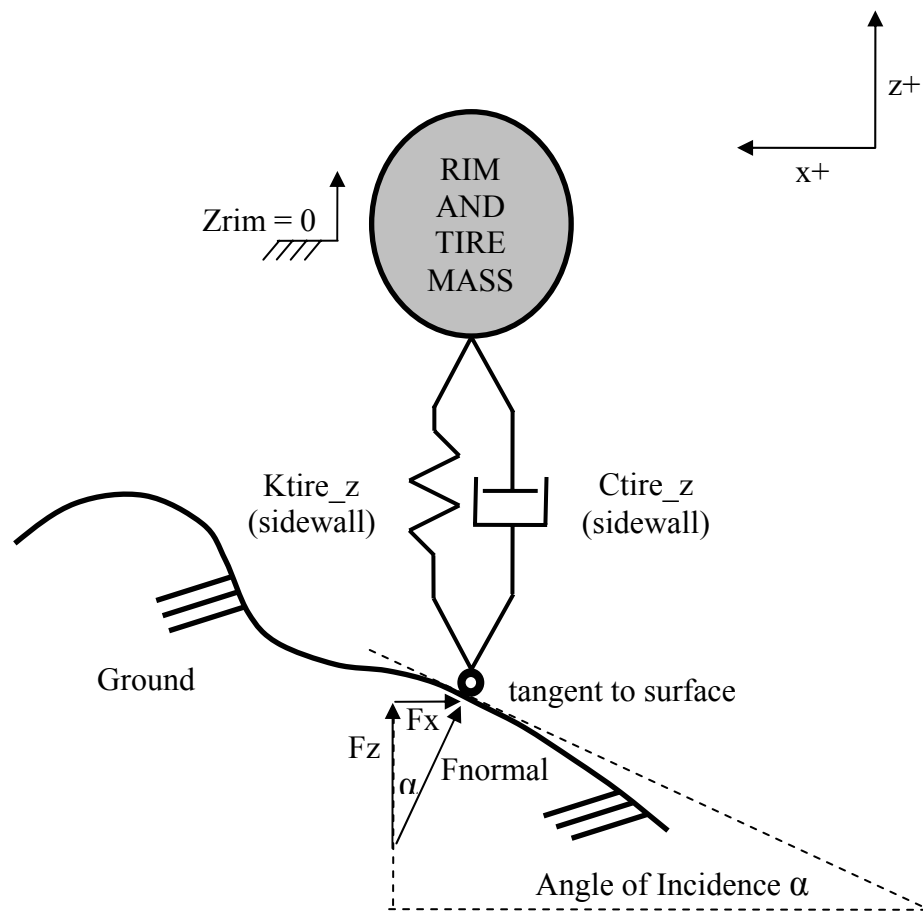


Figure A.1: Single Point Contact Follower for Integrated Tire/Vehicle Modeling

#### Single Spring and Point Follower with Mass at Wheel Center

The development of a single contact point follower model for two dimensional ride comfort – vertical and longitudinal - requires the following significant assumptions:

- The vertical profile (contour) of the roadway and obstacle is transmitted instantaneously to the point follower via a point contact that is directly below the center of the tire.

- Tire forces are in compression only – the tire contact force goes to zero when the tire extends to its natural uncompressed length and does not go negative (the tire is not pulled towards the ground in extension, it merely leaves the ground)
- The tire mass can be represented by an equivalent single lumped mass
- A single point contact and vertical tire spring can only transmit forces in the vertical direction

The equations of motion for the simple point follower shown in Figure A.1 are derived using Newton's method – defining a set of coordinates, drawing an appropriate free body diagram for each of the masses and then solving for the equations of motion directly. Since all of the unsprung mass – the tire, rim, brake hardware, and suspension system – is represented by a single lumped mass, and the contact point following the roadway is without mass, the free body diagram in this most elementary embodiment of a tire model for the vertical coordinate  $Z$  is simply:

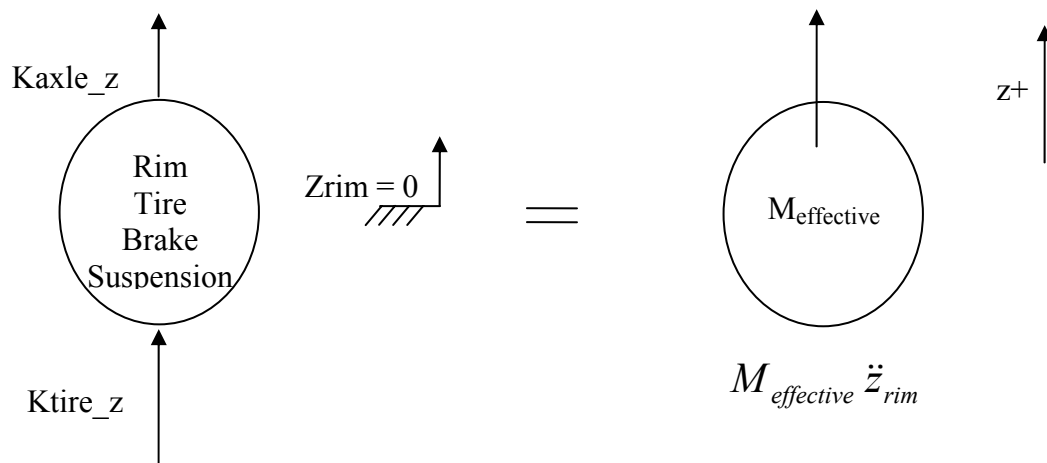


Figure A.2: Free Body Diagram (FBD) of Single Point Contact Follower

Writing the forces in the z direction positive upwards and neglecting the damping term for clarity (as it is easily added by substituting velocities for displacement terms and damping rates for spring rates) yields:

$$-k_{axle\_z}(z_{rim} - z_{car}) - k_{tire\_z}(z_{rim} - z_{contact}) = M_{effective}\ddot{z}_{rim} \quad (A.1)$$

Solving for the rim vertical acceleration term:

$$\ddot{z}_{rim} = -\frac{k_{axle\_z}}{M_{effective}}(z_{rim} - z_{car}) - \frac{k_{tire\_z}}{M_{effective}}(z_{rim} - z_{contact}) \quad (A.2)$$

Adding the damping term for the tire sidewall damping ( $C_{tire\_z}$ ) and the vertical vehicle suspension damping ( $C_{suspension}$ ), and gathering terms yields the final equation for the vertical component of the contact point follower model:

$$\ddot{z}_{rim} = -\frac{1}{M_{effective}} \left\{ \begin{array}{l} k_{axle\_z}(z_{rim} - z_{car}) - k_{tire\_z}(z_{rim} - z_{contact}) + \\ c_{axle\_z}(\dot{z}_{rim} - \dot{z}_{car}) - c_{tire\_z}(\dot{z}_{rim} - \dot{z}_{contact}) \end{array} \right\} \quad (A.3)$$

In order to develop a representative force in the horizontal direction, a constraint is added such that the total resultant force at the contact point is always normal to the surface of the road profile ( $F_{normal}$ ). If the slope, or angle of incidence  $\alpha$ , is known and the vertical force  $F_z$  is calculated, the longitudinal reaction force  $F_x$  and the total normal force  $F_{normal}$  can be calculated using simple trigonometry. Calculating  $F_x$ :

$$\text{Tangent } \alpha = \frac{\text{opposite}}{\text{adjacent}} = \frac{F_x}{F_z} \quad (A.4)$$

$$F_x = F_z \text{ Tan } \alpha \quad (A.5)$$

Calculating Fnormal:

$$\text{Cosine } \alpha = \frac{\textit{adjacent}}{\textit{hypotenuse}} = \frac{F_Z}{F_{NORMAL}} \quad (\text{A.6})$$

$$F_{NORMAL} = \frac{F_Z}{\cos \alpha} \quad (\text{A.7})$$

The value for  $F_x$  is necessary to calculate the longitudinal acceleration of the tire mass and vehicle body, and  $F_{normal}$  is required as one input to calculate tire traction forces.

The assumption that the resultant force is always normal to the point of contact is valid for most terrains where the wavelength of the undulating roadway surface is large compared to the length of the tire contact patch and the frequency of the vertical input is small compared to the natural vertical frequency of the tire. As the obstacle wavelength becomes shorter, the surface normal resultant force becomes more horizontal and the required horizontal component for the total force to remain normal becomes excessive as the relationship is proportional to the tangent of the angle of incidence,  $\alpha$ . Note that this excessive horizontal force is mitigated when the surface input is better physically represented by the length of the tire footprint – the contact patch – as opposed to the simple single point follower model.

### Two Spring and Point Follower with Effective Summit Mass

For comparing tire models using fixed spindle height data, the simple point follower model depicted above needs to be modified as the tire mass lump cannot be accounted for in the rim - there is no degree of vertical freedom afforded by a car body sprung mass or vehicle suspension. Therefore a single point follower for fixed spindle height testing was developed that could both emulate the fixed spindle height test and also use the measured tire parameters obtained from the polyvalent machine testing and physical mass measurements. For this model, the tire mass associated with the tire bead was removed from the total tire mass, as was one-half of the mass associated with the tire sidewalls. The remaining sidewall mass, steel summit area and tread were used to represent the bulk mass of the tire summit, as these components would be free to translate in the vertical direction. In addition, the tire mass would be bounded underneath by the vertical spring rate of the tread blocks ( $K_{tread\_vr}$ ) and between the top and the rim by the combined tire pneumatic and structural spring rate  $K_{tire\_z}$ . The same constraint which required the resultant tire force to be normal to the contact surface is applied for the generation of  $F_x$ . This modified single point follower model is depicted in figure A.3, below:

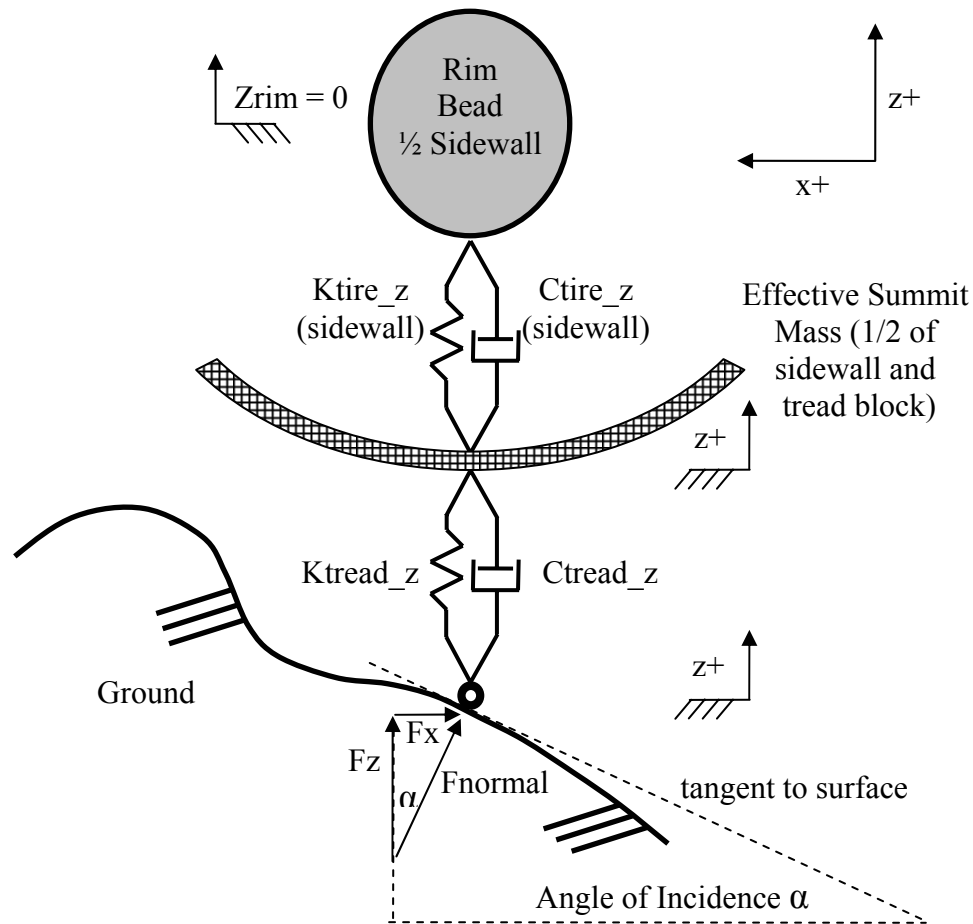


Figure A.3: Two Spring Point Follower Model for Fixed Spindle Simulation

The development of the two spring version of the point follower model for fixed spindle machine testing simulation requires the same assumptions as the single mass point follower model described above, with the following additions:

- The tire, rim suspension and sidewall effective point mass does not include the entire mass of the sidewall. One half of the sidewall mass is attributed to the rim mass, and one half of the mass is attributed to the rigid ring belt/summit mass.



- The amount of mass in the tread that is attributed to the belt/summit mass is constant and can be approximated using the fraction of the tread mass in the static contact patch under nominal tire load
- The vertical tread block stiffness, although normally affected by shear and torsion between adjacent tread blocks attached to the summit belt package and bending in the summit, is constant and adequately represented by a single bulk vertical tread stiffness.

The equations of motion for the two spring point follower model shown in Figure A.3 are derived in the same manner as the simple point follower. For vehicle vertical ride comfort simulations, the model has two vertical degrees of freedom – one for each of the rim and summit masses. For laboratory road wheel cleat strike simulations, the rim vertical displacement is fixed and the model contains only one vertical degree of freedom. For vehicle vertical ride comfort simulations, the equations of motion are derived by first developing the free body diagram, as shown in Figure A.4, below:

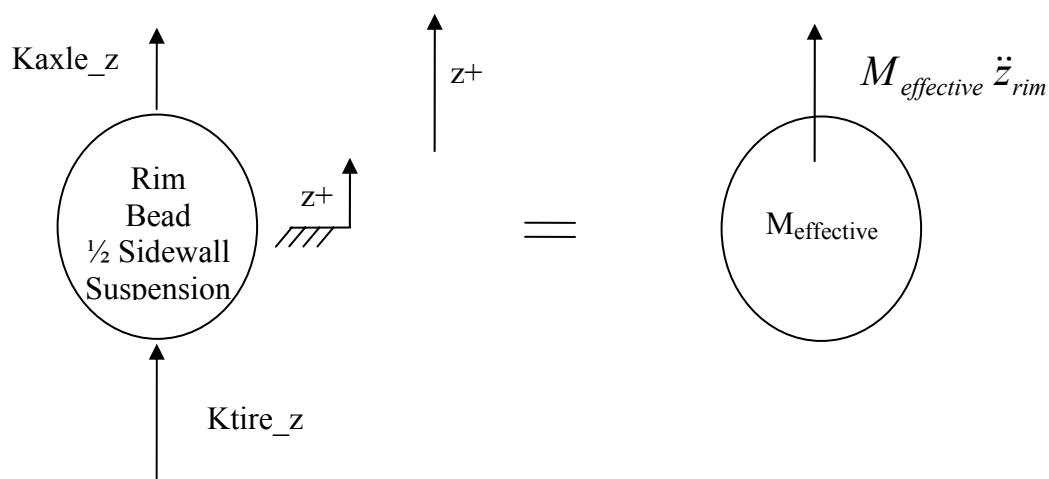


Figure A.4: Free Body Diagram (FBD) of Two Spring Model Rim Mass

Writing the forces in the z direction positive upwards, temporarily neglecting the damping term for clarity, and using a slightly modified effective mass due to the redistribution of the sidewall mass yields the identical equation as for the single mass point follower:

$$-k_{axle\_z}(z_{rim} - z_{car}) - k_{tire\_z}(z_{rim} - z_{summit}) = M_{effective}\ddot{z}_{rim} \quad (A.8)$$

Adding the damping terms and solving for the rim vertical acceleration yields the final equation for the rim vertical component of the two spring two mass point follower:

$$\ddot{z}_{rim} = -\frac{1}{M_{effective}} \left\{ k_{axle\_z}(z_{rim} - z_{car}) - k_{tire\_z}(z_{rim} - z_{summit}) + \right. \\ \left. c_{axle\_z}(\dot{z}_{rim} - \dot{z}_{car}) - c_{tire\_z}(\dot{z}_{rim} - \dot{z}_{summit}) \right\} \quad (A.9)$$

Drawing the free body diagram in preparation for solving the vertical equations of motion for the summit mass:

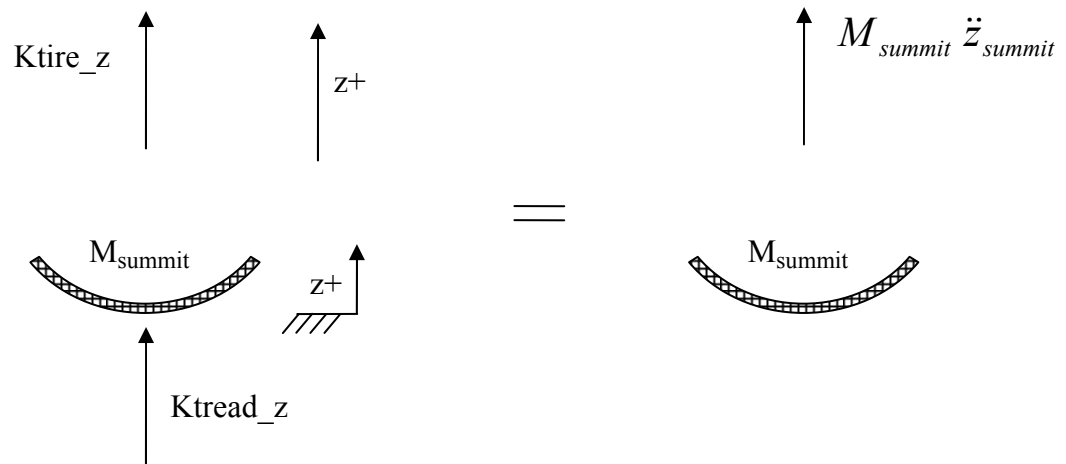


Figure A.5: Free Body Diagram (FBD) of Two Spring Model Rim Mass

Writing the forces in the z direction positive upwards and neglecting the damping term for clarity yields:

$$-k_{tire\_z}(z_{summit} - z_{rim}) - k_{tread\_z}(z_{summit} - z_{contact}) = M_{summit} \ddot{z}_{summit} \quad (A.10)$$

Solving for the summit vertical acceleration term:

$$\ddot{z}_{summit} = -\frac{k_{tire\_z}}{M_{summit}}(z_{summit} - z_{rim}) - \frac{k_{tread\_z}}{M_{summit}}(z_{summit} - z_{contact}) \quad (A.11)$$

Adding the damping term for the tire sidewall vertical damping ( $C_{tire\_z}$ ), the tread element vertical damping ( $C_{tread\_z}$ ), and the vehicle suspension vertical damping ( $C_{suspension}$ ) yields the following equation of motion for the summit package:

$$\ddot{z}_{summit} = -\frac{1}{M_{summit}} \left\{ k_{tire\_z}(z_{summit} - z_{rim}) - k_{tread\_z}(z_{summit} - z_{contact}) + \right. \\ \left. c_{tire\_z}(\dot{z}_{summit} - \dot{z}_{rim}) - c_{tread\_z}(\dot{z}_{summit} - \dot{z}_{contact}) \right\} \quad (A.12)$$

Equations A.9 and Equations A.12 represent the EOMs for the two vertical degrees of freedom for the rim and summit masses, respectively. When simulating a cleat impact on a fixed spindle hub on a laboratory road wheel, only the latter equation is applicable.

## Appendix B

### B. Ring Follower Simulink Model

#### Description

The simple single point follower provides a convenient way to input a road profile into the tire model – the description of the vertical obstacle height as a function of longitudinal displacement is applied to the tire model directly. However, the input into the tire model does emulate the filtering effect which occurs in the contact patch. Obstacles whose wavelengths are shorter than the length of the contact patch are attenuated by the envelopment or “draping” of the contact patch around the obstacle, and the effective wavelength of the obstacle is increased and its effective amplitude is diminished.

The single point follower is still useful for ride comfort modeling because the car chassis and suspension act as low pass filters. Use of the point contact follower is generally considered adequate for road input frequencies of up to 20 or 30 Hz. Therefore, a means of attenuating the frequency of short wavelength obstacles is required. One method that has been used with success is to replace the point contact follower with a rigid ring. A discussion of tire contact patch envelopment will be followed by the development of the rigid ring.

Because of the nature of its structure, the tire’s interaction with obstacles is quite complex. In general, this is due to the tire’s requirement to deform upon vertical loading, creating a ‘contact patch’ between the tire and the ground. Since the structural contribution to the vertical stiffness of tires is generally small compared to that of the

pneumatic portion, many tire models are constructed such that the total area in the contact patch (the contact patch length times the contact patch width) times the inflation pressure of the tire equals the vertical loading of the tire, or:

$$F_{vertical} = P_{inflation} \times \textit{Contact Patch Length} \times \textit{Contact Patch Width} \quad (\text{B.1})$$

For our 2-D modeling, the contact patch length,  $2a$ , is simply proportional to the vertical load divided by the width of the tire in the contact patch. The static length of the contact patch, for many tire applications, is of the same order as the width of the tire, but can vary greatly depending upon the tire application. For example, wide contact patch widths having contact patch “footprints” with rectangular corners are typically associated with maximum lateral tire force generation for handling performance at the limit, whereas narrow contact patch widths having contact patch “footprints” with rounded corners are typically associated with ride comfort.

In the case of tire modeling for ride and comfort analysis, a single point follower may not sufficiently represent the tire/obstacle interaction that will occur as the tire contact patch traverses across the obstacle, particularly with obstacles whose wavelength is shorter than the length of the tire contact patch. This is because the tire contact patch will tend to engulf, or “drape” over the obstacle when the obstacle passes between the entrance and the exit of the contact patch. The bending characteristics of the tire tread band and the architecture in the tire summit will become important factors for how the obstacle wavelength and amplitude content are transmitted into the tire structure. Two obstacle cases are illustrated in Figure B.1, below:

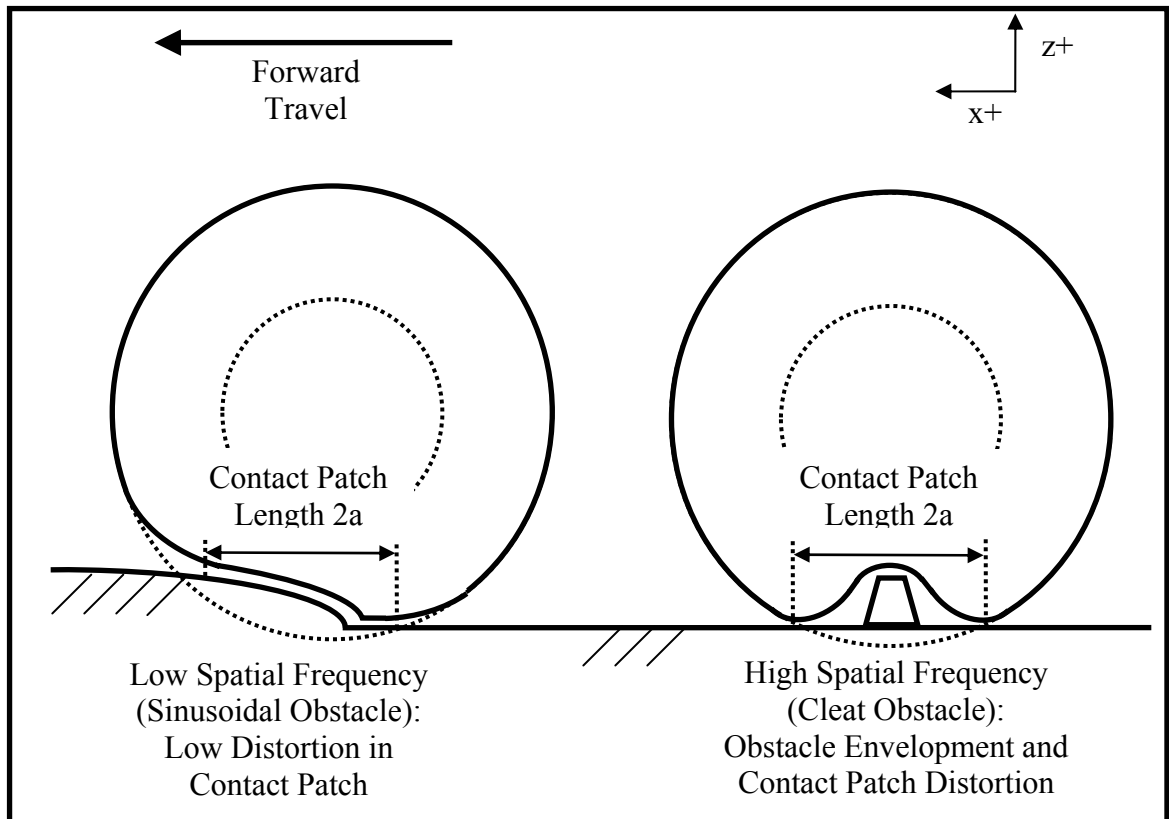


Figure B.1: Comparison of Contact Patch Shape vs. Obstacle Spatial Frequency

Because the contact patch and its compliance results in both:

1. a mitigating effect on the vertical input, as well as
2. a smoothing effect which filters the vertical frequency input

to the tire model, a means of applying these effects to the simple single point follower is needed. One simple means by which at least one of these effects can be emulated is by replacing the point follower with a fixed ring follower, or “roller wheel.” This physical manifestation of the tire contact patch and obstacle interaction does not model the physics of the compliance of the tire tread and summit structure in the contact patch, but does have the potential to produce vertical attenuation and obstacle filtering without the need

for introducing complex bending stiffness in the rigid ring tire model. A schematic of this rigid ring follower is illustrated in figure B.2, below:

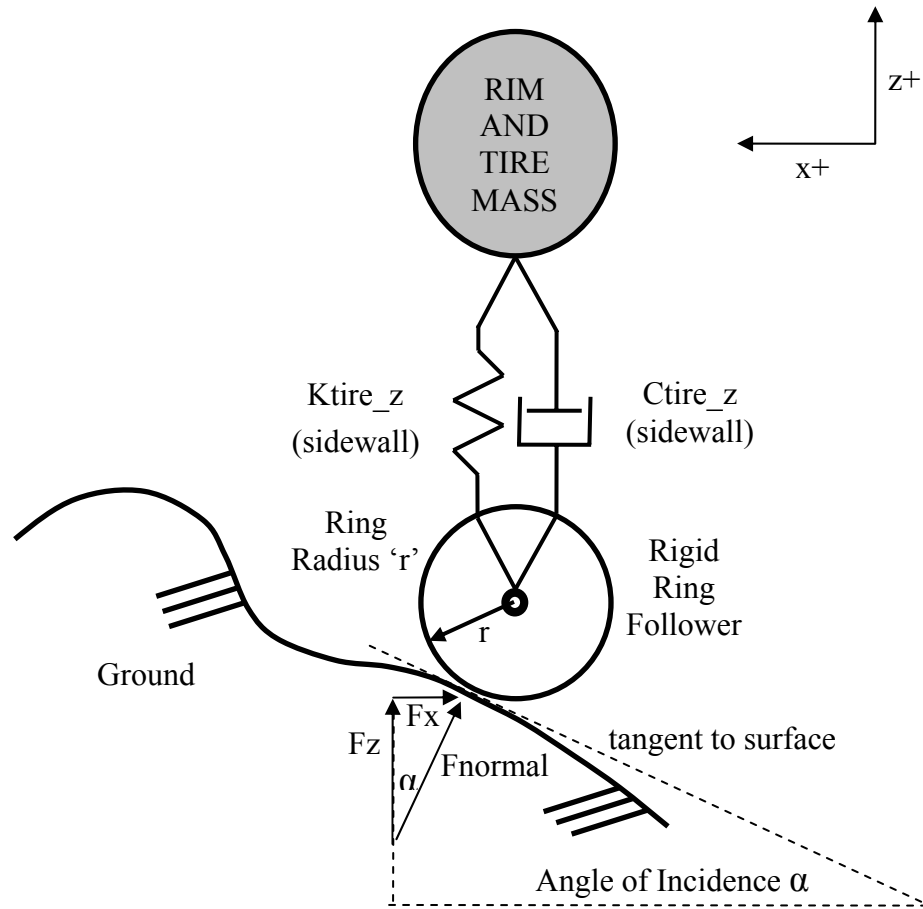


Figure B.2: Rigid Ring Contact Follower for Integrated Tire/Vehicle Modeling

The tire model remains essentially unchanged from the single point follower, but the characteristic of the input to the tire model changes in that:

- the obstacle is engaged sooner
- the obstacle is disengaged later

- the peak vertical input height is preserved for convex obstacles (bumps), but may be potentially attenuated for concave obstacles (potholes).

Note that the model in Figure B.2 is the simplest embodiment of the rigid ring follower. This simple embodiment is only applicable for integrated tire/vehicle modeling, as the mass of the tire and wheel assembly is assumed to be at the wheel spindle. Just as with the single point follower, the tire model will need to be modified in order to accommodate fixed spindle simulations, i.e., the tire mass needs to be repartitioned between the summit and the center of the wheel in order to account for some of the dynamic properties within the tire itself.



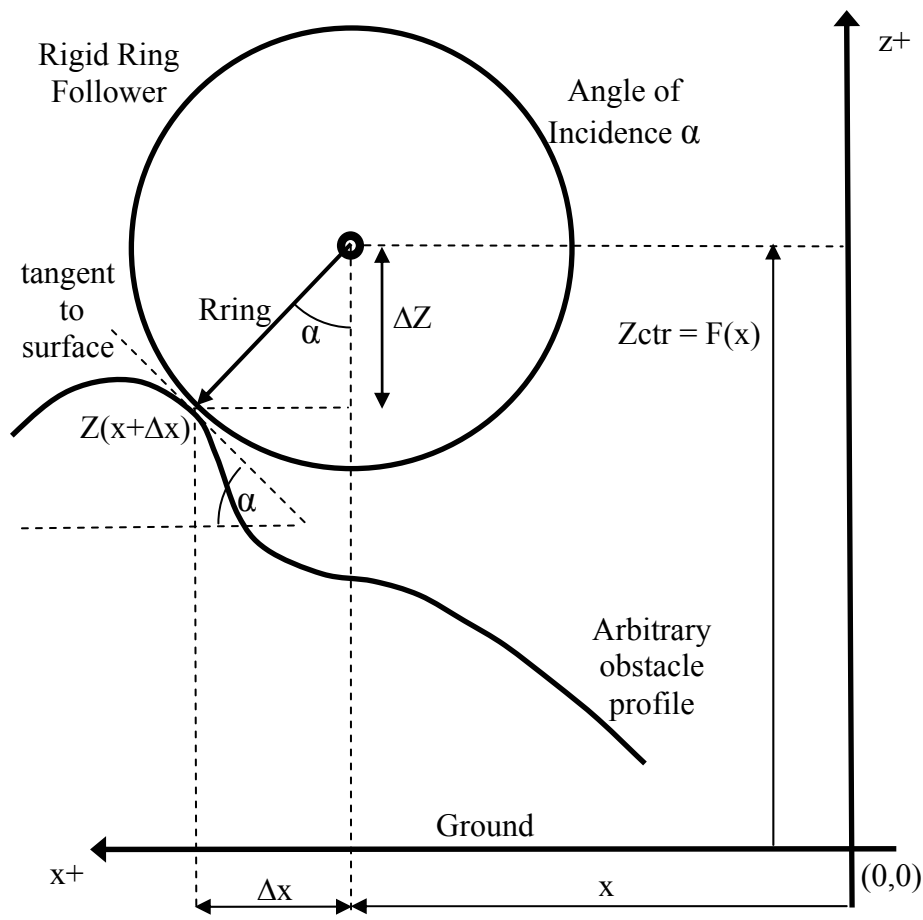


Figure B.3: Rigid Ring Contact Follower Geometry

In Figure B.3, above, the height of the obstacle above the horizontal ground plane is defined as a function of the longitudinal position along the ground,  $x$ . The tangent at the point of contact between the rigid ring follower and the obstacle surface is used to describes the the obstacle “engagement angle,” angle  $\alpha$ . Distance  $x$  is the longitudinal displacement of the center of the rigid ring follower. Distance  $\Delta x$  is the additional distance along the direction of positive  $x$  displacement due to the contour of the obstacle and the radius of the rigid ring follower, radius  $R_{ring}$ .

If the conditions are limited such that obstacle contact occurs on the lower half of the rigid ring (as when the tire model is situated above the obstacle), then contact can occur ahead of, directly underneath, or behind the longitudinal displacement of the rigid ring center. These conditions of admissible contact for an arbitrary obstacle are illustrated in Figure B.4. The rigid ring is effectively filtering the input to the tire model by not allowing the center of the ring to ‘drop’ into the obstacle whose characteristic wavelength is smaller than the rigid ring radius  $R_{ring}$ .

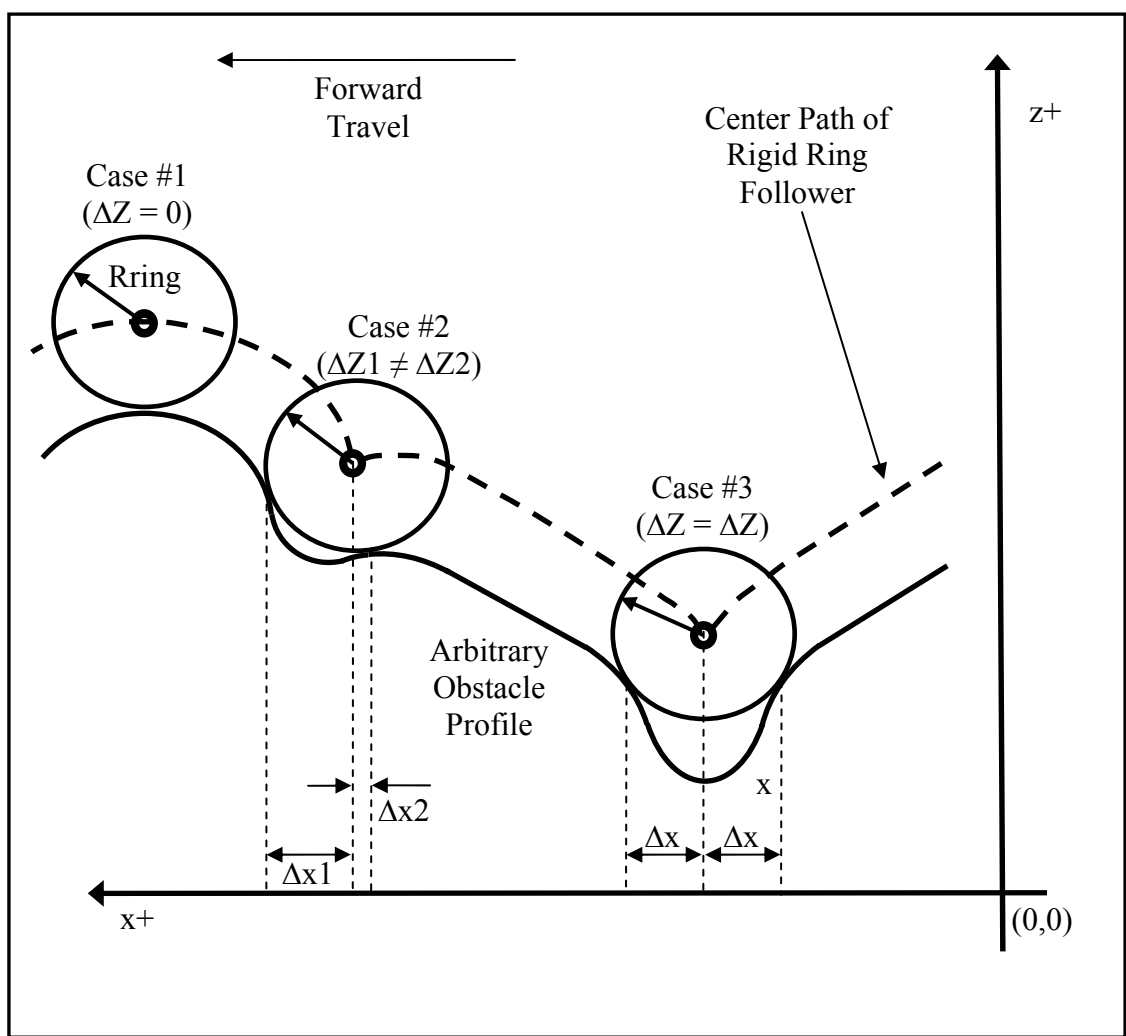


Figure B.4: Admissible Conditions of Simultaneous Contact – Resulting Path

Just as with the single point follower, there is no physical contact patch with the rigid ring follower through which a longitudinal force can be developed. Therefore, the same scheme that was used to develop a representative force in the horizontal direction for the single point follower model is used, i.e., a constraint is added such that the total resultant force at the contact point is always normal to the surface of the road profile ( $F_{normal}$ ). This technique is described in detail for the single point follower in Appendix A.

Adapting the rigid ring follower model in MatLab Simulink can be done in a variety of manners. The method that was chosen is to describe the complete lower half circumference of the rigid ring centered about each  $x$  point on the original obstacle profile, and use the surface contact constraint to determine which point on the rigid ring will describe the highest point of obstacle. This generates the  $Z$  height of the modified obstacle profile. The logic is relatively straightforward to implement and will work for the general case where there are obstacles both above the reference ground plane ('bumps') and below ('potholes').

### Ring Follower Obstacle Filtering

The characteristic consequences of vertical obstacle filtering using the rigid ring model are not necessarily always intuitive and can perhaps best be communicated by examining some specific examples using simple sinusoidal obstacles. For well-behaved sinusoidal obstacles that are above the reference ground plane ('bumps'), several generalities will always apply:

- The peak vertical displacement of the obstacle will always pass unattenuated into the tire model.
- The effective length of the obstacle (from the point of engagement as the follower meets the obstacle to the point of disengagement when the follower no longer interacts with the obstacle) will always be
  1. equal to or longer than the physical length of the obstacle and
  2. less than the length of the physical obstacle plus twice the radius of the rigid ring follower.

This results in the effective obstacle spatial frequency always being either equal to or lower than the spatial frequency of the obstacle.

These two effects result in an effective obstacle whose:

- peak amplitude is always equal, and
- spatial frequency is always either equal or lower

than that of the original obstacle 'bump'. These effects can be visualized as illustrated in Figure B.5, below:

### Rigid Ring Obstacle (Bump) Filtering: $Z_{ctr} = F_{cn}(\text{Ring Radius})$

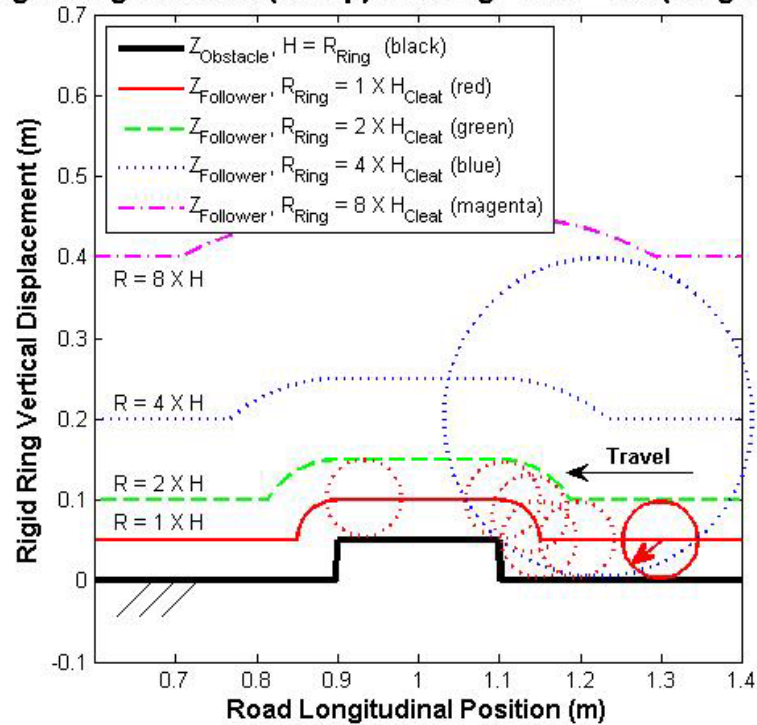


Figure B.5: Alteration of Obstacle Amplitude and Frequency by Rigid Ring Follower

Likewise, well-behaved obstacles that are depressed below the reference ground plane ('potholes') also follow several generalities:

- The peak vertical displacement of the depression will be attenuated in the case where the 1<sup>st</sup> harmonic wavelength of the depression is lower than twice the diameter of the rigid ring follower
- The effective length of the obstacle (from the point of engagement as the follower meets the obstacle to the point of disengagement when the

follower no longer interacts with the obstacle) will always be less than the physical length of the depression.

These two effects result in an effective obstacle whose:

- peak amplitude is always either equal to or lower, and
- spatial frequency is always either equal to or higher

than that of the original obstacle “pothole.” These effects can be visualized as illustrated in Figure B.6, below:

**Rigid Ring Depression (Pothole) Filtering:  $Z_{ctr} = Fcn(\text{Ring Radius})$**

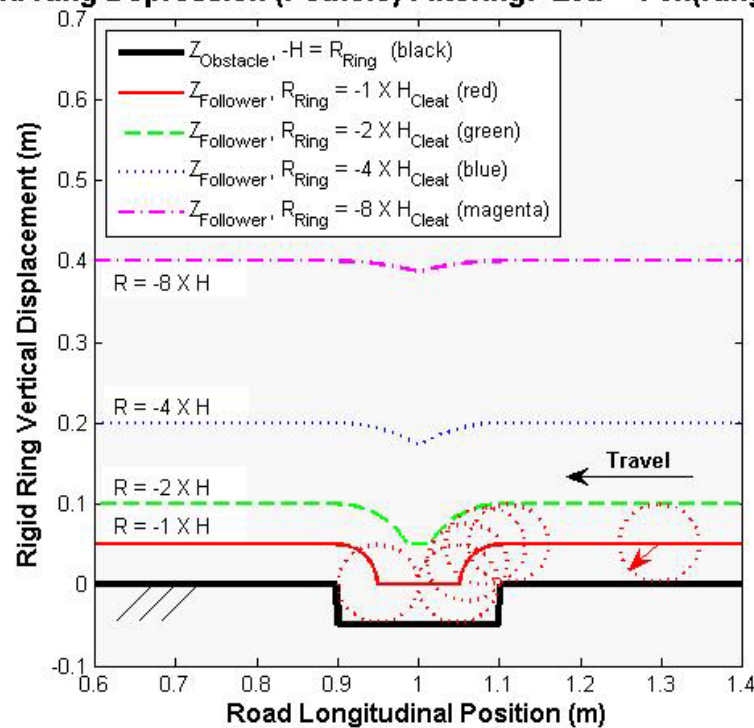


Figure B.6: Alteration of Pothole Amplitude and Frequency by Rigid Ring Follower

In order to validate the tire model with real-world data, a laboratory test was set up in which a road wheel drum was fitted with a cleat. The tire run over the cleat at fixed

spindle heights and speeds, and the vertical and horizontal spindle forces of the free-rolling tire were measured versus time. It was chosen to generate a sinusoidal obstacle model that was equivalent to the cleat. The reason for this model was twofold:

- the local deformation of the tread blocks as they encounter the rectangular cleat can better be approximated by a sinusoid rather than the step input represented by the cleat, and
- generation of an obstacle function with a continuous first order derivative should speed simulation time

The sinusoidal function that was chosen to represent the equivalent input of the rectangular cleat was chosen such that:

- the peak height of the sinusoidal representation is equal to the height of the cleat,
- the cross sectional area of the cleat was equivalent to the cross sectional area of the sinusoidal representation
- the first order derivative of the obstacle height is continuous

The results of the vertical displacement input for the tire model, using the transformation of the original 9.5 mm high by 19 mm long cleat into a sinusoidal equivalent and filtered by rigid ring follower or varying radii, are shown in Figure B.7, below:

### Rigid Ring Follower Trajectories Over Sinusoidal Laboratory Road Wheel Cleat

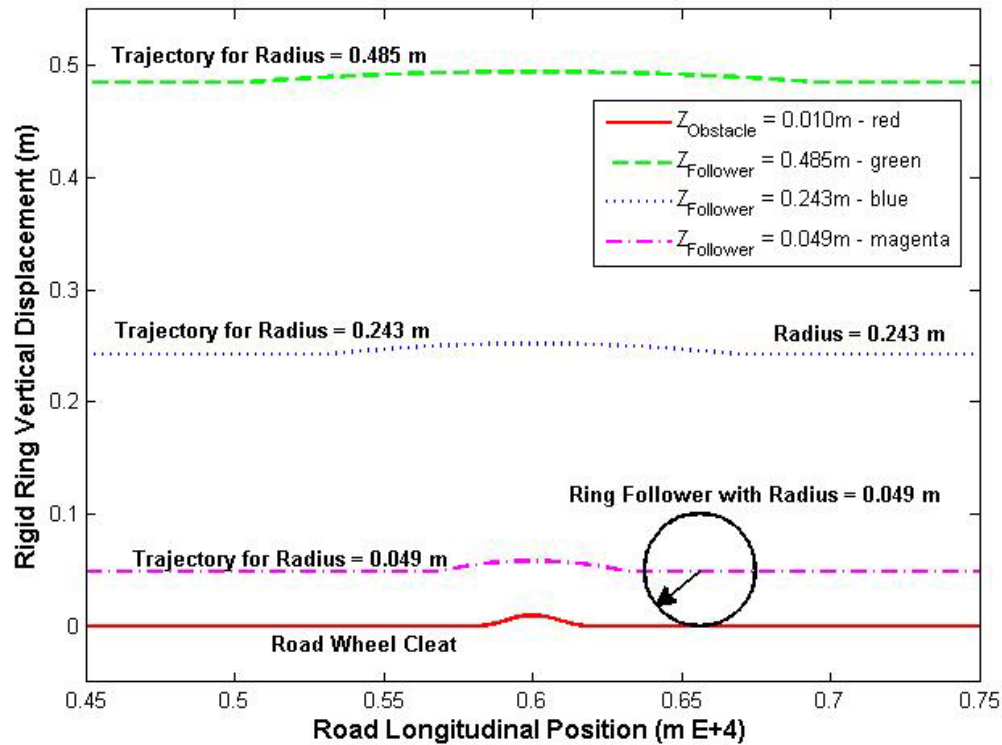


Figure B.7: Rigid Ring Follower Filtering for the Machine Test Cleat Equivalent

In the end, a rigid ring follower that encounters a general obstacle containing both concave-up ‘bump’ and concave-down ‘depression’ elements can introduce a complex shift in both frequency content and amplitude over the original obstacle signature. Because the flexible carcass of a rolling tire deforms considerably when carrying a load and forms a longitudinal contact patch, it principally attenuates those obstacles whose spatial frequencies are below the mode shapes of the tire, even when rolling quasi-statically over the obstacle. Hence, the lack of vertical attenuation of the rigid ring follower for obstacle bumps is an inherent weakness for short obstacles, but the lowering of the frequency is a strength. Conversely, the increase of obstacle frequency of the rigid



ring follower for an obstacle pothole is an inherent weakness, but the attenuation of the vertical amplitude is a strength. Thus the rigid ring follower can be considered an improvement over a point follower if its characteristics and the nature of the obstacle are carefully considered, but the rigid ring model will ultimately always be limited for ride modeling and provide only marginal improvements over a point follower.

## Appendix C

### C. Constant Footprint Simulink Model

As was demonstrated in Appendix A, a model of the tire/obstacle interaction within the contact patch as the tire traverses an obstacle can improve simulations for tire/vehicle ride and comfort analysis. This is necessary as the interactions within the contact patch, such as the envelopment or ‘draping’ of the tread blocks around the obstacle edges, filter the frequency and the magnitude of the obstacle vertical displacement before it is passed from the obstacle into the model system. The use of a rigid ring follower in the place of a simple contact point follower, for example, effectively filters the vertical frequency content of the obstacle, which in turn improves the tire model fidelity for comfort. This is accomplished with the use of a rigid ring follower because the rigid ring follower, as developed in Appendix B, increases the engagement distance between the obstacle and the tire for obstacles with positive height (‘bump’) by distances of up to twice the radius of the rigid ring, and maintains the engagement distance for obstacles with negative height (‘potholes’). However, the rigid ring model is limited in its ability to duplicate the effect of vertical compliance within the contact patch (and the resulting obstacle envelopment) as it is unable to mitigate the magnitude of the obstacle height for positive height obstacles. This is because the rigid ring must pass over the peak of the obstacle without any benefit of compliance in exactly the same manner as a simple point follower. Therefore it also passes the peak obstacle displacement directly and unmitigated to the tire model. Hence, additional approaches

can be developed which improve obstacle filtering within the compliant contact patch, for both spatial frequency and for amplitude.

One such approach for improving the modeling of obstacle envelopment within the contact patch is to replace the single point follower with a representative tire/ground footprint of constant contact patch length. This approach, developed by Captain et al [5] is implemented here as both the solution of continuous integration as well as the use of discrete elements along the length of the contact patch. It can be found, that for linear modeling of the vertical compliance and damping, the two solutions are identical.

The development of the constant footprint tire model from the single point model is, like the development of the rigid ring follower, a matter of replacing the single contact point with a mechanism which will more closely emulate the desired spatial and magnitude filtering effects that occur in the tire contact patch. The constant footprint model does this by assuming that the interaction between the tire and the ground occurs within a constant finite length along the ground, as opposed to an infinitesimal contact length of the contact point follower, and is illustrated in Figure C.1, below:

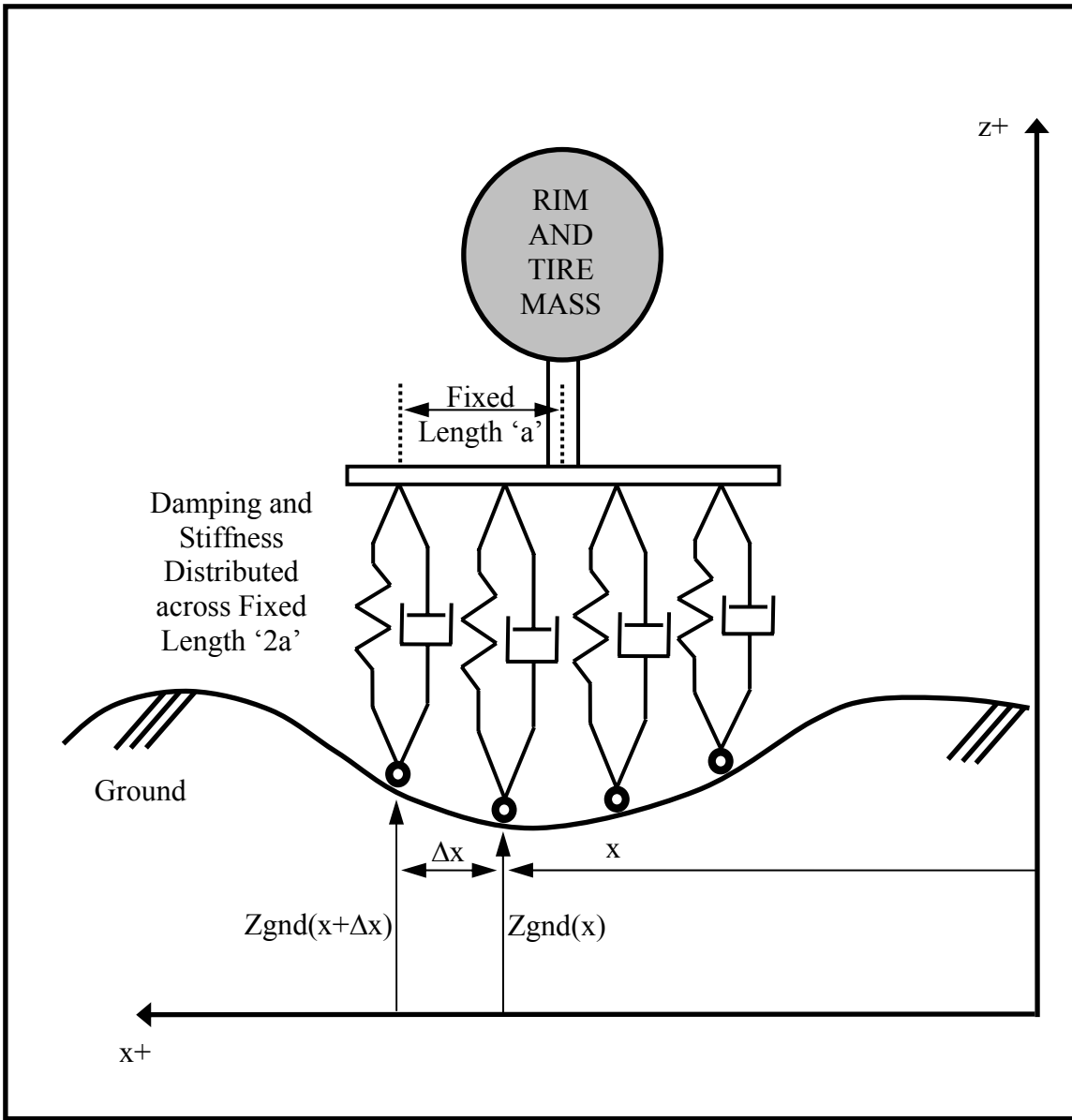


Figure C.1: Constant Footprint Follower for Tire/Vehicle Comfort Modeling

As shown in Figure C.1, the contact patch is assumed to be centered directly below the wheel spindle, and of constant length  $2a$ . Both the vertical compliance and damping of the tire are assumed to be equally distributed along its length and to act normal to the ground surface, i.e., the force acts only vertically. In addition, the mass of the tire,

sidewall, and tread band are associated with the rim at the spindle center  $Z_{ctr}$ , thus allowing the forces that are directed towards the spindle to be solely the function of the spring and damping characteristics of the tire and the relative motion between the wheel spindle and the contact patch, without inertial effects.

Assuming that the form of the equations will be similar for both displacement and velocity, the equations describing the forces can be written for simplicity using displacement and spring rates only. The damping terms can be added by rewriting the displacement equations, substituting velocity for displacement and damping for the spring constants, and then adding this new equation to the original displacement equation. Using this approach and starting with the vertical force in the contact patch as a function of vertical displacement from static equilibrium for arbitrary vertical displacement  $Z(x)$  yields:

$$F_z = \int_0^{2a} \int_0^{Z_{gnd}(x) - Z_{ctr}} K dz dx \quad (C.1)$$

where  $F_z$  is the change in vertical force on the spindle due to displacement from the vertical equilibrium position in the contact patch,  $Z_{gnd}(x)$  is the vertical displacement of the ground as a function of longitudinal position  $x$ ,  $Z_{ctr}$  is the displacement from the vertical equilibrium position of the wheel spindle at the wheel center, and  $K$  is the combined vertical spring rate of the tire sidewall per longitudinal unit length (associated with the tire carcass stiffness, the pneumatic inflation stiffness, and tire tread element stiffness) within the contact patch length  $2a$ .

Using similar logic, the vertical force in the contact patch as a function of the rate of the vertical displacement is:

$$F_z = \int_0^{2a} \int_0^{\dot{z}_{gnd}(x) - \dot{z}_{ctr}} C dz dx \quad (C.2)$$

Where  $F_z$  is the vertical force due to the damping  $C$  across the length of the contact patch  $2a$ ,  $\dot{z}_{gnd}(x)$  is the local rate of change in the vertical displacement of the ground as a function of longitudinal position  $x$ ,  $\dot{z}_{ctr}$  is the vertical velocity of the wheel spindle at the wheel center. Damping  $C$  is associated with the damping rate of the tire sidewall per longitudinal unit length, and is a function of the tire carcass and tread element materials. The force elements due to the spring elements (equation C.1) and the damping elements (equation C.2) can then be combined to yield an expression for the total force at the wheel center as a function of the relative vertical displacements and velocities:

$$F_z(ctr) = \left\{ \int_0^{2a} \int_0^{z_{gnd}(x) - z_{ctr}} K dz dx + \int_0^{2a} \int_0^{\dot{z}_{gnd}(x) - \dot{z}_{ctr}} C dz dx \right\} \quad (C.3)$$

$\dot{z}_{gnd}(x)$ , the local rate of change in the vertical displacement of the ground as a function of longitudinal position  $x$ , is defined by the forward velocity of the wheel spindle center multiplied by the change in the ground height  $Z_{gnd}(x)$ , or:

$$\dot{z}_{gnd}(x) = \dot{X}_{Wheel\ Spindle} \frac{dZ_{gnd}(x)}{dx} \quad (C.4)$$

In order to develop a representative force in the horizontal direction, a constraint is added such that the total resultant force generated by the vertical forces in the contact

patch is always normal to the surface of the road profile ( $F_{normal}$ ). If the slope, or angle of incidence  $\alpha$ , is known and the vertical force  $F_z(ctr)$  is calculated, the longitudinal reaction force  $F_x$  can be calculated using simple trigonometry in the exact same manner as for the single point contact follower model. Calculating  $F_x$ :

$$\text{Tangent } \alpha = \frac{\textit{opposite}}{\textit{adjacent}} = \frac{dZ_{gnd}(x)}{dx} = \frac{F_x}{F_z} \quad (\text{C.5})$$

$$F_x = F_z \text{ Tan } \alpha \quad (\text{C.6})$$

Where  $F_z$  is the total vertical force associated with the displacement of the wheel spindle from its vertical equilibrium position and  $F_x$  is the total longitudinal force on the wheel spindle.  $F_x$  is necessary to calculate the longitudinal acceleration of the tire mass and vehicle body. Additionally, the normal force,  $F_{normal}$ , is required to calculate the tractive forces generated between the tire and the ground surface. This is again done using simple trigonometry and the tangent angle, or engagement angle  $\alpha$ , as follows:

$$\text{Cosine } \alpha = \frac{\textit{adjacent}}{\textit{hypotenuse}} = \frac{F_z}{F_{NORMAL}} \quad (\text{C.7})$$

$$F_{NORMAL} = \frac{F_z}{\cos \alpha} \quad (\text{C.8})$$

Although the development of the constant footprint model per Figure C.1 is sufficient for integrated tire/vehicle ride modeling, it suffers from the same limitation for fixed spindle cleat response modeling as the constant point follower model in Appendix A – the masses are concentrated at the wheel spindle center, which is constrained not to move vertically when the tire is subjected to cleat testing on a laboratory roadway drum. Therefore, the tire model is modified so that the effective mass of the tread band associated with the contact patch and the rigid ring, which represents the relatively inextensible laminate rubber/steel belt package, is modeled separately from the wheel center spindle. The resulting model, developed in Appendix A for the single point contact follower, has the appearance as shown in Figure C.2 for the constant footprint model:



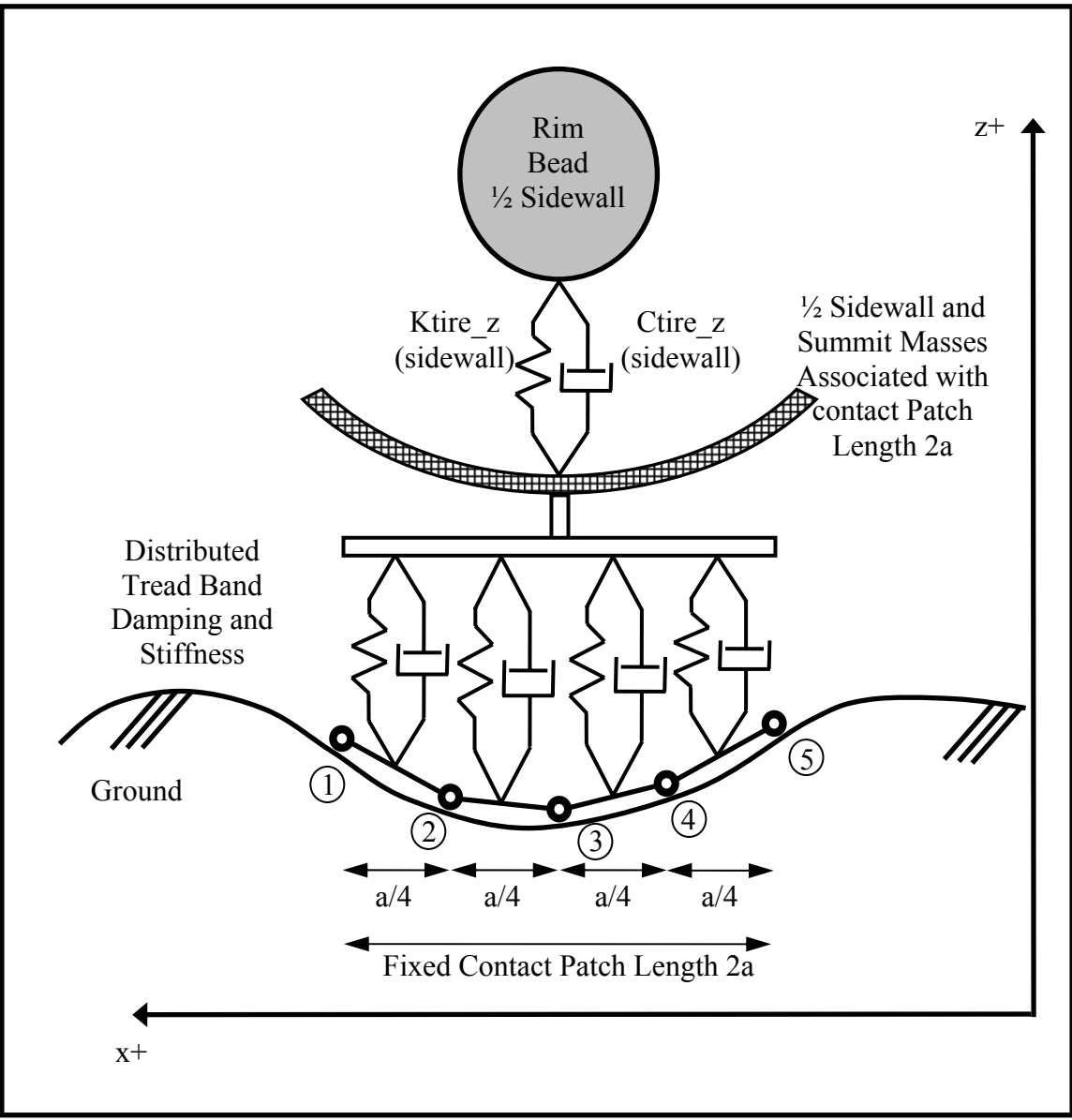


Figure C.2: Constant Footprint Follower for Fixed Spindle Tire Modeling

For this model, the dynamic inertial effects of the tire mass associated with the tread and tire belt summit package are modeled. This type of model is therefore more appropriate for fixed spindle laboratory road wheel experiments intended to explore the tire enveloping power associated with tread band flexibility within the contact patch.

In the special and quite common case where the characteristic spring and damping elements associated with the fixed contact patch are assumed linear, the solution of the continuous integral and that for discrete finite tire segment lengths in the contact patch will be identical. As an illustration, consider the fixed contact patch length shown as four individual segments in Figure C.2. If the average vertical displacement along each individual tread element is known, the forces provided by the individual springs can be added. The summed force will be equal to the force of the combined stiffness of the springs multiplied by their average displacement - the sum of the forces will be the same no matter the number of distributed elements. Because the solution is the same for any number of elements, the solution for the continuous integral of the vertical displacements along the length of the contact patch will be identical. This infers that when using discrete tread elements to model the tire, the number of tread segment elements needed depends solely upon the wavelength of the obstacles, and not the characteristics of the tire model.

Unfortunately, the vertical stiffness of actual tires is not evenly distributed in the contact patch. This is the result of the shearing forces and bending moments which occur in the tread band and summit reinforcing belts. One must conclude that application of this relatively simple tire model may be inadequate when modeling large amplitude, short wavelength, or 'sharp' deflections, even when integrating across discrete tread elements with very fine resolution.

The additional cost and effort associated with the greater complexity of the fixed footprint model compared to the rigid ring contact follower is rewarded by vertical filtering characteristics that in some cases more closely resembles that of a physical tire.

In the case of obstacles that are above the ground plane (“bumps”), using the constant footprint model, the peak vertical amplitude passed into the tire model:

- is equal to the magnitude of the obstacle when the contact patch length  $2A$  is less than the length of the obstacle,
- is less than the magnitude of the obstacle when the contact patch is greater than the length of the obstacle.

These characteristics roughly emulate the enveloping power of the tire as the contact patch passes over obstacles. This effect is illustrated for various ratios of contact patch length to obstacle length in Figure C.3, below:

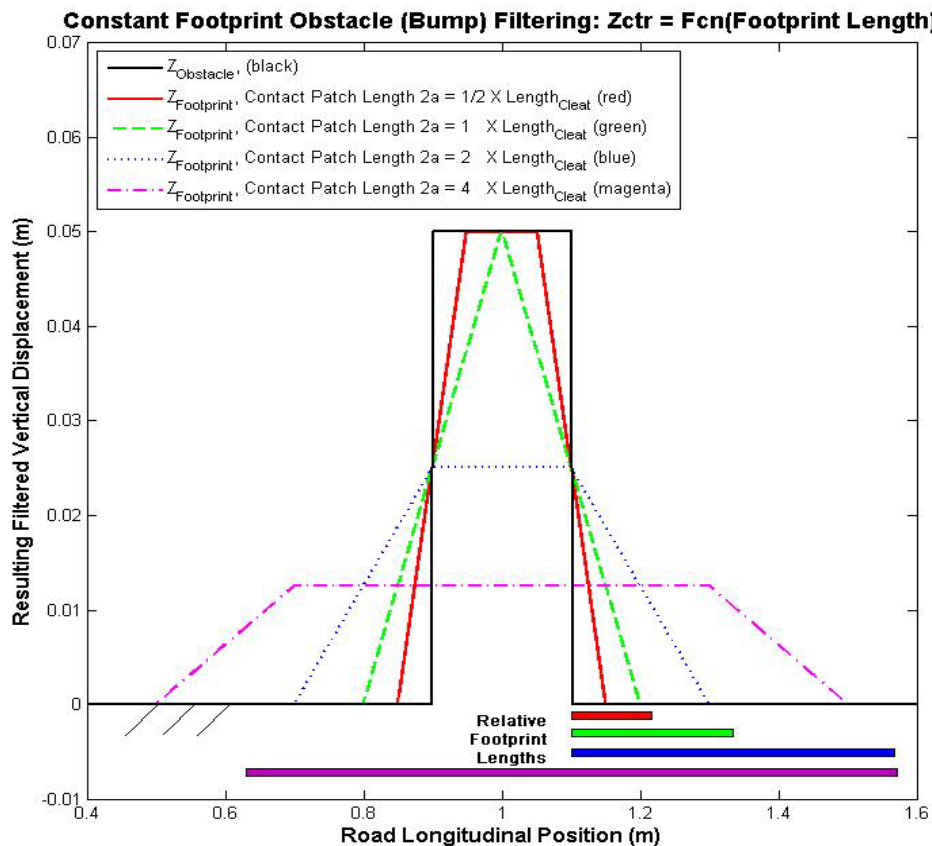


Figure C.3: Constant Footprint Obstacle Envelopment for Various Footprint Lengths

The constant footprint model exactly emulates these same vertical obstacle envelopment characteristics for negative obstacles (“potholes”) as for positive obstacles (“bumps”).

This is illustrated in Figure C.4, below:

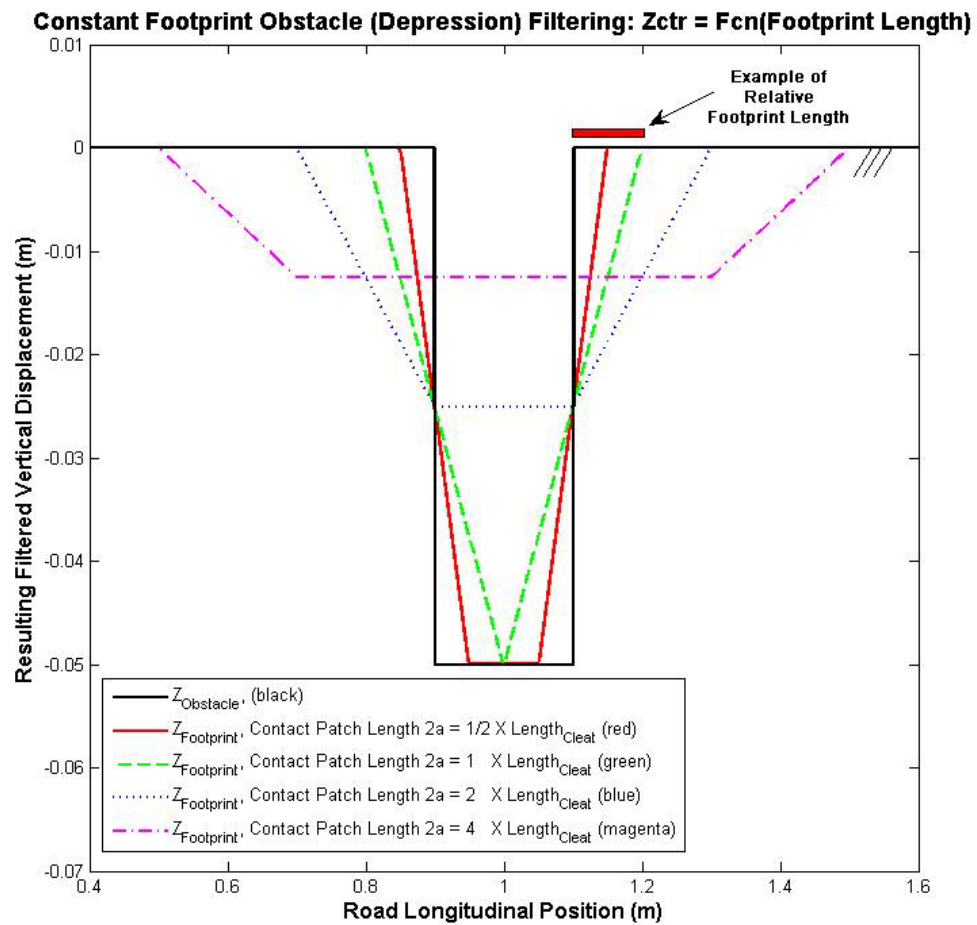


Figure C.4: Constant Footprint “Pothole Envelopment” for Various Footprint Lengths

From the above two figures C-3 and C-4, one can conclude that the constant footprint model is apparently well suited for modeling positive height “bump” obstacles in that it characteristically:

- increases the effective obstacle wavelength

- correctly “envelops” the obstacle for various ratios of obstacle length to contact patch length

In the case of modeling negative height “pothole” obstacles, the constant footprint model correctly increases the wavelength (lowers the spatial frequency). The constant footprint model also appears to function correctly for filtering the vertical magnitude of potholes whose length is reasonable compared to that of the contact patch. However, just as with the rigid ring follower, there is no provision to prevent deep potholes whose lengths are:

- greater than that of the contact patch, but
- shorter than the diameter of the tire

from passing the complete pothole depth to the tire model. For a real tire, the pothole depth would be sharply mitigated as the diameter of the tire would make the tread band sector “catch” on the front and rear edges of the pothole as the tire enters down and into the pothole, thus mitigating the pothole depth. So although the constant footprint model is an apparent improvement over the rigid ring follower model, it is clear once again that no model can be blindly applied without understanding the model assumptions and limitations in order to determine its domain of applicability.

As the tire models are being verified using laboratory test data of the modeled tire as it passes over a rectangular cleat mounted to a road wheel, a comparison of the effects of varying the ratio of the tire contact patch length to the length of cleat is desired. As with the comparison of the single contact point and rigid ring follower models in Appendices A and B, respectively, the physical dimensions of the rectangular cleat’s height and width are converted into a sinusoidal cleat profile of identical height. In order to obtain the

same area under the sinusoidal equivalent cleat profile as the area of the actual rectangular cleat, the wavelength of the sinusoidal curve is increased. The constant footprint contact patch model is then simulated for various ratios of contact patch length to the sinusoidal obstacle length. The result of this simulation is shown in Figure C.5.

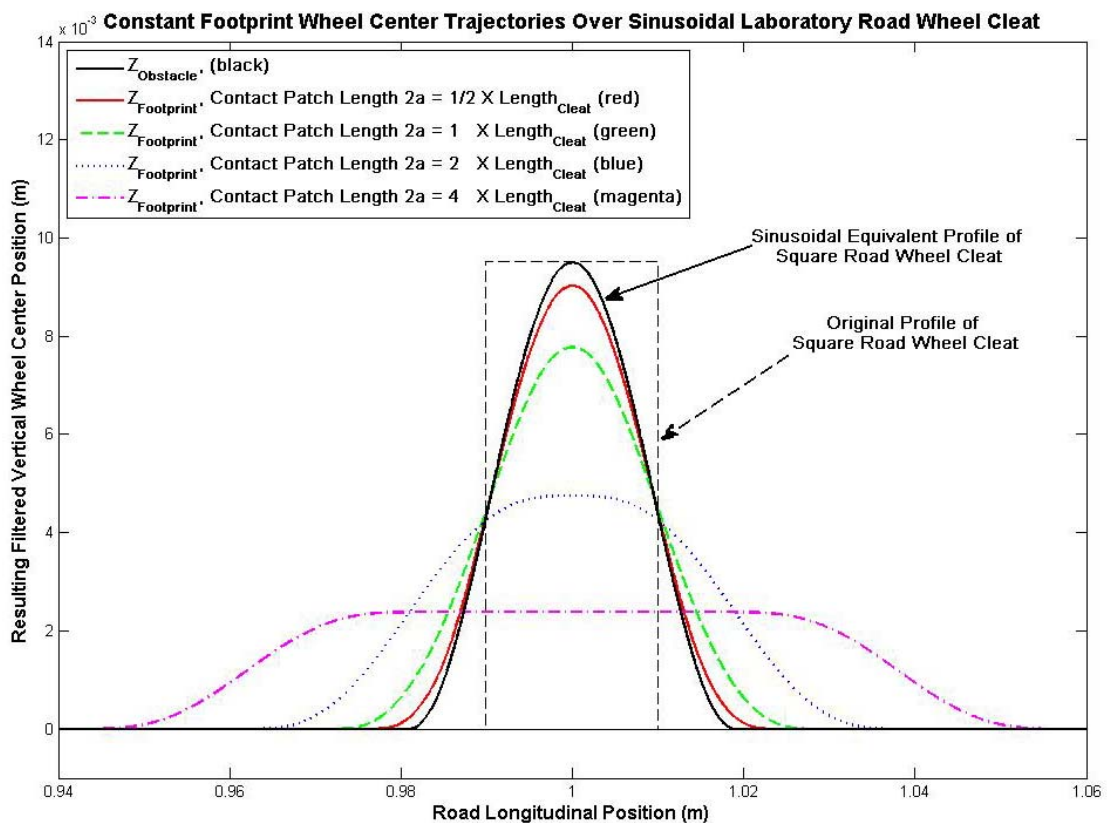


Figure C.5: Constant Footprint Filtering for the Machine Test Cleat Equivalent

From the plots above it can be seen that the constant footprint model appears to approximate the enveloping characteristics of the contact patch by both 1) increasing the effective wavelength of the cleat obstacle and by 2) mitigating the maximum vertical

deflection. In addition, the constant footprint model is capable of maintaining the continuous first order derivative characteristics of the equivalent sinusoidal cleat. This is because the solution to the constant footprint model is continuous throughout the states of the contact patch interaction (contact patch prior to obstacle engagement, contact patch engaging the obstacle, contact patch disengaging the obstacle, and contact patch after leaving the obstacle).

For the cases where encounters between the obstacle and the constant footprint model are limited to circumstances that do not violate the assumptions that the tire vertical stiffness is linear and can be evenly distributed along the length of the contact patch, the constant footprint model provides apparent and clear advantages over both the single point contact follower and the rigid ring follower. In the case where the obstacle is of high amplitude and short wavelength, the ring contact model may be better adapted than the constant footprint model. The selection of the best tire model will depend upon the domain of application and the purpose of the tire/vehicle study.

## Appendix D

### D. Adaptive Footprint Simulink Model

#### Overview of the Adaptive Footprint Model

The constant footprint model was developed in Appendix C by replacing the single point follower developed in Appendix A with a representative tire/ground footprint of constant contact patch length. This approach is perhaps the simplest and most direct approach for modeling the effect of the contact patch ‘draping’ over obstacles as they enter into the contact patch. However, the constant footprint model is somewhat limited in that:

- The vertical elements of the constant footprint model do not provide a direct means for modeling longitudinal forces within the contact patch - longitudinal forces are determined by vector addition such that the resultant sum of the vertical and horizontal forces at the wheel center is normal to the average slope within the contact patch length
- As there is no evolution to the size of the contact patch with varying load, the vertical stiffness due to the internal inflation pressure is constant. It is therefore also assumed that the structural stiffness is also a constant and combined with the pneumatic stiffness.

By allowing the contact patch to vary in length as a function of vertical load, the total force due to the pneumatic stiffness component varies. It is therefore desirable to treat and apply the vertical stiffness associated with the tire structural components separately



from the pneumatic stiffness. Since the contact patch is allowed to vary in length with changing vertical load conditions, the vertical force component due to the pneumatic stiffness component can be calculated by integrating the inward radial pressure forces across the angle of an arc subtending the length of the contact patch. This scheme is also applied to for the development of longitudinal forces as a result of the inward radial displacement within the contact patch. Since the internal tire pressure develops a rearward force when an vertical 'bump' begins to enter the front of the contact patch (and conversely, a forward force when the same obstacle exits at the rear of the contact patch), it is convenient to develop the model such that the angle describing the longitudinal position in the contact patch over which the pressure force is integrated be referenced to the vertical centerline of the tire (zero degrees being the vertical from the center of the wheel spindle downward to the center of the contact patch).

Intuitively, the adaptive footprint model seems to reasonably mimic an actual tire in that longitudinal forces:

- due to irregular obstacle envelopment cannot occur when load (and therefore the contact patch length) goes to zero,
- are larger as a function of vertical displacement within the contact patch, due to either higher peak obstacle height or higher tire static loading

This can perhaps best be visualized as a quasi-static rolling envelopment of an obstacle of positive height (a cleat or other 'bump') that is shorter than the static footprint length by a perfectly elastic pneumatic membrane that has been compressed radially downward. As the obstacle enters the contact patch, the elastic membrane will move upwards and engulf

the obstacle. Because the pressure force is always normal to the surface, the obstacle intrusion will result in an unbalanced horizontal pressure force component in the rearward direction. After the obstacle is entirely engulfed the unbalanced horizontal component (and hence the rearward net spindle reaction force) goes to zero. After the obstacle passes the vertical tire centerline and begins to exit at the rear of the contact patch, a positive rearward force is generated by the unbalanced pressure horizontal pressure force component. The horizontal force component (and the strain energy that was generated by the obstacle envelopment) goes to zero as the obstacle exits the contact patch. Figure D.1, below, illustrates the generation of fore/aft longitudinal force during obstacle envelopment within the contact patch of the adaptive footprint model.

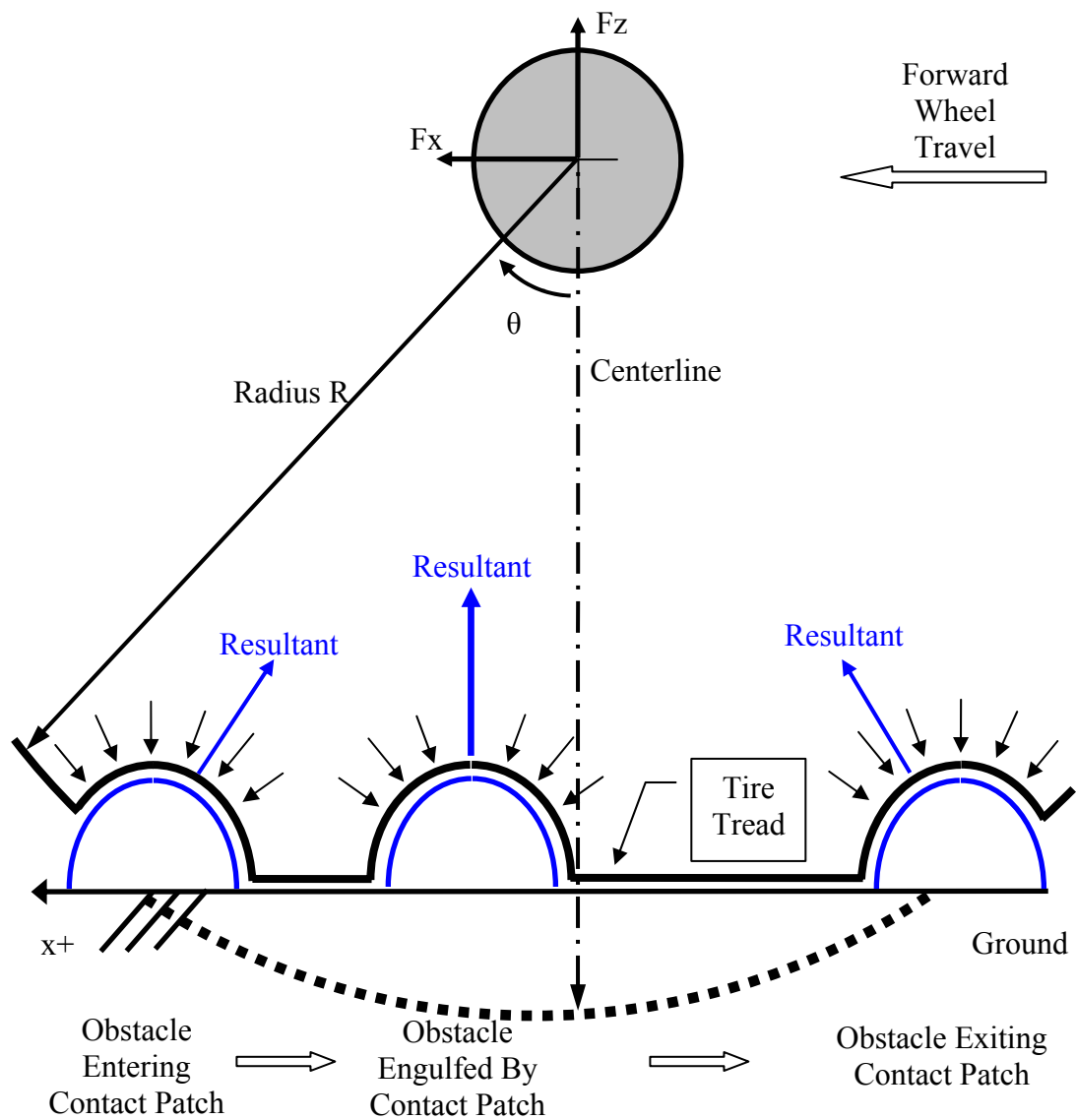


Figure D.1: Adaptive Footprint Tire Model Obstacle Envelopment

## Derivation of the Static Portion of the Adaptive Footprint Model

The concepts for the derivation of the adaptive footprint model come from Khusroo M. Captain, et al, as described by their paper on the development of analytical tire models for dynamic vehicle simulation [1]. The details of the derivation and its implementation were verified by Judhajit Roy as part of his ongoing PhD dissertation work on heavy truck ride modeling at Clemson University's International Center for Automotive Research under the tutelage of Professor E. Harry Law. The details presented here on Captain's and Judhajit's derivations are presented with expanded details for clarity.

The assumptions for the derivation of the adaptive footprint model include:

1. The tire mass properties are concentrated at the wheel center
2. Each differential tread element conforms exactly to the obstacle
3. Each differential tread element can rotate and translate independently from its adjoining tread elements, i.e., there are no shear, bending, or tensile/compressive stresses imposed by the relative motion between the tread elements ('perfect membrane flexibility').
4. The tire assumes its natural circular profile outside of the contact patch
5. The width of the contact patch,  $width_{cp}$ , is constant
6. The characteristics of the tire force-deflection can be represented as the sum of the following components:

- a. a non-pneumatic structural component that can be expressed as distributed radial stiffness  $k_{\text{structure}}$ , and damping coefficient  $c_{\text{structure}}$ , across the length of the contact patch
- b. a pneumatic force due to a constant inflation pressure  $P_{\text{infl}}$  acting along the length of the contact patch

Although it is not necessary for the derivation of the model, there is no constraint that the non-pneumatic structural component be linear. However, practical experience with tire measurements over reasonable ranges of vertical deflection indicate that this structural stiffness component can typically be well approximated as a constant times the vertical displacement. This will not be the case, however, under the following conditions:

- the obstacle height is ‘sharp and high’ in comparison to sidewall height,
- the tire is operating at significantly lower inflation pressure than for which it was designed,
- the structural component of its vertical stiffness is significant compared to the pneumatic component,
- the model is being used for reinforced sidewall, bullet-proof military, run flat tires, or other tires whose structural rigidity is a significant portion of the total tire vertical rigidity.

It should also be noted that there are several assumptions that are used in the adaptive footprint model that can, as with other lumped parameter models, degrade the model fidelity for certain applications. On one hand, the assumption that the forces generated by any tread element is not affected by the relative position of its adjacent tread

elements (the ‘membrane flexibility’ assumption) will necessarily limit the performance of this model over short wavelength and high amplitude obstacles. This is because the bending stiffness of the tire summit (tread elements, and the summit composite structure consisting of the metallic belts and the carcass material) will inhibit the tire’s ability to conform to the obstacle. In this particular case, the adaptive footprint assumptions are violated and the tire model is better represented by a rigid ring model, such as that proposed by Mustafa El-Gindy at Pennsylvania University [2]. On the other hand, the additional complication of models that take into account the summit package bending stiffnesses, such as F-Tire by Gipser at TNO Delft University, add considerable model complexity, computational time, and testing requirements to obtain the parameters for their model. When using these more complex models, it will require the application of sound engineering principals and experience to determine which of the following sets of assumptions:

- contact patch ‘flexible membrane’ for the adaptive footprint model,
- rigid summit for the rigid ring model,
- superposition of measured summit composite bending stiffnesses for the F-Tire model

is most suited or even applicable for the particular modeling domain of applicability, or if finite element or modal modeling (and its inherent complexity) is required.

In developing the adaptive footprint tire model, it is perhaps easiest to start by examining the development of the contact patch vertical forces for a static, loaded tire on a flat surface, as illustrated in Figure D.2, below:

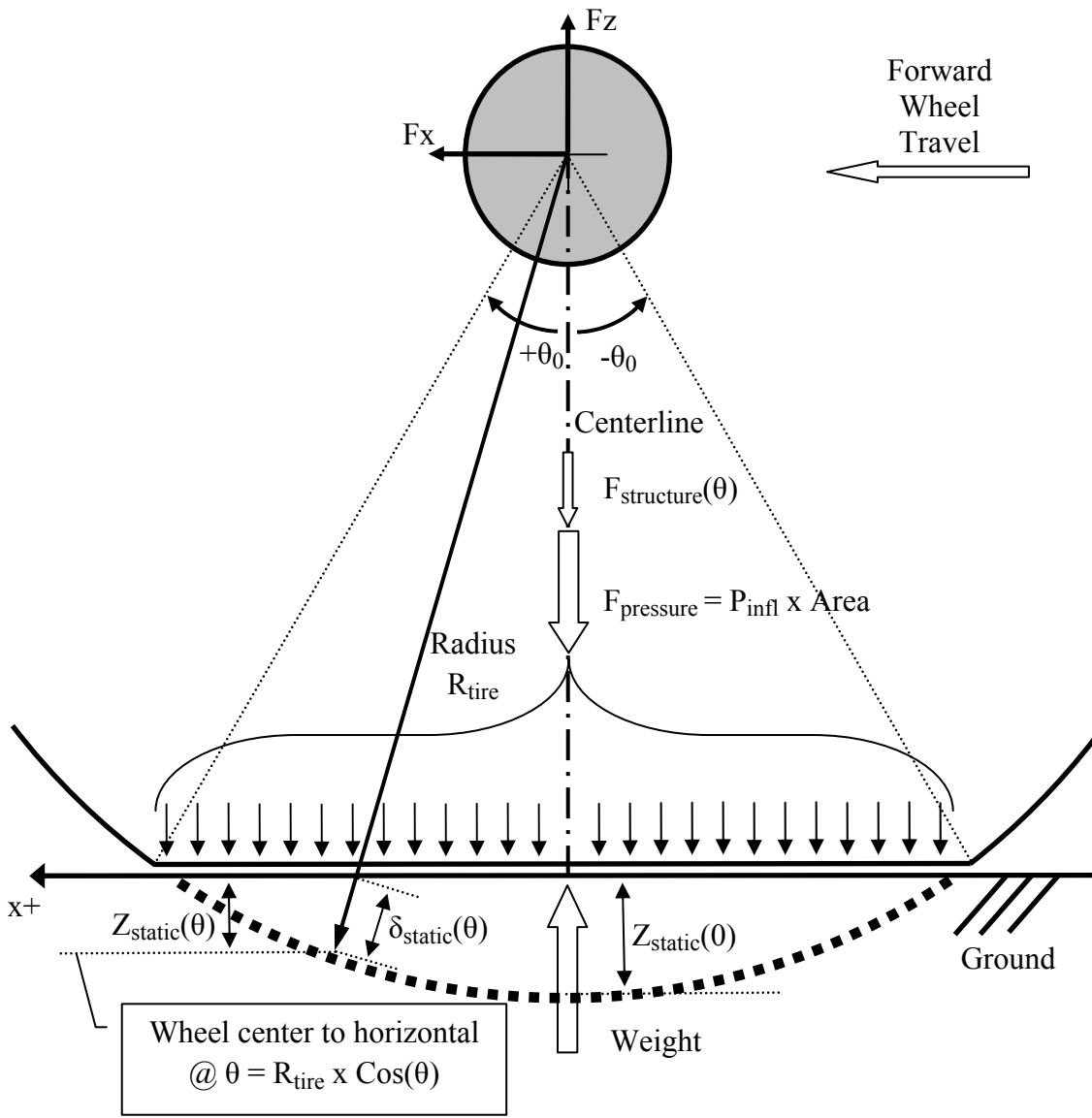


Figure D.2: Geometry for Development of Vertical Forces in the Adaptive Contact Patch

In the static condition, the tire deflection is greatest directly below the centerline of the wheel spindle. Since the length of the contact patch ahead of and behind the wheel center

is equal, then the half contact angle referenced to the vertical from the wheel center is calculated using the following formula:

$$\theta_0 = \frac{R_{tire} - Z_{static}(\theta = 0)}{R_{tire}} \quad (D.1)$$

where:

- $\theta_0$  is the half contact angle referenced to the vertical line drawn at the wheel center
- $R_{tire}$  is the relaxed, or unloaded free radius of the tire
- $Z_{static}(\theta)$  is the vertical static deflection at angle  $\theta$  referenced from the vertical line drawn at the wheel center

To obtain the structural component of the vertical force, an equilibrium equation for the vertical forces across the face of the contact patch is used. Summing forces in the vertical direction:

$$F_{structure}(\theta, Z(\theta)) + F_{press}(P_{inf}, Area) = Weight \quad (D.2)$$

where:

- $F_{structure}$  is the vertical structural force as a function of  $\theta$  and the vertical deflection  $Z$  at  $\theta$ ,
- $F_{press}$  is the vertical force of the tire pressure as a function of inflation pressure  $P_{inf}$  and the area of the contact patch, 'Area'
- $Weight$  is the static vertical weight deflecting the tire



Since  $F_{structure}$  is a function of the angle defining the position in the contact patch and the vertical deflection at that point in the contact patch multiplied by the stiffness, then the total vertical force due to the deflection of the structure across the length of the contact patch can be expressed as:

$$F_{structure} = \int_{-\theta_0}^{+\theta_0} \int_0^{Z_{static}\theta} K_{structure} dz d\theta \quad (D.3)$$

where  $K_{structure}$  is the radial tire stiffness per meter per unit radian. Since  $K_{structure}$  is most normally approximated as a distributed constant across the length of the contact patch, it can be brought out from the integral:

$$F_{structure} = K_{structure} \int_{-\theta_0}^{+\theta_0} \int_0^{Z_{static}\theta} dz d\theta \quad (D.4)$$

and evaluated to yield:

$$F_{structure} = K_{structure} \int_{-\theta_0}^{+\theta_0} Z_{static}(\theta) d\theta \quad (D.5)$$

Since  $F_{structure}$  can be obtained by static testing of the tire vertical spring rate at various pressures, an expression needs to be derived for  $Z_{static}(\theta)$  so that the integral can be evaluated for  $K_{structure}$ . Since  $K_{structure}$  is considered a constant, this can be done by writing an expression for the geometry during deflection on a flat test surface (refer again to Figure D.2, above).

The vertical distance from the wheel center to the relaxed, or undeflected, element at the tire tread at any point along the contact patch is simply  $R_{tire}$  times the cosine of the

angle  $\theta$ . The vertical static deflection at any point along the contact patch is  $Z_{static}(\theta)$ . The difference between these two distances is identical to the free radius of the tire  $R_{tire}$  and the vertical static deflection at the tire centerline,  $Z_{static}(0)$ . This yields the following equation:

$$R_{tire} \cos(\theta) - Z_{static}(\theta) = R_{tire} - Z_{static}(0) \quad (D.6)$$

Solving for  $Z_{static}(\theta)$  :

$$-Z_{static}(\theta) = R_{tire} - Z_{static}(0) - R_{tire} \cos(\theta) \quad (D.7)$$

Multiplying by negative one and rearranging the order:

$$Z_{static}(\theta) = Z_{static}(0) + R_{tire} \cos(\theta) - R_{tire} \quad (D.8)$$

Finally, gathering the  $R_{tire}$  terms:

$$Z_{static}(\theta) = Z_{static}(0) + R_{tire} (\cos(\theta) - 1) \quad (D.9)$$

Substituting the above equation D.9 into the integral for  $F_{structure}$

(equation D.5) so that we can solve for  $K_{structure}$  yields:

$$F_{structure} = K_{structure} \int_{-\theta_0}^{+\theta_0} (Z_{static}(0) + R_{tire} (\cos(\theta) - 1)) d\theta \quad (D.10)$$

Since  $R_{tire}$  is a constant, the integral can be divided into the sum of three definite integrals and re-written as:

$$F_{structure} = K_{structure} \left\{ \int_{-\theta_0}^{+\theta_0} Z_{static}(0) d\theta + R_{tire} \int_{-\theta_0}^{+\theta_0} \cos(\theta) d\theta - R_{tire} \int_{-\theta_0}^{+\theta_0} d\theta \right\} \quad (D.11)$$

Since  $Z_{static}(0)$  is a constant, evaluating the three definite integrals yields the following expression:

$$F_{structure} = K_{structure} \left\{ Z_{static}(0)\theta \Big|_{-\theta_0}^{+\theta_0} + R_{tire} \sin(\theta) \Big|_{-\theta_0}^{+\theta_0} - R_{tire} \theta \Big|_{-\theta_0}^{+\theta_0} \right\} \quad (D.12)$$

This expression can be written out as:

$$F_{structure} = K_{structure} \left\{ Z_{static}(0)(+\theta_0 + \theta_0) + R_{tire} (\sin(+\theta_0) - \sin(-\theta_0)) - R_{tire} (+\theta_0 + \theta_0) \right\} \quad (D.13)$$

Using the property that  $\sin(+\theta)$  equals  $-\sin(-\theta)$ , the expression can be further simplified:

$$F_{structure} = K_{structure} \left\{ Z_{static}(0)2\theta_0 + 2R_{tire} \sin(\theta_0) - 2R_{tire}\theta_0 \right\} \quad (D.14)$$

Finally, gathering like terms yields the final expression for  $F_{structure}$ :

$$F_{structure} = 2K_{structure} \left\{ Z_{static}(0)\theta_0 + R_{tire} (\sin(\theta_0) - \theta_0) \right\} \quad (D.15)$$

Since the vertical force due to the structural component is expressed as a function of the structural stiffness and the half angle subtended by the contact patch, the vertical force expression for  $F_{structure}$ , equation D.15, can be substituted into the static equilibrium equation for forces at the contact patch, equation D.2, to yield:

$$2K_{structure} \left\{ Z_{static}(0)\theta_0 + R_{tire} (\sin(\theta_0) - \theta_0) \right\} + F_{press} = Weight \quad (D.16)$$

This equation can now be rearranged to solve for the vertical stiffness associated with the structural component,  $K_{structure}$ , in terms of the half angle associated with the length of the contact patch,  $\theta_0$ :

$$K_{structure} = \frac{Weight - F_{press}}{2(Z_{static}(0)\theta_0 + R_{tire} (\sin(\theta_0) - \theta_0))} \quad (D.16)$$

where  $F_{press}$  is equal to the area of the contact patch times the tire inflation pressure  $P_{infl}$ .

### Derivation of the Dynamic Portion of the Adaptive Footprint Model

The vertical structural and pneumatic components of the tire have been solved explicitly for a given initial static tire loading condition and can now be expressed as a single term  $K_{\text{structure}}$  (equation D.16). Next the expressions for the vertical and horizontal components of the dynamic portion of the adaptive footprint model need to be developed. This is done by evaluating the integral expression for elemental tire segments inside the contact patch along the contact patch angle  $\theta$ . Coordinates and expressions for the location of the differential tread elements relative to the wheel spindle and ground are shown in Figure D.3, below, and are described in the following paragraphs.

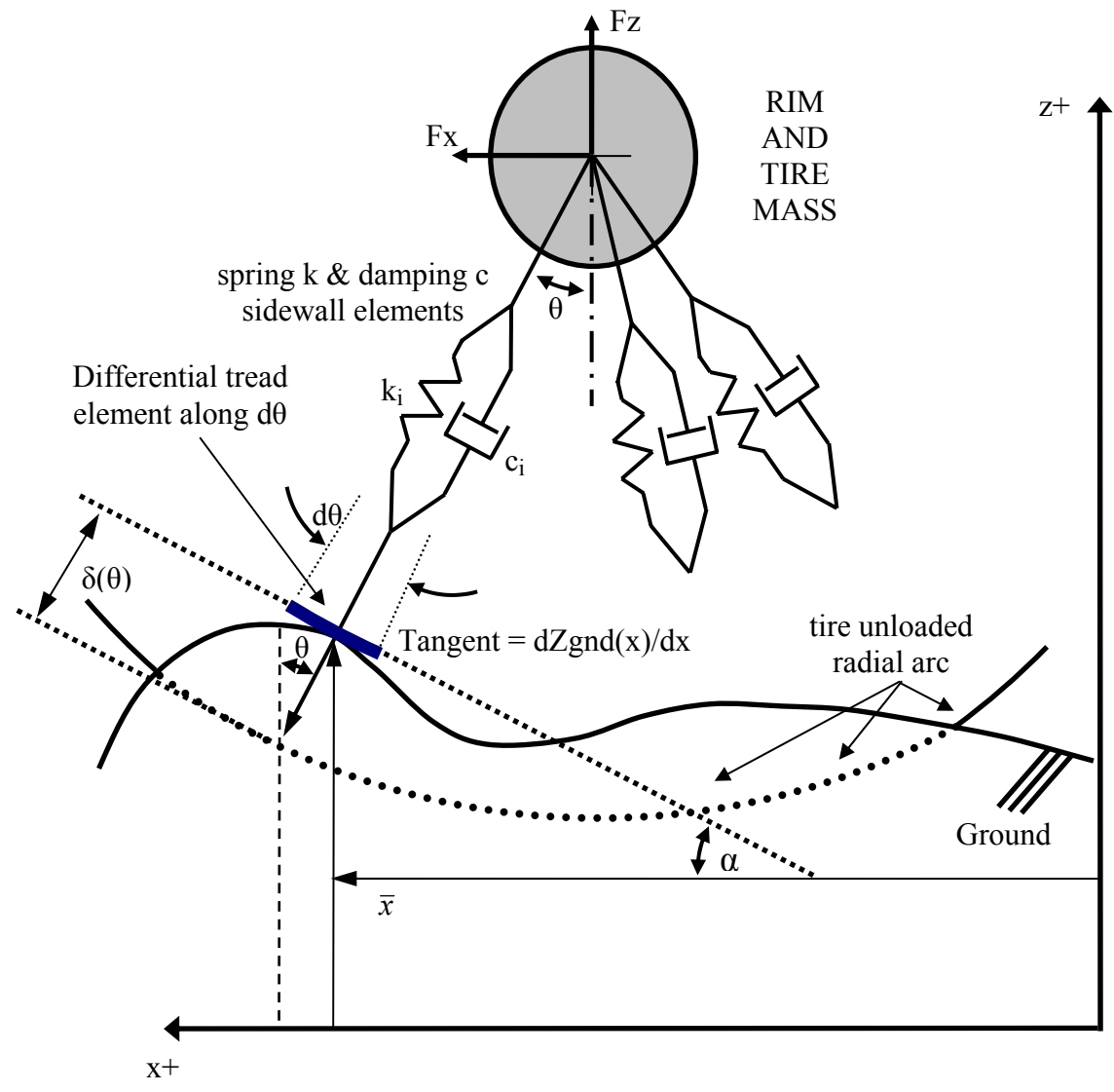


Figure D.3: Adaptive Footprint Tire Model for Tire/Vehicle Comfort Modeling

Derivation of the adaptive footprint model is started by first defining the differential element and its coordinate system. The coordinate of the differential tread element in the positive x direction is:

$$\bar{x}_{element} = R_{tire} (\sin \theta) \quad (D.17)$$

The rate of change of the x position of the differential element with respect to the angle  $\theta$  in the contact patch relative to vertical is simply the derivative of the above equation D.18, or:

$$d\bar{x}_{element} = R_{tire} (\cos \theta) d\theta \quad (D.18)$$

Next, the differential force of the elemental tread segment at angular position  $\theta$  due to compression in the radial direction,  $\delta(\theta)$  due to the tire stiffness and damping can be written as:

$$dF_{radial}(\theta) = \int_0^{\delta(\theta)} K_{structure} d\delta + \int_0^{\dot{\delta}(\theta)} C_{structure} d\dot{\delta} \quad (D.19)$$

where  $\delta(\theta)$  is the deflection of the elemental segment in the radial direction (positive compressive inward) and  $\dot{\delta}(\theta)$  is the rate change of the radial position with respect to time.

If both the structural spring rate  $K_{structure}$  and the damping  $C_{structure}$  are constant as functions of radial position regardless of their angular position within the contact patch  $\theta$ , then they can be brought out from their respective integrals:

$$dF_{radial}(\theta) = K_{structure} \int_0^{\delta(\theta)} d\delta + C_{structure} \int_0^{\dot{\delta}(\theta)} d\dot{\delta} \quad (D.20)$$

The resulting expression for the change in radial compressive force  $dF_{radial}(\theta)$  as a function of angular position within the contact patch becomes:

$$dF_{radial}(\theta) = K_{structure} \delta(\theta) + C_{structure} \dot{\delta}(\theta) \quad (D.21)$$

This expression for the contribution of elemental tread to the total radial force is useful if we can write expressions for the radial compression,  $\delta(\theta)$  and its time derivative. The resulting expression, if integrated across all of the differential tread elements, will then represent the final resultant force for the tire. This requires a closer examination of the expression for the geometry associated with  $\delta(\theta)$ , which can be aided by using simplified Figure D.4, below:

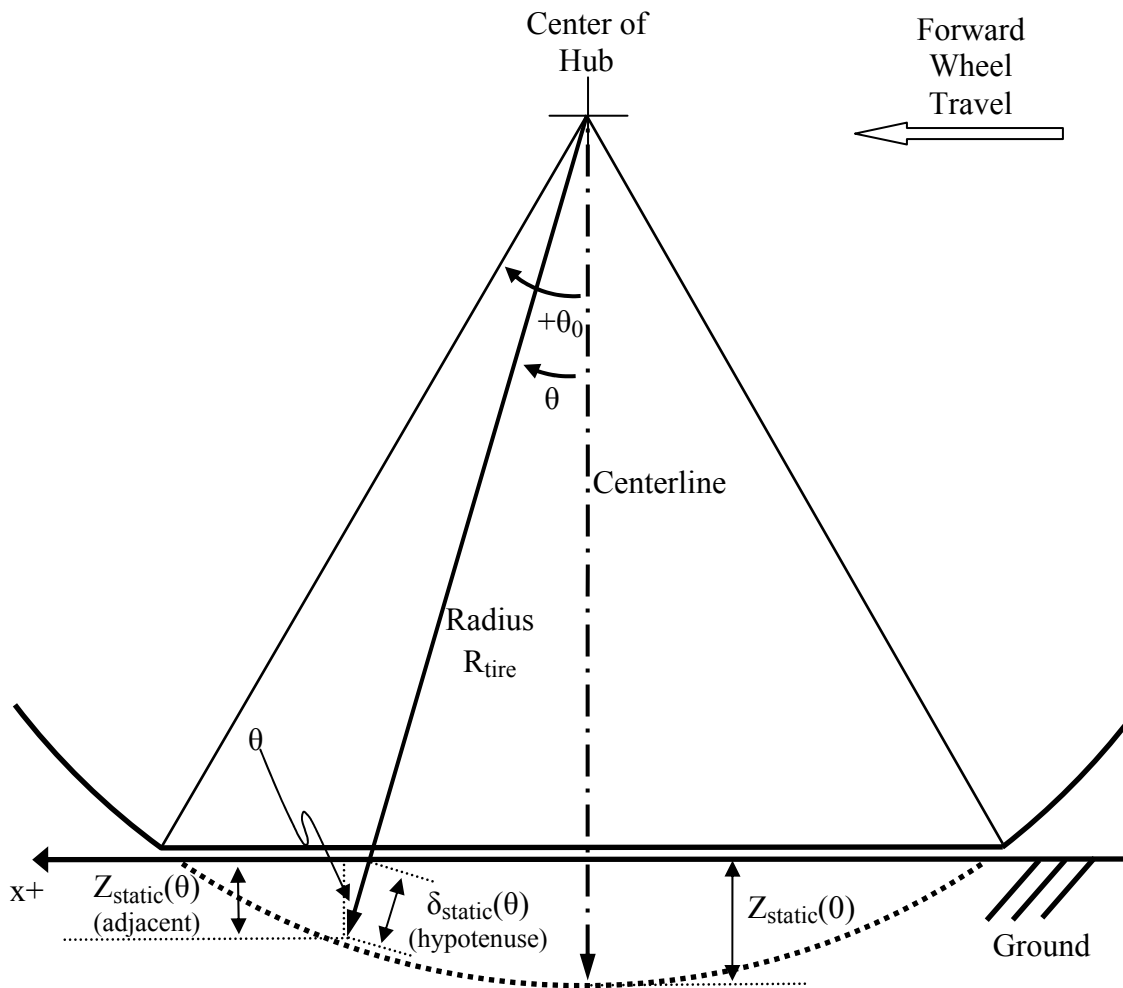


Figure D.4: Simplified Geometry for a Tread Element in the Adaptive Contact Patch

In order to determine  $\delta_{static}(\theta)$ , the radial distance that the tire is statically compressed relative to the ground at any particular position in the contact patch described by angle  $\theta$ , one must first determine  $Z_{static}(\theta)$  relative to the measured tire deflection along the centerline,  $Z_{static}(0)$ . This is done using simple trigonometry. If  $\theta$  describes the angle to the vertical wheel centerline and  $Z_{static}(\theta)$  describes the vertical deflection of the tire at that angle  $\theta$ , then:

$$\begin{aligned} \text{If } Z_{static}(\theta) &= \text{adjacent to } \theta \text{ and } \delta_{static}(\theta) = \text{hypotenuse to } \theta \\ \Rightarrow \cos(\theta) &= \frac{\text{adjacent}}{\text{hypotenuse}} = \frac{Z_{static}(\theta)}{\delta_{static}(\theta)} \end{aligned} \quad (D.22)$$

Rearranging to solve for  $\delta(\theta)$ :

$$\delta_{static}(\theta) = \frac{Z_{static}(\theta)}{\cos(\theta)} \quad (D.23)$$

Substituting the previous expression for  $Z_{static}(\theta)$  in terms of  $Z_{static}(0)$ ,  $R_{tire}$ , and  $\theta$  from equation D.9 yields:

$$\delta_{static}(\theta) = \frac{Z_{static}(0) + R_{tire}(\cos(\theta) - 1)}{\cos(\theta)} \quad (D.24)$$

Expanding the expression by multiplying the terms in the numerator and separating the terms over the common denominator  $\cos(\theta)$  yields:

$$\delta_{static}(\theta) = \frac{Z_{static}(0)}{\cos(\theta)} + \frac{R_{tire} \cos(\theta)}{\cos(\theta)} - \frac{R_{tire}}{\cos(\theta)} \quad (D.25)$$

Canceling the  $\cos(\theta)$  from the numerator and denominator of the middle term of the right hand side and moving it to the first position on the right hand side yields:



$$\delta_{static}(\theta) = R_{tire} + \frac{Z_{static}(0)}{\cos(\theta)} - \frac{R_{tire}}{\cos(\theta)} \quad (D.26)$$

Finally, gathering terms over the common denominator,  $\cos(\theta)$ , and exchanging the position of the second and third terms yields:

$$\delta_{static}(\theta) = R_{tire} - \frac{R_{tire} - Z_{static}(0)}{\cos(\theta)} \quad (D.27)$$

This expression is suitable for the tire if the ground has no vertical definition (other than a flat plane) and the tire is static, i.e., the center of the hub does not move vertically. In order to include the dynamics associated with encountering obstacle geometry along the ground plane, an expression for  $\delta(\theta)$  needs to be developed for the  $Z$  height of the tread element and the changing height of the center of the wheel (i.e., the spindle),  $Z_{wheel\ ctr}$ . A geometry expression for  $\delta(\theta)$  which incorporates the changes in both the ground plane height at the tread element and the wheel center height  $Z_{wheel\ ctr}$  is derived using simple trigonometry in a manner similar to that of equation D.27. The resulting expression is:

$$\delta(\theta) = \delta_{static}(\theta) + \frac{Z_{tread\ element}(\bar{x}) - Z_{wheel\ ctr}}{\cos(\theta)} \quad (D.28)$$

Taking the derivative of equation D.28 with respect to time yields the velocity of the tread element in the radial direction. Since  $\delta_{static}(\theta)$  is constant, the resulting expression for the radial velocity of the tread element at a given angular position  $\theta$  is simply:

$$\dot{\delta}(\theta) = \frac{\dot{Z}_{tread\ element}(\bar{x}) - \dot{Z}_{wheel\ ctr}}{\cos(\theta)} \quad (D.29)$$

Now that the expression for radial compression includes dynamic changes in the tread element segment height (ground plane change due to an obstacle) and the dynamic changes in the vertical position of the wheel center, it is simply a matter of substituting equation D.27, the expression of the static radial deflection,  $\delta_{static}(\theta)$ , into the expression for the general expression of the radial deflection of a tread element, D.28. The resulting equation is:

$$\delta(\theta) = R_{tire} - \frac{R_{tire} - Z_{static}(0)}{\cos(\theta)} + \frac{Z_{tread\ element}(\bar{x}) - Z_{wheel\ ctr}}{\cos(\theta)} \quad (D.30)$$

The general equation for the velocity of the tread element in the radial direction can be solved by inspection. Using equation D.29, one only needs to consider that the rate of change in the height of the tread element is the slope of the road or obstacle at the midpoint of the tire segment, or:

$$\dot{\delta}(\theta) = \frac{slope(\bar{x}) - \dot{Z}_{wheel\ ctr}}{\cos(\theta)} \quad (D.31)$$

Equations D.30 and D.31 are the necessary equations to determine the resultant compression of the tire tread elements in the radial direction. This, in conjunction with equation D.21, the expression for the generation of tire force in the radial direction due to radial compression and radial compression velocity, would be sufficient for calculating the radial force of the individual tread elements. However, we are interested in the separate component forces in the vertical and horizontal directions due to deflections across the entire contact patch. These component forces are determined as follows.

Starting with the vertical component,  $F_{vert}$ , the change in vertical force for the differential elements will consist of the dynamic and static components and can be written as:

$$dF_{vert}(\theta) = dF_{comp}(\theta) \cos \theta d\theta + P_{inf}(Width \times d\bar{x}) \cos \alpha \quad (D.32)$$

where  $\alpha$  is the angle of engagement of the tread element relative to the horizontal,  $P_{inf}$  is the inflation pressure, and Area in this case is the area associated with the differential tread element. Note that:

- the compressive force  $dF_{comp}(\theta)$  is in the radial direction, and therefore its vertical component is the cosine of the tire segment angle  $\theta$ , measured at the wheel spindle and referenced vertically downward along the centerline of the contact patch.
- the normal force due to the tire inflation pressure and the area of the differential tread element is normal to the tire/roadway interface and therefore its vertical component is the cosine of the engagement angle  $\alpha$ , or the angle between the horizontal reference plane and the tangent to the roadway surface

The expression for the rate of change of the x position of the differential element  $dx$  with respect to the angle  $\theta$  in the contact patch, equation D.18, can be substituted directly into the equation for the change in vertical force for the differential elements, equation D.32.

The resulting equation is:

$$dF_{vert}(\theta) = dF_{comp}(\theta) \cos \theta d\theta + P_{inf}(Width \times R_{tire}(\cos \theta)d\theta) \cos \alpha \quad (D.33)$$

Using trigonometric identities, the equation can be simplified further. Since  $\sec(\alpha)$  is the inverse of  $\cos(\alpha)$ :

$$dF_{vert}(\theta) = dF_{comp}(\theta) \cos \theta d\theta + \frac{P_{inf} Width \times R_{tire}(\cos \theta)}{\sec \alpha} d\theta \quad (D.34)$$

Since  $\sec(\alpha)$  is identical to the square root of one plus the square of  $\tan(\alpha)$ :

$$dF_{vert}(\theta) = dF_{comp}(\theta) \cos \theta d\theta + \frac{P_{inf} Width \times R_{tire}(\cos \theta)}{\sqrt{1 + \tan^2(\alpha)}} d\theta \quad (D.35)$$

Recalling that  $\tan(\alpha)$  is the slope of the differential element  $dx$ , the final form of the equation for the differential force component in the vertical direction is:

$$dF_{vert}(\theta) = dF_{comp}(\theta) \cos \theta d\theta + \frac{P_{inf} Width \times R_{tire}(\cos \theta)}{\sqrt{1 + (\text{slope}(\bar{x}))^2}} d\theta \quad (D.36)$$

This equation can be used directly in the MatLab Simulink environment either as individual elements or as a custom block function.

Similarly, the change in horizontal force for the differential elements will consist of the dynamic and static components. These horizontal components can be derived in the same manner as the vertical components were in equation D.32, above, by simply substituting the appropriate trigonometric function (sine) for the horizontal component instead of the vertical component (cosine). The resulting expression for the horizontal force differential is:

$$dF_{horiz}(\theta) = dF_{comp}(\theta) \sin \theta d\theta + P_{inf} (Width \times d\bar{x}) \sin \alpha \quad (D.37)$$

Just as with the differential expression for the vertical force component, the goal is to rewrite the expression for the horizontal force component in terms of the angular position of the differential element within the contact patch ( $\theta$ ) and the slope, or engagement angle of the differential element with the obstacle ( $\alpha$ ). The procedure is as follows:

Equation D.37 will need to be re-written such that the expression for  $\sin(\alpha)$  can be expressed using  $\secant(\alpha)$ . This will enable the expression to be re-cast in terms of  $\tangent(\alpha)$ , which is the slope of the differential element at x. Since by basic trigonometric identities,  $\sin(\alpha)$  is equivalent to  $\tangent(\alpha)$  divided by  $\secant(\alpha)$ , these definitions can be substituted into equation D.37 to yield:

$$dF_{horiz}(\theta) = dF_{comp}(\theta) \sin \theta d\theta + P_{inf}(Width \times d\bar{x}) \left( \frac{\tan(\alpha)}{\sec(\alpha)} \right) \quad (D.38)$$

Since  $\tan(\alpha)$  is the same as the slope of the differential element, the equation can be re-arranged to yield:

$$dF_{horiz}(\theta) = dF_{comp}(\theta) \sin \theta d\theta + P_{inf}(Width) \left( \frac{slope(\bar{x})}{\sec(\alpha)} \right) dx \quad (D.39)$$

As with the derivation for the vertical component, the expression for the rate of change of the x position of the differential element dx with respect to the angle  $\theta$  in the contact patch, equation D.18, can be substituted directly into the equation D.39 to yield:

$$dF_{horiz}(\theta) = dF_{comp}(\theta) \sin \theta d\theta + P_{inf}(Width) \left( \frac{slope(\bar{x})}{\sec(\alpha)} \right) R_{tire} \cos \theta d\theta \quad (D.40)$$

Substituting the trigonometric identity which defines  $\secant(\alpha)$  as identical to the square root of one plus the square of  $\tangent(\alpha)$ :

$$dF_{horiz}(\theta) = dF_{comp}(\theta) \sin \theta d\theta + \frac{P_{inf} Width \times R_{tire} (\cos \theta) slope(\bar{x})}{\sqrt{1 + \tan^2(\alpha)}} d\theta \quad (D.41)$$

Finally, recognizing that the slope of the differential element at x is the same as  $\tangent(\alpha)$  at position x yields:

$$dF_{horiz}(\theta) = dF_{comp}(\theta) \sin \theta d\theta + \frac{P_{inf} \text{Width} \times R_{tire} \text{slope}(\bar{x})}{\sqrt{1 + (\text{slope}(\bar{x}))^2}} (\cos \theta) d\theta \quad (\text{D.42})$$

This equation can be used directly in the MatLab Simulink environment for the horizontal force component at the wheel center, either as individual elements or as a custom block function.

## Appendix E

### E. Two Point Follower Rigid Ring Software

#### Two Point Rigid Ring Matlab MAIN Code

The following MAIN program executes a single Simulink Simulation. This main program control is for a single model – in this case, the Two Point Rigid Ring Simulink Model. All of the other Simulink models were controlled in a similar manner.

The following supporting scripts are called to support MAIN:

```
- input_model_parameters_PS2           (tire model parameters)
- generate_obstacle_sinusoidal_cleat_LUTS_2pt  (obstacle definition)
- generate_initial_conditions             (simulation ICs)
- generate_CAR_Ftrac_LUT                 (traction tables)
- generate_CAR_shift_and_engine_torque_LUTS  (drive torque tables)
```

```
% *****
% ***** MAIN PROGRAM *****
% *****
% CP_2dof_ring_model_for_2pt_cleat_CAR_revd_workfeed.m      25 Mar 2009
% MAIN Program to launch 2 point rigid ring Simulink Model

% ----- Housekeeping
clc;                               % clears command window history
clear;                             % clears variables
close all;                         % closes all graphics windows
my_home_dir = pwd;
delete sim_record.txt
diary sim_record.txt
% ----- Set up all the variables for 'one quarter' drive position
cd('C:\Thesis\MatLab\Eight_A\Veh_Common_Gen_Data')          %Data repository
input_model_parameters_PS2

% ----- Obstacle dimensions
L = 0.0190;           % 0.019m = MT Cleat obstacle length (m)
H = 0.0095;          % 0.0095m = MT Cleat obstacle height (m)
D0 = 0.50;           % distance from center of cleat to center of tire
(m)
Fineness = 10000;   % multiply by 10,000 to convert 0.0001 m to integers
a_rnd = round(a*Fineness)/Fineness % round off one-half Contact
                                     % patc length (a) for indexing

% ----- generate 2-Pt Follower over obstacle LUTs
cd('C:\Thesis\MatLab\Eight_A\Veh_Common_2Pt_Data')          %Data repository
generate_obstacle_sinusoidal_cleat_LUTS_2pt
%generate_obstacle_square_cleat_LUTS_2pt

% ----- Set up the initial condtions
```

```

% Set model initial conditions here in m, m/s (propagates to
components)
cd('C:\Thesis\MatLab\Eight_A\Veh_Common_Gen_Data') %Data repository
generate_initial_conditions

% ----- generate Longitudinal Traction Fz = Fcn(Fnorm, %Slip) LUT
cd('C:\Thesis\MatLab\Eight_A\Veh_Common_Gen_Data') %Data repository
generate_CAR_Ftrac_LUT

% ----- load the transmission gear ratios and shift point LUT
cd('C:\Thesis\MatLab\Eight_A\Veh_Common_Gen_Data') %Data repository
generate_CAR_shift_program_and_engine_torque_LUT

% ----- Run the Simulink model
t_end = 0.5;
time_step = 0.0001;
t = (0:time_step:t_end)';

% Change directories and run the simulink model
cd('C:\Thesis\MatLab\Eight_A\Veh_Common_Models')
sim('Rigid_Ring_2Pt_QV_revb',t, simset('Solver','ode23t','RelTol',
5e-14))
disp(' ')
disp('Completed Rigid_ring_model_for_2pt_cleat_FixedSpindle_revb...')
disp(' ')

% ----- Seed Structured Array Output and Save
% seed the simulation output parameters
test_name = ' QV'; % Fixed Spindle (FS) or Quarter Vehicle (QV);
model_name = ' 2Pt'; % Models include:
                                % ATAC_1PtK_, ATAC_1_PtKM_
                                % ATAC_RingK_, ATAC_RingKM_
                                % ATAC_ConstK_, ATAC_ConstKM_
                                % ATAC_Adapt_
                                % 2Pt_, 5Pt_
                                % FTire_
obstacle_name = ' MTSin'; % MTSqr_ or MTSin_ or BMP_
load_name = strcat(num2str(Mcar,3),'Kg '); % Mass of vehicle
speed_name = strcat(num2str(Xdot_init*3.6,2),'Kph '); % 08, 10,30,50 kph
tire_press_name = strcat(num2str(Tire_press_bar,2),'b'); % 2b or 3b
sim_comment = '';
final_name = strcat(test_name, model_name, obstacle_name,load_name,
speed_name, tire_press_name, sim_comment);
file_name = 'Vehicle Cleat - 2 Point Rigid Ring Chassis Accelerations';
% generate the simulation output structure - return 'sim_data'
structure
cd('C:\Thesis\MatLab\Eight_A\Veh_Common_Gen_Data')
my_2Pt_rigid_ring_struc_revb

% ----- Save the 'sim_data' data structure
cd('C:\Thesis\MatLab\Eight_A\Veh_Common_Out')
QV_2Pt_MTSin_589Kg_8Kph_2b = sim_data;
save QV_2Pt_MTSin_589Kg_8Kph_2b

```



```

% ----- Time when the metrics will be calculated
t_begin_wave = 0.1809; % set Fx engagement for each individual model
t_end_wave   = 0.2686; % set for Fx disengagement for each model
t_delta_wave = t_end_wave-t_begin_wave;

% ----- check simulation results
figure
plot(sim_data.Chassis.time , sim_data.Chassis.fz, 'm',...
      sim_data.Chassis.time , sim_data.Chassis.fx, 'b')
title('MT Cleat - Raw Quarter Vehicle Chassis Forces')
legend('Chassis Fz',...
       'Chassis Fx'    )
xlabel('Time (sec)')
ylabel('Raw Chassis Forces from Matlab (N)')
grid on

new_sim_data.Rim.time = sim_data.Rim.time;
new_sim_data.Rim.fz   = sim_data.Rim.fz;
new_sim_data.Rim.fx   = sim_data.Rim.fx;

new_sim_data.Chassis.time = sim_data.Chassis.time;
new_sim_data.Chassis.fz   = sim_data.Chassis.fz;
new_sim_data.Chassis.fx   = sim_data.Chassis.fx;

new_sim_data.Chassis.zdotdot = sim_data.Chassis.zdotdot;
new_sim_data.Chassis.xdotdot = sim_data.Chassis.xdotdot;

% find average chassis fz and fx force levels before and after impulse
my_outer_i = 0;
for my_i = 1:length(new_sim_data.Chassis.time)
    if new_sim_data.Chassis.time(my_i)<= t_begin_wave || ...
       new_sim_data.Chassis.time(my_i)>= t_end_wave
        my_outer_i = my_outer_i + 1;
        my_meaner_fz(my_outer_i) = new_sim_data.Chassis.fz(my_i);
        my_meaner_fx(my_outer_i) = new_sim_data.Chassis.fx(my_i);
    end
end
my_mean_outer_fz = mean(my_meaner_fz);
my_mean_outer_fx = mean(my_meaner_fx);

% Subtract out the mean offsets
new_sim_data.Chassis.fz = new_sim_data.Chassis.fz - my_mean_outer_fz;
new_sim_data.Chassis.fx = new_sim_data.Chassis.fx - my_mean_outer_fx;

% generate the wave = zero outside the valid impact time
for my_i = 1:length(new_sim_data.Chassis.time)
    if new_sim_data.Chassis.time(my_i)<= t_begin_wave || ...
       new_sim_data.Chassis.time(my_i)>= t_end_wave % time in sec
        new_sim_data.Rim.fz(my_i)   = 0;
        new_sim_data.Rim.fx(my_i)   = 0;
        new_sim_data.Chassis.fz(my_i) = 0;
        new_sim_data.Chassis.fx(my_i) = 0;
        new_sim_data.Chassis.zdotdot(my_i) = 0;
        new_sim_data.Chassis.xdotdot(my_i) = 0;
    end
end

```

```

end
end

figure
plot(new_sim_data.Rim.time ,      sim_data.Rim.fz, 'm',...
      new_sim_data.Rim.time , new_sim_data.Rim.fz, 'b')
title('MT Cleat - Quarter Vehicle Rim Forces - Fz')
legend('Old Rim Fz',...
       'New Rim Fz'      )
xlabel('Time (sec)')
ylabel('Fz Rim Force (N)')
grid on

figure
plot(sim_data.Rim.time ,      sim_data.Rim.fx, 'm',...
      sim_data.Rim.time , new_sim_data.Rim.fx, 'g')
title('MT Cleat - Quarter Vehicle Rim Forces - Fx')
legend('Old Rim Fx',...
       'New Rim Fx'      )
xlabel('Time (sec)')
ylabel('Fx Rim Force (N)')
grid on

figure
plot(new_sim_data.Chassis.time ,      sim_data.Chassis.fz, 'm',...
      new_sim_data.Chassis.time , new_sim_data.Chassis.fz, 'b')
title('MT Cleat - Quarter Vehicle Chassis Forces - Fz')
legend('Old Chassis Fz',...
       'New Chassis Fz'      )
xlabel('Time (sec)')
ylabel('Fz Chassis Force (N)')
grid on

figure
plot(sim_data.Chassis.time ,      sim_data.Chassis.fx, 'm',...
      sim_data.Chassis.time , new_sim_data.Chassis.fx, 'g')
title('MT Cleat - Quarter Vehicle Chassis Forces - Fx')
legend('Old Chassis Fx',...
       'New Chassis Fx'      )
xlabel('Time (sec)')
ylabel('Fx Chassis Force (N)')
grid on

figure
plot(new_sim_data.Chassis.time ,      sim_data.Chassis.zdotdot/9.81,
      'm',...
      new_sim_data.Chassis.time , new_sim_data.Chassis.zdotdot/9.81,
      'b')
title('MT Cleat - Quarter Vehicle Chassis Z Acceleration')
legend('Old Chassis Z Acceleration',...
       'New Chassis Z Acceleration'      )
xlabel('Time (sec)')
ylabel('Chassis Z Acceleration (g)')
grid on

```

```

figure
plot(sim_data.Chassis.time ,      sim_data.Chassis.xdotdot/9.81, 'm',...
      sim_data.Chassis.time , new_sim_data.Chassis.xdotdot/9.81, 'g')
legend('Old Chassis X Acceleration',...
       'New Chassis X Acceleration'      )
xlabel('Time (sec)')
ylabel('Chassis X Acceleration (g)')
grid on

% ----- Final Acceleration Plots
% Load Appropriate FTire simulation and FTire suspension forces
load('C:\Thesis\MatLab\Eight_A\Y_FTire_Cleat_Sinus\Fsuspension_cleat')
load('C:\Thesis\MatLab\Eight_A\Y_FTire_Cleat_Sinus\FTire_cleat')

figure
plot(sim_data.Chassis.time, sim_data.Chassis.zdotdot/9.81,'m',...
      QVFTireMTSqr589Kg8Kph2b.Chassis.time-1,...
      QVFTireMTSqr589Kg8Kph2b.Chassis.zdotdot/9.81,'g',...
      new_sim_data.Chassis.time, new_sim_data.Chassis.zdotdot/9.81,...
      'b','linewidth',2);
title('Check Accelerations for
TRAPZ','FontSize',10,'FontWeight','bold');
xlabel('Time (sec)','FontSize',08,'FontWeight','bold');
ylabel('Chassis Acceleration (g)','FontSize',08,'FontWeight','bold');
legend('Sim Data Chassis Accel Az (g)',...
       'SIMPACK and FTire Az (g)',...
       'New Sim Data Chassis Az (g)')
set(gca,'FontSize',08,'FontWeight','bold')
set(gcf,'Color',[1 1 1])
box on, grid on

figure
plot(sim_data.Chassis.time, sim_data.Chassis.xdotdot/9.81,'m',...
      QVFTireMTSqr589Kg8Kph2b.Chassis.time-1,...
      QVFTireMTSqr589Kg8Kph2b.Chassis.xdotdot/9.81,'g',...
      new_sim_data.Chassis.time, new_sim_data.Chassis.xdotdot/9.81,...
      'b','linewidth',2);
title('Check Accelerations for
TRAPZ','FontSize',10,'FontWeight','bold');
xlabel('Time (sec)','FontSize',08,'FontWeight','bold');
ylabel('Chassis Acceleration (g)','FontSize',08,'FontWeight','bold');
legend('Sim Data Chassis Accel Ax (g)',...
       'SIMPACK and FTire Ax (g)',...
       'New Sim Data Chassis Ax (g)')
set(gca,'FontSize',08,'FontWeight','bold')
set(gcf,'Color',[1 1 1])
box on, grid on

figure
subplot(2,1,1)
plot(sim_data.Chassis.time-t_off, sim_data.Chassis.zdotdot/9.81,'r',...
      QVFTireMTSqr589Kg8Kph2b.Chassis.time-1,...
      QVFTireMTSqr589Kg8Kph2b.Chassis.zdotdot/9.81,'g','linewidth',2);

```

```

title(file_name,'FontSize',10,'FontWeight','bold');
ylabel('Vertical Acceleration Az
(g)','FontSize',08,'FontWeight','bold');
legend('Model Accel Az','SIMPACK and FTire Az')
axis([ 0.0, 0.5, -0.1, 0.1])
set(gca,'FontSize',08,'FontWeight','bold')
set(gcf,'Color',[1 1 1])
box on, grid on

subplot(2,1,2)
plot(sim_data.Chassis.time-t_off, sim_data.Chassis.xdotdot/9.81, 'b',...
      QVFTireMTSqr589Kg8Kph2b.Chassis.time-1,...
      QVFTireMTSqr589Kg8Kph2b.Chassis.xdotdot/9.81, 'g', 'linewidth',2);
xlabel('Time (sec)','FontSize',08,'FontWeight','bold');
ylabel('Longitudinal Accel Ax (g)','FontSize',08,'FontWeight','bold');
legend('Model Accel Ax','SIMPACK and FTire Ax','location','southeast')
axis([ 0.0, 0.5, -0.2, 0.2])
set(gca,'FontSize',08,'FontWeight','bold')
set(gcf,'Color',[1 1 1])
box on, grid on

% Now save figure
cd('C:\Thesis\Comfort_Thesis\Accel_Graphics')
saveas(gcf,final_name,'bmp')
saveas(gcf,final_name,'fig')

figure
file_name = 'Vehicle Cleat - 2 Point Rigid Ring Suspension Forces';
subplot(2,1,1)
plot(sim_data.Chassis.time-t_off, sim_data.Chassis.fz, 'b',...
      QVFTireMTSqr589Kg8Kph2b.Chassis.time-1,...
      QVFTireMTSqr589Kg8Kph2b.Chassis.fz-5615, 'g', 'linewidth',2);
title(file_name,'FontSize',10,'FontWeight','bold');
ylabel('Vertical Suspension Fz (N)','FontSize',08,'FontWeight','bold');
legend('Model Suspension Fz','SIMPACK and FTire Fz')
axis([ 0.0, 0.5, -1000, 1500])
set(gca,'FontSize',08,'FontWeight','bold')
set(gcf,'Color',[1 1 1])
box on, grid on

subplot(2,1,2)
plot(sim_data.Chassis.time-t_off, sim_data.Chassis.fx, 'b',...
      QVFTireMTSqr589Kg8Kph2b.Chassis.time-1,...
      QVFTireMTSqr589Kg8Kph2b.Chassis.fx, 'g', 'linewidth',2);
xlabel('Time (sec)','FontSize',08,'FontWeight','bold');
ylabel('Longitudinal Suspension Fx
(N)','FontSize',08,'FontWeight','bold');
legend('Model Suspension Fx','SIMPACK and FTire
Fx','location','southeast')
axis([ 0.0, 0.5, -1000, 1000])
set(gca,'FontSize',08,'FontWeight','bold')
set(gcf,'Color',[1 1 1])
box on, grid on

```

```
% Now save figure
cd('C:\Thesis\Comfort_Thesis\Force_Graphics')
saveas(gcf,final_name,'bmp')
saveas(gcf,final_name,'fig')

% ----- Generate Output Metrics
cd('C:\Thesis\Comfort_Thesis\Diary')

diary ('QV_Az_Ax_PkFz_PkFx_ImpFz_ImpFx_chassis.txt')
disp(' ')
disp(file_name)
fprintf('%0.5f \n', max(new_sim_data.Chassis.zdotdot/9.81),...
        min(new_sim_data.Chassis.xdotdot/9.81),...
        max(new_sim_data.Rim.fz),...
        min(new_sim_data.Rim.fx),...
        trapz(sim_data.Chassis.time,sim_data.Chassis.fz),...
        trapz(sim_data.Chassis.time,sim_data.Chassis.fx)

diary off
% ----- Home directory
%cd('C:\Thesis\MatLab\Eight_A\A_Point_K_Cleat_Sinus')
cd(my_home_dir);
```

## Two Point Rigid Ring Matlab Support Code

```

% *****
% ***** INPUT MODEL PARAMETERS PS2 *****
% *****
% input_model_paramters_PS2.m                                08 Feb 2009
%
% File contains the following information:
% - tire data from Michelin Machine Rigidity Testing
% - tire data from tire omega cuts and weighing the components
% - simple 1/4 car model mass estimates (total mass: max load at 2.0b)
% - tire data comes from Michelin Machine Rigidity Testing
%
% T&RA Data is as follows:
% - 26 psi / 180 kPa : 589 kg
% - 29 psi / 200 kPa : 631 kg
% - 32 psi / 220 kPa : 671 kg
% - 35 psi / 240 kPa : 710 kg
% - Max Section Width = 243mm, 677 OD
% - Max RTW = 95% of Max overall width (0.95*243 = 231 mm)
%
% Advertised Specifications
% - 25 lbs => 11.3 Kg
% - Revs per mile = 778 => DLR = (1,609.344)/2/pi/778
% - DLR (Dynamic Loaded Radius) =0.3292 m
% - O/A diameter = 26.7 inches (678.18 mm)

% *** VEHICLE MASS Properties - weight based upon 2 bar design load
% MT data was taken at 362 or 589 kgf at 2.0 bar
% Spindle_mass = 362;      % For minimum solicitation and CP length (kg)
% Spindle_mass = 589;      % For maximum solicitation and CP length (kg)
% Mcar = Spindle_mass      % (kg) !NF This is for one quarter vehicle

% *** TIRE MASS Properties - from tire that cut & measured manually.
% Values used are in the Mass and MOI spreadsheet for rigid ring model.
% Mbead_meas      = 2.252;      % decortilage cut (kg)
% Msidewall_meas  = 1.798;      % decortilage cut (kg)
% Msummit_meas    = 5.871;      % decortilage cut (kg)
% Mtread_meas     = 1.993;      % decortilage cut (kg) using CSR estimates
% Mtire = Mbead_meas + Msidewall_meas + Msummit_meas + Mtread_meas; % (kg)
% Ibead_meas      = 0.148;      % decortilage cut (kg-m^2)
% Isidewall_meas  = 0.155;      % decortilage cut (kg-m^2)
% Isummit_meas    = 0.632;      % decortilage cut (kg-m^2)
% Itread_meas     = 0.222;      % decortilage cut (kg-m^2)
% Itire = Ibead_meas+Isidewall_meas+Isummit_meas+Itread_meas; % (kg-m^2)

% *** RIM MASS Properties
% Values used in the Mass and MOI spreadsheet for the rigid ring model.
% Mrim = 17.330;          % test rim-measured by MT-alum rim ~10 (kg)
% Irim = 0.725;          % test rim-measured by MT-spin MOI (kg m^2)

% *** AXLE Inputs 2007 Lexus IS350 from Michelin K&C Test FW601
%                                dated 7 Nov 07 w/ 4 people          ***

```

```

Maxle = (106/2)-Mrim-Mtire; % mass of axle for one wheel position(kg)
                                % 1/4 car - '07 IS350 V-6 RWD (kg)
Kaxle = 1000*(29.4+28.6+34.1+34.6)/4; % avg spring rate (N/m)
Caxle = (1400+4500)/2; % Typical avg. comp./rebound [N/(m/s)]
Mdrive = 0; % driveline input torque to rim (Nm)

% *** TIRE/RIM SIZE Inputs ***
SW = 0.245; % Section Width (m)
RTW = 0.183; % Rolling Tread Width fm contact patch (m)
%RTW = 0.197; % Rolling Tread Width (m)
AR = 45; % Aspect Ratio
Rim = 18; % Rim seat diameter (in)
% Reff = ((0.5*Rim*25.4)+(AR/100)*SW)/1000; % => 0.3389 (m)
% Reff = 0.3920; % Eff. Rolling Radius from TP^2 program (m)
% Reff = 0.3292; % RPM data-dynamic loaded radius (m)
Reff = 0.3292;

% *** CONTACT PATCH LENGTH ***
% Calculate One-Half Contact Patch Length 'a' (use Z Force=Press*Area)
% Calculating a (1/2 contact patch length) for tire at 2.0 bar(32 psi)
% at a loading of spindle_mass kg's static loading using F = P*A. The
% rolling tread width RTW is approximated by the mean width of the two
% subtread belts, measured on the tire omega cut.
Tire_press_psi = 29; % tire pressure (lb/in^2)
% Note:35 psi~2.20b
Tire_press_bar = 1.0*round(10*(Tire_press_psi*0.06894757))/10; % (bar)
Tire_press_kPa = 29*6.894757; % tire pressure (kPa)
Tire_press_Pa = 29*6894.757; % tire pressure (Pa)

CP_Area_in2 = Spindle_mass*2.204623/Tire_press_psi; % CP area (in^2)
CPL_pneu = (CP_Area_in2*0.00064516/RTW); % CP length (m)
% CP_Area_m2 = (Spindle_mass)*9.80665/Tire_press_Pa; % CP area (m^2)
% CPL_pneu_metric = (CP_Area_m2/RTW); % CP length (m)

% Half contact patch length 'a' is used in the models
a = 0.5 * CPL_pneu; % 1/2 * CPL (m)
disp(' ')
disp('Calculated Contact Patch Length: '),a
disp(' ')

% *** TIRE MOI Corrections within the contact patch
% Appropriate sidewall mass and inertia to bead and summit
Mbead = Mbead_meas + 0.5*Msidewall_meas; % (kg)
Ibead = Ibead_meas + 0.5*Isidewall_meas; % (kg m^2)

% Appropriate tread mass & inertia to summit according to in/out of CP
frac_CP = (2*a)/(2*pi*Reff); % fraction of circumference w/in CP
Mring=Msummit_meas+0.5*Msidewall_meas+(1-frac_CP)*Mtread_meas;% (kg)
Iring=Isummit_meas+0.5*Isidewall_meas+(1-frac_CP)*Itread_meas;% (kg-m^2)

Mtread = frac_CP*Mtread_meas; % (kg)
Itread = frac_CP*Itread_meas; % (kg-m^2)

Ktire_z = 261347; % vertical spring constant (N/m)

```

```
Ctire_z = 0.0008*Ktire_z;      % est. of damping constant (N-s/m)

Ktire_x = 1354447;            % longitudinal spring constant (N/m)
Ctire_x = 0.0010*Ktire_x;    % est. of damping constant (N-s/m)

Ktire_theta = 60057;         % tire torsional stiffness (Nm/rad)
Ctire_theta = 0.0012*Ktire_theta; % est. torsional damping (Nms/rad)

Ktread_vr = 1775149;         % tread block vert. resid. spring (N/m)
Ctread_vr = 0.0010*Ktread_vr; % tread block vert. resid. damping(N-s/m)

Ktread_cr = 2692900;         % tread block circum. resid. spring (N/m)
Ctread_cr = 0.0010*Ktread_cr; % tread block circum. resid. damp (N-s/m)

% *** ADD'L CALCULATED VALUES ***
Msprung = Spindle_mass - Maxle - Mrim - Mtire; % 1/4 sprung mass (kg)

disp(' ')
disp('Completed Input Model Parameters for PS2...')
disp(' ')
```



```

% *****
% ***** GENERATE OBSTACLE SINUSOIDAL CLEAT LUTS 2PT *****
% *****
% generate_obstacle_sinusoidal_cleat_LUTS_1pt.m          03 April 2008
%
% 1. Obstacle dimensions
D0 =0.50;          % distance fm center of cleat to center of tire (m)
L = 0.019;        % 0.019m = MT Cleat obstacle length (m)
H = 0.0095;       % 0.0095m = MT Cleat obstacle height (m)
Fcorr = 2;        % correct rounded cleat to same area as MT cleat
new_L = Fcorr*L;  % corrects length of cleat so sinusoidal area is
                  % identical to area under rectangular cleat

% NOTE: The model runS only after all necessary variables are loaded.
% Variable 'a' is calculated from 'input_model_parameters_(Tire).m'
% Variable 'a' is the half contact patch length (m)

% 2. Generate x positions and corresponding z heights for the 1-D LUT
% preallocate arrays for speed
Xroad      = zeros(1,2*D0*10000);
Zroad_lead = zeros(1,2*D0*10000);
Zroad_trail = zeros(1,2*D0*10000);
Zroad_eff  = zeros(1,2*D0*10000);
Alpha_road = zeros(1,2*D0*10000);

for i = 1:1:2*D0*10000; % 2 X distance to obstacle, in 0.1 mm
increments
                % to provide the necessary resolution in X

Xroad(i) = i/10000; % converts distances back to meters

    % Now determine the sin function for the leading point
    if      Xroad(i) < (D0 - 0.5*new_L)
        Zroad_lead(i) = 0;
        Alpha_road(i) = 0;

    elseif (D0 - 0.5*new_L) <= Xroad(i) && Xroad(i) <= D0 + 0.5*new_L
        Zroad_lead(i) = ((H/2)*(1+cos((2*pi/new_L)*...
(Xroad(i)-(D0-0.5*new_L))-pi)));
        Alpha_road(i) = atan(-sin((2*pi/new_L)*...
(Xroad(i)-(D0-0.5*new_L))-pi));

    else      Zroad_lead(i) = 0;
        Alpha_road(i) = 0;

    end

    % Now calculate the effective Z plane height and angle alpha
    % Zroad_eff(i) = (Zroad_lead(i) + Zroad_trail(i)) / 2;
    Zroad_eff(i) = Zroad_lead(i);

end

% Now check the results of the obstacle inputs

```

```

figure
plot(Xroad,Zroad_lead, 'r',...
      Xroad,Zroad_trail, 'g',...
      Xroad,Zroad_eff, 'b')
title('MT Cleat Sinusoidal Geometry for BASIC 1 Pt Follower',...
      'FontWeight','bold')
xlabel('X Road (m)')
ylabel('Road Z (m)')
legend('Zroad lead (r in m)',...
       'Zroad trail (g in m)',...
       'Zroad eff (b in m)')
%axis([0.1,0.15,-0,+1])
% axis([0,0.2,-0,+0.01])
% axis([9.7,10.3,-0.2,+0.2])
grid on

figure
plot(Xroad,Alpha_road, 'm')
title('MT Cleat Sinusoidal Approach Angle for BASIC 1 Pt Follower',...
      'FontWeight','bold')
xlabel('X Road (m)')
ylabel('Alpha (rad)')
legend('Alpha road (m in rad)')
%axis([0.1,0.15,-0,+1])
% axis([0,0.2,-0,+0.01])
% axis([9.7,10.3,-0.2,+0.2])
grid on

disp(' ')
disp('Completed Generate Obstacle Sinusoidal Cleat LUTs 1 Point...')
disp(' ')

```

```

% *****
% ***** GENERATE INITIAL CONDITIONS *****
% *****
%
% Initial conditions for the 'integrated system'
Z_init      = 0 ;           % m
Zdot_init   = 0 ;           % m/s
X_init      = 0;           % m
Xdot_init   = (8) * (1/3.6) % enter kph to yield m/s
Theta_init  = X_init/Reff;  % rad/sec
Thetadot_init = Xdot_init/Reff; % rad/sec

Throttle_initial = 0.00; % initial throttle fraction (0 to 1)
Throttle_final   = 0.00; % final throttle fraction (0 to 1)
Throttle_step_time = 0.00; % throttle step time (sec)
Throttle_lag      = 0.00; % throttle lag of 0.05 seems reasonable

% disp('Initial system velocity '); Xdot_init
% print speed table and prompt for speed in m/sec (13.42 m/sec=30 mph)
% for i = 1:1:8
%     x(:,i) = [(5*i) ; (5*i*3.6/1.609344)];
% end
% disp('');
% disp('    m/sec    mph');
% disp(x')
% disp(' ')
% Xdot_init= ('Initial speed in (m/s)? ')

% % prompt for simulation time, t_end
% disp(' ');
% t_end = ('Simulation end time (sec)? ')
% disp(' ')

% Assign each mass component its initial conditions
% Z conditions for all components
Z_ring_0      = Z_init;
Zdot_ring_0   = Zdot_init;
Z_rim_0       = Z_init;
Zdot_rim_0    = Zdot_init;
Z_truck_0     = Z_init;
Zdot_truck_0  = Zdot_init;

% X conditions for all components
X_ring_0      = X_init;
Xdot_ring_0   = Xdot_init;
X_rim_0       = X_init;
Xdot_rim_0    = Xdot_init;
X_truck_0     = X_init;
Xdot_truck_0  = Xdot_init;
X_tread_0     = X_init;
Xdot_tread_0  = Xdot_init;

% Theta conditions for all components

```

```
Theta_ring_0      = Theta_init;
Thetadot_ring_0  = Thetadot_init;
Theta_rim_0       = Theta_init;
Thetadot_rim_0   = Thetadot_init;
Theta_tread_0    = Theta_init;
Thetadot_tread_0 = Thetadot_init;

% Physical constants needed for the simulation
rho = 1.204;      % air density [kg/m^3]
Area = 1.8*1.5/4; % 1/4th the frontal area of the car [m^2]
Cd = 0.4;         % non-dimensional coefficient of aero
disp(' ')
disp('Completed Generate Initial Conditions...')
disp(' ')
```

```

% *****
% ***** GENERATE CAR FTRAC LUT *****
% *****

% generate_CAR_Ftrac_LUT                                16 Mar 07
% generates 3 Fx=fcn(Fz, slip G)

% clear
% format short
% format compact
% -----Input data For low vertical load Fz -----
disp(' ')
disp('Generating Fx as Fcn(Fz, Percent Slip)');
B=80; C=1.7; D=1; E=0.97;
for i = 1:1:201;
    G(i) = (i-101)/100;
    mu_lo_Fz(i) = -D*sin(C*atan(B*G(i)-E*(B*G(i)-atan(B*G(i)))));
end;
close all;
% Plot the 1st results
% figure
z = [G', mu_lo_Fz'];
plot(z(:,1),z(:,2),'r')
title('Mu vs Percent Longitudinal Slip and Fz',...
      'FontWeight','bold')
xlabel('Longitdinal Slip G')
ylabel('Longitudinal Mu (Fx/Fz)')
% legend('accel', 'vel','position')
grid on
hold on

% ---Generate the second curve for Medium vertical load Fz -----
B=20; C=2.0; D=1; E=0.99;
for i = 1:1:201;
    G(i) = (i-101)/100;
    mu_med_Fz(i) = -D*sin(C*atan(B*G(i)-E*(B*G(i)-atan(B*G(i)))));
end;

% Plot the 2nd results
% figure
z = [G', mu_med_Fz'];

% ---Generate the third curve for High vertical load Fz -----
B=8; C=2.2; D=1; E=1.01;
for i = 1:1:201;
    G(i) = (i-101)/100;
    mu_hi_Fz(i) = -D*sin(C*atan(B*G(i)-E*(B*G(i)-atan(B*G(i)))));
end;

% Plot the 3rd results
% figure
z = [G', mu_hi_Fz'];
% plot(z(:,1),z(:,2),'b')

```

```

% legend('Fz = 9.45 kN', 'Fz = 24.8 kN','Fz = 40.9 kN')
% -----
load_vector = [508*9.801*0.25 , 508*9.801*1.00, 508*9.801*2.00 ]';
slip_vector = G;
Fx_table = [ mu_lo_Fz *load_vector(1,1)  ;
             mu_med_Fz*load_vector(2,1)  ;
             mu_hi_Fz *load_vector(3,1)  ];

figure
plot(G, Fx_table(1,:), 'r-', G, Fx_table(2,:), 'g:', G, Fx_table(3,:), 'b-.')
title('Typical Fx vs. Longitudinal Slip For Constant Loads Fz',...
      'FontWeight','bold')
xlabel('Longitdinal Slip G')
ylabel('Longitudinal Force Fx')
legend('Fz = 1.245 kN', 'Fz = 4.979 kN','Fz = 9.957 kN')
grid on

disp(' ')
disp('Completed Generate Car Ftrac Look Up Tables...')
disp(' ')

```

```

% *****
% ***** GENERATE CAR SHIFT AND ENGINE TORQUE LUTS *****
% *****

% generate_CAR_shift_program_and_engine_torque_LUT
% MANUAL transmission
diff_ratio      = 4.10;          % 2.64 in spec sheet
efficiency      = 0.95;          % total driveline efficiency
% Reff          = 0.480;          % effective tire radius (m)
% Only use this Reff for troubleshooting - must synchronize
% with the initial condition file -

% MANUAL transmission only gear ratios
gear_ratio_6    = 0.84;
gear_ratio_5    = 1.00;
gear_ratio_4    = 1.25;
gear_ratio_3    = 1.72;
gear_ratio_2    = 2.61;
gear_ratio_1    = 4.46;

% AUTOMATIC transmission only gear ratios
%gear_ratio_4   = 0.69;
%gear_ratio_3   = 1.00;
%gear_ratio_2   = 1.57;
%gear_ratio_1   = 2.84;

% Speed (mps)to shift to next higher gear = mph*(1 mph = 0.44704 m/sec)

MPS_5_6 = 90*0.44704; % 90 MPH * 0.44704 = 40.2336 m/sec (5th => 6th)
MPS_4_5 = 75*0.44704; % 23
MPS_3_4 = 50*0.44704; % 18
MPS_2_3 = 35*0.44704; % 14
MPS_1_2 = 20*0.44704; % 9   4.0234 m/sec

% Data for RPM vs Torque LUT
% RPM and TORQUE in Nm
% Six Cylinder 60deg V, 3778 cc 230.5 in^3, 12 OHV, roller followers,
% Hydraulic lifters, SMPFI
% Peak 205HP (153 kW) @ 5200 RPM, 240 ft-lb torque (325 Nm)
Engine_RPM_Breakpoints = [400 800 1200 1600 2000 2400 2800 3200 3600...
                          4000 4400 4800 5200 5600 6000 6400];
Engine_Torque_Data = [ 0 182 198 206 212 220 217 224 233...
                      233 232 227 211 191 161 0];

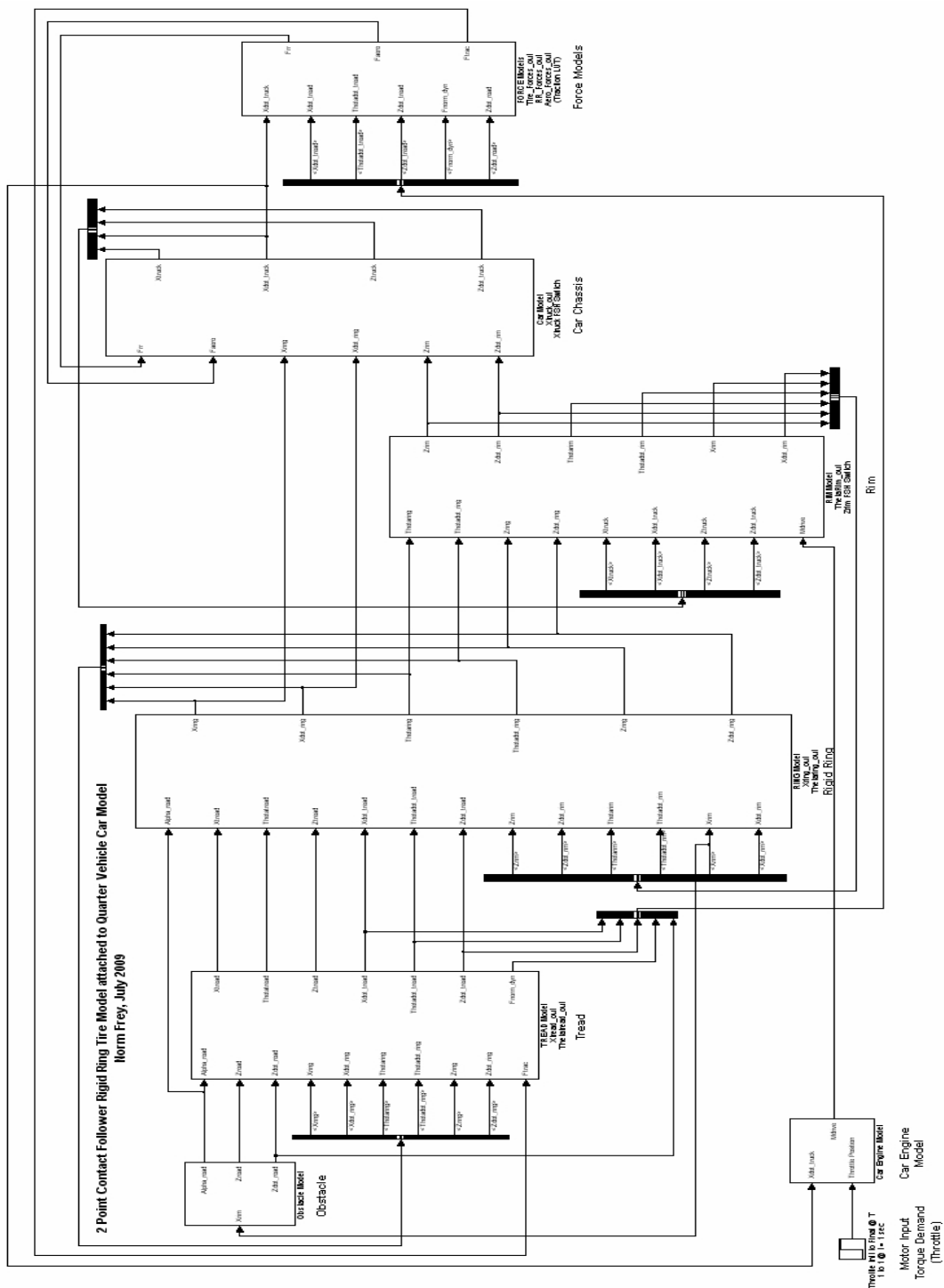
%convert torque to Nm
Engine_Torque_Data = 1.35582 .* Engine_Torque_Data;

disp(' ')
disp('Completed Car shift program and engine torque Look up tables...')
disp(' ')

```

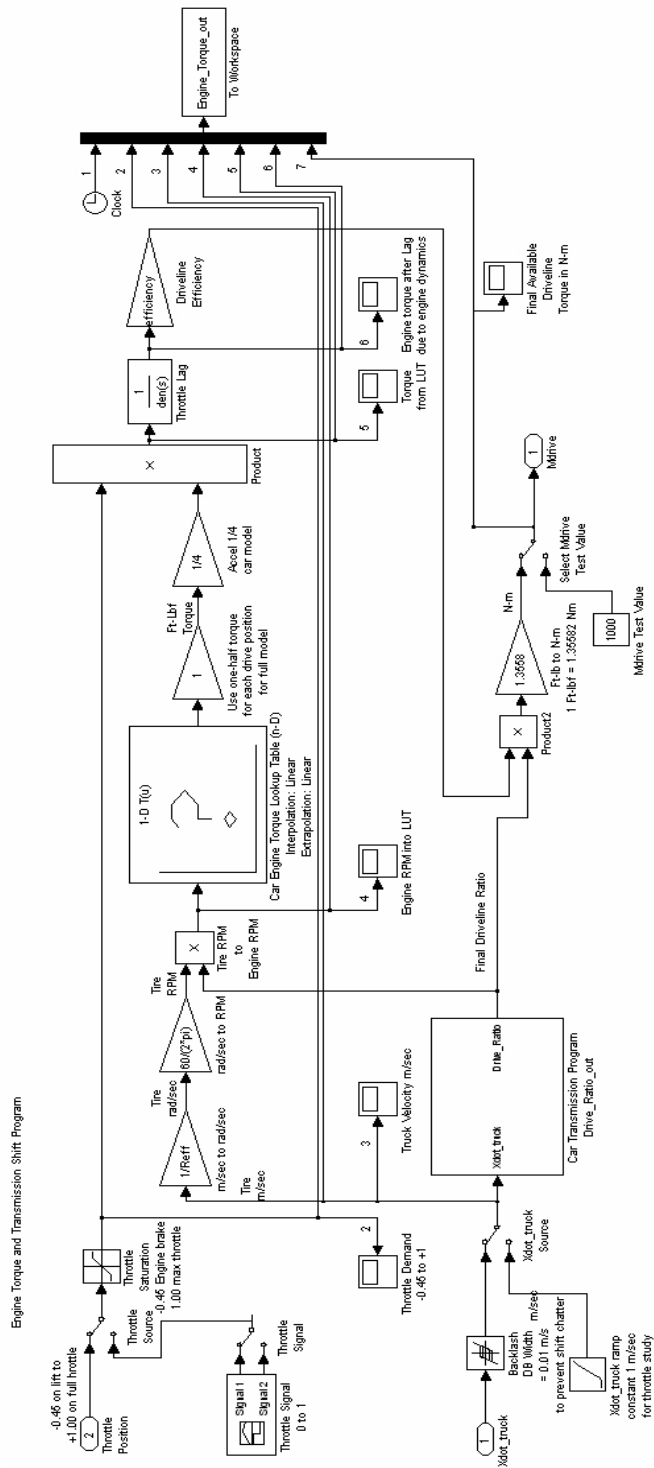
## Two Point Rigid Ring Simulink Diagrams

### Quarter Vehicle – Main Program Level (1 of 18)

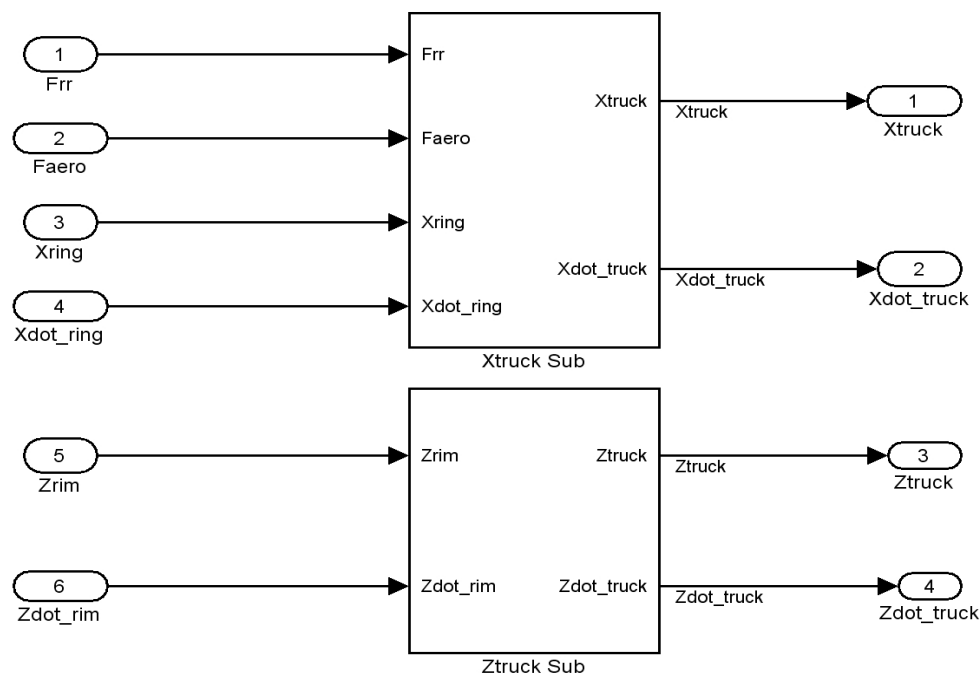
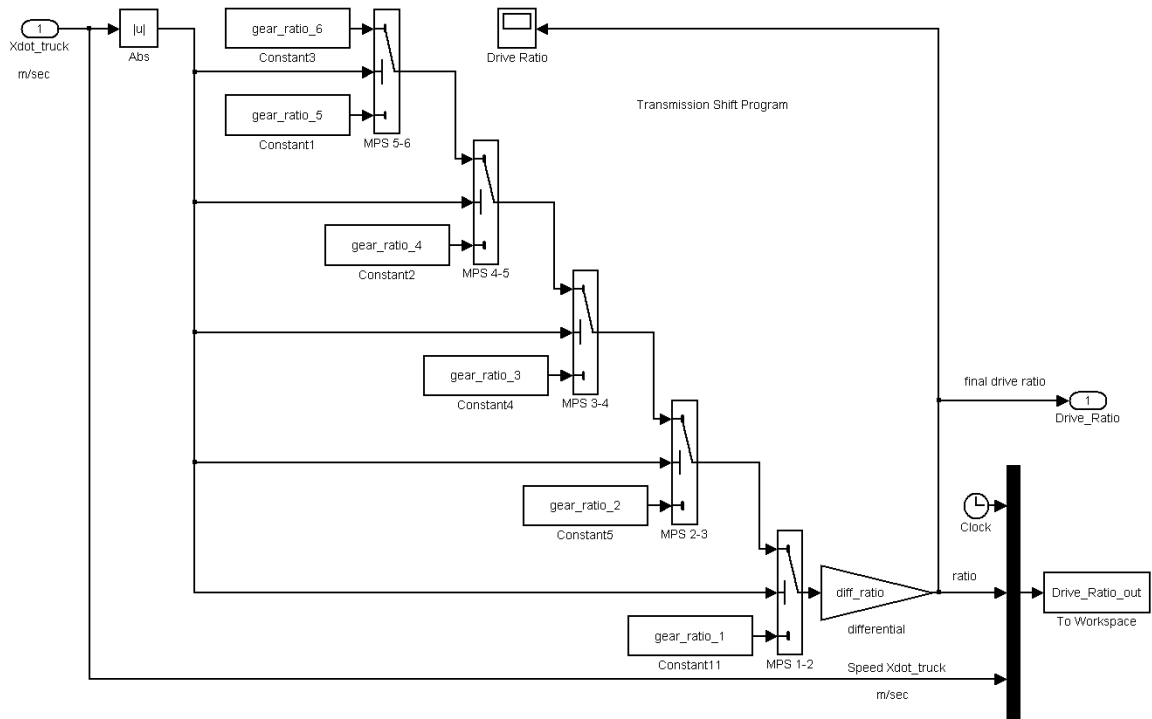




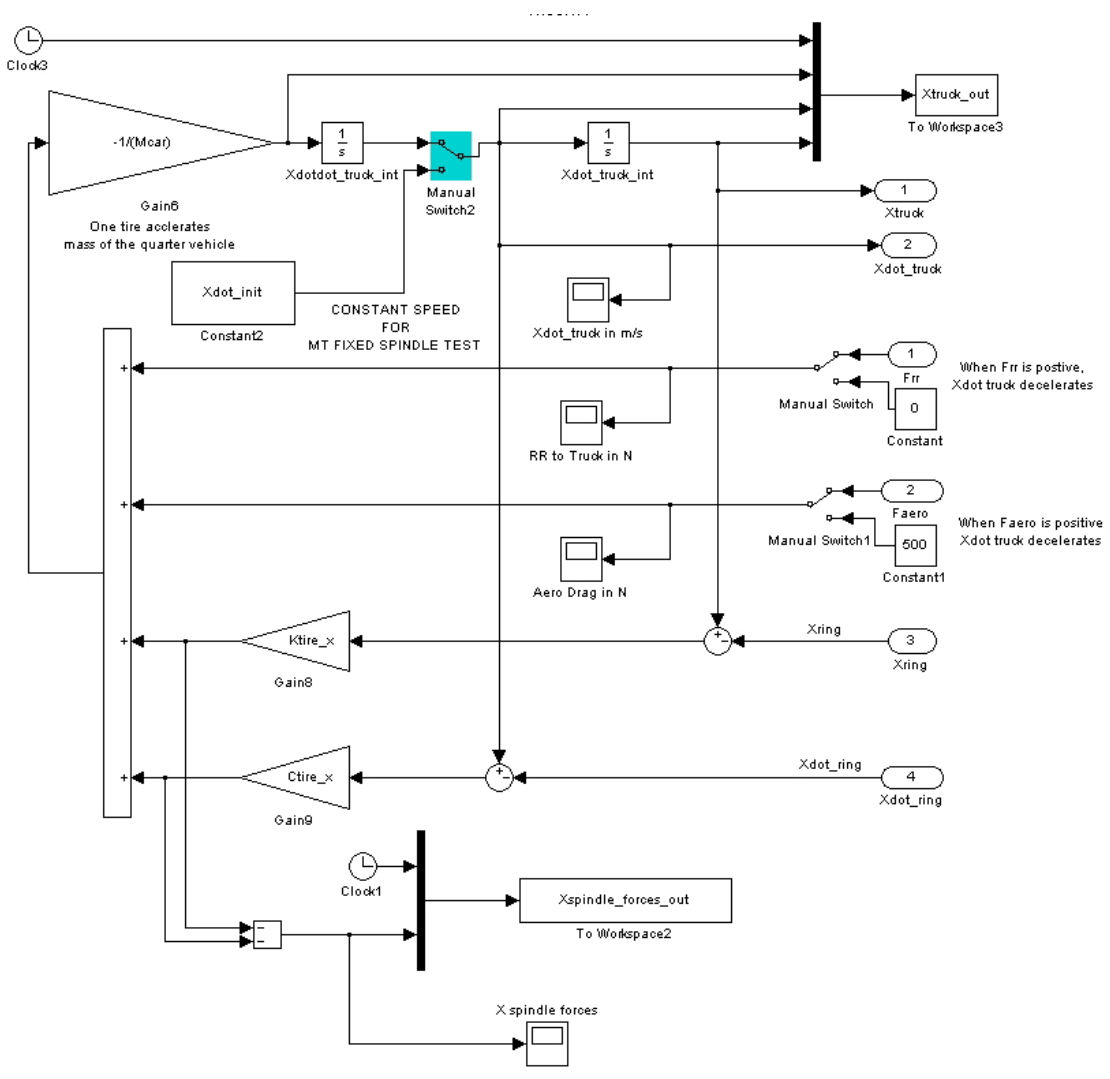
Quarter Vehicle – Engine Torque Demand Program (2 of 18)



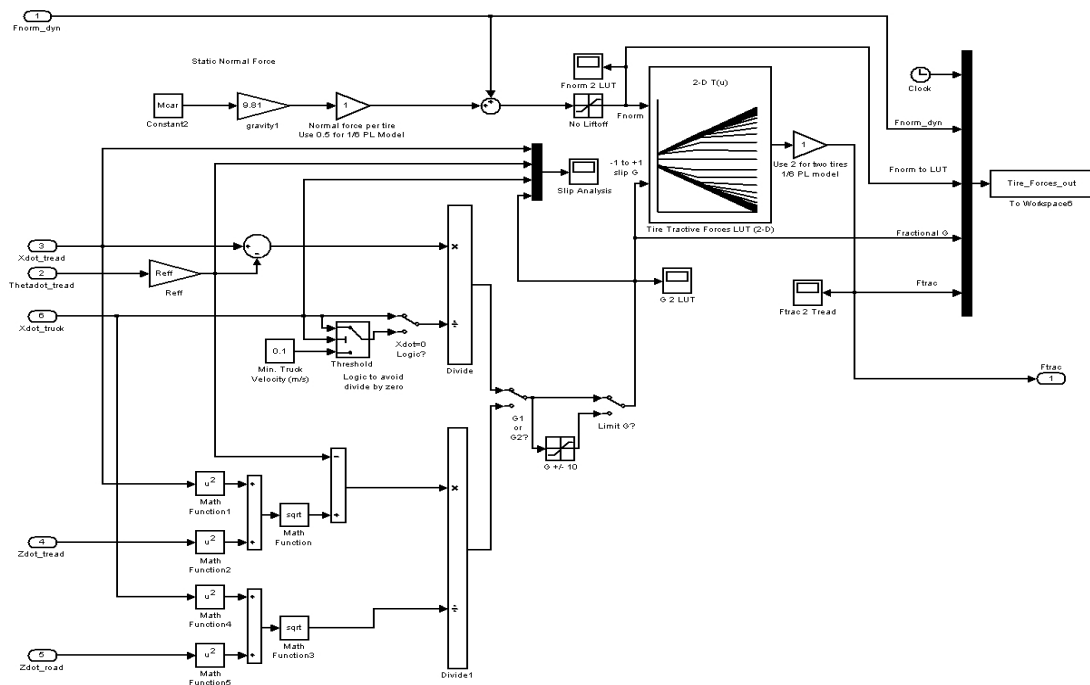
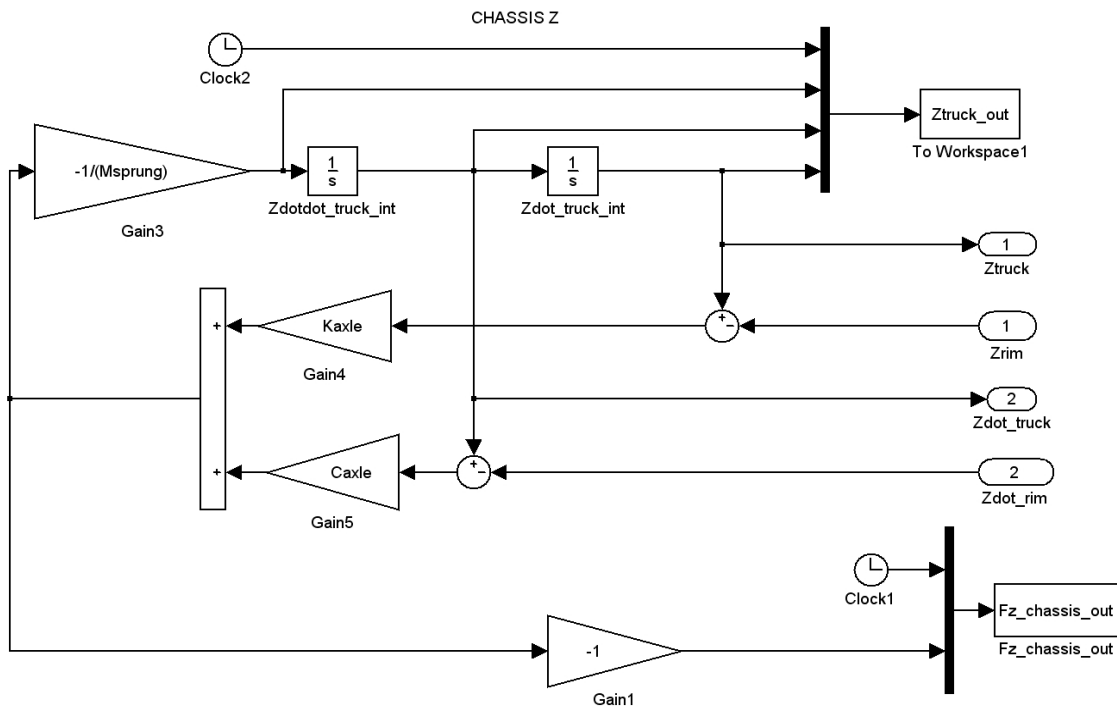
Quarter Vehicle – Transmission Shift and Chassis Top Level (3 of 18)



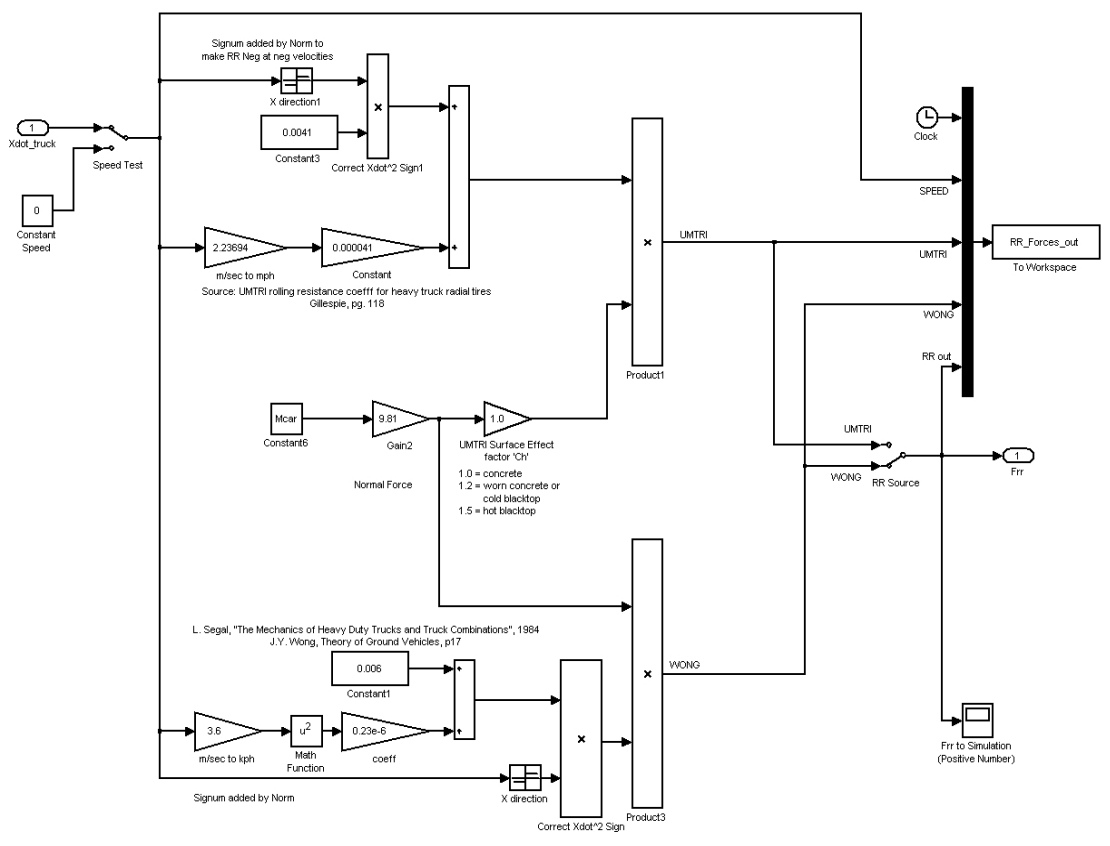
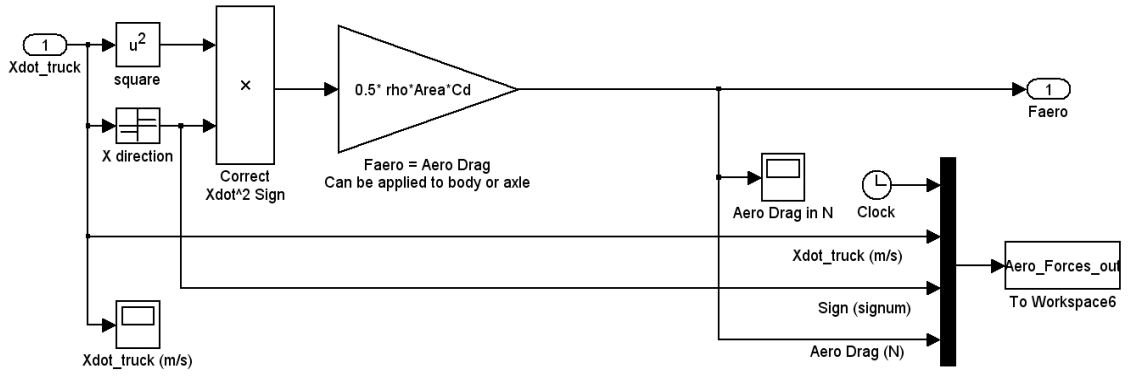
### Quarter Vehicle – Chassis Longitudinal X (4 of 18)



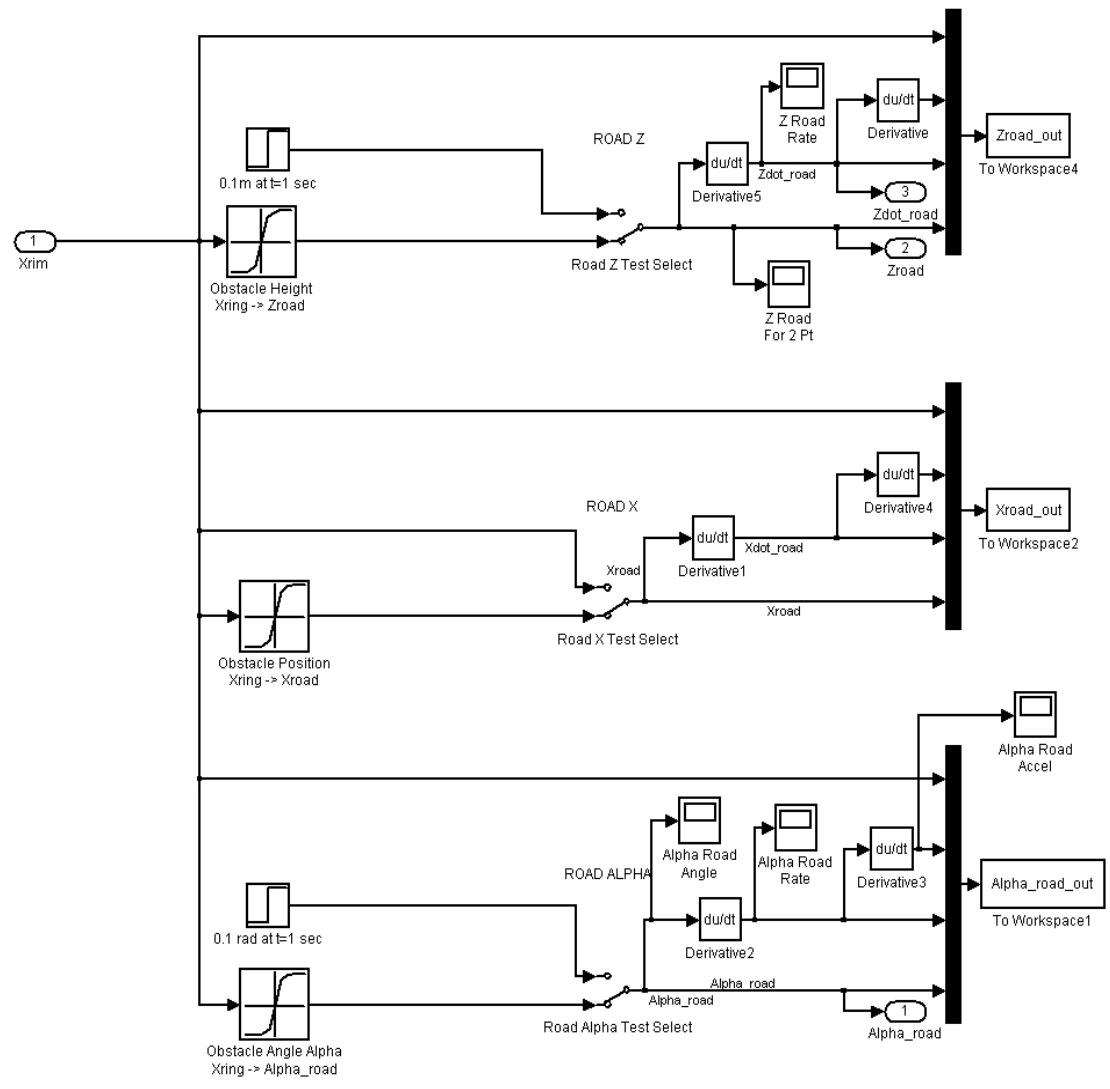
Quarter Vehicle – Chassis Vertical Z and Traction Model (5 of 18)



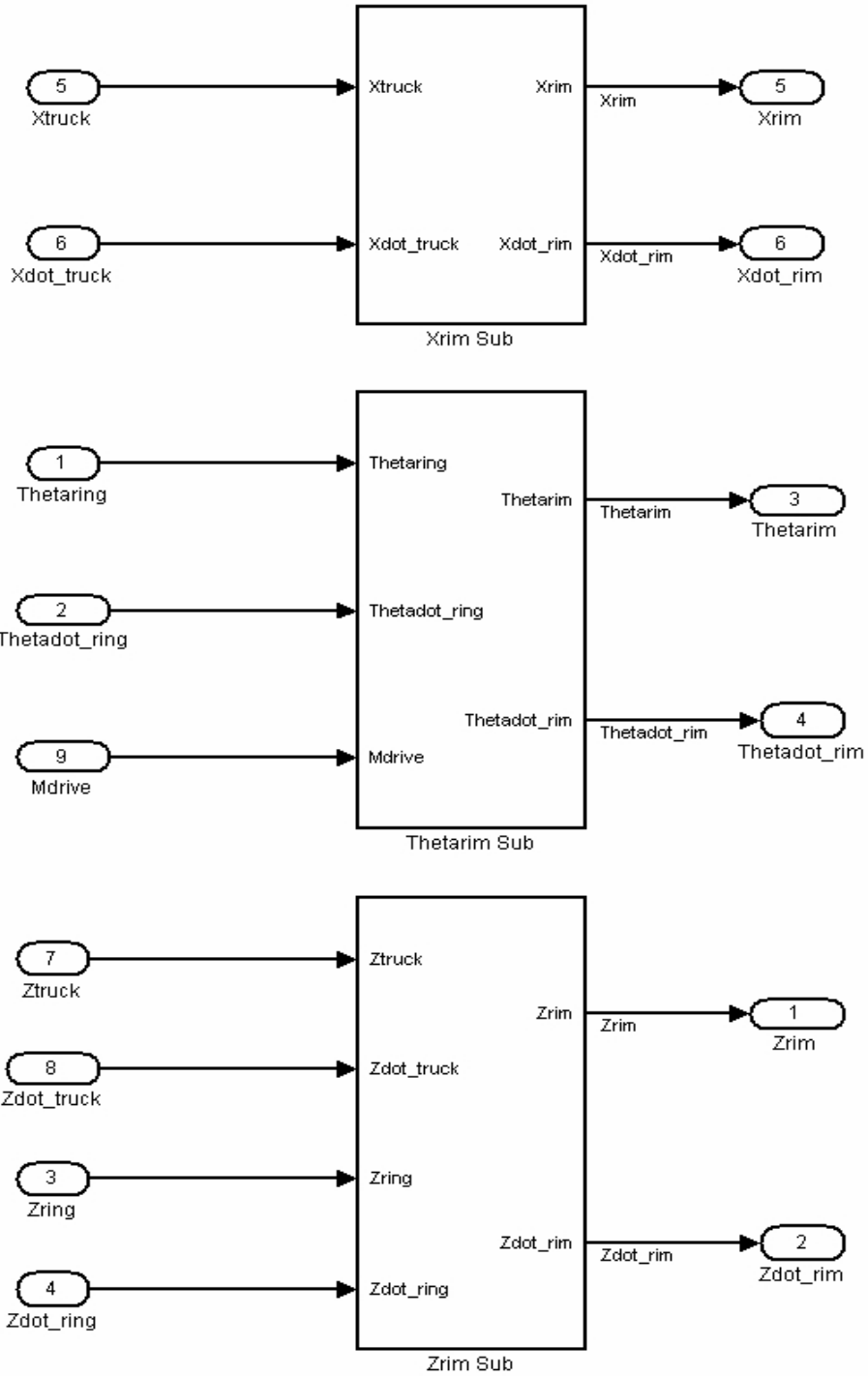
Quarter Vehicle – Aero Drag and Rolling Resistance Models (6 of 18)



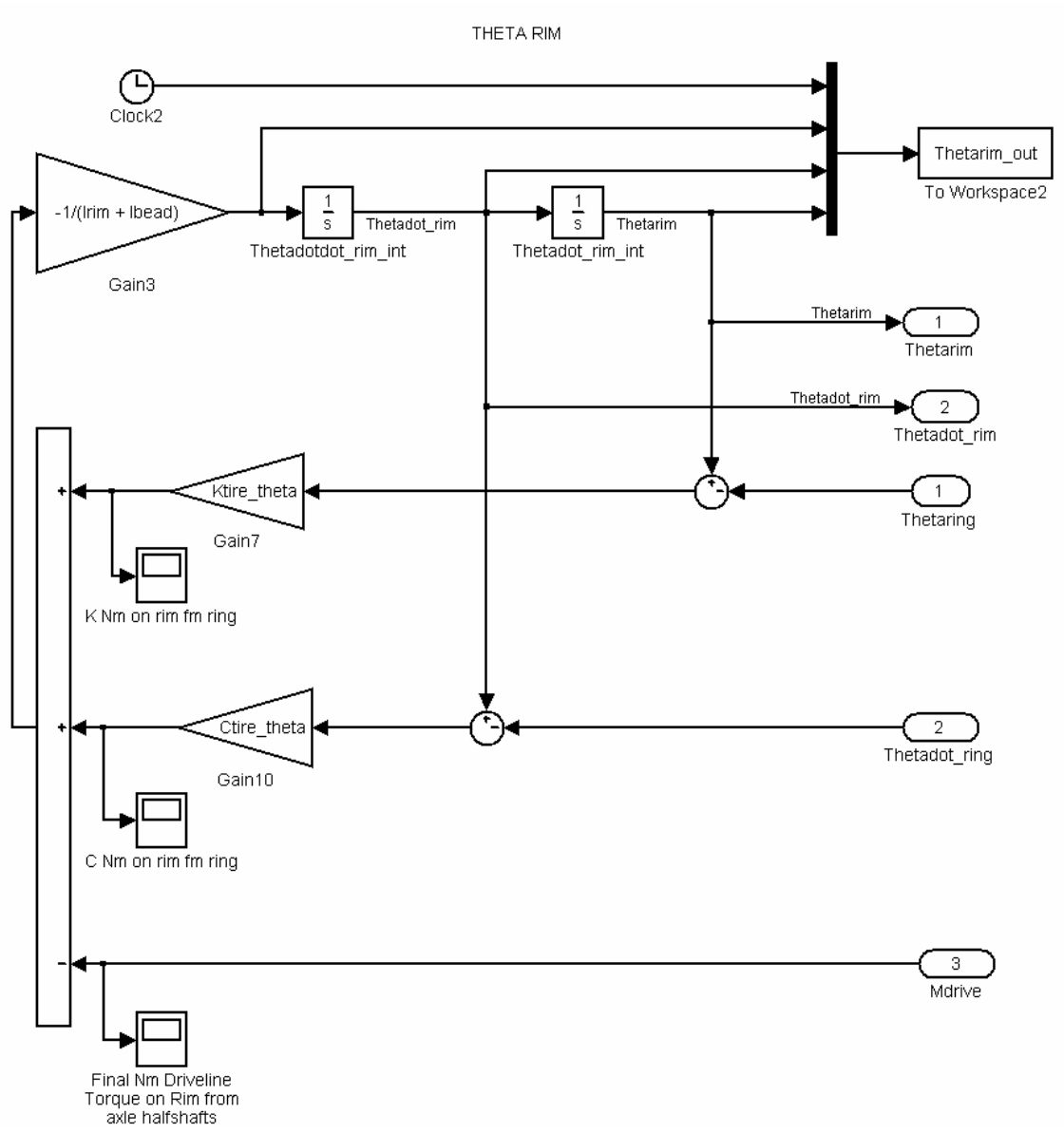
### Quarter Vehicle – Obstacle Look Up Tables (7 of 18)



## Quarter Vehicle – Rim Model Top Level (8 of 18)

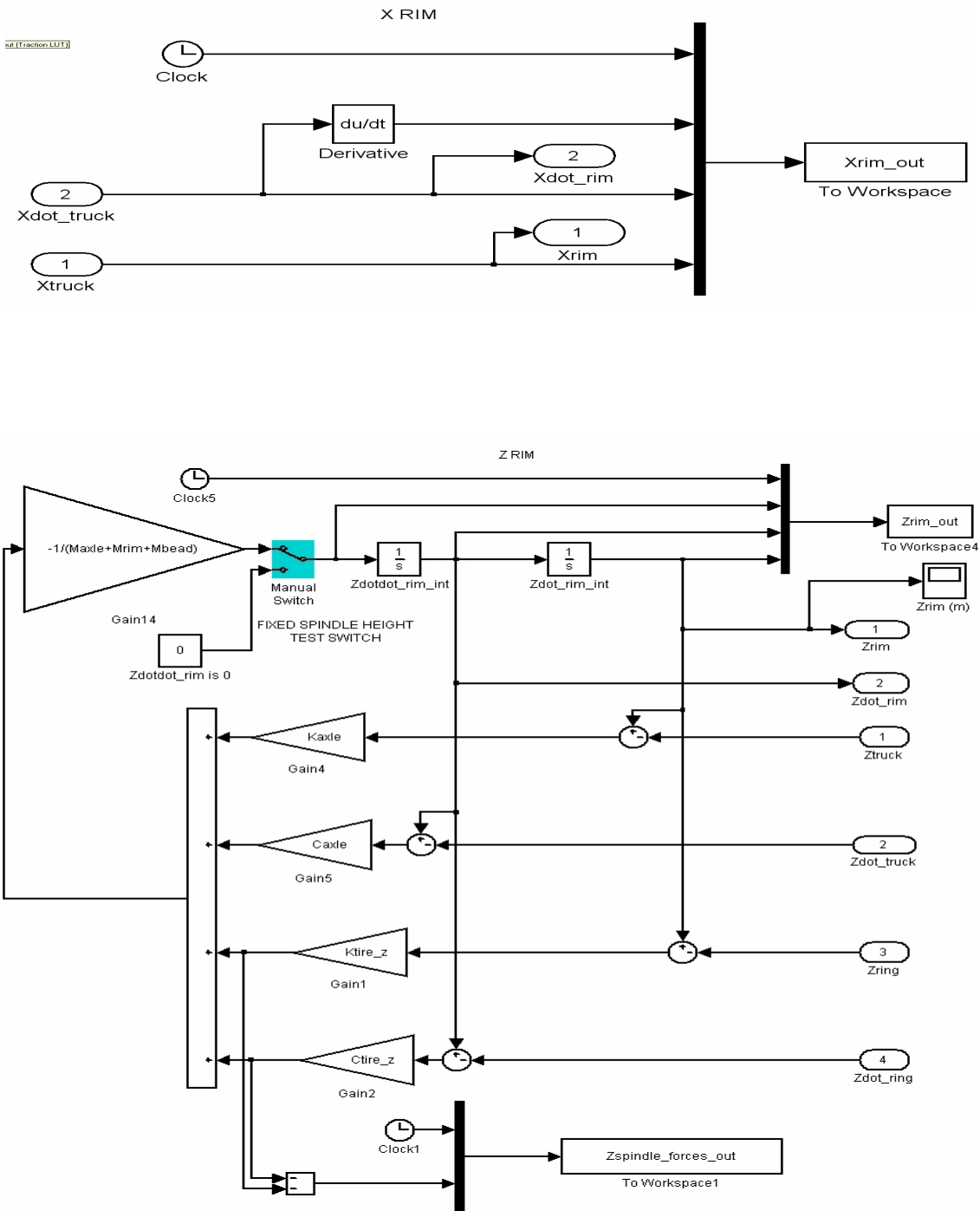


Quarter Vehicle – Rim Rotational Model (9 of 18)

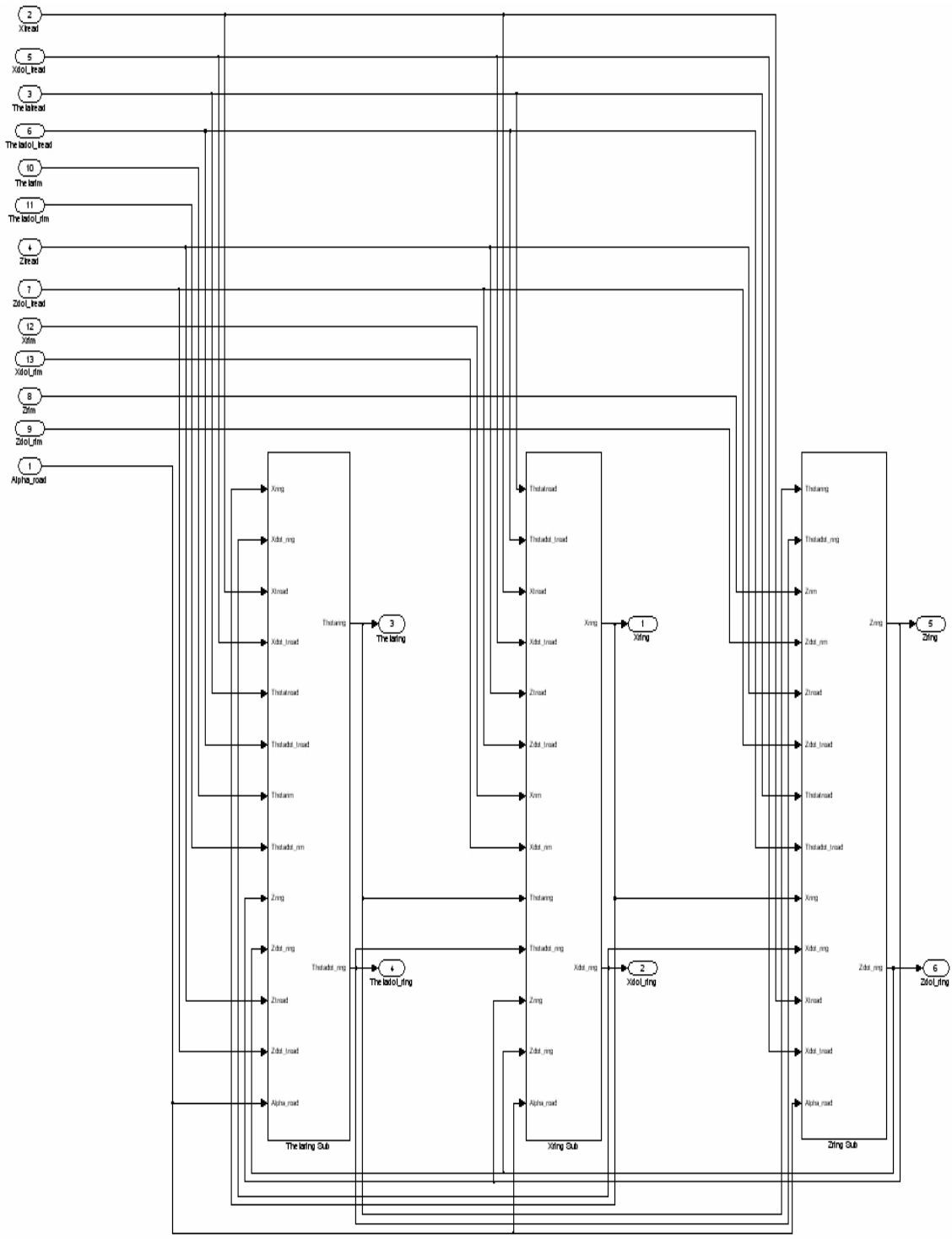




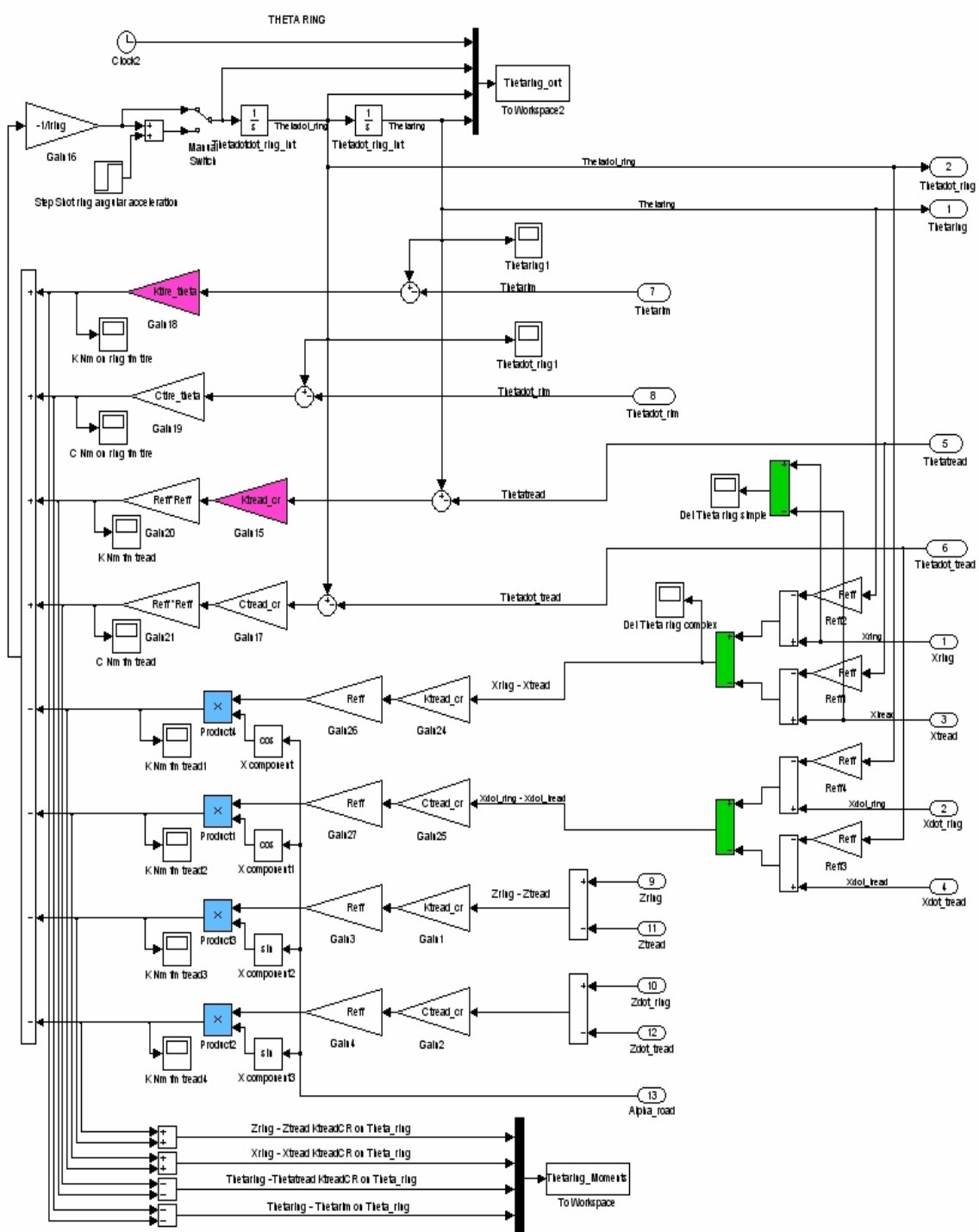
Quarter Vehicle – Rim Longitudinal X and Vertical Z (10 of 18)



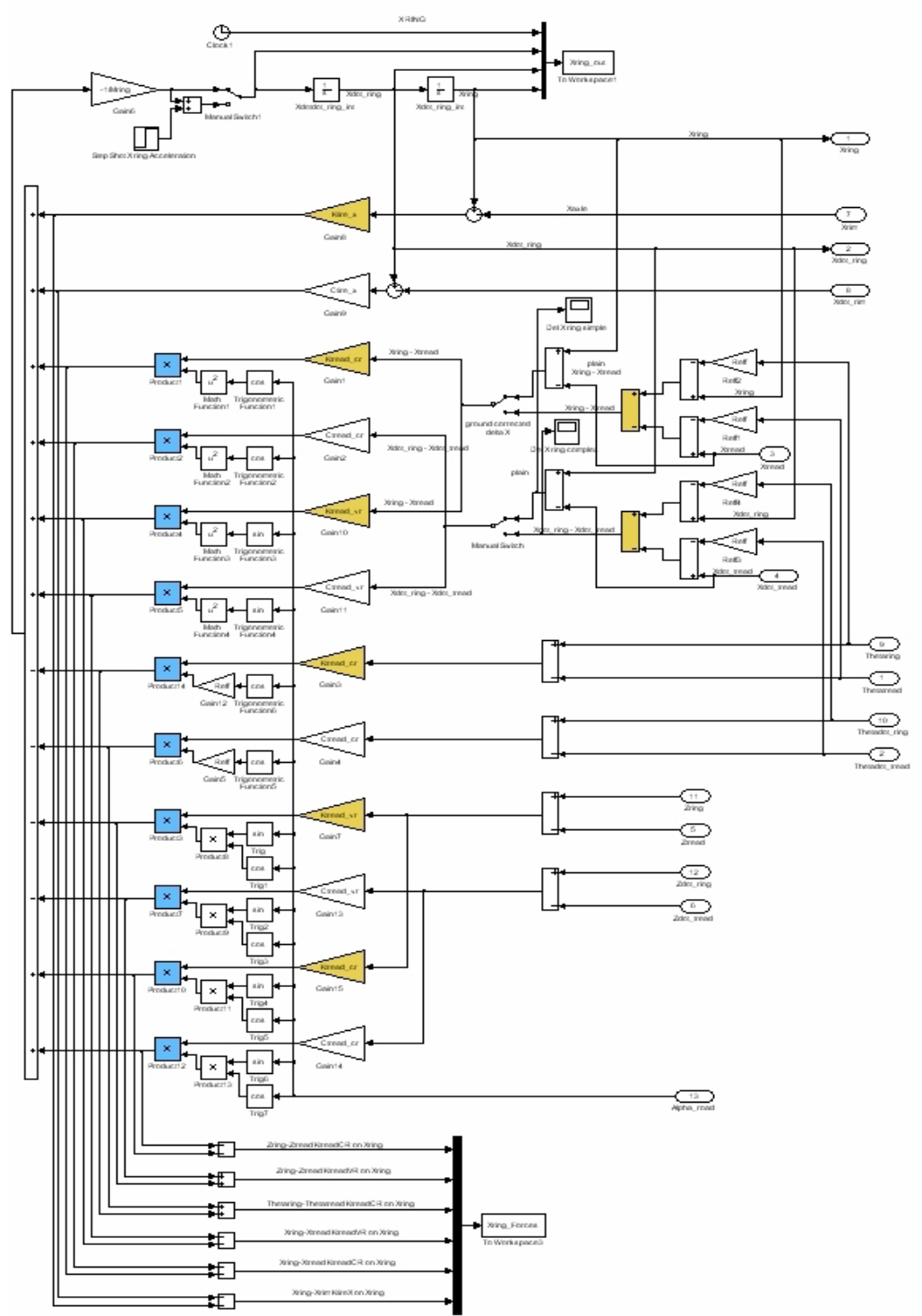
### Quarter Vehicle – Ring Model Top Level (11 of 18)



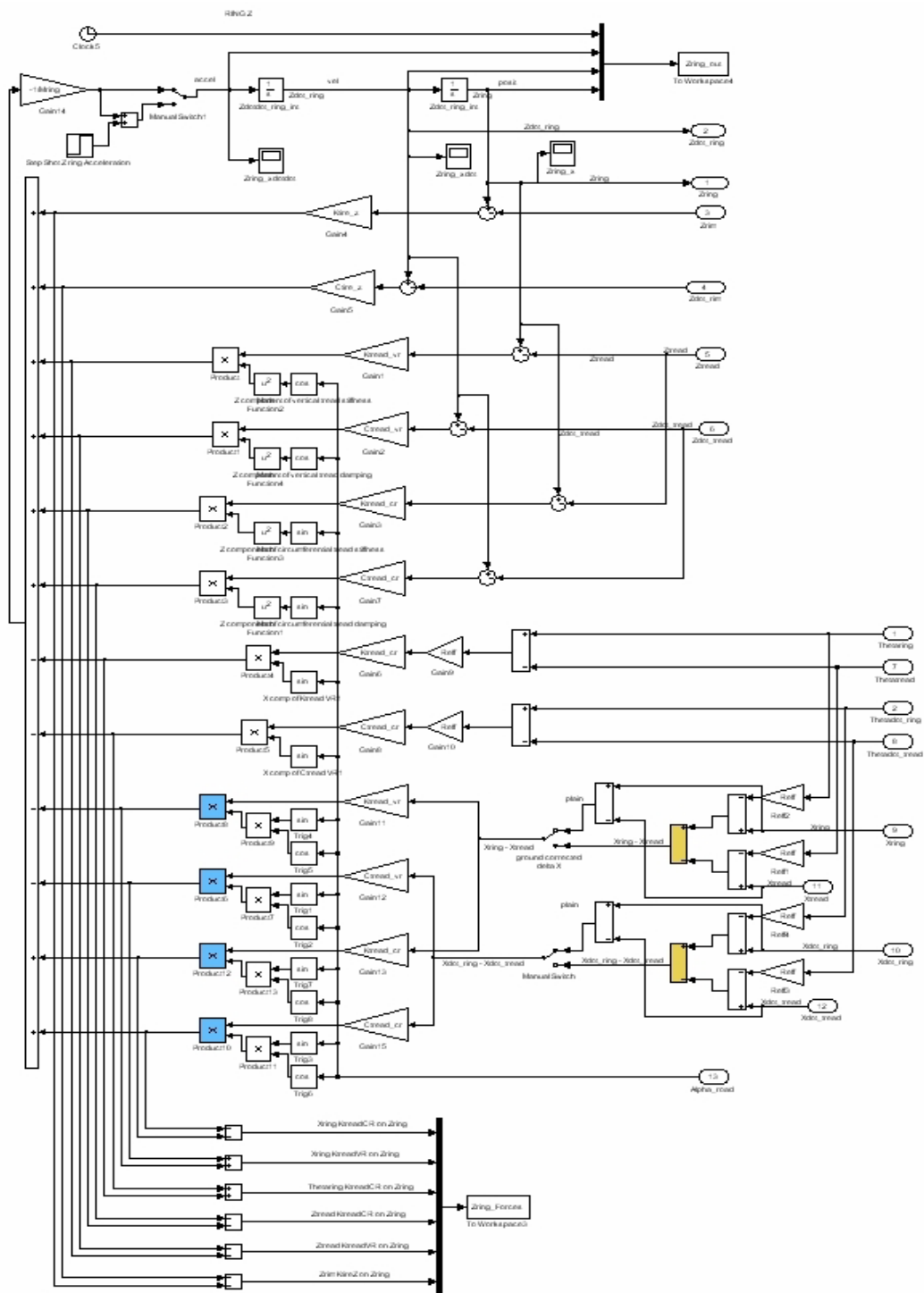
Quarter Vehicle – Ring Rotational Model..(12 of 18)



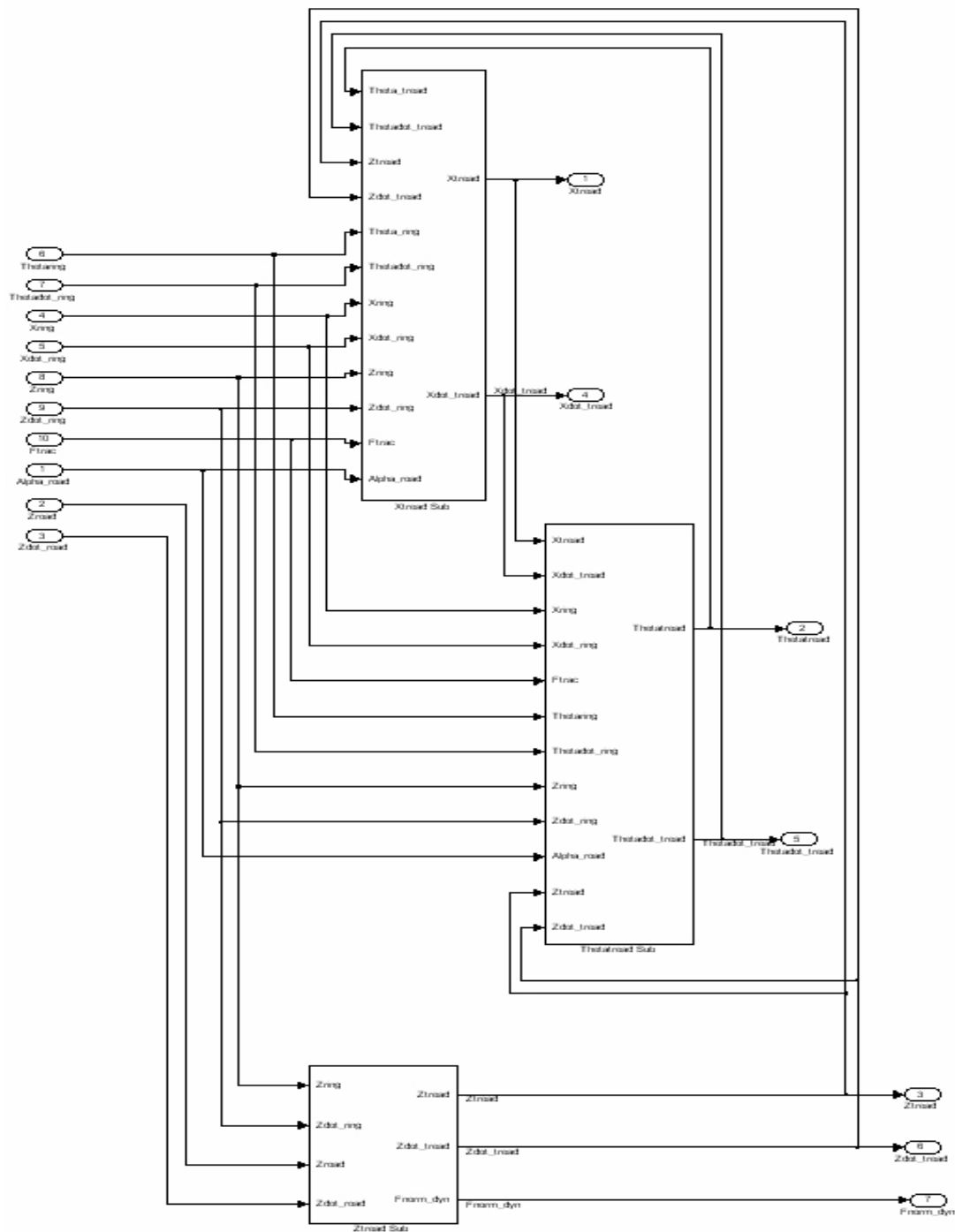
### Quarter Vehicle – Tire Rigid Ring Longitudinal Model (13 of 18)



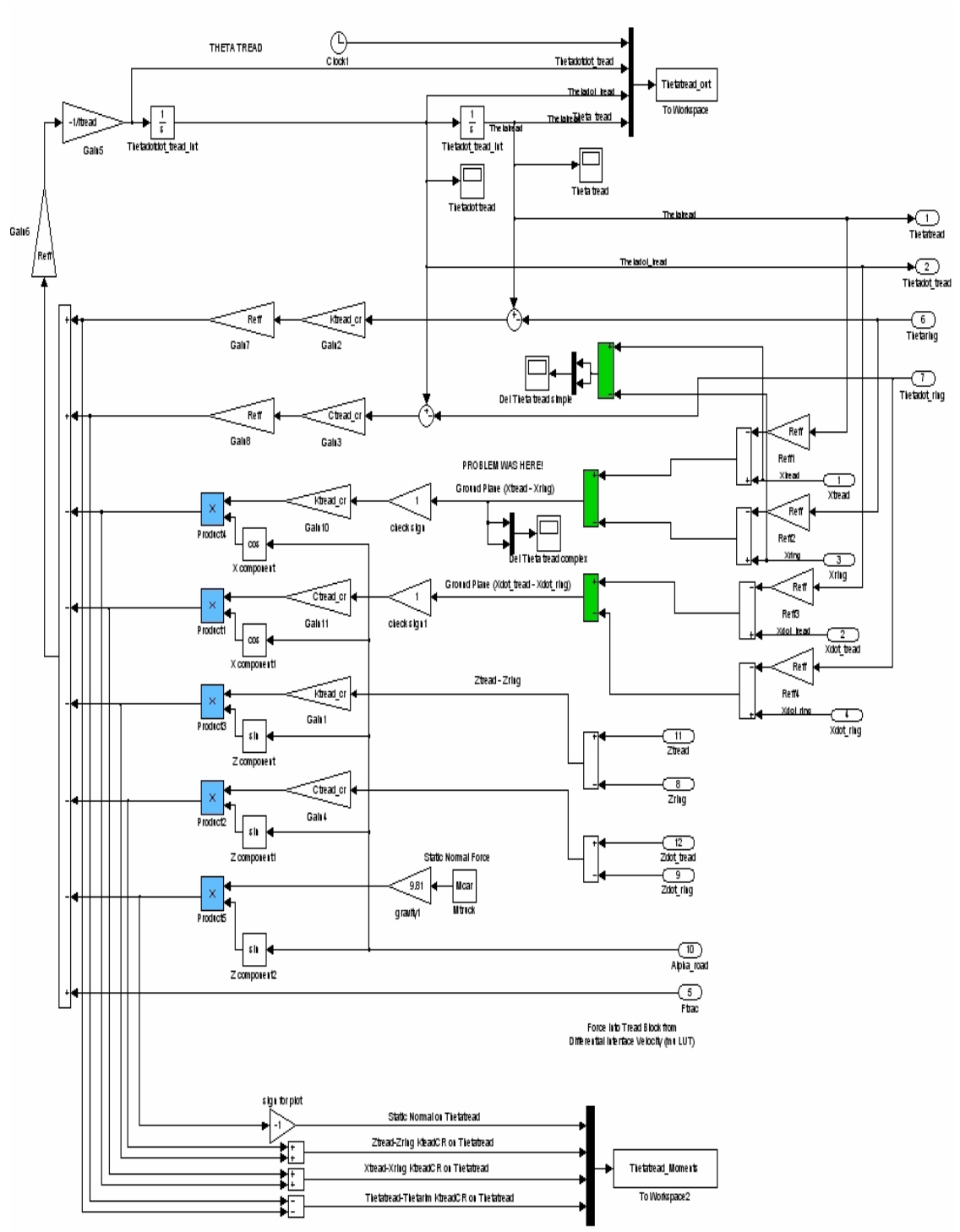
Quarter Vehicle – Tire Rigid Ring Vertical Model (14 of 18)



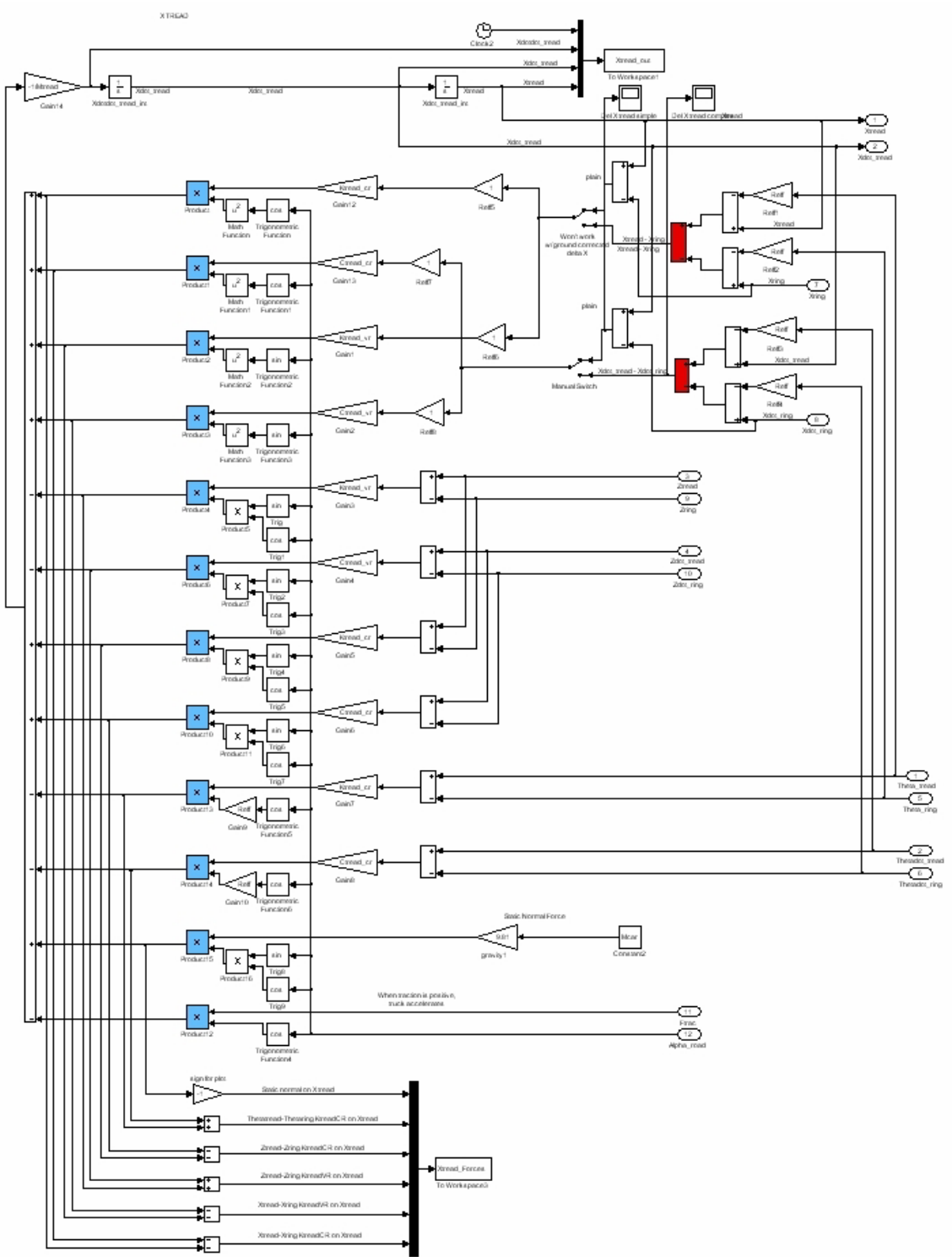
Quarter Vehicle – Tire Tread Model – Top Level (15 of 18)



### Quarter Vehicle – Tire Tread Rotational Model (16 of 18)

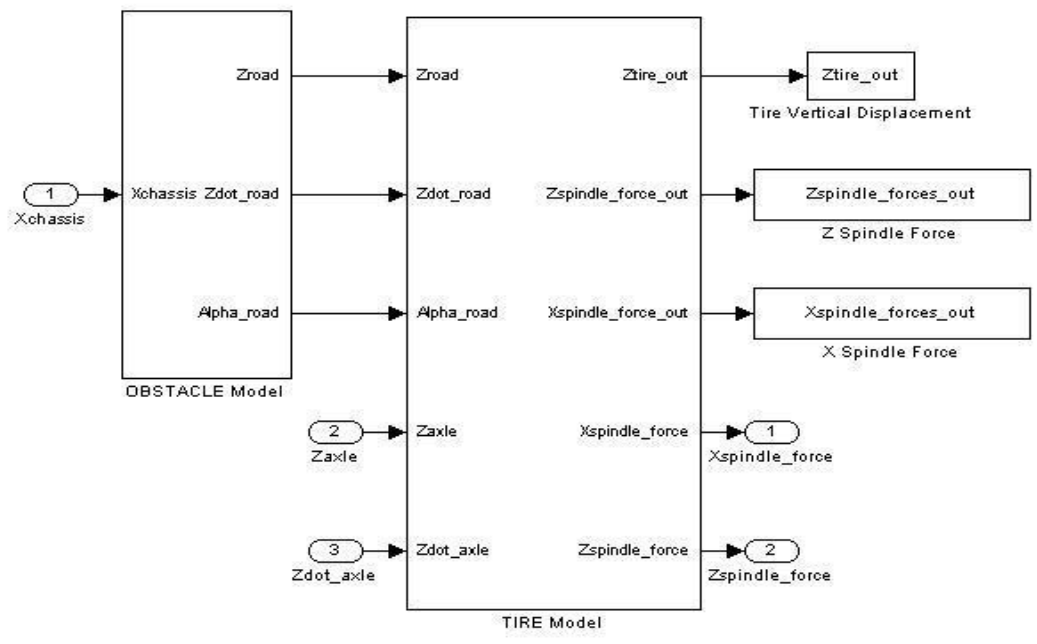
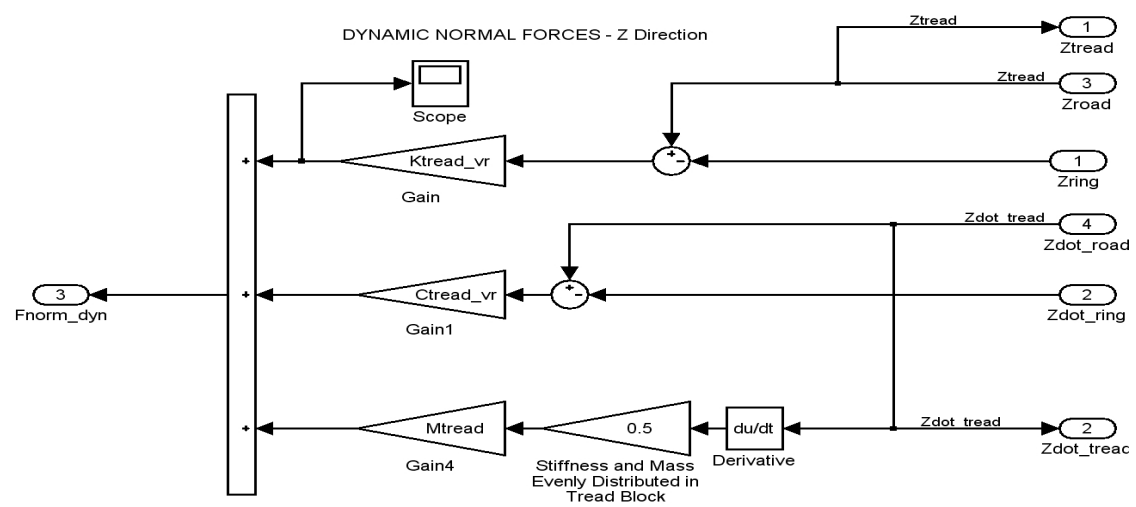


### Quarter Vehicle – Tire Tread Longitudinal Model (17 of 18)





Quarter Vehicle – Tire Tread Vertical Model and Tire Model Top Level (18 of 18)



## Appendix F

### F. Development of the Roadway Smooth Bump and Cleat Obstacles

#### Spatial Frequency Analysis

The original intention of the tire model was to provide a means of determining the effect of basic tire mass and stiffness properties on vehicle comfort as the vehicle traversed over a relatively long (12 inches) and tall (4 inches) speed bump at parking lot speeds. The vehicle itself could be either coasting or accelerating as it traversed the speed bump. Assuming that the maximum speed during engagement of the obstacle was 10 Kph, a calculation of the spatial frequency was necessary to calculate the approximate frequency range of interest in order to determine the required complexity of the tire model to ensure that it was suitable for exciting the vehicle. The calculation of the spatial frequency is performed using Equation F.1, below:

$$\text{spatial frequency } \nu = \frac{1}{\text{wavelength } \lambda} \text{ cycles per second (cps)} \quad (\text{F.1})$$

Ignoring the frequency content associated with the transition between the sinusoidal waveform bump and the horizontal roadway, the sinusoidal bump will represent one wavelength of the fundamental frequency. Substituting in a vehicle speed of 10 Kph into equation F.1 and converting into MKS units yields:

$$\nu = \frac{1 \text{ cycle}}{(12 \text{ inches} * 0.0254 \text{ m / inch})} \times \frac{1000 \text{ m}}{\text{km}} \times \frac{10 \text{ km}}{\text{hr}} \times \frac{1 \text{ hr}}{3600 \text{ sec}} \text{ cps} \quad (\text{F.2})$$

Solving for  $\nu$ :

$$\text{spatial frequency } \nu = 9.1 \text{ Hz} \quad (\text{F.3})$$

Using the engineering “rule of thumb” that the model of a system must be able to accurately represent a frequency approximately ten times greater than the frequency of interest, the tire model must therefore be capable of reasonable fidelity of approximately 91 Hz at the highest anticipated vehicle speed. Thus both the Cosin FTire and SIMPACK Automotive Plus multi-body simulation program would be operating within their domain of applicability.

This application of spatial frequency analysis and engineering rule of thumb assumes that the sinusoidal bump input can be represented by a true sinusoidal input. In reality, the slope of the roadway and the sinusoidal bump is not continuous and therefore represents a higher frequency input. However, this has not proven to be an issue with the robust solvers of either MatLab Simulink or Intec SIMPACK software suites. In addition, the relatively small magnitude of the instantaneous change in slope (dependent upon how the tire model represents the contact patch and its engagement with the obstacle) is overshadowed by the magnitude of the lower-frequency sinusoidal input.

Both the spatial frequency and the discontinuity in slope have to again be considered in the case of the cleat input. By the nature of the tire test machine (fixed spindle height, variable spindle force), the cleat is limited in height (9.5 mm) so as not to over-range the spindle force sensors during operation with the highest anticipated tire dynamic vertical spring rates. Likewise, by the nature of the intended testing of the machine, the cleat is also limited in length to 19mm in order to observe the ability of a tire to absorb road irregularities shorter in length than the tire footprint, or the so called

“enveloping power” of the tire. Since the square cleat represents one wavelength per every 19 mm, one can substitute the appropriate values into Equation I.2 to yield the spatial frequency of the cleat obstacle to at 10 Kph:

$$\nu = \frac{1 \text{ cycle}}{(19 \text{ mm} * 1 \text{ m} / 1000 \text{ mm})} \times \frac{1000 \text{ m}}{\text{km}} \times \frac{10 \text{ km}}{\text{hr}} \times \frac{1 \text{ hr}}{3600 \text{ sec}} \text{ cps} \quad (\text{F.4})$$

Calculating the frequency in cps (Hz) yields an ideal maximum solicitation frequency at 10 Kph.

$$\text{spatial frequency } \nu = 146 \text{ Hz} \quad (\text{F.5})$$

If one is to again follow the engineering thumb rule that a model or a measurement system must be able to support reasonable fidelity at a frequency ten times that of the frequency of interest, our best case scenario requires model fidelity at 1,460 Hz – none of the available tire models or MBS packages are representative at this frequency. In the case of the tire response, the mode shapes of the tire are excited as a complex continuous media and which can not be suitably modeled by the simple system of lumped masses and rigid belt ring in the summit. The tread band and summit band ring interactions need to be taken into consideration, and the true physical mechanisms by which the tire generates vertical, torsional, and longitudinal stiffnesses must be more accurately represented. From the perspective of the MBS software, the bodies making up the tire model need to be sufficiently small and their boundary interactions sufficiently defined so that the mode shapes at these higher frequencies are captured - essentially requiring a complex collection of masses and dampers approaching that of a finite element mesh. Simply stated, the tire modes that occur at approximately 100 Hz cannot be reasonably

modeled using a lumped parameter approach, and therefore the transfer function between the tire contact patch and the wheel spindle cannot be represented by this approach. The only options for representing a cleat response, per Equation (F.4), is to either 1) develop a cleat with a long width to increase the path length or to 2) slow the tire longitudinal path velocity.

Assuming that the upper limit of frequency response for our models is 100 Hz and that the engineering thumb rule for sampling frequency holds true, the spatial frequency must be less than 10 Hz. Using the spatial frequency equation, the maximum speed  $V_{max}$  at which the tire model can be modeled as it encounters an obstacle can be calculated.

Substituting in 10 Hz and 19mm into the spatial frequency equation F.4 yields:

$$v_{max} = \frac{1 \text{ cycle}}{(19 \text{ mm} * 1 \text{ m} / 1000 \text{ mm})} \times \frac{1000 \text{ m}}{\text{km}} \times \frac{V_{max}}{\text{hr}} \times \frac{1 \text{ hr}}{3600 \text{ sec}} \text{ cps} \quad (\text{F.6})$$

Substituting in for the maximum spatial frequency of 10 Hz yields:

$$10 \text{ Hz} = \frac{1 \text{ cycle}}{(19 \text{ mm} * 1 \text{ m} / 1000 \text{ mm})} \times \frac{1000 \text{ m}}{\text{km}} \times \frac{V_{max}}{\text{hr}} \times \frac{1 \text{ hr}}{3600 \text{ sec}} \text{ cps} \quad (\text{F.7})$$

Rearranging, converting Hz to cycles/sec and solving for  $V_{max}$  in Kph yields:

$$\frac{10 \text{ cycles}}{\text{sec}} \times \frac{1 \text{ km}}{1000 \text{ m}} \times \frac{3600 \text{ sec}}{1 \text{ hr}} \times \frac{(19 \text{ mm} * 1 \text{ m} / 1000 \text{ mm})}{1 \text{ cycle}} = \frac{V_{max} \text{ km}}{\text{hr}} \quad (\text{F.8})$$

Hence  $V_{max}$  is approximately 0.7 Kph. Unfortunately, this is not only well below the 8 Kph minimum speed of the available test machine that was hoped to provide correlation data between the tire model and experimental results, it also assumes that the cleat represents frequency content that is no higher than that of a sinusoidal input equal to the

cleat length. Therefore, the use of the fixed spindle height machine test at 8 Kph to validate the model as it runs over the cleat is not considered capable of providing more than a qualitative result to test for robustness as opposed to the mathematical correctness of the tire model.

### Development of the Sinusoidal Bump Obstacle

The sinusoidal bump is one of a variety of commercially available parking lot speed bumps designed to limit the speed of parking lot vehicular traffic to speeds typically less than 10 Kph. The pre-formed sinusoid bumps are made of a variety of materials, including fiberglass/resin composite, plastic, high density polymers and other appropriate materials. They can be designed such that they are anchored permanently during the asphalt paving process, or installed with spikes or screw anchors that are intended to provide either permanent or semi-permanent installation on pre-existing pavement.

The size of the sinusoid bump used in this study is approximately 12 inches long and 4 inches high. The geometry of the sinusoidal bump needs to be described in both horizontal and vertical distances relative to the ground reference so that the forces on the components of the tire model can be solved by the time step integration solvers of either MatLab Simulink or Intec SIMPACK multi-body simulation software. The geometry of the sinusoidal bump and the tire tread blocks are illustrated in Figure F.1, below.

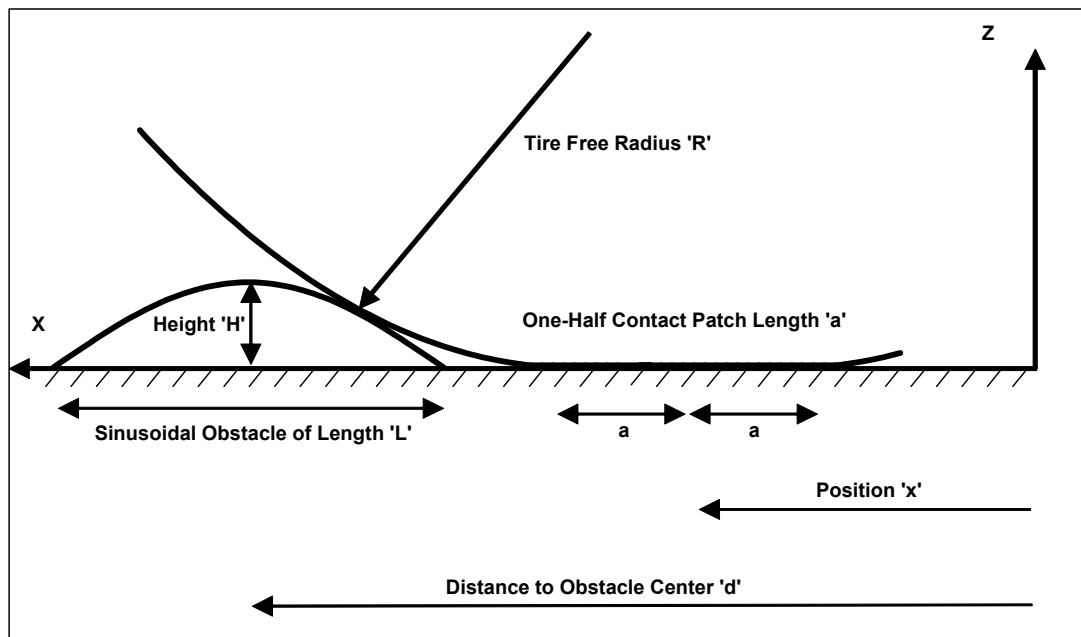


Figure F.1 Geometry of Sinusoidal Roadway Obstacle and Tire

The interaction between the tire model and the roadway obstacle geometry is distinct and dependent upon the tire model. The simplest tire and roadway interaction is that described by the single point contact model, which can be represented by the above geometry when the half contact patch length of the tire 'a' is zero. The point contact model interaction with the roadway is assumed to be in continuous contact with the roadway surface (no wheel hop) and is written mathematically for three distinct operating states:

$$\begin{aligned}
 z &= 0 && \text{for } x < (d - \frac{1}{2} L) \\
 z &= H \sin \frac{\pi}{L} (x - (d - \frac{1}{2} L)) && \text{for } (d - \frac{1}{2} L) \leq x \leq (d + \frac{1}{2} L) \\
 z &= 0 && \text{for } x > (d + \frac{1}{2} L)
 \end{aligned} \tag{F.9}$$

If one considers the contact patch, then the leading edge of the contact patch and the trailing edge of the contact patch each require their own mathematical equations. This is

accomplished simply by re-writing the three states for vertical position  $z$  with a displacement offset of  $a$ , one-half the length of the contact patch. In the case of the leading edge, the roadway obstacle is encountered before the centroid of the tread band contact patch by a distance equal to  $a$ . This phase shift is incorporated into the three states for the vertical position of the leading edge  $z_L$ , the first interface to encounter the obstacle, as follows:

$$\begin{aligned}
 z_L &= 0 && \text{for } x < (d - \frac{1}{2}L - a) \\
 z_L &= H \sin \frac{\pi}{L} (x - (d - \frac{1}{2}L - a)) && \text{for } (d - \frac{1}{2}L - a) \leq x \leq (d + \frac{1}{2}L - a) \quad (\text{F.10}) \\
 z_L &= 0 && \text{for } x > (d + \frac{1}{2}L - a)
 \end{aligned}$$

A similar phase shift of one-half contact patch length is applied to the  $z$  height at the trailing edge (the exit point of the obstacle at the rear) of the contact patch,  $z_R$ . This results in the following three state equations for  $z_R$ :

$$\begin{aligned}
 z_R &= 0 && \text{for } x < (d - \frac{1}{2}L + a) \\
 z_R &= H \sin \frac{\pi}{L} (x - (d - \frac{1}{2}L + a)) && \text{for } (d - \frac{1}{2}L + a) \leq x \leq (d + \frac{1}{2}L + a) \quad (\text{F.11}) \\
 z_R &= 0 && \text{for } x > (d + \frac{1}{2}L + a)
 \end{aligned}$$

For a single point follower model, the effective vertical height of the roadway surface into the tire model is the vertical displacement of a single point. For the two point contact patch model, the effective height of the contact patch,  $z_{\text{EFF}}$ , is the average vertical



position of the leading edge  $z_L$  (entry point of the contact patch) and rearmost edge,  $z_R$ , (exit point of the contact patch) of the flat plane approximation of the contact patch:

$$z_{eff} = \text{average vertical displacement} = \frac{z_L + z_R}{2} \quad (\text{F.12})$$

Since the length of the contact patch ( $2a$ ) and the difference in heights between the leading and trailing edges of the contact patch are known, the angle of incidence of the effective contact patch plane  $\alpha$ , is:

$$\sin \alpha = \frac{(z_L - z_R)}{2a} \text{ radians} \quad (\text{F.13})$$

The geometry of the effective contact patch plane, for a single segment contact patch encountering a sinusoidal roadway obstacle, is illustrated below.

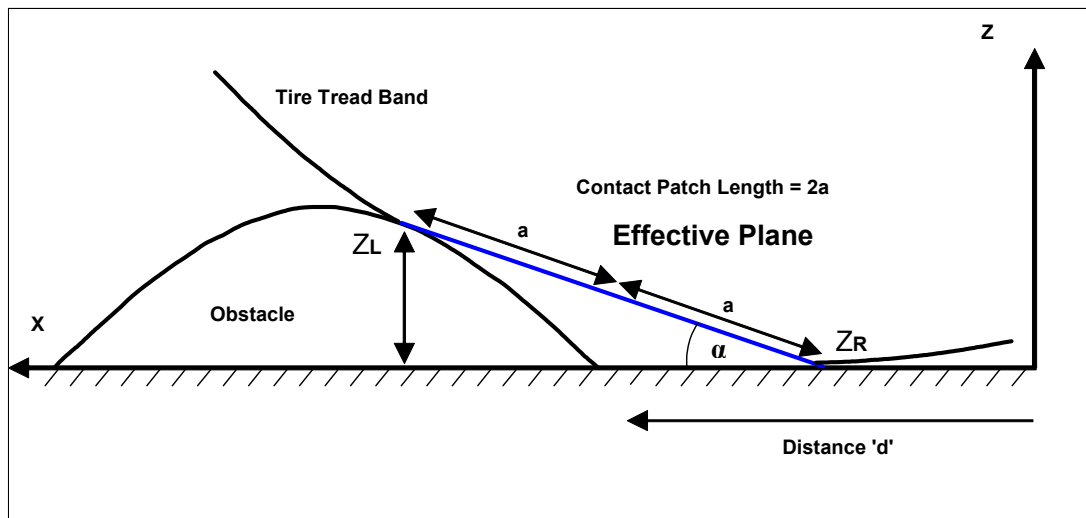


Figure F.2 Geometry of Effective Contact Patch Plane

Understanding the mathematical description of the contact patch leading and trailing edge heights and the model geometry provide insight as to the resulting effective z plane height  $z_{EFF}$  and angle of incidence  $\alpha$  as the tire model traverses the obstacle. Some of the

geometry interactions are quite obvious. One obvious conclusion is that for any given upwardly-protruding roadway obstacle (“bump” as opposed to a “dip”) is that the effective contact patch plane height is:

1. maximum for a point follower (when  $a = \text{zero}$ , maximum vertical input into the tire model is equal to the height of the roadway obstacle)
2. always less than the height of the roadway obstacle for a two point contact patch model
3. zero when the obstacle is in the center of the contact patch, if the length of the obstacle is less than the contact patch length  $2a$ , regardless of the actual obstacle height  $H$

Although far from ideal, it is clear that the single plane contact patch footprint model is an improvement over the single point follower model in that it provides for a representation of the vertical envelopment power of the tire – a mitigating effect of the contact patch length - as the tire rolls over an obstacle. In addition, the single plane footprint model provides a means to determine the angle of incidence  $\alpha$  between the tire and the roadway obstacle. This angle  $\alpha$  is a reasonable physical approximation by which the longitudinal forces can be calculated as the tire contact patch engages and departs from the obstacle. This contrasts with the development of longitudinal forces in the single point follower model. Longitudinal forces in the single point follower model are generated by a relatively crude assumption that there exists a horizontal force component that, when combined with the vertical force generated by the spring and damper, generates a resultant force that is always be normal to the road surface profile at the point

of contact. Note that these calculated resultant longitudinal forces are distinct and separate from traction driving or braking forces generated as a result of any differential interface velocity between the tread band and the roadway/obstacle surface.

### Development of the Rectangular Cleat

The rectangular roadway obstacle, or cleat, is a practical excitation method for indoor tire testing on a laboratory test drum. Cleats can be either perpendicular to the direction of travel (parallel to the tire spin axis) or angled. Although angled cleats can be used to test the generation of lateral force ( $F_y$ ) and compliance about the vertical steering axis ( $M_z$ ) in three dimensional tire modeling, perpendicular cleats are still a primary means of exciting both two and three dimensional models for comfort modeling. A simple perpendicular rectangular cleat has several intrinsic advantages for measuring tire comfort performance as it:

1. provides an input pulse much like what is seen when a tire encounters many relevant real-world obstacles, such as concrete highway expansion joints,
2. represents a complete spectrum of excitation frequencies,
3. solicits the enveloping power of the tire (the tire's ability to drape over an obstacle as it passes through the contact patch as opposed to deflecting up and above the obstacle).

Unfortunately, use of a rectangular cleat also presents some distinct limitations. For example, the period of the pulse, or the engagement time of the cleat, is linked to the test speed of the drum. Since the dynamic response of a rolling tire depends not only upon the

speed of the tire rotation but also the length of the cleat engagement relative to the length of the contact patch, the width of the cleat cannot be adjusted to provide a constant period of engagement for different speeds – the effect of the cleat width and the tire speed are intrinsically confounded.

Another important consideration with cleats is the selection of their dimensions. Cleat height and cleat width both greatly influence the solicitation of the many distinct physical regimes of the tire structure. For example, a small cleat comprised of relatively low cross section height will solicit principally the tread band and potentially the belt package in the summit but will not significantly solicit the sidewall or the bead area surrounding the rim. If the test wheel is fitted with a progressively higher cleat cross section height while maintaining a constant cleat width, not only are there increases in the tread band localized contact pressures, but also greater changes in the radius of curvature in the composite belt structure as the contact patch traverses the cleat. One must progress to larger cleat heights before beginning to significantly alter solicitation of the sidewall carcass composites and even further still for the bead area adjacent to the rim. Similar arguments can be made for the width of the cleat. For example, the wider the cleat (longer length relative to the tire contact patch) for a given constant cleat height, the greater the solicitation of the carcass plies due to the corresponding increase in sidewall deflection and carcass ply deradialization to accommodate the increase in vertical spindle load forces.

Generation of a model to represent a rectangular cleat for both MatLab Simulink and SIMPACK MBS requires a mathematical definition for vertical cleat height as a

function of longitudinal position of the tread band along the roadway. Since the time step integration process is more robust and is solved more quickly with continuous functions, an approximation of the rectangular cleat is needed. The criteria chosen for the development of the function for the rectangular cleat are:

1. the function should be continuous through the first derivative
2. the function will be convex within the prescribed length of the cleat (i.e., the second derivative will be negative between  $-L/2$  and  $+L/2$ )
3. the original cleat height will be maintained (i.e., the peak value of the function will be equal to the height of the cleat)
4. the cross sectional area of the rectangular cleat and the cleat function will be equal

Based upon the above criteria it becomes mathematically expedient to choose a cosine function as the basis for the cleat vertical displacement model. Since the height of the cleat and the peak value of the mathematical function are to be identical, satisfaction of the constant area criteria and the convex criteria dictate that the length of the function representing the cleat will be greater than the width of the cleat. It becomes convenient, when using the trig functions, to define the length of the mathematical function to be a multiple of the cleat width. For cleat and tire contact patch length geometry typically used in laboratory testing, the length of the cleat is reasonably represented by modeling the width by a factor of two – the cosine function representing the width of the modeled cleat will be twice the width of the cleat.

The above criteria - modeling a rectangular cleat to be twice as long as its actual width - appears to be a reasonable approximation. This is because the enveloping phenomenon as the tire contact patch drapes over a cleat is not only a global effect along the length of the contact patch, it is also a local effect that occurs at the leading and trailing edges of the cleat. As the leading edge of the contact patch encounters the cleat, the tread sculpture deforms in response to the high local stresses at the square shoulder of the cleat. The same phenomenon occurs in reverse when the edge of the tread disengages from the cleat edge. The result is that the cleat is in effect functionally wider and its interaction with the tire contact patch is less abrupt, much like the sinusoidal approximation. Additional physical effects of the engagement between the tread and the cleat include a reduction in the peak deformation forces and a suppression of the high frequency content of the rectangular cleat's impulse. Since the amount of force and frequency attenuation will depend upon the shape and rigidity of the tread blocks relative to the size and shape of the cleat, the stiffness of the under tread and belt package, etc. – one cannot take this into account without modal and finite element modeling. Therefore, these mitigating effects will be assumed to be relatively constant and reasonably approximated using this approach.

The representation of an equivalent model for a two-dimensional cleat to be used with the tire models is illustrated in Figure F.3, below.

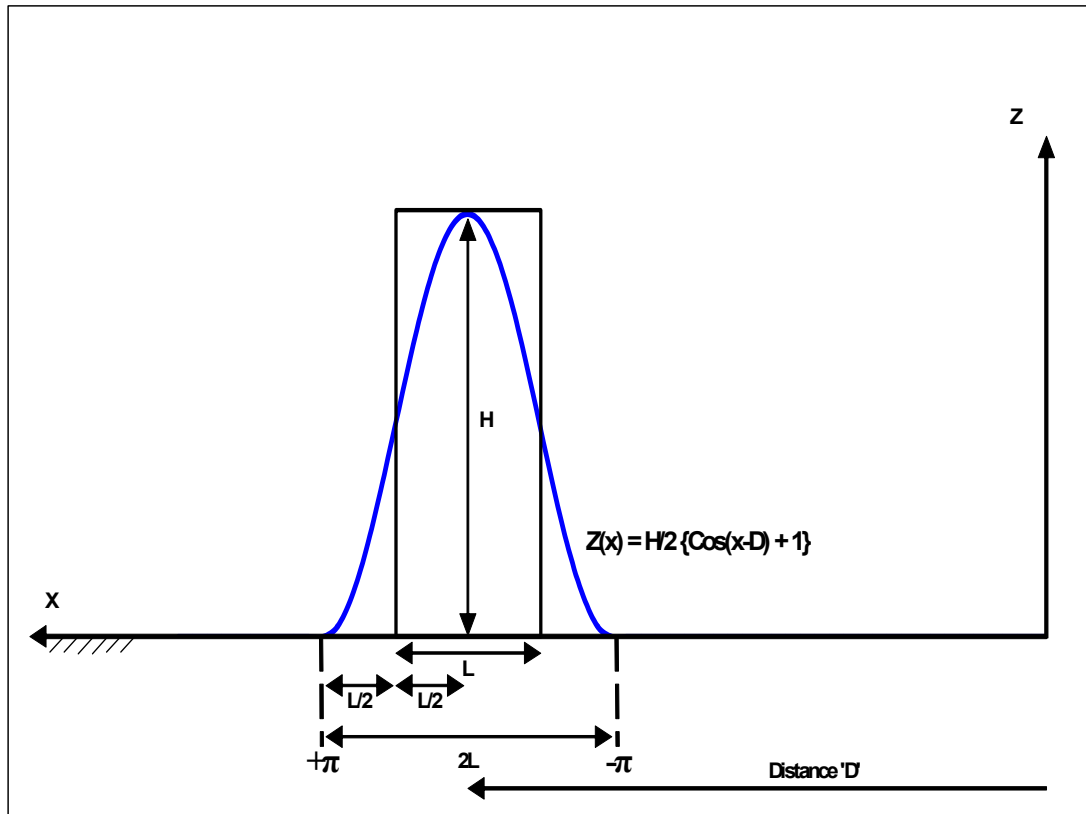


Figure F.3 Geometry of an Equivalent Model for a Rectangular Cleat

The mathematical expression for the cleat is obtained using the same strategy as that used for the sinusoidal bump - defining the three states before, during, and after the tread band encounters the obstacle:

$$\begin{aligned}
 z &= 0 && \text{for } x < (d - \pi) \\
 z &= \frac{H}{2} (\cos(x - d) + 1) && \text{for } (d - \pi) \leq x \leq (d + \pi) \\
 z &= 0 && \text{for } x > (d + \pi)
 \end{aligned} \tag{F.14}$$

The above cosine expression satisfies the first three criteria for the mathematical representation of the cleat for cleat length  $L = \pi$ , i.e., the first derivative of the function is piecewise continuous, the function is convex within the length  $L$  of the cleat and concave or planar elsewhere, and the original cleat height  $H$  is maintained.

In order to satisfy the final criteria, the cross sectional area of the rectangular cleat must be identical to area of the modeling functions. This can be most easily achieved mathematically by 1) evaluating the function without the initial offset distance  $d$  and then 2) changing the limits of integration for the function in  $x$  using  $L = \pi$ , which maintains one complete spatial wavelength period of the cosine function over distance  $2L$ . The results can be checked by integrating the obstacle function over one complete spatial cycle to determine if its area remains equal to the area of the cleat being modeled.

Writing the cleat model without the offset distance  $d$  yields the following:

$$\text{Area of cleat} = HL \Leftrightarrow \text{Area of function} = \int_{-\pi}^{\pi} \frac{H}{2} (\cos(x + 1)) dx \quad (\text{F.15})$$

Evaluate the right hand side by taking advantage of the symmetry of the even function:

$$\text{Area of function} = 2 \times \frac{H}{2} \int_0^{\pi} (\cos(x + 1)) dx \quad (\text{F.16})$$

Splitting the function into two definite integrals:

$$\text{Area of function} = H \left\{ \int_0^{\pi} \cos(x) dx + \int_0^{\pi} 1 dx \right\} \quad (\text{F.17})$$

Substituting variables and the corresponding limits of the definite integrals:

$$\text{Area of function} = H \left\{ \int_0^L \cos\left(\frac{\pi}{L}x\right) dx + \int_0^L \frac{\pi}{L} dx \right\} \quad (\text{F.18})$$

Integrating and simplifying the resulting definite integrals:

$$\text{Area of function} = H \left\{ \sin\left(\frac{\pi}{L}x\right) \Big|_0^L + \left(\frac{\pi}{L}x\right) \Big|_0^L \right\} \quad (\text{F.19})$$



$$\text{Area of function} = H\{\sin(\pi) - \sin(0) + \pi - 0\} \quad (\text{F.20})$$

$$\text{Area of function} = H\pi \quad (\text{F.21})$$

By inspection, when  $L = \pi$  the area of the function ( $H\pi$ ) is equal to the area of the cleat (HL). Therefore substituting:

$$\frac{\pi}{L}x \Rightarrow x \quad (\text{F.22})$$

into the state equations I.13 satisfies all of the established model criteria and provides the necessary mathematical representation for simulating the rectangular cleat:

$$\begin{aligned} z = 0 & \quad \text{for } x < (d - \frac{\pi}{L}) \\ z = \frac{H}{2} \left( \cos(\frac{\pi}{L}x - d) + 1 \right) & \quad \text{for } (d - \frac{\pi}{L}) \leq x \leq (d + \frac{\pi}{L}) \\ z = 0 & \quad \text{for } x > (d + \frac{\pi}{L}) \end{aligned} \quad (\text{F.23})$$

The final state equations for the point follower just developed for the cleat obstacle are modified for the two point contact patch model in a manner identical to that of the sinusoidal bump obstacle (equations I.9 and I.10). The equations for the contact patch leading edge ( $z_L$ ) and trailing edge ( $z_R$ ) are offset by subtracting or adding one half of the contact patch length 'a', respectively. For the leading edge of the contact patch ( $z_L$ ):

$$\begin{aligned}
z &= 0 && \text{for } x < \left(d - \frac{\pi}{L} - a\right) \\
z &= \frac{H}{2} \left( \cos\left(\frac{\pi}{L}x - d\right) + 1 \right) && \text{for } \left(d - \frac{\pi}{L} - a\right) \leq x \leq \left(d + \frac{\pi}{L} - a\right) \\
z &= 0 && \text{for } x > \left(d + \frac{\pi}{L} - a\right)
\end{aligned} \tag{F.24}$$

Similarly, for the trailing edge of the contact patch ( $z_R$ ):

$$\begin{aligned}
z &= 0 && \text{for } x < \left(d - \frac{\pi}{L} + a\right) \\
z &= \frac{H}{2} \left( \cos\left(\frac{\pi}{L}x - d\right) + 1 \right) && \text{for } \left(d - \frac{\pi}{L} + a\right) \leq x \leq \left(d + \frac{\pi}{L} + a\right) \\
z &= 0 && \text{for } x > \left(d + \frac{\pi}{L} + a\right)
\end{aligned} \tag{F.25}$$

Once the heights of the leading and trailing edges of the contact patch are defined, the expressions for the contact patch effective plane height (equation I.11) and the angle of incident  $\alpha$  (equation I.12) are identical.

## Appendix G

### G. Future Simulation Improvements

#### Modifications to the Constant Footprint Model

For obstacles whose wavelength is significantly shorter than the contact patch length, the averaging effect of the constant footprint results in an underestimation of the vertical spindle forces. This is because the vertical stiffness in the contact patch is obtained by measuring the vertical deflection stiffness on a flat plate – there are no bending moments or shear forces between the tread elements and the summit that would be present if the measurements were taken with a cleat in the contact patch. As a result, the “window averaging” of the vertical stiffness in the constant footprint contact model will underestimate the vertical spindle forces as the model assumes no bending stiffness in the contact patch. Since the horizontal spindle components are calculated such that the resultant force vector is always normal to the obstacle surface, the horizontal spindle forces will also be underestimated. Figure G.1 illustrates these underestimations for the constant footprint model while traversing a rectangular cleat.

In order to improve the vertical response, it is possible to adjust the distributed vertical stiffness in the contact patch models by a ratio of the contact patch length to the obstacle length, thereby restoring a representative value for the vertical spring stiffness. This improvement results in the simulated spindle forces as shown in Figure G.2:

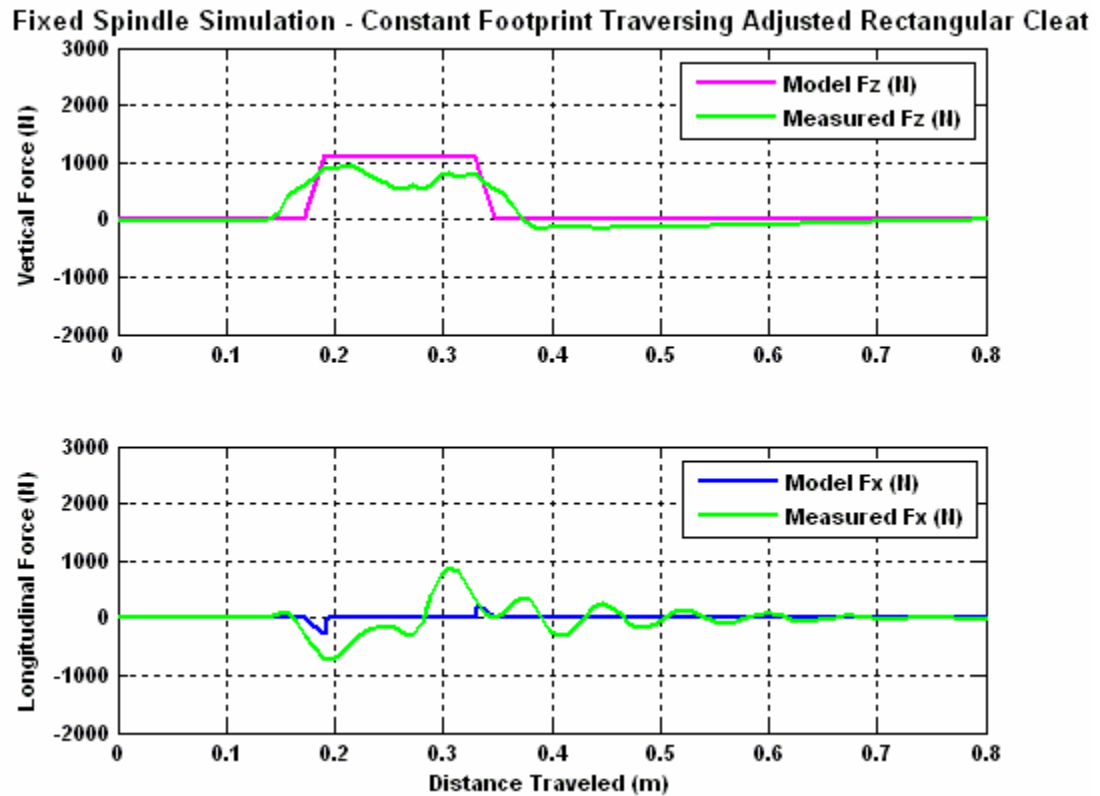


Figure G.1: “Simple” Constant Footprint Model – Adjusted Vertical Stiffness

Although the vertical spindle forces are improved, the horizontal forces are still underestimated. This is because the effective average angle of the constant footprint as it “drapes” over the filtered obstacle is small at the entry and exit of the contact patch, and zero as long as the entire obstacle is enveloped within the confines of the contact patch. Figure G.2 illustrates the potential to “tune” the constant footprint model by adjusting the engagement angle by a constant factor, thereby increasing or decreasing the horizontal spindle force gain.

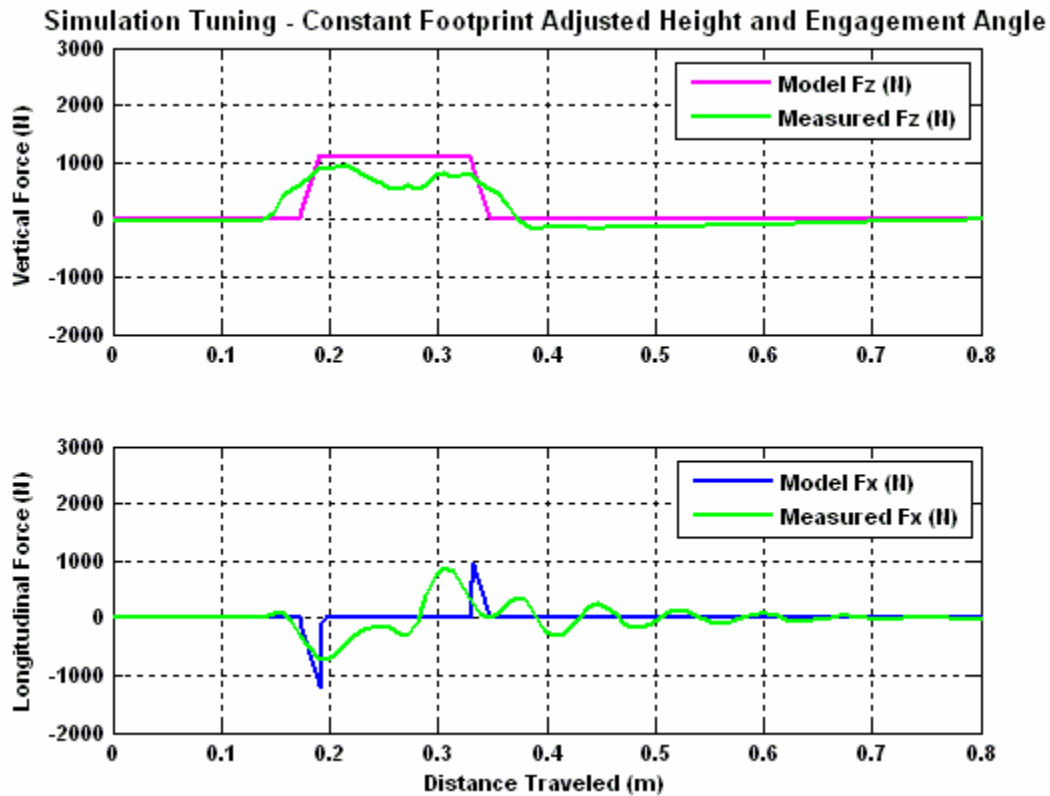


Figure G.2: “Simple” Constant Footprint – Adjusted Model Traversing Cleat

These two modifications on the work by Captain et al [5] – vertical stiffness and obstacle engagement angle – can provide significant improvements in the simulated spindle forces when the contact patch length is greater than the obstacle length (in this instance, the constant footprint is 8.3 times the length of the rectangular cleat). Although adjusting the vertical stiffness by the ratio of the contact patch length to cleat length can be justified, there is no clear justification for selecting a gain factor for the engagement angle. Since the purpose of this investigation is to evaluate the models without the benefit of *a priori* knowledge of the model performance, no gain or tuning adjustments are used in any of the simulations except for this illustrative example.

### FTire Simulated Contact Patch Length

Fixed spindle, tire force simulations indicate a discrepancy between the apparent engagement lengths of the cleat and the tire for all tire models. There are two reasons for this discrepancy:

1. All the models assume a flat road surface instead of a curved laboratory road wheel.
2. The MatLab Simulink models assume that the obstacle engagement length is the same as the contact patch length – the models do not take into account the effect of obstacle height on engagement length, as shown in Figure G.3.

The engagement length for all tire models, with the exception of the FTire model, was assumed to be the same length as the contact patch. The FTire model engagement length accounts for the obstacle height automatically. Although the FTire model can simulate the curved surface of a laboratory road wheel, for consistency a flat surface was chosen for all models.

The change in contact patch geometry on a road wheel versus a flat surface will depend upon:

1. structural characteristics of the tire
2. geometry associated with the loading of a small diameter tire on a large diameter road wheel

Although these effects of road wheel curvature are complex, they are considered to be small and constant between all of the tire models and will not be taken into account for this investigation.

The geometry with which to calculate the exact change in obstacle engagement length, even on a flat surface, is complicated by the distortion of the tire radius before the entrance and after the exit of the contact patch. However, an approximation can be obtained by using geometry associated with the free radius of the tire, the tire contact patch length, and the height of the obstacle.

The first step in approximating a percentage change in the engagement length is to analyze the geometry of a cleat engaging a deflected tire on a flat surface as in Figure G.3.

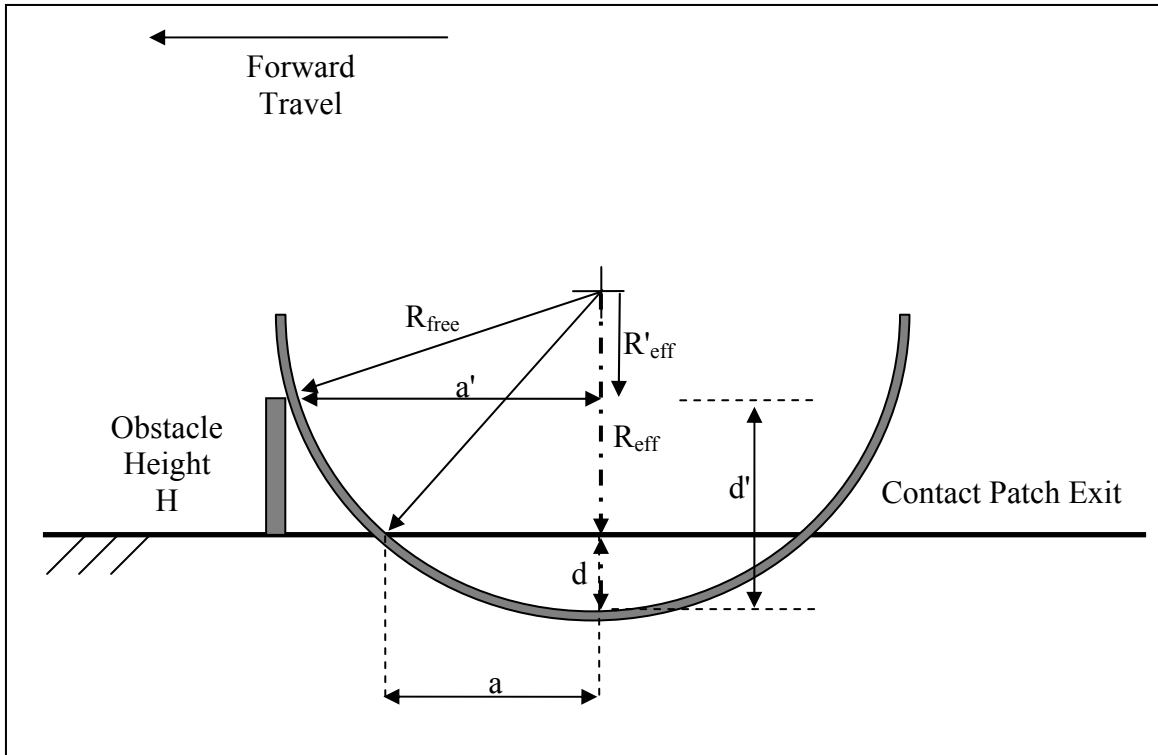


Figure G.3: Cleat Engagement of the Contact Patch on a Flat Surface

For our models,  $R_{eff}$  is the effective radius of the tire such that the tire spin velocity times the effective radius is equal to the forward velocity of the tire/wheel assembly (free rolling, no slip). The contact patch length,  $2a$ , was previously determined for a given static vertical load by setting the load equal to the contact patch area multiplied by the inflation pressure. Using the prime notation to denote those variables whose length has been altered by taking into account the cleat obstacle height  $H$ :

$$R'_{eff} = R_{eff} - H \quad (G.1)$$

Using the Pythagorean Theorem to solve for the half contact patch lengths  $a$  and  $a'$  yields:

$$a = \sqrt{R_{free}^2 - R_{eff}^2} \quad (G.2)$$



$$a' = \sqrt{R_{free}^2 - R_{eff}^2} \quad (G.3)$$

Writing the lengths of the half contact patch as a ratio of Equations G.2 and G.3:

$$\frac{a'}{a} = \sqrt{\frac{R_{free}^2 - R_{eff}^2}{R_{free}^2 - R_{eff}^2}} \quad (G.4)$$

Substituting in the expression for the effective radius taking into account the cleat height,  $R'_{eff}$ , from Equation 5.1:

$$\frac{a'}{a} = \sqrt{\frac{R_{free}^2 - R_{eff}^2 + 2HR_{eff} - H^2}{R_{free}^2 - R_{eff}^2}} \quad (G.5)$$

Substituting for  $R_{free}^2$  from Equation 5.2 and simplifying yields:

$$\frac{a'}{a} = \sqrt{\frac{a^2 + 2HR_{eff} - H^2}{a^2}} \quad (G.6)$$

Or, to find the value of  $a'$  given  $a$ ,  $H$ , and  $R_{eff}$  yields:

$$a' = \sqrt{a^2 + 2HR_{eff} - H^2} \quad (G.7)$$

Substituting in values for our road wheel, cleat height, and effective rolling radius of the deflected tire, it can be determined that the height of the cleat obstacle on a flat surface increases the effective engagement length by approximately 38% for this tire/load/obstacle combination.

The MatLab Simulink models all use the contact patch length to define the engagement length. Referring to the simulation outputs, it can be seen that the MatLab Simulink simulations all underestimate the engagement length on the laboratory road wheel by approximately 30%. This underestimation is a combination of both:

- cleat geometry

- road wheel curvature

The FTire simulation results for a flat surface overestimates the engagement length as measured on the road wheel by approximately 8%. Since the FTire simulations take into account the cleat geometry on a flat surface, one can assume that the 8% error is due to the road wheel curvature. One can then assume that the 30% underestimation of engagement length for the MatLab Simulink models is the combination of the 38% calculated underestimation due to cleat geometry on a flat surface and the 8% overestimation due to the drum curvature.

The change in cleat engagement length using this calculation helps account for the differences in engagement lengths. However, the calculation is only a first order approximation, as it does not take into account the true radius of curvature of the tire before and after the contact patch, or differences associated with either the cleat length or cleat geometry (rectangular, sinusoidal, or trapezoidal). Therefore it was decided that the simulations would continue to use the contact patch length as the engagement length, and accounting for cleat height and geometry effects with the different models would be relegated to future work.

## REFERENCES

- [1] Schmeitz, Antonious Jacobus Catherinus “A Semi-Empirical Three Dimensional Model of the Pneumatic Tyre Rolling over Arbitrarily Uneven Road Surfaces,” Technische Universiteit Delft, Netherlands, ISBN 90-9018380-9, September 2004
- [2] Chae, S., El-Gindy, M., Johansson, I., Öijer, F., Trivedi, M. “In-Plane and Out-of-Plane Dynamic Response Predictions of a Truck Tire Using Detailed Finite Element and Rigid Ring Models,” Source: Proceedings of the 2005 ASME International Mechanical Engineering Congress and Exposition, Florida, USA, IMECE2005-79083, November 5-11, 2005
- [3] Gough, V.E. and Jones, P.W.B., “Tyre Testing,” Source: Automobile Engineer, January 1952
- [4] Lippmann, S.A. and Nanny, J.D., “A Quantitative Analysis of the Enveloping Forces of Passenger Tires,” SAE Paper No. 670174, January 1967
- [5] Captain, Khushroo M. et al., “The Development and Comparative Evaluation of Analytical Tire Models for Dynamic Vehicle Simulation,” Foster Miller Associates, Inc., Prepared for the Army Tank Automotive Command (ATAC), Source: National Technical Information Service, U.S. Department of Commerce, May 1974
- [6] Kisilowski, J. et al., “Modelling and Simulating the Braking Process of Automotive Vehicle on Uneven Surface,” (Warsaw Technical Univ, Inst of Transport, Warsaw, Pol), Source: Vehicle System Dynamics, v 14, n 1-3, Jun, 1985, p 82-86
- [7] Zegelaar, P.W.A. et al., “Tyre Models for the Study of In-Plane Dynamics,” (Delft Univ of Technology), Source: Vehicle System Dynamics, v 23, n SUPPL, 1994, p 578-590
- [8] Guo, Konghui and Liu, Qing, “A Model of Tire Enveloping Properties and Its Application on Modelling of Automobile Vibration Systems,” SAE Paper 980253, 1998.
- [9] Schmeitz, Antonious Jacobus Catherinus, et al., “Application of a Semi-Empirical Dynamic Tyre Model for Rolling Over Arbitrary Road Profiles,” International Journal of Vehicle Design, Volume 36, Nov 2-3, 2004, p 194-215.

- [10] Gipser, M., "FTire – the tire simulation model for all applications related to vehicle dynamics," *Vehicle System Dynamics*, Vol. 45, Supplement, 2007, p 139-151
- [11] Eichberger, A. and Schittenhelm, M., "Implementations, Applications and Limits of Tyre Models in Multibody Simulation," *Vehicle System Dynamics*, Vol. 43, Supplement, 2005, p 18-29
- [12] Lugner, P. et al. "Recent Advances in Tyre Models and Testing Procedures," *Vehicle System Dynamics*, Vol. 43, No. 6-7, June-July 2005, p 413-436
- [13] Wong, J.Y., "Theory of Ground Vehicles," 3rd Edition, John Wiley & Sons, Inc., New York, N.Y., 2001.
- [14] Kreyszig, E., "Advanced Engineering Mathematics," 8<sup>th</sup> Edition, John Wiley & Sons, Inc., New York, N.Y., 1999.
- [15] Tiwari, S. et al., "AMGA: An Archive-based Micro Genetic Algorithm for Multi-Objective Optimization," *Genetic and Evolutionary Computation Conference 2008, Special Interest Group for Genetic and Evolutionary Computation, Association for Computing Machinery, July 12-16, 2008, Atlanta, Georgia*